Geochemical kinetics during CO_2 sequestration: the reactivity of the Hontomín **caprock** and the hydration of **MgO**

Gabriela Dávila Ordoñez

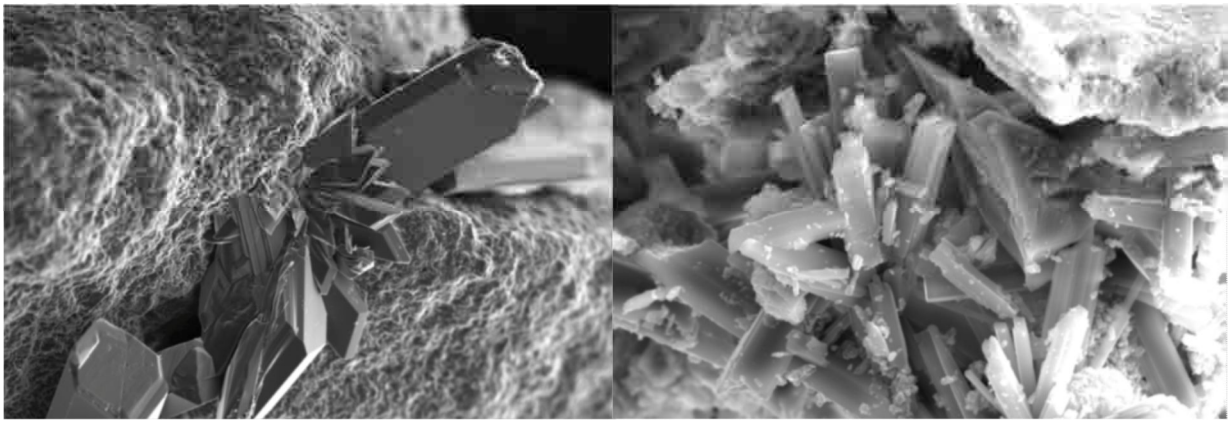

PhD Thesis

Department of Geotechnical Engineering and Geo-Sciences (ETCG)
Technical University of Catalonia (UPC)

Supervisors:
Dr. Jordi Cama Dra. Linda Luquot Dr. Josep M. Soler

Institute of Environmental Assessment and Water Research
(IDAEA-CSIC)

UPC idaea CSIC CONSEJO SUPERIOR DE INVESTIGACIONES CIENTÍFICAS

UNIVERSITAT POLITÈCNICA DE CATALUNYA
BARCELONATECH
Escola de Doctorat

Acta de calificación de tesis doctoral	**Curso académico:**

Nombre y apellidos: MARIA GABRIELA DÁVILA ORDOÑEZ

Programa de doctorado:

Unidad estructural responsable del programa

Resolución del Tribunal

Reunido el Tribunal designado a tal efecto, el doctorando / la doctoranda expone el tema de la su tesis doctoral titulada

_____

_____.

Acabada la lectura y después de dar respuesta a las cuestiones formuladas por los miembros titulares del tribunal, éste otorga la calificación:

☐ NO APTO ☐ APROBADO ☐ NOTABLE ☐ SOBRESALIENTE

(Nombre, apellidos y firma) Presidente/a	(Nombre, apellidos y firma) Secretario/a	
(Nombre, apellidos y firma) Vocal	(Nombre, apellidos y firma) Vocal	(Nombre, apellidos y firma) Vocal

_____, _____ de _____ de _____

El resultado del escrutinio de los votos emitidos por los miembros titulares del tribunal, efectuado por la Escuela de Doctorado, a instancia de la Comisión de Doctorado de la UPC, otorga la MENCIÓN CUM LAUDE:

☐ SÍ ☐ NO

(Nombre, apellidos y firma) Presidente de la Comisión Permanente de la Escuela de Doctorado	(Nombre, apellidos y firma) Secretario de la Comisión Permanente de la Escuela de Doctorado

Barcelona a _____ de _____ de _____

TECHNICAL UNIVERSITY OF CATALONIA (UPC)
DEPARTMENT OF GEOTECHNICAL ENGINEERING AND GEO-SCIENCES (ETCG)

Geochemical kinetics during CO_2 sequestration: the reactivity of the Hontomín **caprock** and the hydration of **MgO**

Thesis presented by

Gabriela Dávila Ordoñez

Work conducted in the Institute of Environmental Assessment and Water Research (IDAEA-CSIC) under the supervision of

Dr. Jordi Cama i Robert

Institute of Environmental Assessment and Water Research (IDAEA), CSIC

Dra. Linda Luquot

Institute of Environmental Assessment and Water Research (IDAEA), CSIC

Dr. Josep M. Soler

Institute of Environmental Assessment and Water Research (IDAEA), CSIC

Barcelona, November 2015

This thesis has been supported by a JAE-Predoc grant under the Program “Junta para la Ampliación de Estudios” by CIUDEN (project ALM11/009), Spanish Government Project CGL2010-20984-CO2-01 and the PANACEA project (European Community’s Seventh Framework Programme FP7/2007-2013 under grant agreement number 282900).

It is Only Impossible If You don´t Try!

Abstract

A test site for CO_2 geological storage is situated in Hontomín (Burgos, Northern Spain) with a reservoir rock that is mainly composed of limestone. The reservoir rock is a deep saline aquifer, which contains a NaCl- and sulfate-rich groundwater in equilibrium with calcite and gypsum, and is covered by a very low permeability formation composed of marls, marly limestone and bituminous shales which acts as a caprock. During and after CO_2 injection, since the resident groundwater contains sulfate, the resulting CO_2-rich acid solution may give rise to the dissolution of calcite (carbonate mineral) and albite, illite and clinochlore (Si-bearing minerals), and secondary sulfate-rich mineral precipitation (gypsum or anhydrite) together with that of Si-bearing minerals (clay and zeolites) may occur. These reactions that may imply changes in the porosity, permeability and pore structure of the rock could alter the CO_2 seal capacity of the caprock.

Therefore, performing reliable experiments and reactive transport modeling to gain knowledge about the overall process of gypsum precipitation at the expense of calcite dissolution in CO_2-rich solutions and its implications for the hydrodynamic properties of the caprock is necessary.

A first aim of this thesis is to better understand these coupled reactions by assessing the effect that P, pCO_2, T, mineralogy, acidity and solution saturation state exert on these reactions. To this end, flow-through experiments with illite powder samples and flow-through experiments and columns filled with crushed marly limestone, bituminous black shale and marl are conducted under different P–pCO_2 conditions (atmospheric: $1–10^{-3.5}$, subcritical: 10–10 bar and supercritical: 150–37 bar), T (25 and 60 °C) and input solution compositions (gypsum-undersaturated and gypsum-equilibrated solutions). The CrunchFlow numerical code was used to perform 1D reactive transport simulations of the experiments to evaluate mineral reaction rates in the system and quantify the porosity variation along the columns.

A second aim of this PhD study is to evaluate the interaction between the Hontomín marl and CO_2-rich sulfate solutions under supercritical CO_2 conditions (P_{Total} = 150 bar, pCO_2 = 61 bar and T = 60 °C). Percolation experiments were performed using artificially fractured cores to elucidate (*i*) the role of the composition of the injected solutions (*S-free* and *S-rich* solutions) and (*ii*) the

effect of the flow rate (0.2, 1 and 60 mL h^{-1}) on fracture permeability. Major dissolution of calcite (*S-free* and *S-rich* solutions) and precipitation of gypsum (*S-rich* solution) together with minor dissolution of the silicate minerals contributed to the formation of an altered skeleton-like zone (mainly made up of unreacted clays) along the fracture walls. Dissolution patterns changed from face dissolution to wormhole formation and uniform dissolution with increasing Peclet numbers.

In *S-free* experiments, fracture permeability did not significantly change regardless of the flow rate despite the fact that a large amount of calcite dissolved. In *S-rich* solution experiments, fracture permeability decreased under slow flow rates (0.2 and 1 mL h^{-1}) because of gypsum precipitation that sealed the fracture. At the highest flow rate (60 mL h^{-1}), fracture permeability increased because calcite dissolution predominated over gypsum precipitation.

2D reactive transport models were used to interpret the results of the experiments (not at 60 mL h^{-1}) and reproduced the variation in the outflow composition with time and the observed width of the alteration zone along the fractures. The good match was achieved by using an initial D_{eff} value from 3×10^{-13} m^2 s^{-1} to 1×10^{-13} m^2 s^{-1} under slow flow rate and by increasing it by a factor of 20 (6×10^{-12} m^2 s^{-1}) in the rock matrix under fast flow rate. Additionally, a slight change in the calcite reactive surface areas contributed to the fit of the model to the experimental data.

The modeling reproduced the large dissolution of calcite, minor dissolution of clinochlore and gypsum precipitation. Calcite dissolution was favored by increasing the flow rate and gypsum precipitation was large under 1 mL h^{-1} flow conditions. Minor precipitation of dolomite, kaolinite and two zeolites (mesolite and stilbite) along the altered zone was likely. The magnitude of these reactions is consistent with the measured increase in porosity over the altered zone, which was fairly reproduced.

The third aim is to study caustic magnesia (MgO) as an alternative to Portland cement, not only to be used in the space between the well casing and the rock but also to seal rock fractures (grouting). The overall MgO-carbonation process is considered to happen when MgO hydrates rapidly to form brucite ($Mg(OH)_2$). When brucite dissolves in a Ca-rich and CO_2-saturated solution, the solution supersaturates with respect to Ca and/or Mg carbonates (e.g., dolomite

($CaMg(CO_3)_2$), nesquehonite ($MgCO_3 \cdot 3(H_2O)$), hydromagnesite ($Mg_5(CO_3)_4(OH)_2 \cdot 4(H_2O)$) and magnesite ($MgCO_3$)). Different T and pCO_2 conditions will determine the formation of these carbonates. The molar volumes of the implicated minerals ($cm^3\ mol^{-1}$) [($Mg(OH)_2$ (24.63), $CaCO_3$ (36.93), $MgCO_3$ (28.02), $CaMg(CO_3)_2$ (64.37), $Mg_5(CO_3)_4(OH)_2 \cdot 4(H_2O)$ (208.08), $MgCO_3 \cdot 3(H_2O)$ (75.47)], with large molar volumes for the secondary phases, favor a potential decrease in porosity and hence the sealing of cracks in cement structures, preventing CO_2 leakage.

As a preliminary study for the potential use of MgO as an alternative to Portland cement in injection wells, MgO carbonation has been studied by means of batch experiments under subcritic (pCO_2 of 10 and 50 bar and T of 25, 70 and 90 °C) and supercritic (pCO_2 of 74 bar and T of 70 and 90 °C) CO_2 conditions.

Magnesium oxide reacts with CO_2-containing and Ca-rich water nearly equilibrated with respect to calcite. MgO quickly hydrates to brucite which dissolves causing the precipitation of magnesium carbonate phases. Precipitation of these secondary phases (magnesite and/or metastable phases such as nesquehonite or hydromagnesite depends on pCO_2, temperature and solid/water content. In a constant solid/water ratio, the precipitation of the non-hydrated Mg carbonate is favored by increasing temperature and pCO_2.

The experimental variation of Mg and Ca concentrations and pH with time at the different temperatures and pCO_2 has been simulated using the CrunchFlow reactive transport code. Simulations reproduce the experimental evolution of the aqueous concentrations and indicate a decrease in porosity when increasing temperature and pCO_2. This decrease in porosity would be beneficial for the sealing properties of the cement. These results have been used in the simulation of an application case with a deep borehole surrounded by MgO cement at 90 °C.

Resum

Un lloc de prova per a l'emmagatzematge geològic de CO_2 es troba en Hontomín (Burgos, nord d'Espanya) on la roca reservori es compon principalment de roca calcària. La roca reservori és un aqüífer salí profund, que conté una aigua subterrània rica en NaCl- i sulfat en equilibri amb calcita i guix, i està coberta per una formació de molt baixa permeabilitat composta de margues, calcàries margoses i lutites bituminoses, que actua com a roca segell. Durant i després de la injecció de CO_2, com que l'aigua subterrània resident conté sulfat, la solució àcida resultant rica en CO_2 pot donar lloc a la dissolució de calcita, albita, illita i clinoclor (minerals rics en Si), i precipitació de minerals de sulfat (guix o anhidrita), juntament amb la de minerals rics en Si (argiles i zeolites). Aquestes reaccions que poden implicar canvis en l'estructura de la porositat, la permeabilitat i dels porus de la roca podrien variar la capacitat de segellat de CO_2 de la roca segell.

Per tant, és necessària la realització d'experiments fiables i la modelització del transport reactiu per adquirir un millor coneixement sobre el procés general de la precipitació de guix, a costa de la dissolució de calcita en solucions riques en CO_2 i les seves implicacions per a les propietats hidrodinàmiques de la roca segell.

Un **primer objectiu** d'aquesta tesi és poder comprendre aquestes reaccions acoblades mitjançant l'avaluació dels efectes que la P, pCO_2, T, la mineralogia, l'acidesa i l'estat de saturació de la solució exerceixen sobre aquestes reaccions. Amb aquesta finalitat, es duen a terme els experiments de flux continu amb mostres de pols amb illita i experiments de flux i de columna plens amb llim margós, bituminós negre i margues triturades en diferents condicions (P_{Total}–pCO_2 atmosfèrica: 1–$10^{-3.5}$, subcríticas: 10–10 bar i supercríticas: 150–37 bar), T (25 i 60 °C) i diferents composicions de la solució d'entrada (solucions subsaturades i en equilibri respecte del guix). Es va utilitzar el codi numèric CrunchFlow per dur a terme simulacions de transport reactiu 1D per avaluar les velocitats de reacció mineral al sistema i quantificar la variació de la porositat al llarg de les columnes.

Un **segon objectiu** d'aquest estudi de doctorat és avaluar la interacció entre la marga d'Hontomín i solucions de sulfat riques en CO_2 sota condicions de CO_2 supercrític (P_{Total} = 150 bar, pCO_2 = 61 bar i T = 60 °C). Es van realitzar experiments de percolació usant testimonis fracturats artificialment per dilucidar (*i*) el paper de la composició de les solucions injectades (solucions sense S i solucions riques en S), (*ii*) l'efecte de la velocitat de flux (0.2, 1 i 60 ml h^{-1}) en la permeabilitat de la fractura. Una major dissolució de calcita (ambdós solucions), i la precipitació de guix (solució rica en S), juntament amb una menor dissolució dels minerals de silici, van contribuir a la formació d'una zona alterada (constituïda principalment d'argiles gairebé sense reaccionar) al llarg de les parets de la fractura. Els patrons de dissolució van canviar de tipus "dissolució d'entrada" (face dissolution) a "forat de cuc" (wormhole) i "dissolució uniforme" (uniform dissolution) amb l'increment del número de Peclet.

En els experiments en solucion sense S, la permeabilitat de la fractura no va canviar significativament, independentment de la velocitat de flux i de la dissolució significativa de calcita. En els experiments en solució rica en S, la permeabilitat de la fractura es va reduir a velocitat baixes de flux (0,2 i 1 mL h^{-1}) a causa de la precipitació de guix que va segellar la fractura. A la velocitat de flux més alta (60 ml h^{-1}), la permeabilitat de la fractura va augmentar a causa de la dissolució de calcita que va predominar sobre la precipitació de guix.

Es van realitzar models 2D de transport reactiu per interpretar els resultats dels experiments (no els de 60 ml h^{-1}) que van reproduir la variació en la composició de flux de sortida amb el temps i l'amplada de la zona d'alteració observada al llarg de les fractures. Es va aconseguir un bon resultat amb l'ús d'un valor inicial de D_{eff} de 3×10^{-13} m^2 s^{-1} fins a 1×10^{-13} m^2 s^{-1} a cabal lent i amb un valor D_{eff} vint vegades major (6×10^{-12} m^2 s^{-1}) a cabal ràpid. A més a més, un lleuger canvi en les àrees de superfície reactiva de al calcita va contribuir a l'ajust del model amb les dades experimentals.

El model reprodueix la gran dissolució de calcita, la menor dissolució del clinoclor i la precipitació de guix. La dissolució de calcita es va veure afavorida per l'augment de la velocitat de flux i mentre que la precipitació de guix va augmentar a 1 mL h^{-1}. S'ha vist probable una precipitació menor de dolomita, caolinita i dos zeolites (mesolita i estilbita) al llarg de la zona

alterada. La magnitud d'aquestes reaccions és consistent amb l'augment de porositat mesurat a la zona alterada.

El **tercer objectiu** és l'estudi de la magnèsia càustica (MgO) com una alternativa al ciment Portland, no només per ser utilitzat en l'espai entre el revestiment del pou i la roca, sinó també per segellar les fractures de roca. El procés de carbonatació del MgO es considera que passa quan el MgO s'hidrata ràpidament per formar brucita (Mg $(OH)_2$). Quan la brucita es dissol en una solució rica en Ca i saturada en CO_2, la solució se sobresatura respecte dels carbonates de Ca i/o de Mg (per exemple, dolomita (CaMg $(CO_3)_2$), nesquehonita ($MgCO_3 \cdot 3$ (H_2O)), hidromagnesita ($Mg_5(CO_3)_4(OH)_2 \cdot 4$ (H_2O)) i magnesita ($MgCO_3$)). Diferents condicions de T i pCO_2 determinen la formació d'aquests carbonats. Els volums molars dels minerals implicats (cm^3mol^{-1}) [($Mg(OH)_2$ (24.63), $CaCO_3$ (36.93), $MgCO_3$ (28.02), CaMg $(CO_3)_2$ (64.37), $Mg_5(CO_3)_4(OH)_2 \cdot 4(H_2O)$ (208.08), $MgCO_3 \cdot 3(H_2O)$ (75.47)], amb volums molars més grans per a les fases secundàries, juguen a favor d'una possible disminució de la porositat, i per tant, del segellat d'esquerdes en les estructures de ciment, impedint les fuites de CO_2 .

Com a estudi preliminar per a l'ús potencial de MgO com alternativa al ciment Portland en els pous d'injecció, s'ha estudiat la carbonatació del MgO per mitjà d'experiments en condicions de CO_2 subcrític (pCO_2 de 10 i 50 bar i T de 25, 70 i 90 °C) i CO_2 supercrític (pCO_2 de 74 bar i T de 70 i 90 °C).

L'òxid de magnesi reacciona amb l'aigua rica en CO_2 dissolt i Ca, gairebé equilibrada amb calcita. El MgO s'hidrata ràpidament a brucita que es dissol provocant la precipitació de fases carbonatades de magnesi. La precipitació d'aquestes fases secundàries (magnesita i/o fases metastables com ara nesquehonita o hidromagnesita depèn de la pCO_2, la temperatura i el contingut de sòlids/aigua. En una relació sòlid/aigua constant, la precipitació del carbonat de Mg no hidratat es veu afavorida per l'augment de la temperatura i de la pCO_2.

S'han simulat les variacions experimentals de les concentracions de Mg i Ca i del pH amb el temps a les diferents temperatures i pCO_2 utilitzant el codi de transport reactiu CrunchFlow. Les simulacions reprodueixen l'evolució experimental de les concentracions aquoses i indiquen una

disminució de la porositat en augmentar la temperatura i la pCO_2. Aquesta disminució de la porositat beneficiaria les propietats de segellat del ciment. Aquests resultats s'han utilitzat en la simulació d'un cas d'aplicació amb un pou profund envoltat per ciment de tipus MgO a 90 ° C.

Resumen

Una planta piloto para el almacenamiento geológico de CO_2 se encuentra ubicada en Hontomín (Burgos, norte de España). Hontomín es un yacimiento que se compone principalmente de roca caliza. El reservorio es un acuífero salino profundo, que contiene un agua subterránea rica en NaCl- y sulfato, dicha agua se encuentra en equilibrio con calcita y yeso. Este reservorio está cubierto por una formación que tiene muy baja permeabilidad y está constituida principalmente de margas, calizas margosas y lutitas bituminosas, las cuales actúan como roca sello. Durante y después de la inyección de CO_2, ya que el agua subterránea residente contiene sulfato, la solución acida rica en CO_2 resultante da lugar a la disolución de calcita (minerales de carbonato) y de albita, illita y Clinochloro (minerales ricos en Si), así como la precipitación de minerales ricos en sulfato (e.g. yeso o anhidrita) y en silicio (e.g. arcilla y zeolitas). Estas reacciones que se producen pueden implicar cambios en la estructura (porosidad), la permeabilidad y en los poros de la roca los cuales podrían variar la capacidad de sellado de la roca. Por lo tanto es indispensable realizar experimentos de laboratorio y modelizar mediante transporte reactivo con el fin de adquirir los conocimientos sobre el proceso de la precipitación de yeso, a expensas de la disolución de la calcita en soluciones ricas en CO_2 y las implicaciones que tiene en las propiedades hidrodinámicas de la roca sello.

Un **primer objetivo** de esta tesis se basa en comprender el comportamiento de dichas reacciones acopladas y los efectos que la P_{Total}, pCO_2, T, mineralogía y acidez de la solución ejercen sobre dichas reacciones. Para tal fin se llevan a cabo experimentos de flujo continuo con muestras de illita trituradas en polvo y experimentos de flujo a través de columnas rellenas con roca margas, calizas margosas y lutitas bituminosas. Dichos experimentos se realizan bajo diferentes condiciones experimentales (P_{Total}–pCO_2 atmosférica: $1–10^{-3.5}$, subcríticas: 10–10 bar y supercríticas: 150–37 bar), T (25 y 60 ° C), así como diferentes soluciones de entrada (subsaturada con respecto a yeso y equilibrada con yeso). Los datos experimentales son reproducidos mediante simulaciones 1D de transporte reactivo utilizando el código numérico CrunchFlow con el fin de evaluar las velocidades de reacción de los minerales en el sistema y cuantificar la variación de la porosidad a lo largo de las columnas.

Un **segundo objetivo** de este estudio de doctorado es evaluar la interacción entre la marga de Hontomín y soluciones ricas en sulfato y CO_2 bajo condiciones de CO_2 supercrítico (P_{Total} = 150 bar, pCO_2 = 61 bar y T = 60 °C). Para dicho estudio se realizaron experimentos de percolación de flujo a través de columnas usando muestras de cores fracturados artificialmente con el fin de dilucidar (*i*) el papel que juega la composición de las soluciones inyectadas (soluciones ricas y libres en sulfato), y (*ii*) el efecto de la velocidad de flujo (0.2, 1 y 60 ml h^{-1}) que ejercen sobre la permeabilidad de la fractura. La disolución de calcita (en ambas soluciones de entrada), y la precipitación de yeso (en la solución rica en sulfato) junto a la disolución de los minerales de silicato (en menor proporción), contribuyen a la formación de una zona esquelética alterada (principalmente compuesta por arcillas no reaccionadas) a lo largo de las paredes de la fractura. Un crecimiento en el número de *Pe* rige los cambios en los patrones de disolución (disolución de cara, disolución de agujero y disolución uniforme).

En los experimentos realizados con el agua sin sulfato, la permeabilidad de la fractura no cambió significativamente, independientemente de la velocidad de flujo a pesar del hecho de que una gran cantidad de calcita se disolvió. Contrariamente, en los experimentos realizados con el agua rica en sulfato, la permeabilidad de la fractura se redujo en presencia de flujos lentos (0.2 y 1 mL h^{-1}), esto se debe a que la precipitación de yeso se encarga de sellar la fractura. A velocidad de flujo alto (60 ml h^{-1}), la permeabilidad de la fractura aumentó debido a que la disolución de la calcita predominó sobre la precipitación de yeso.

Se utilizaron modelos 2D de transporte reactivo para interpretar los resultados de los experimentos (excepto a 60 mL h^{-1}) y se reproduce la variación en la concentración de salida con el tiempo, así como la anchura observada de la zona de alteración a lo largo de las fracturas. El mejor ajuste encontrado fue obtenido mediante el uso de un valor de D_{eff} inicial de 3×10^{-13} m^2 s^{-1} para el caudal lento y 1×10^{-13} m^2 s^{-1} para el caudal medio, teniendo que aumentar por un factor de 20 (6×10^{-12} m^2 s^{-1}) en la matriz de roca a caudal rápido. Conjuntamente con un ligero cambio en el área reactiva de la calcita contribuyó al ajuste del modelo a los datos experimentales.

El modelado reproduce la gran disolución de calcita y en menor proporción la disolución de clinochloro y la precipitación de yeso. La disolución de calcita se vio favorecido por el aumento

de la velocidad de flujo y la precipitación de yeso. La precipitación en menor proporción de dolomita, caolín y zeolitas (mésolite y estilbita) a lo largo de la zona alterada fue calculada mediante las simulaciones. La magnitud de estas reacciones es consistente con el aumento en la porosidad medida en la zona alterada.

El **tercer objetivo** es el estudio de magnesia cáustica (MgO) como una alternativa al cemento Portland, no sólo para ser utilizado en el espacio entre el revestimiento del pozo y la roca, sino también para sellar las fracturas de roca (lechada). El proceso general de carbonatación del MgO se considera que ocurra cuando MgO se hidrata rápidamente para formar brucita ($Mg(OH)_2$). Cuando la brucita se disuelve en una solución rica en Ca y CO_2-saturado, la solución se supersatura con respecto a los carbonatos de Ca y/o Mg (e.g. dolomita ($CaMg(CO_3)_2$), nesquehonita ($MgCO_3 \cdot 3(H_2O)$), hidromagnesita ($Mg_5(CO_3)_4(OH)_2 \cdot 4(H_2O)$) y magnesita ($MgCO_3$)). Diferentes condiciones de pCO_2 y T determinarán la formación de estos carbonatos. Los grandes volúmenes molares de las fases secundarias ($cm^3\ mol^{-1}$) [$MgCO_3$ (28.02), $CaMg(CO_3)_2$ (64.37), $Mg_5(CO_3)_4(OH)_2 \cdot 4(H_2O)$ (208.08), $MgCO_3 \cdot 3(H_2O)$ (75.47)], con respecto a los primarios [($Mg(OH)_2$ (24.63), $CaCO_3$ (36.93)], favorecen una posible disminución de la porosidad y por lo tanto, el sellado de grietas en estructuras de cemento así como la prevención de fugas de CO_2.

Un estudio preliminar para el uso potencial MgO como una alternativa al cemento Portland en pozos de inyección, la carbonatación del MgO ha sido estudiado por medio de experimentos por lotes bajo condiciones de CO_2 subcrítico (pCO_2 de 10 y 50 bar y T de 25, 70 y 90 ° C) y supercrítico (pCO_2 de 74 bar y T de 70 y 90 ° C).

El óxido de magnesio reaccionado junto con el agua rica en CO_2 y equilibrada con respecto a la calcita, promueven la disolución de brucita provocando la precipitación de diferentes fases de carbonato de magnesio. La precipitación de estas fases secundarias (magnesita y/o fases metaestables tales como nesquehonita o hidromagnesita dependen de la pCO_2, T y contenido de sólidos/agua. En una relación sólido/agua constante, la precipitación del carbonato de Mg no hidratado se ve favorecida por el aumento de la temperatura y la pCO_2.

La variación temporal de las concentraciones de Mg y Ca junto con el pH medidos experimentalmente a las diferentes condiciones de T y pCO_2 han sido reproducidas mediante simulaciones utilizando el código de transporte reactivo CrunchFlow. Las simulaciones reproducen la evolución experimental de las concentraciones acuosas y se obtiene una disminución en la porosidad al aumentar la temperatura y la pCO_2. Dicha disminución en la porosidad es de gran beneficio para las propiedades de sellado del cemento. Los resultados obtenidos han sido utilizados en las simulaciones de un caso de aplicación de un pozo profundo rodeado por el cemento MgO a 90 °C.

Acknowledgements

The work presented in this Ph.D. study contains the results collected through six years of research in the Groundwater Hydrology Group (UPC-CSIC). For this reason, the list of people who has contributed and supported it cannot be exhaustive.

I want to thank my supervisor Jordi Cama whose encouragement, guidance, support and trust, enabled me to obtain the results achieved. I also thank him for teaching me how to carry out laboratory experiments and interpret and quantify the results. I am in debt with him and hope to keep our collaboration up in the near future. It has been a honor to be his Ph.D. student.

Thanks are due to my supervisor Dr. Josep M. Soler for teaching me how to use the CrunchFlow reactive transport code and model and analyze properly the experimental results. Many times after feeling "I've tried all", he looked at the files and came out with a new idea.

I would like to thank my supervisor Dr. Linda Luquot for her constant help in every kind of practical and theoretical problem, at any moment, day or night. Thanks also for your special support over long nights at the ESRF Synchrotron (Grenoble) and during the hard weeks working with the ICARE apparatus at the University of Montpellier.

I am heartily thankful to Dr. Jesús Carrera to give me the chance to join this group.

I am very grateful to Javier Gargía-Veigas and Maite Romero from the Scientific and Technical Services of the University of Barcelona (CCiT-UB) for their technical assistance in the SEM-EDX and ICP-AES analyses, Natàlia Moreno (IDAEA-CSIC) for her help in the XRD analyses and Elisenda Seguí (CCiT-UB) for her assistance in the X-ray fluorescence analyses.

My sincere thanks also go to Dr. Carlos Ayora (IDAEA) and Dr. Salvador Galí (University of Barcelona) for their immeasurable interest in science and their invaluable help in all kinds of scientific issues. I am also grateful to Dr. Maarten Saaltink (UPC) and Dr. Francesca de Gaspari (UPC) for the valuable guidance and encouragement extended to me in the Cheproo-Traconf initialization.

I also place on record, my sincere thanks to Dr. Charlotte Garing (Stanford University) and Dr. Philippe Gouze (CNRS-Montpellier) for their constructive comments that have improved the quality of this Ph.D. manuscript.

Many thanks to Dr. Anna Russian (UPC) for her unconditional help and support over these years of research. My time at the IDAEA was largely enjoyable in a large part thanks to my friends, who have become part of my life: Maria García, Francesco Offeddu, Cristina Valhondo, Yoar Cabeza, Victor Bezos, Ester Torres and Eike Thaysen (and baby Magnus). They have helped making life easier and funnier at the institute. I also want to thank all the IDAEA team for having good time.

Lastly but not less important, I would like to thank my family for all their encouragement, understanding and love. I´d like to thank my mother Marlene Ordoñez to support, help and advise me throughout this long journey, without you I would not have done it. And most of all for my loving, supportive, encouraging, and patient husband Gabriel Dávila whose faithful support during the final stages of this Ph.D. is so appreciated. I would also thank my sisters Virginia, Lourdes and Lorena and my father Alberto who raised me with patience and supported me in all my pursuits. I am also very grateful to Alejandro Ferrer, Charlie Alonso, Cristian Clement, Daniela Murzi, Maria Rojas, Veronica Ramos, Melissa Balza, Beatriz Canchica, Gabriela Flores, Isabel Dávila, Rolando Olvier and Fabiana Valecillos who all helped me in numerous ways during various stages of my Ph.D.

Table of contents

Chapter I

Chapter II

Chapter V

Chapter VI

List of figures

List of tables

List of appendixes

Abbreviations

∇P = pressure gradient

A = cross section area of the core

A_g = grain surface area

$A_{geometric}$= geometric reactive mineral surface area

a_{H+}^{n} = term describing the effect of the pH on the rate

a_i^{ni}= term describing a catalytic/inhibitory effect by another species on the rate

$A^{initial}$ = initial mineral surface area

A_m = mineral surface area

$A_{reactive}$ = adjusted reactive surface area

$A_{specific}$ = BET specific surface area

C_i and C_o = input and output concentrations (flow-through experiments)

C_j = concentration of the component j

$C_{j(out)}$ = total concentration of the element j in the output solution

$CO_{2(sc)}$ = supercritical CO_2 state

D = combine dispersion-diffusion coefficient

D_a = apparent diffusion coefficient

D_o = diffusion coefficient in water

D_{eff} = effective diffusion coefficient

$D_{eff(i)}$ = initial effective diffusion coefficient

d_g = grain diameter

-diss = mineral dissolution

E_a = apparent activation energy of the reaction

EDS = energy dispersive spectroscopy

eq.Ca = water equilibrated with respect to calcite

ESEM = Environmental Scanning Electron Microscopy

h = fracture aperture

IAP = ionic activity product of the solution with respect to the mineral

ICP-AES = Inductively Coupled Plasma Atomic Emission Spectroscopy

k = permeability in the crushed samples

k_f = fracture permeability

$k_{f\text{-}initial}$ = initial fracture permeability

$k_{f\text{-}final}$ = final fracture permeability

K_{eq} = equilibrium constant

$K_{m,T}$ = reaction rate constant at the temperature

ℓ = diameter of the core sample

L = length of the core sample

L_{Cell} = length of the reaction cell

m = cementation exponent

M = number of precipitated minerals

m_2 and m_1 = parameters affecting the dependence on the rate on solution saturation state

M_{ilt} = mass of illite sample

m_{Rock} = mass of the rock sample

MW_m = molecular weight of the phase

N = number of dissolved minerals

n_m = total number of moles of dissolved or precipitated mineral

$p\mathrm{CO}_2$ = partial pressure of CO_2

P_{Total} = total pressure

-ppt = mineral precipitation

Q = flow rate

R = gas constant

r_{Cell} = radii of the reaction cell

r_g = grain radii

R_j = total reaction rate affecting component j

R_m = reaction rate of the mineral m

r_{Si} = illite dissolution rate

SEM = Scanning Electron Microscopy

SI = saturation index

S_{ilt} = illite specific surface area

t = experimental duration

T = temperature

v_D = Darcy velocity

V_{bulk} = effective volume of the cell

V_{cell} = volume of the cell

V_f = equivalent water fracture volume

$V_{f\text{-}initial}$ = initial fracture volume

$V_{f\text{-}final}$ = final fracture volume or final pore volume associated with the reacted core

V_m = molar volume of the solid phase

V_m = volume of dissolved and precipitated mineral

V_p = number of pore volumes

V_{pore} = pore volume

$V_{reac\text{-}zone}$ = volume of reacted zone

V_{rock} = volume of the rock

V_{tank} = tank volume

$V_{total\text{-}Cal}$ = volume of calcite of the core if the core were 100% composed of calcite

v_{jm} = number of the moles of j in m

v_m = molar volume of the mineral

vol. = volume fraction of the mineral (m)

vol.%. = percentage of volume fraction of the mineral (m) or component (j)

w = fracture width

wt.%. = weight fraction of the mineral (m) or component (j)

x = distance normal to the fracture

XMT = X-ray MicroTomography

XRD = X-Ray Diffraction

XRF = X-Ray Fluorescence

ΔC_j = difference between the output and the input concentrations of the element j

ΔG = Gibbs free energy

ΔP = pressure difference between the inlet and outlet

α = stoichiometric coefficient of element j in the mineral

α_L = longitudinal dispersivity

α_T = transversal dispersivity

ε = absolute error of the element j

ϕ = porosity

$\phi_{(f)}$ = final porosity

$\phi_{(i)}$ = initial porosity

ϕ_m = individual mineral volume fraction

$\phi_{m(i)}$ = initial individual mineral volume fraction

ϕ_{vol} = porosity over the reacted zone

μ = viscosity of the fluid

ρ_{Rock} = density of the rock sample

τ = residence time

υ_{Si} = Si stoichiometric coefficient in the illite sample

Chapter I

Introduction

1.1 CO_2 emissions

Nowadays the energy demand is divided among fuel and electricity and comes largely from fossil or non-regenerative sources. The conventional increase in the use of fossil fuels adds greenhouse gases (GHGs), predominantly CO_2 as reported by the International Energy Agency (80-90% from 1971 to 2012; IEA, 2014) and in a lesser extent CH_4, N_2O and others, to the atmosphere. Anthropogenic emissions (63%; IEA, 2012) arise from energy production, of which roughly 41% come from electricity and heat generation and 22% from transport (IEA, 2012). Agriculture and deforestation make substantial non-energy contributions to the balance.

Industrial CO_2 emissions, primarily from the use of coal, oil and natural gas, and from the production of cement, currently contribute about 49 $GtCO_2eq/yr$ in 2010 (IPCC, 2014). The human population produces an estimated 0.6 $GtCO_2$ per year just by exhaling. Notwithstanding, per capita emissions vary greatly from country to country. The top overall CO_2 emitters are listed in Fig.1.1. Industrialized countries currently lead (as China and United State), and those in a phase of active growth, such as India and Brazil, will increase emissions dramatically as their economies grow. Accordingly, in 1997 a Kyoto Protocol treaty was established and entered into force until 2005, which extended the 1992 United Nations Framework Convention on Climate Change (UNFCCC) to commit State Parties to reduce greenhouse gases emissions (Fig. 1.2).

GHGs have been accumulated in the atmosphere to the point where they are very likely contributing to the clime even more strongly as they accumulate further over the last few centuries (from 27 $GtCO_2eq/yr$ in 1970 to 49 $GtCO_2eq/yr$ in 2010; IPCC, 2014). This brings as a consequence a global average temperature increase by 2 °C since pre-industrial levels (IEA, 2013) and a pH of the ocean's surface water decrease by 0.1 units compared to pre-industrial values (Haugan and Drange, 1996).

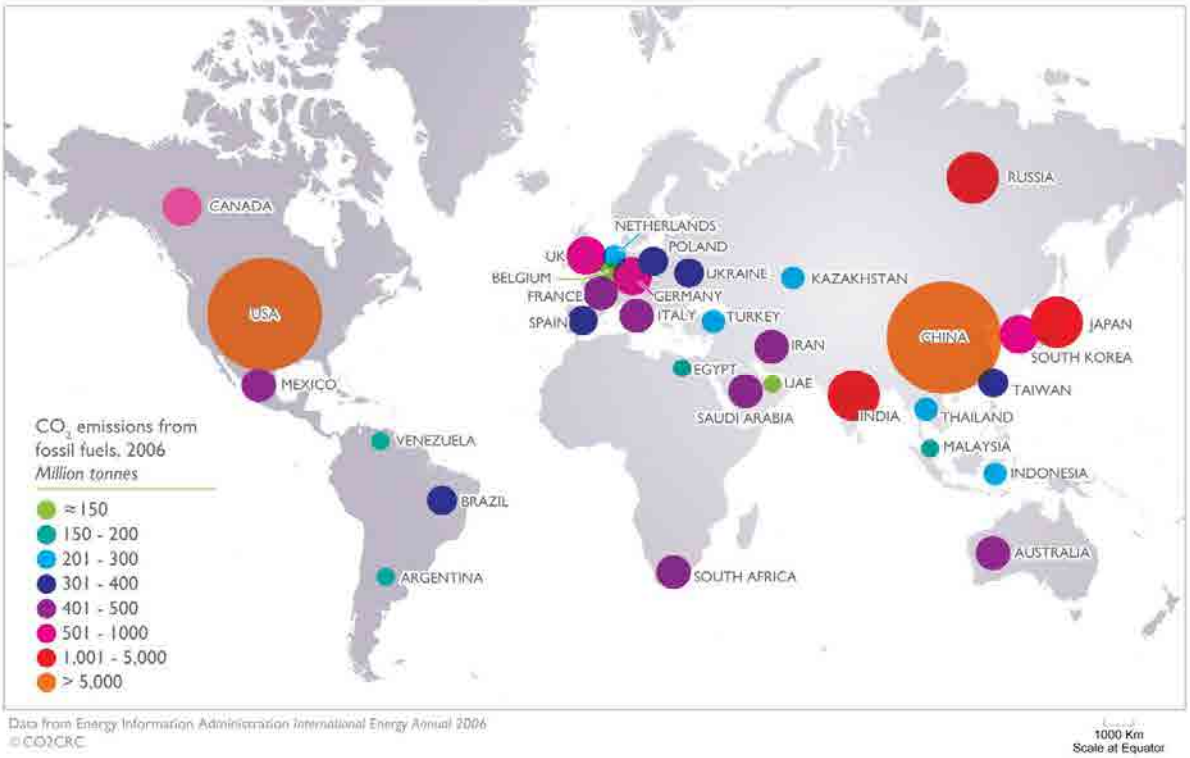

Figure 1.1 *World CO_2 emissions from fossil fuels used by country. Data from International Energy Annual 2006, Energy information Administration (CO_2CRC, 2015).*

Figure 1.2 *GHG trends and projections 1990-2020 of the CO_2 equivalent. Total emissions by the European Environmental Agency (EEA, 2012).*

Therefore, reducing the impact of CO_2 emissions on the atmosphere and global climate change is considered one of the main challenges of this century. (e.g. Lackner, 2003; Pacala and Scolow, 2004; Oelker and Schott, 2005; Broecker, 2005; Schrag, 2007). Geological storage of CO_2 has been proposed as a type of carbon storage alternative to reduce these emissions (Benson and Cole, 2008; Adams and Caldeira, 2008; Oelkers et al., 2008 and references therein).

1.2 Geological Storage

Geological storage relies on the injection of CO_2 into porous rock formations (Holloway, 2001; Friedmann, 2007; Benson and Cole, 2008). It involves separating CO_2 at power stations or other industries plants, compressing it, transporting to the storage site and injecting it into permeable strata at depths. Sedimentary basins are considered suitable as CO_2 storage reservoirs (Oelkers and Cole, 2008). Reservoir formations are deep aquifers covered by very low permeability formations that act as a caprock. An impermeable caprock is essential because CO_2 density is generally less than that of water at depth temperature and pressure conditions, so buoyancy tends to drive CO_2 upwards, back to the surface. Several industrial-scale geologic CO_2 storage programs are already underway, including the Norwegian Sleipner project in the North Sea (Korbøl and Kaddour, 1995) and the Weyburn project in Canada (Emberley et al., 2005); at these sites, a million tons or more of CO_2 is injected into the subsurface each year. Moreover, other current worldwide CCS projects are currently running (In Salah (Algeria), K12B (Netherlands), Snøhvit (Norway) among others). Some of these storage sites also consist of exploited gas or fuel reservoirs, and CO_2 injection is used to enhance oil recovery.

Several processes may act to further stabilize the CO_2 trapped by geological structures beyond the stratigraphic seal, increasing the efficiency and safety of CO_2 storage (Fig. 1.3). The fraction of CO_2 trapped depends both on the magnitude of the residual CO_2 saturation and on the volume of the reservoir swept by the CO_2 plume (Hesse et al., 2008). A variety of processes will tend to stabilize the CO_2 including: *1)* capillary trapping in bubbles of CO_2 after the CO_2 plume has passed (Fig. 1.3; inset A), *2)* dissolution in formation brines which forms a denser fluid which will sink (Fig. 1.3; inset B), where fingering along bedding-related heterogeneities will enhance dissolution (Fig. 1.3; inset C), and *3)* precipitation of CO_2 in solid form as carbonate minerals as a result of reactions between CO_2-charged brines and silicate minerals (Kampman et al., 2014).

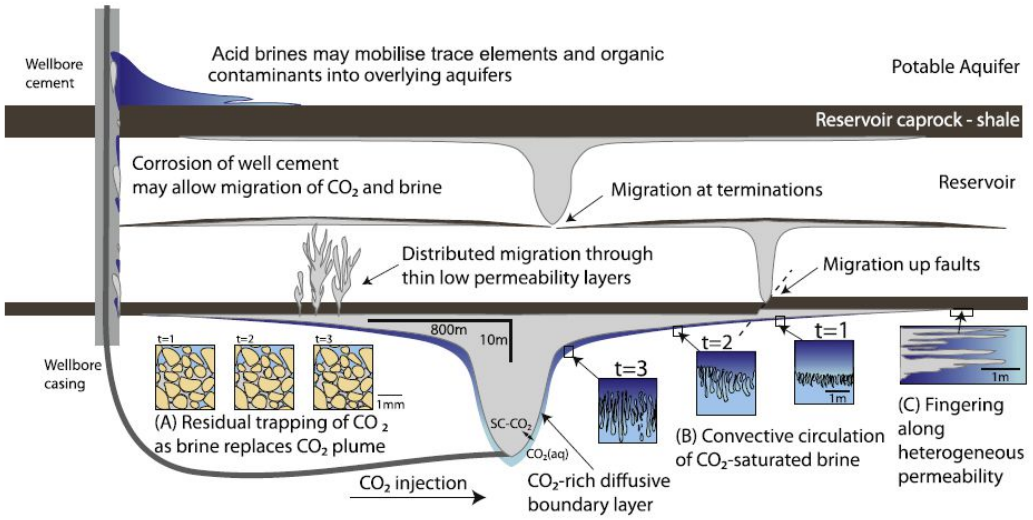

Figure 1.3 *Diagrammatic illustration of geological carbon storage. CO_2 from concentrated sources is separated from other gasses compressed and injected into porous geological strata at depths >800 m where it is in a dense or supercritical phase. The CO_2 is lighter than formation brines, rises and is trapped by impermeable strata. The risks are that the light CO_2 will exploit faults or other permeable pathways to escape upwards and acid CO_2-charged brines might corrode the caprocks or fault zones (Kampman et al., 2014).*

The criteria for suitability are, first, that there is sufficient pore volume to store a significant portion of CO_2 emissions, second, that there is a structural trap with enough integrity to contain the buoyant CO_2 for hundreds to thousands of years and third, that permeability is high enough to inject at high flow rate.

1.3 CO_2 leakage through caprock and wells

Implementation of CO_2 storage in geological media requires a proper assessment of the risk of CO_2 leakage from storage sites. As illustrated in Fig. 1.3, there are several pathways from where CO_2 can escape. During and after injection, CO_2 can leak through zones of high permeability (Deng et al., 2013), through reactivated faults, fractures or microcracks in the caprock (Angeli et al., 2009, Shukla et al. 2010, Tongwa et al., 2013) or can create or reactivate leakage pathways through abandoned and injection wells (Celia et al., 2005; Watson and Bachu, 2008; Angeli et al., 2009, Huerta et al., 2011). Consequently, even if the potential of leakage is small, the success of long-term CO_2 storage will ultimately depend on the caprock sealing capacity and the well cement.

1.3.1 Caprock

Investigating the interaction between the caprock and CO_2-rich brine through potential pathways is of paramount importance to evaluate the long-term caprock sealing capacity (Kaszuba et al., 2005; Noiriel et al., 2007; Andreani et al., 2008; Busch et al., 2008; Hangx et al., 2010; Ellis et al., 2011; Berrezueta et al., 2013; Smith et al. , 2013). Acidified CO_2-rich brines may react with caprock minerals that are susceptible to dissolve, releasing ions into the solution that could lead to mineral precipitation (Knauss et al., 1993; Brady and Carroll, 1994, Pokrovsky et al., 2009; Hellmann et al., 2010; Smith and Carroll, 2014). Mineral dissolution rates relevant to the reactions taking place under these conditions were previously obtained (Chou and Wollast, 1985; Jeschke et al., 2001; Domènech et al., 2002; Köhler et al., 2003; Palandri and Kharaka, 2004; Lowson et al., 2007; Bandstra et al., 2008; Xu et al., 2012; Smith et al., 2013). Mineralogical changes affect porosity, pore structure and hydrodynamic and mechanical properties of caprocks (Park et al., 2011; Vilarrasa et al., 2013).

In the last decade, caprock reactivity in CO_2-rich solutions has been studied using batch and flow-through experiments (Kaszuba et al., 2005; Kohler et al., 2009; Alemu et al., 2011; Credoz et al., 2011; Liu et al., 2012; Garrido et al., 2013). The authors reported significant mineral alterations and changes in pore volume owing to dissolution and precipitation of carbonate and clay minerals, illitization of smectite and formation of swelling clays. Flow-through laboratory-scale experiments under atmospheric and supercritical CO_2 conditions have been conducted to better understand how the caprock reactivity may affect the hydraulic and mechanical properties of the rocks. In these experiments, core and fractured core samples made up of marl, shale, limestone or evaporite rocks were used (Noiriel et al., 2007; Andreani et al., 2008; Angeli et al., 2009; Berrezueta et al., 2013; Ellis et al., 2011; Deng et al., 2013; Smith et al., 2013). Other mineral alterations including reorganization of clay minerals in a fracture and an altered layer on the fracture surface led to variations in fracture permeability (Noiriel et al., 2007; Andreani et al., 2008).

Furthermore, a continuous exposure of the caprock could allow formation of preferential dissolution paths and brine circulation through these localized channels, creating a degraded zone. Likewise, re-activation of micro cracks could play an important role in the flow of CO_2 (Angeli et al., 2009). Ellis et al. (2011) observed that the low content of clay minerals, compared with those

in samples used by Noiriel et al. (2007), Andreani et al. (2008) and Angeli et al. (2009), prevented the formation of a continuous clay coating along the fracture. Moreover, Smith et al. (2013) highlighted a strong control of local heterogeneity on the location of preferential pathways at the microscale. Ultimately, chemical reactions between the caprock and CO_2-rich solution led to a change in fracture surface roughness and originated degraded zones with banding of reactive and non-reactive minerals (Deng et al., 2013). Predicting long-term CO_2 leakage is challenging considering the long list of factors influencing the leakage risk, such as type of clay, flow rate, minerals composing the rock matrix, permeability (k) and total pressure (P_{Total}).

1.3.2 Well

Wells, through which CO_2 phase is injected into the deep reservoir formations, could constitute a risk of migration pathways because firstly, they form a direct connection between the surface and the reservoir, and secondly, they are composed of manmade materials that may corrode over long periods of time (Fig. 1.4).

It is a common practice to inject cement into the space between the well casing and the rock (Rahman et al., 1988). The cement acts as a barrier to isolate the reservoir from the environment and, in the case of CO_2 storage site, to prevent CO_2 leakage and pollution either from or to the reservoir (Nogues et al., 2011). Nevertheless, the cement can become a potential pathway to CO_2 leakage. Indeed, as illustrated in Fig. 1.4, the leakage may occur through the interface between casing and cement, cement plug and casing, or through the cement pore space and fractures (Gasda et al., 2004; Celia et al., 2005; Watson and Bachu, 2008; Jung et al., 2014).

Cement in contact with the acid CO_2–rich water will react and modifying the cement material structure. Portland cement (PC), used predominantly as concrete for conventional wells, will react with the CO_2 when water is present dissolving the major phases of the hydrated cement (portlandite and C-S-H gel) and forming calcium carbonate (calcite, aragonite, vaterite; Kutchko et al., 2007). Carbonation may be associated with significant changes in the flow, transport and mechanical properties of the cement and could lead to a loss of insulating properties (Dewaele et al., 1991; Scherer et al., 2005; Bachu and Bennion 2009; Kutchko et al., 2008; Duguid, 2009; Luquot et al., 2013). Laboratory studies suggest that Ca-based cement paste with low

water/cement ratios may not be as susceptible to CO_2 attack due to the formation of a quasi-impermeable carbonate layer at the contact between the CO_2-rich brine and the cement, which forms a barrier to further cement degradation (Kutchko et al., 2007; 2008). These laboratory findings are supported by the good performance of Portland cement in boreholes that have been exposed to CO_2 for 30 years (Carey et al., 2007).

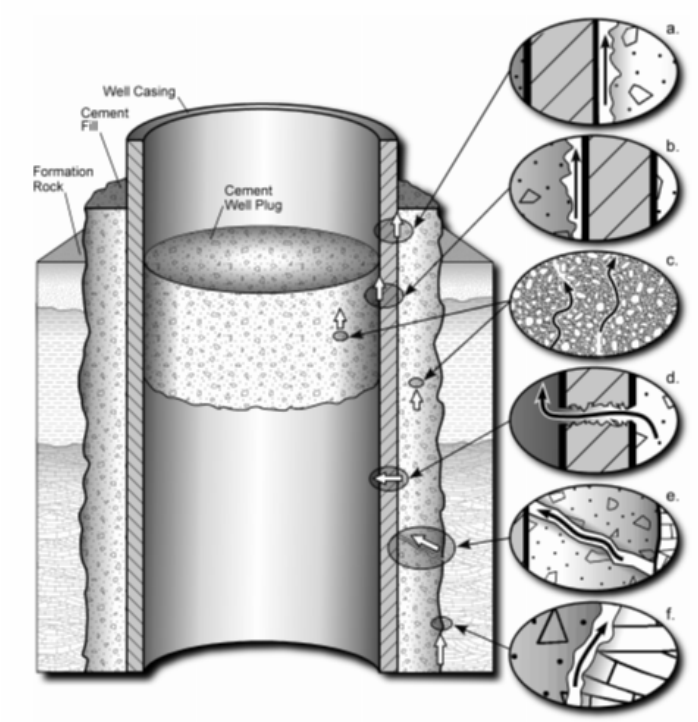

Figure 1.4 *Diagrammatic representation of possible leakage pathways through an abandoned well. a) Between casing and cement; b) between cement plug and casing; c) through the cement pore space; d) through casing; e) through fractures in cement; and f) between cement and rock (Gasda et al. 2004).*

Nonetheless, as explained below, other laboratory studies showed differences in carbonation processes, which affected the flow, transport and mechanical properties. The cement composition varied according to the American Petroleum Institute (API) specification of the oil and gas industry, depending on temperature and pressure (from class A to G cements). Under atmospheric pressure and between 20-50 °C, in core cement pastes embedded in sandstones and limestones it was observed that the changes in permeability took place at the rock interface where faster degradation occurred (Duguid et al., 2011). It was also observed that during injection of CO_2-rich

brine at ca. 40 bar, most portlandite was lost in the intermediate solid/fluid contact zone due to carbonation which lead Ca concentration out (Yalcinkaya et al., 2011). Under high pressure (100 bar) and 95 °C, PC was highly reactive; released Ca will react with the dissolved Mg in deep saline brines to form poorly-crystalline solids (Carroll et al., 2011).

The increase in the ability of the cementitious material to fill (healing) pre-existing fractures, improving the sealing properties of the cement with time will be a consequence of the flow rate (Q) which may cause a decrease in porosity and permeability (Liteanu and Spiers, 2011). When the flow rate is insufficient to remove the results of carbonation reactions, formation of a protective layer is likely to develop, preventing permeability enhancement (Bachu and Bennion 2009). Abdoulghafour et al. (2013) reported that at high flow rate permeability remained constant after C-S-H dissolution, whereas at low flow rate formation of a Si-rich amorphous phase caused a permeability decrease.

Given the time scale associated with geological CO_2 sequestration, the use of alternative cements that are not subject to potential harmful effects of carbonation would be advisable. Reactive magnesium oxide (MgO) can be successfully blended together with Portland cement to improve the sustainability, strength and many other properties of concretes (Harrison, 2001). The advantages of MgO over Portland cement include precipitation of higher resistance secondary phases, less sensitive to impurities, and its obtainment as a by-product from other industrial processes (Unluer and Tabbaa, 2013). MgO cement as an expansive additive has been mainly used to compensate the thermal shrinkage of mass concrete, particularly in concrete dams with height less than 150 m (Mo et al., 2014).

1.4 Motivation

The European Energy Programme for Recovery (EEPR) was established in 2009 to address both Europe's economic crisis and European energy policy objectives. Almost €4 billion were assigned to co-finance EU energy projects that would boost the economic recovery, increase the security of energy supply and contribute to the reduction of greenhouse gas emissions. The three sectors meeting these conditions were gas and electricity infrastructure, offshore wind energy and carbon capture and storage (CSS) projects. One of these CCS projects, namely The Compostilla project, is

leaded by a three partner consortium (Endesa, CIUDEN (CIUDad de la ENergía foundation) and Foster Wheeler Energia Oy (FWEOy)), and is located in Ponferrada, Northern Spain. The project is in charge of three Technology Development Plants (TDPs) at pilot scale: the CO_2 capture and transport TDPs in Cubillos del Sil (León, Spain) and the CO_2 geological storage TDP in Hontomín (Burgos, Spain).

This thesis falls within the context of CO_2 geological storage in Hontomín. The Hontomín reservoir formation for CO_2 storage is a deep saline aquifer in Mesozoic sedimentary sequences that is covered by a very low permeability formation which acts as a caprock (Fig. 1.5). At the storage TDP, it is programmed to inject less than 100000 tonnes of CO_2 into a 1500-meter-deep dome-like saline aquifer over a period of five years. Five existing wells (H1-5) were used to characterize the structure of the geological formation and two new wells were drilled, one for the CO_2 injection (H-I) and another one for monitoring (H-A). The 100-meter-thick host reservoir rock is mainly composed of limestone and sandstone and has an upper impermeable seal made up of marls, marly limestones and bituminous shales mainly composed of carbonate minerals and clays, which should prevent CO_2 from escaping to the surface.

The first part of this thesis deals with the interaction between the saline solution and the caprock at Hontomín when CO_2 injection is performed. The resident saline groundwater is sulfate-rich, equilibrated with calcite, dolomite and gypsum, with neutral pH and an ionic strength of 0.6 M (Table 1.1). Injection of CO_2 will lead to the formation of a CO_2-rich acid solution which will promote the dissolution of carbonate minerals (*e.g.*, Gherardi et al., 2007; Nogues et al., 2013; Smith et al., 2013) and in minor proportion dissolution of silicate minerals (*e.g.*, Bertier et al., 2006; Fisher et al., 2010; Wigand et al., 2008). Since the resident groundwater contains sulfate, secondary sulfate-rich mineral precipitation (gypsum or anhydrite) may occur. These reactions imply changes in the porosity, permeability and the general pore structure of the caprock.

Table 1.1 Average composition of the Hontomín groundwater (± 10%) in terms of total concentration (mol/kgw) and pH. It was provided by CIUDEN after extraction from the H-2 existing well.

Ca	SO_4^{2-}	Mg	K	Na	Cl^-	HCO_3^-	pH
4.62×10^{-2}	2.07×10^{-2}	3.72×10^{-2}	1.23×10^{-2}	4.14×10^{-1}	5.35×10^{-1}	4.90×10^{-3}	≈6.9

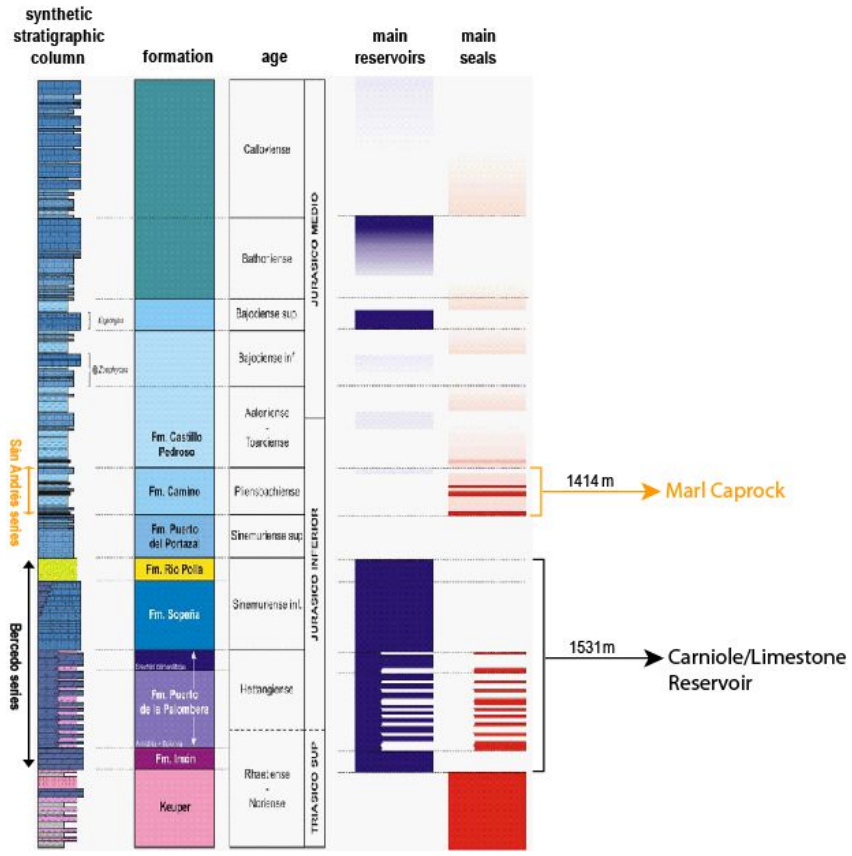

Figure 1.5 *Scheme of the stratigraphic column of the Hontomín site (GEOMODELS, University of Barcelona). Depth of CO_2 injection in the reservoir is between 1414-1530 m.*

In the second part, caustic magnesia (MgO) is studied as an alternative to Portland cement, not only to be used in the space between the well casing and the rock but also to seal rock fractures (grouting). The overall MgO-carbonation process is considered to happen when MgO hydrates rapidly to form brucite ($Mg(OH)_2$) (see reactions below). When brucite dissolves in a Ca-rich and CO_2-saturated solution, the solution supersaturates with respect to Ca and/or Mg carbonates (e.g., dolomite ($CaMg(CO_3)_2$), nesquehonite ($MgCO_3{\cdot}3(H_2O)$), hydromagnesite ($Mg_5(CO_3)_4(OH)_2{\cdot}4(H_2O)$) and magnesite ($MgCO_3$)). Different T and pCO_2 conditions will determine the formation of these carbonates. The molar volumes of the implicated minerals (cm^3 mol^{-1}) [($Mg(OH)_2$ (24.63), $CaCO_3$ (36.93), $MgCO_3$ (28.02), $CaMg(CO_3)_2$ (64.37), $Mg_5(CO_3)_4(OH)_2{\cdot}4(H_2O)$ (208.08), $MgCO_3{\cdot}3(H_2O)$ (75.47)], with large molar volumes for the secondary phases, favor a potential decrease in porosity and hence the sealing of cracks in cement structures, preventing CO_2 leakage.

The motivation of this study is mainly to evaluate, first, the caprock reactivity in contact with CO_2-rich solutions in order to estimate the sealing efficiency of the fractured caprock and, second, the reactivity of MgO-based cement as a potential material to be used in injection wells. Hence, the main goals are:

1) Regarding the caprock reactivity:

1.1) characterization of the Hontomín caprock and its reactivity with CO_2-rich acidic solution with and without sulfate under subcritical and supercritical CO_2 conditions using flow-through and column experiments together with 1D reactive-transport modeling to reproduce, interpret and quantify the occurring processes.

1.2) assessment of the Hontomín caprock reactivity with CO_2-rich acidic solution under supercritical CO_2 conditions using percolation experiments with fractured cores. Changes in rock porosity and permeability are determined. In this case, performance of 2D reactive-transport modeling allows reproduction, interpretation and quantification of the occurring processes along the fractures.

2) Regarding the Mg-based cement reactivity:

To examine the efficiency of the MgO-based cement as a potential material with seal capacity, MgO-based cement is studied in aqueous solutions equilibrated with respect to calcite under subcritical (pCO_2 of 10 and 50 bars and T of 25, 70 and 90 °C) and supercritical (pCO_2 of 74 bar and T of 70 and 90 °C) CO_2 conditions using batch, autoclaved experiments. The results are interpreted by means of 0D reactive-transport modeling.

1.5 Thesis outline

This thesis is divided in six Chapters.

Chapter I describes the motivation and scientific context of this study, together with the state of the art and the objectives.

Chapter II presents a detailed description of (*i*) the experimental methodology followed to perform the flow-through, column, percolation and batch experiments and (*ii*) the parameters used in the 0D, 1D and 2D modeling of these experiments.

Chapter III presents the results of the flow-through and column experiments regarding the caprock-CO_2 rich brine interaction. The content of this chapter will be submitted to *Chemical Geology*.

Chapter IV shows the results of the percolation experiments of CO_2-rich brine at in situ conditions using fractured caprock samples. This Chapter is based on submitted papers to the *International Journal of Greenhouse Gas Control*. The objective of these two chapters was to study the alteration of the Hontomín caprock in contact with CO_2-rich solutions under subcritical and supercritical CO_2 conditions in order to assess the Hontomín caprock sealing capacity. 1D and 2D reactive transport modeling has been performed to quantify the dissolution and precipitation processes that occurred during the circulation of CO_2-rich solutions through the crushed and fractured marl cores samples described in *Chapter III* and *IV*, respectively.

Chapter V presents the results of the batch experiments performed to study MgO carbonation in aqueous solutions equilibrated with respect to calcite under subcritical (pCO_2 of 10 and 50 bars and T of 25, 70 and 90 °C) and supercritical (pCO_2 of 74 bar and T of 70 and 90 °C) CO_2 conditions. The experimental results were numerically reproduced using the CrunchFlow reactive transport code. At last, a possible application case (CO_2-rich water interacting with MgO in a borehole), using the laboratory results, was simulated. This chapter is also based on submitted papers to the *International Journal of Greenhouse Gas Control*.

Chapter VI provides a summary of the main contributions of this thesis.

Two appendixes are included, displaing the data used for the reactive transport modeling applied for the marl reactivity study (Appendix 1) and for the MgO-based cement study (Appendix 2).

Chapter II

Materials and Methods

2.1 Experimental methodology

This chapter describes the experimental methodology used to perform *(1)* the flow-through, column and percolation experiments in order to study the caprock reactivity with acidic solutions (*Chapters III and IV)* and *(2)* the batch experiments to study MgO reactivity with CO_2-rich solution (*Chapter V)*. In this PhD study, four types of samples have been used. Some of them were composed of a pure mineral phase such as illite or MgO, and others were rocks such as limestone and marls.

2.1.1 Analytical methods

The solid samples were characterized before and after the experiments by X-Ray Diffraction (XRD), X-Ray Fluorescence (XRF), Scanning Electron Microscopy (SEM), Environmental Scanning Electron Microscopy (ESEM) and X-ray Microtomography (XMT). Input and output solutions were analyzed by Inductive Coupled Plasma-Atomic Emission Spectrometry (ICP-AES). Likewise, pH of the input and some output solutions were measured using pH meters at the different temperatures and pressures used during the experiments.

To identify the mineral content of the solid samples, XRD was performed on thoroughly crushed samples using a Bruker D8 A25 Advance X-ray diffractometer θ-θ, with $CuK_{\alpha 1}$ radiation, Bragg-Brentano geometry, and a position sensitive LynxEyeXE detector. The diffractograms were obtained from 4º to 120º of 2-θ with a step of 0.015º, a counting time of 0.5 s and the sample in rotation. The crystalline phase identification was carried out by using the computer program ‘‘EVA’’ (©Bruker) and the TOPAS software (Bruker AXS TOPAS, general profile and structure analysis software for powder diffraction data, V2.0, Bruker AXS, Karlsruhe, Germany, 2000). Mineralogical composition of the samples was determined by Rietveld analyses with an uncertainty of 3 *wt.*% (Young, 1995). A fundamental parameter approach was used for Rietveld refinement. The optimized parameters were background coefficients, zero-shift error, peak shape parameters, scale factor and cell parameters. The values of the pattern dependent Rwp (the R-factor normally employed in Rietveld refinement), disagreement factor and statistical reliability factor of Bragg, RB, were evaluated and they indicated that fits were satisfactory. The Rwp obtained in all these measurements were less than 20, which indicates an accurate Rietveld refinement.

XRF was used to performed elemental analysis of the solid samples. Samples were prepared by mixing 0.3 g of crushed and dried sample (grain size < 63 μm) with 5.7 g of lithium tetraborate and 5 mg of lithium iodide as surfactant factor. The elemental composition measurements were performed using an Axios Advanced spectrometer (PANalytical) equipped with Rh anode X-ray tube with a maximum power 2.4 kW.

ESEM was used before and after the experiments. ESEM images was acquired on C-coated crushed samples used for the column and batch experiments described in *Chapters III and V*, respectively, using JEOL JSM-840 and Hitachi H-4100FE instruments under a 15-20 kV potential and low vaccum conditions. Thin sections produced from the core samples described in *Chapter IV* were examined by ESEM using the same instrument under a 15-20 kV potential in a high vacuum configuration and using the backscattered electron detector (BSD).

In order to identify the progress and location of the reactions 3D images of the fractured core samples (*Chapter IV*) were obtained by using XMT (see *Section 2.1.4.4*). XMT is a non-destructive method which allows imaging in 3D with a high resolution (few micrometers) the pore size and mineral distribution. Gray scale values in the images (density contrast) can be converted into mineral concentration. Two sets of X-ray microtomography (XMT) images were taken using two different X-ray sources. This was imposed by the time availability for the instruments. The first set was taken at the National Institute for Lasers, Plasma and Radiation Physics (NILPRP, Bucharest-Magurele, Romania). The XMT equipment worked with Cone beam CT rapid scan (180° + 1/2 fan angle), Oblique View Cone Beam. X-ray energy was 225 kV with a maximum power of 10/15 W, using a tungsten filament source. The columns were mounted on a rotary stage, and images were collected every 0.5°. The linear detector, using 1024 scintillator – photo diode assemblies, yielded 16-bit output digital files that were reconstructed using the ImageJ software. A final pixel size of ≈15.0 μm was obtained. The second set was taken at the ESRF (European Synchrotron Radiation Facility, Grenoble, France) using the ID19 beam line. The cores were mounted on a rotary stage and images were collected every 0.036° through a full 180° rotation using an exposure time of 0.25 s. Image segmentation processing was applied to XMT images to quantify the variation in mineral content using the ImageJ software. This method allowed separation of rock and voids and measurement of the pore space between mineral grains over the whole image pack. A final pixel size of 7.5 μm was obtained.

MicroRaman spectroscopy allowed identification of secondary phases using a Jobin-Yvon LabRam HR 800 coupled with an Olympus BXFM optic microscope with a wavelength of 532 nm pixel size of the analysis.

Total concentrations of Ca, S, Mg, Si, Na, Al, K and Fe of the input and output solutions were analyzed by ICP-AES, using a Perkin Elmer Optima 3200 RL. The detection limit for Ca, S, Mg, Si, Na, Al, K and Fe was 1.25×10^{-6}, 6.24×10^{-6}, 2.06×10^{-6}, 1.78×10^{-6}, 1.30×10^{-4}, 1.85×10^{-6}, 1.28×10^{-5} and 3.58×10^{-7} mol L^{-1}, respectively. The accuracy of the measurements was estimated to be 3%.

pH of the input and output solutions under atmospheric pressure condition was measured using a Crison© combined glass electrode at room temperature (22 ± 2 °C) with an error of ± 0.02 pH units. The electrode was calibrated regularly with buffer solutions at pH 2.02 and 7.00. At intermediate pressure condition (10 bar) pH was measured using Hamilton Polilyte Plus XP 120 pH electrodes (accuracy ± 0.02), which allow measurements under conditions up to 60 °C and 50 bar. The electrodes were calibrated using the same Crison buffer solutions. At high pressure conditions (P_{Total} = 150 bar), the pH was not measured.

2.1.2 Sample characterization

In this study, four different samples (illite, limestone, marl and MgO) were used to perform flow-through, column, percolation and batch experiments and consisted of either powder, crushed or core samples (Tables 2.1, 2.3 and 2.5).

The flow-through experiments (*Chapter III*) were performed using three different samples: illite du Puy (Gabis, 1958), Garraf limestone and *S2.4* Hontomín marly limestone. Illite du Puy is from the Massif Central region in France (Köhler et al., 2003) and with a chemical formula of $(Si_{3.55}Al_{0.45})(Al_{1.27}Fe(III)_{0.36}Mg_{0.44})O_{10}(OH)_2(Ca_{0.01}Na_{0.01}K_{0.53}X(I)_{0.12})$ Bardot (1998). The illite sample was ground to a fraction size of < 63 μm. The limestone sample is from the Roca Quarry in the Garraf area (Barcelona) and is only composed of calcite (XRD profile showed only calcite peaks; Soler et al., 2008; Offeddu et al., 2015). The limestone sample was crushed to obtain fragments with a size between 1 and 2 mm grain size. The marly limestone sample is one of the three types of marl that were provided by CIUDEN and

belongs to the Camino Formation from the San Andres series. The marly limestone sample was crushed between 1 and 2 mm diameter grain size (Tables 2.1, 2.3 and 2.5).

Table 2.1 Experimental setups, number, label and crushed samples characteristics used in the flow-through and column experiments described in *Chapter III*.

			mineral or rock	
Experimental setup	**N° exp.**	**label**	**description**	**grain size**
Flow-through (*atm*-CO_2)	1	Ilt-25-1	*illite*	< 63 µm
	2	Ilt-25-2	*illite*	
	3	Ilt-25-3	*illite*	
	4	Ilt-25-4	*illite*	
	5	Ilt-Cal-1	*illite/limestone*	< 63 µm and 1-2 mm
	6	Ilt-Cal-2	*illite/ limestone*	
	7	Mar-25-3	*marly limestone (S2.4)*	1-2 mm
	8	Mar-25-4		
Column *atm*-CO_2	9	Marc-25-1		
	10	Marc-25-2a		
	11	Marc-60-2a		
	12	Marc-25-5	*bituminous black shale (S3.4)*	
	13	Marc-25-6a		
	14	Marc-60-6a		
	15	Marc-25-3	*marl (S4.3)*	
	16	Marc-25-4a		
	17	Marc-60-4a		
Column *subc*.-CO_2 (pCO_2 = 10 bar)	18	Marc-25-8		
	19	Marc-60-8		
Column *supc*.-CO_2 ICARE Lab CSS I (pCO_2 = 37 bar)	20	S3.4b-1	*bituminous black shale (S3.4)*	280-500 µm
	21	S4.3b-1	*marl(S4.3)*	280-500 µm

The column experiments (*Chapter III*) were carried out using the three marl samples with different mineralogical compositions (*S2.4*, *S3.4* and *S4.3*; Table 2.1) selected from different lithologies that constitute the Hontomín caprock unit (Fig. 2.1).

sample	*S2.4*	*S3.4*	*S4.3*
lithology	marly limestone	bituminous black shale	marl
used as	powder and crushed	powder and crushed	crushed and core
			

Figure 2.1 *Picture of caprock samples from the Hontomín reservoir: marly limestone, bituminous black shale and marl. Inset images show powder (< 63 µm), crushed sample (1-2 µm) and core (18 mm in length and 9 mm in diameter).*

The column experiments at atmospheric and 10 bar of pCO_2 were performed using crushed marl samples with a grain size between 1 and 2 mm (Table 2.1 and Fig. 2.1). The *S3.4* and *S4.3* marl samples were ground to a grain size between 280 and 500 µm to carry out the experiments under 37 bar of pCO_2 in order to compare with those experiments at 10 bar. All ground and crushed samples were washed three times with pH 1 solution (HCl) and three times with deionized water to remove microparticles caused by crushing. The washed samples were totally dried in the oven at 45 °C during 2 days.

The mineralogical composition of the marl samples were obtained by X-ray diffraction (XRD) performed on thoroughly crushed samples with a grain size of < 63µm (Young, 1995; Table 2.2).

Table 2.2 XRD and Rietveld analyses of the different lithology of Hontomín marl caprock.

Series	Formation	age	lithology	sample	calcite [*wt.%*]	quartz [*wt.%*]	illite [*wt.%*]	albite [*wt.%*]	gypsum [*wt.%*]	clinochlore [*wt.%*]	anhydrite [*wt.%*]	pyrite [*wt.%*]	trace [*wt.%*]
San Andrés	Camino	pliensbachian	marly limestone	*S2.4*	86.3	4.2	7.6	0.9	1.0	-	-	-	-
			bituminous black shale	*S3.4*	67.1	6.3	15.8	3.1	1.6	3.1	1.0	2.0	0.01
			marl	*S4.3*	71.2	9.7	7.1	6.5	2.0	2.8	0.5	0.2	-

The chemical composition of clinochlore ($Mg_XFe_YSi_3Al_2O_{10}(OH)_8$; $X+Y = 5$) and the normative composition of the marl (*S4.3*) were calculated from the chemical (XRF, *wt.*% elements) and mineralogical (XRD-Rietveld analysis, *wt.*% minerals) compositions.

Ca (mol) in gypsum and anhydrite (Ca_{Gp+Anh}) was obtained from the total Ca (mol from XRF) and the Ca in calcite (mol from XRD-Rietveld).

$$Ca_{Gp+Anh} = Ca_{XRF} - Ca_{Cal-Rietveld} \quad (2.1)$$

S (mol) in gypsum and anhydrite (S_{Gp+Anh}) was calculated using the stoichiometry

$$S_{Gp+Anh} = Ca_{Gp+Anh} \quad (2.2)$$

S and Fe in pyrite (S_{Py} and Fe_{Py}) were calculated from

$$S_{Py} = S_{XRF} - S_{Gp} \quad (2.3)$$

$$Fe_{Py} = \frac{S_{Py}}{2} \quad (2.4)$$

and Fe and Mg in clinochlore (Fe_{Cln} and Mg_{Cln}) were obtained from

$$Fe_{Cln} = Fe_{XRF} - Fe_{Py} \quad (2.5)$$

$$Mg_{Cln} = Mg_{XRF} \quad (2.6)$$

$$Mg_{Cln} + Fe_{Cln} = 5 \quad (2.7)$$

$$\frac{Mg_{Cln}}{Fe_{Cln}} = Z \quad (2.8)$$

Resulting in: Z = 1.38; X = 2.9 and Y = 2.1 ($Mg_{2.9}Fe_{2.1}Si_3Al_2O_{10}(OH)_8$).

Al and Si in clinochlore (Al_{Cln} and Si_{Cln}) were calculated from the stoichiometry of the mineral:

$$Al_{Cln} = \frac{2}{5}\left(Mg_{Cln} + Fe_{Cln}\right) \quad (2.9)$$

$$Si_{Cln} = \frac{3}{2} Al_{Cln} \quad (2.10)$$

K (mol) in illite (K_{Ilt}) was calculated from the ideal stoichiometry of the mineral, assuming and ideal composition (muscovite)

$$K_{Ilt} = K_{XRF} \quad (2.11)$$

$$Al_{Ilt} = 3K_{Ilt} \quad (2.12)$$

$$Si_{Ilt} = 3K_{Ilt} \quad (2.13)$$

Al in the albite (Al_{Ab}) was calculated from mass balance and the Na and Si in albite (Na_{Ab} and Si_{Ab}) were calculated using the stoichiometry of the mineral

$$Al_{Ab} = Al_{XRF} - Al_{Cln} - Al_{Ilt} \quad (2.14)$$

$$Na_{Ab} = Al_{Ab} \quad (2.15)$$

$$Si_{Ab} = 3\,Al_{Ab} \quad (2.16)$$

Finally the amount of Si in quartz (Si_{Qz}) corresponds to

$$Si_{Qz} = Si_{XRF} - Si_{Cln} - Si_{Ab} - Si_{Ilt} \quad (2.17)$$

The chemical composition of clinochlore is $Mg_{2.9}Fe_{2.1}Si_3Al_2O_{10}(OH)_8$, which is assumed to be the same in the other two marl samples.

SEM was performed on C-coated crushed samples before and after some flow-through and column experiments. Fig. 2.2 shows the morphology and surface of the initial *S4.3* marl sample (grains between 1 and 2 mm).

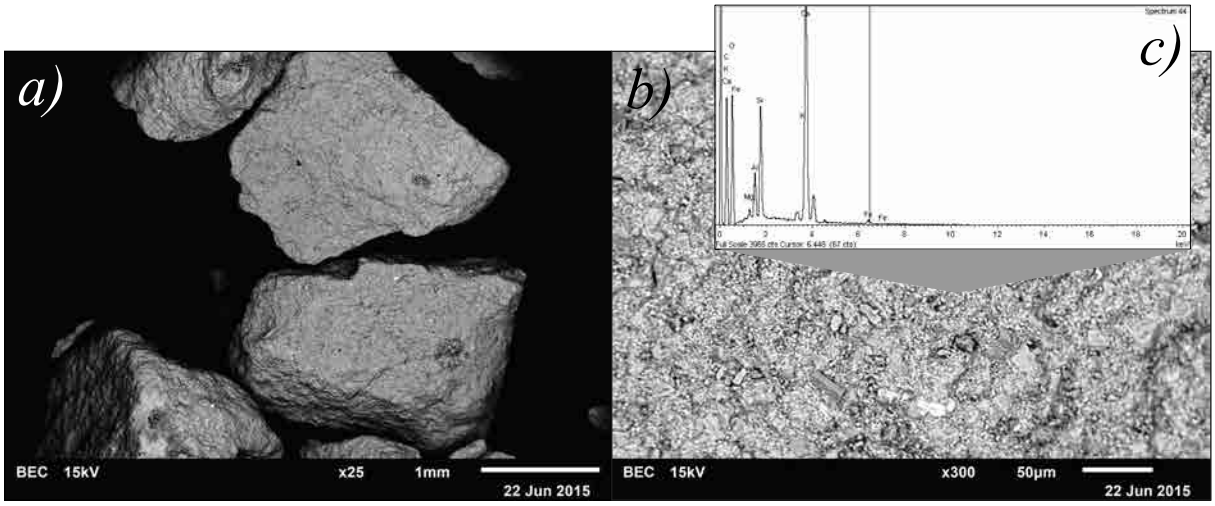

Figure 2.2 *SEM images from the initial S4.3 marl sample. (a) grain size (between 1-2 mm) and (b) surface of the grain. (c) EDS spectrum of the elements present in the sample.*

Seven percolation experiments (*Chapter IV*) under supercritical CO_2 ($CO_{2(sc)}$) conditions were performed using the *S4.3* marl rock. Cylindrical samples were cored from the provided marl (Fig. 2.3a). The core samples had dimensions of 9 mm in diameter and around 18 mm in length (Table 2.3).

Table 2.3 Experimental setups, numbers, labels and core sample characteristics for the experiments used under supc.-CO_2 conditions described in *Chapter IV*.

			mineral or rock		
experimental setup	**N° exp.**	**label**	**description**	**ℓ [mm]**	**L [mm]**
Percolation *supc.*-CO_2 ICARE Lab CSS II	22	S4.3a-4	marl (*S4.3*)	9.0	19.6
	23	S4.3a-3			18.6
	24	S4.3a-2			19.2
	25	S4.3a-1			19.4
Percolation *supc.*-CO_2 ICARE Lab CSS I	26	S4.3a-6			18.7
	27	S4.3a-5			19.3
	28	S4.3a-10			18.4

A fracture was then artificially created by sawing each core in half along the sample length with a circular saw (Fig. 2.3b, c and d). The fracture in each core was laterally sealed using Duralco 4525 epoxy resin (stable mechanical and chemical properties up to 260 °C) to create a cohesive sample and to ensure solution circulation through the fracture.

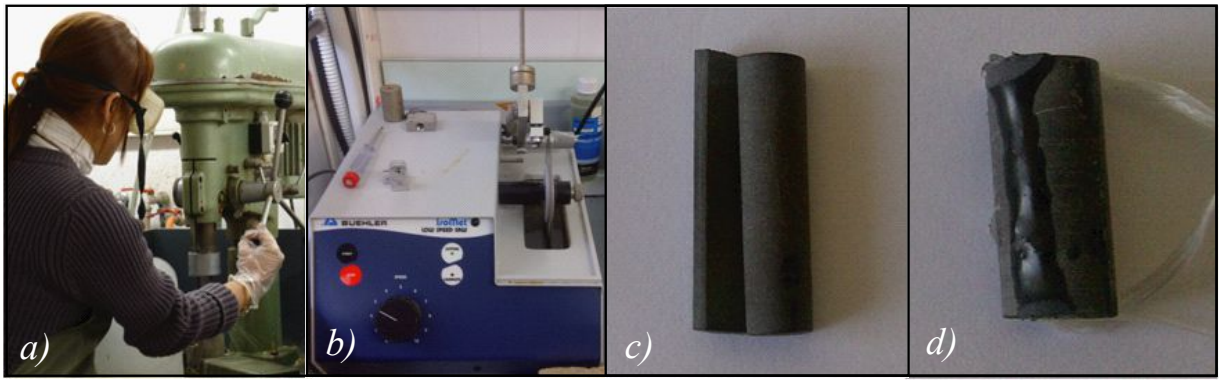

Figure 2.3 *Preparation of the fractured core samples of the S4.3 marl: a) cored, b) clipped, c) fractured and d) sealed.*

Thin sections parallel to the flow direction and perpendicular to the fracture plane were produced to characterize by ESEM grain morphologies (Fig. 2.4) and the fracture apertures before and after the experiments (Fig. 2.5).

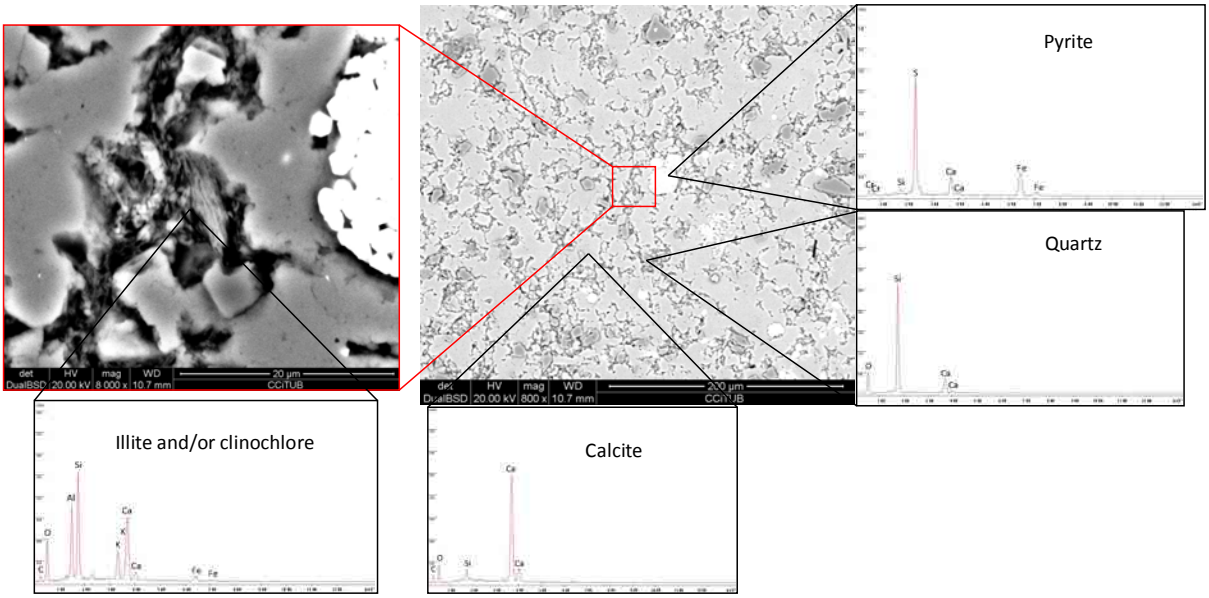

Figure 2.4 *ESEM images of the unreacted S4.3 marl thin section with local spectrum analysis.*

XMT was used to examine the unreacted and reacted fractured cores (Table 2.3). Fig. 2.5b shows the aspect of the fracture with apertures (*h*) that ranged approximately from 3 to 16 µm, yielding fracture volumes from 0.5 to 1.4 mm^3 (Fig. 2.5c).

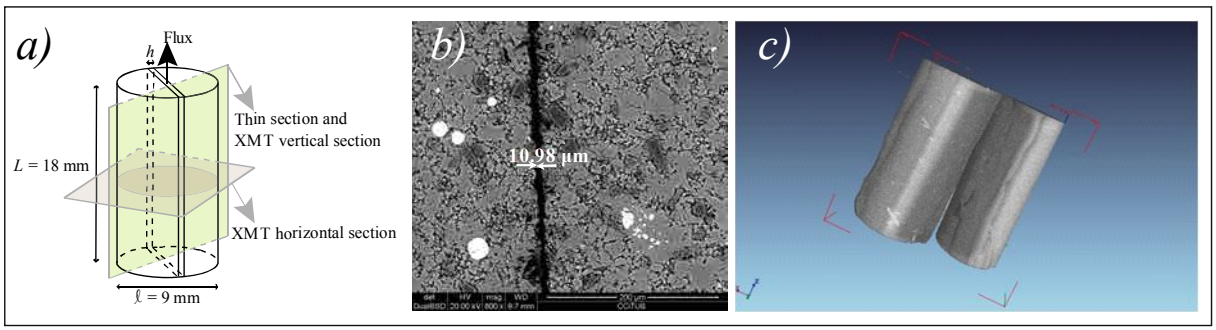

Figure 2.5 *Schematics of ESEM thin section and XMT sections of the core sample (a), ESEM image showing the initial fracture aperture of the exp. 23 (b) and 3D microtomography image of the core sample (c).*

The batch experiments (*Chapter V;* Table 2.4) were performed using a commercial MgO Magna L sample manufactured by Magnesitas Navarras S.A. (Fig. 2.6). The MgO sample was crushed to a grain size between 60 and 150 µm. Thereafter, the ground sample was

washed three times with pH 1 solution (HCl) to dissolve the CaO fraction and obtain a purer MgO sample. The washed sample was also dried in the oven at 45 °C and ground up to further characterization. The samples were examined before and after reaction by XRD and SEM analysis (Table 2.5). The BET specific surface area was measured using 5-point N_2 adsorption isotherms with a Micromeritics ASAP 2000 surface area analyzer. The specific surface area ($A_{specific}$) of the non-reacted sample was 4.8 ± 0.02 m^2 g^{-1}.

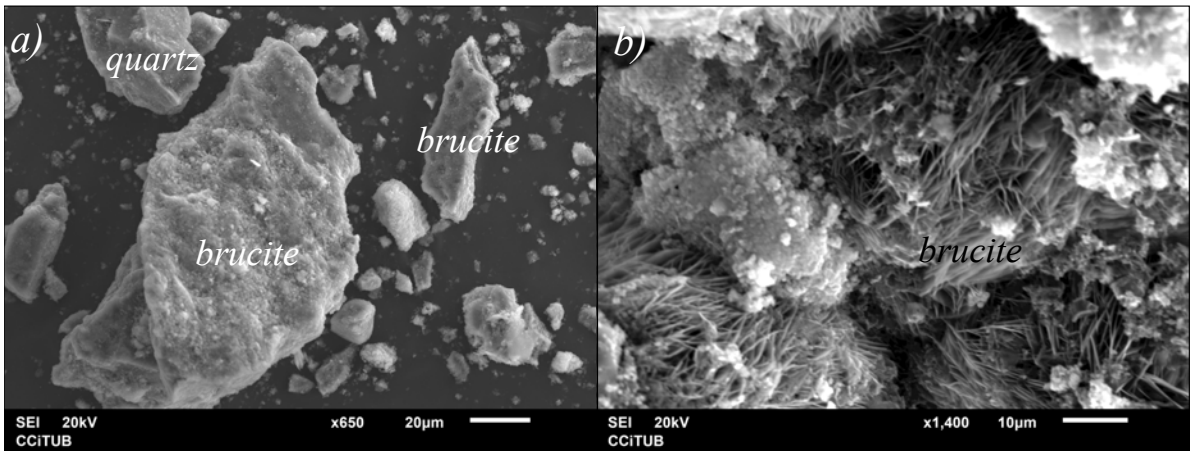

Figure 2.6 *SEM images from the initial MgO sample; a) different grains and b) brucite.*

Table 2.4 Experimental setup, number, label and MgO sample characteristics used in batch experiments under subcritical and supercritical CO_2 conditions described in *Chapter V*. The experimental time spans varied from 5 to 97 h.

				mineral	
experimental setup	**N° exp.**	**amount of experiments (different durations)**	**label**	**composition**	**grain size**
Batch-*subc.*-CO_2 (pCO_2 = 10 bar)	29-33	5	MgO-25-10	MgO	60-150 µm
	34-38	5	MgO-70-10		
	39-42	4	MgO-90-10		
Batch-*subc.*-CO_2 (pCO_2 = 50 bar)	43-48	6	MgO-25-50		
	49-53	5	MgO-70-50		
	54-58	5	MgO-90-50		
Batch-*supc.*-CO_2 (pCO_2 = 74 bar)	59-61	3	MgO-70-74		
	62-66	5	MgO-90-74		

Table 2.5 XRD and Rietveld analyses of the initial MgO sample after acidification with pH=1.

sample	**brucite [*wt.%*]**	**calcite [*wt.%*]**	**quartz [*wt.%*]**	**hydromagnesite [*wt.%*]**	**dolomite [*wt.%*]**	**portlandite [*wt.%*]**
MgO	86.9	3.1	5.3	1.2	0.6	3.1

2.1.3 Injected solutions

2.1.3.1 Flow-through experiments

In the flow-through experiments (*Chapter III*), four HCl solutions with pH ranging from ≈ 2 to ≈ 4 were used in the illite du Puy experiments to investigate the effect of pH on illite dissolution rate (*exps. 1 to 4*; Table 2.6). Solutions were prepared by mixing different amounts of 1M HCl and Millipore MQ water (18.2 MΩ cm). Two HCl solutions of pH ≈ 3 were prepared to obtain the illite dissolution rate by varying the Ca concentration (*exps. 5 and 6*; Table 2.6): one solution was Ca-free, being prepared by pouring 2 mL of 1M HCl solution into 2 L of Millipore MQ water and the other one consisted of a synthetic Hontomín acid brine (*S-rich(a1)*, which was prepared by pouring ≈ 2 mL of 1M HCl and different amounts of analytical reagents (NaCl, $CaCl_2 \cdot 2H_2O$, $MgCl_2 \cdot 6H_2O$, KCl and NaBr, Na_2SO_4; Table 2.6) into 2L of Millipore MQ water (18.2 MΩ cm). The mixture was stirred for 72 h and filtered thereafter using a 0.2 µm Nucleopore polycarbonate membrane filter. Likewise, two similar solutions of pH ≈ 3 (Ca-free HCl solution and S-rich solution (*S-rich(a2)*) were used to investigate marl dissolution *(exps. 7 and 8*; Table 2.6). All solutions were prepared at atmospheric pCO_2 and room temperature (T = 25 °C; Table 2.6).

2.1.3.2 Column experiments

The column experiments (*Chapter III*) at atmospheric pCO_2 were carried out using two solutions: one at pH ≈ 3 (HCl; *exps. 9, 12 and 15*) and the other one being a synthetic Hontomín S-rich acid brine solution (*S-rich(a3)*) at pH = 3.7 *(*HCl + salts; *exp. 10, 11, 13, 14, 16 and 17*; Table 2.6). The column experiments at pCO_2 of 10 and 37 bar (*exps. 18-21*) were performed using three similar synthetic Hontomín S-rich brine solutions (*S-rich(1)*, *S-rich(2)* and *S-rich(3)*; Table 2.6). At pCO_2 > atmospheric, the acidification of the solution comes from the dissolved $CO_{2(aq)}$ (Table 2.6) while at atmospheric conditions comes from the HCl, leading to undersaturation with respect to calcite. The concentration of CO_2 was 0.5 mol kgw^{-1}. The oxygen concentration was estimated to be 3.06×10^{-4} mol L^{-1} (atmospheric O_2 concentration (2.84×10^{-4} mol L^{-1}) plus the O_2 content impurities of the liquid CO_2 bottle). The saturation indexes of the injected solutions were calculated using the PhreeqC v.3 code (Parkhurst and Appelo, 2013) and the PhreeqC database. Initial solution pH was calculated by charge balance and was ≈ 3.60 ± 0.2 (Table 2.6).

2.1.3.3 Percolation experiments

In the percolation experiments (*Chapter IV*), three synthetic solutions were used to study the reactivity of the *S4.3* marl: two sulfate-free solutions with respective ionic strength (*I*) of 0.3 and 0.6 M and a sulfate-rich solution with *I* = 0.6 M. The sulfate-free solutions (*S-free(1) and S-rich(2)*; Table 2.6) were prepared to be equilibrated with respect to calcite at 25 °C by mixing analytical reagents (NaCl, $CaCl_2 \cdot 2H_2O$, $MgCl_2 \cdot 6H_2O$, KCl and NaBr) and Millipore MQ water (18.2 MΩ cm). The sulfate-rich solution (*S-rich(4)*; Table 2.6) was meant to be an analog of the Hontomín reservoir groundwater, equilibrated with respect to calcite, dolomite and gypsum at 25 °C by adding precise amounts of Na_2SO_4. The mixtures were stirred for 72 h and filtered using a 0.2 µm Nucleopore polycarbonate membrane filter. CO_2 was co-injected and mixed together with the *S-free* and *S-rich* solutions at P_{Total} = 150 bar and *T* = 60 °C. The dissolved $CO_{2(aq)}$ acidified the solution (Table 2.6), leading to solution undersaturation with respect to calcite. The concentration of CO_2 for both the *S-free* and *S-rich* solutions was 0.6 mol kgw^{-1}. The oxygen concentration was estimated to be 3.06×10^{-4} mol L^{-1} (atmospheric O_2 concentration (2.84×10^{-4} mol L^{-1}) plus the O_2 content impurities of the liquid CO_2 bottle). The saturation indexes of the injected solutions were calculated using the PhreeqC v.3 code (Parkhurst and Appelo, 2013) and the PhreeqC database. Initial solution pH was calculated by charge balance and was ≈ 3.2.

2.1.3.4 Batch experiments

In the batch experiments (*Chapter V*), Millipore MQ water was equilibrated with respect to calcite (*eq.Ca*) by pouring some calcite fragments into 2L of Millipore MQ water (18.2 MΩ cm) at room *T* and atmospheric pCO_2 conditions (Table 2.5). The mixture was stirred for approximately 34 days. The resulting solution was filtered using a 0.1 µm nucleopore polycarbonate membrane filter. The measured pH and Ca concentration was 7.7 and 1.86×10^{-4} mol kgw^{-1}, respectively. Under atmospheric conditions ($pCO_2 = 390 \times 10^{-6}$ bar), this solution turned out to be still undersaturated with respect to calcite (saturation index *SI* = -1.29).

Table 2.6 Chemical composition and saturation indexes of the initial injected solutions for the experiments described in *Chapter III and IV*.

experimtal setup	Flow-through					Column								Percolation		
label	***Ilt-25-1, Ilt-25-5, Ilt-25-2, Ilt-25-3***	***Ilt-Cal-25-1***	***Ilt-Cal-25-2***	***Mar-25-3***	***Mar-25-4***	***Marc-25-1, Marc-25-3***	***Marc-25-5***	***Marc-25-2a, Marc-25-6a, Marc-25-4a***	***Marc-60-2a, Marc-60-6a, Marc-60-4a***	***Marc-25-8***	***Marc-60-8***	***s3.4b***	***s4.3b***	***S4.3a-4, S4.3a-3, S4.3a-6***	***S4.3a-5***	***S4.3a-2, S4.3a-1, S4.3a-10***
N⁰ exp.	**1**	**5**	**6**	**7**	**8**	**9 and 15**	**12**	**10, 13 and 16**	**11, 14 and 17**	**18**	**19**	**20**	**21**	**22, 23 and 24**	**25**	**26, 27 and 28**
injected solution	HCl	HCl	*S-rich(a1)*	HCl	*S-rich(a2)*	HCl	HCl	*S-rich(a3)*		*S-rich(1)*	*S-rich(2)*	*S-rich(3)*		*S-free(1)*	*S-free(2)*	*S-rich(4)*
P_{Total} **[atm]**	1									10		150				
T **[°C]**	25									25	60	60		60	60	60
rock	*illite*	*Illite + calcite*		*marl (S2.4)*		*marls (S2.4/S4.3)*	*marl (S3.4)*	*marls (S2.4/S3.4/S4.3)*	*marls (S2.4/S3.4/S4.3)*	*marl (S4.3)*		*marl (S3.4)*	*marl (S4.3)*	*marl (S3.4)*	*marl (S4.3)*	*marl (S3.4)*
	concentration (mol kgw^{-1})															
Ca++	-	1.86×10^{-5}	5.01×10^{-2}	2.27×10^{-5}	4.29×10^{-2}	2.12×10^{-6}	3.52×10^{-4}	4.80×10^{-2}		4.74×10^{-2}	5.10×10^{-2}	4.77×10^{-2}		2.20×10^{-2}	4.20×10^{-2}	5.10×10^{-2}
Mg++	-	8.25×10^{-6}	3.80×10^{-2}	7.99×10^{-6}	3.16×10^{-2}	7.64×10^{-7}	1.34×10^{-5}	3.00×10^{-2}		2.86×10^{-2}	3.00×10^{-2}	3.08×10^{-2}		1.60×10^{-2}	3.20×10^{-2}	3.20×10^{-2}
HCO3-	-	1.36×10^{-5}	1.36×10^{-5}	1.36×10^{-5}	1.36×10^{-5}	1.36×10^{-5}	1.36×10^{-5}	8.85×10^{-6}		2.87×10^{-1}	1.47×10^{-1}	4.14×10^{-1}		8.66×10^{-1}	8.66×10^{-1}	8.66×10^{-1}
SO4--	-	1.00×10^{-9}	2.07×10^{-2}	1.00×10^{-9}	1.56×10^{-2}	1.00×10^{-9}	2.27×10^{-5}	2.56×10^{-2}		2.64×10^{-2}	2.84×10^{-2}	2.63×10^{-2}		1.00×10^{-9}	1.00×10^{-9}	2.70×10^{-2}
Na+	-	1.00×10^{-9}	4.38×10^{-1}	1.00×10^{-9}	3.93×10^{-1}	1.00×10^{-9}	1.00×10^{-9}	3.86×10^{-1}		3.51×10^{-1}	3.59×10^{-1}	3.71×10^{-1}		2.00×10^{-1}	3.60×10^{-1}	3.90×10^{-1}
K+	-	1.00×10^{-9}	1.22×10^{-2}	1.00×10^{-9}	1.12×10^{-2}	1.09×10^{-6}	1.00×10^{-9}	1.06×10^{-2}		1.00×10^{-2}	1.13×10^{-2}	1.09×10^{-2}		5.70×10^{-3}	1.10×10^{-2}	1.10×10^{-2}
Al+++	-	1.00×10^{-9}	1.02×10^{-9}	1.00×10^{-9}	1.00×10^{-9}	1.00×10^{-9}	1.00×10^{-9}	1.00×10^{-9}		9.47×10^{-6}	1.00×10^{-9}	1.00×10^{-9}		1.00×10^{-9}	1.00×10^{-9}	1.00×10^{-9}
Cl-	7.1×10^{-3}/6.2×10^{-5}	9.33×10^{-4}	5.74×10^{-1}	8.91×10^{-4}	5.25×10^{-1}	9.49×10^{-4}	1.69×10^{-3}	4.91×10^{-1}		4.48×10^{-1}	4.77×10^{-1}	4.86×10^{-1}		2.75×10^{-1}	4.85×10^{-1}	5.01×10^{-1}
Br-	-	1.00×10^{-9}	5.74×10^{-1}	1.00×10^{-9}	5.12×10^{-1}	1.00×10^{-9}	1.00×10^{-9}	1.13×10^{-2}		1.14×10^{-2}	1.13×10^{-2}	1.00×10^{-9}		5.69×10^{-3}	1.14×10^{-2}	1.14×10^{-2}
Fe++	-	1.00×10^{-9}	3.12×10^{-6}	1.00×10^{-9}	3.12×10^{-6}	1.00×10^{-9}	1.00×10^{-9}	3.58×10^{-7}		1.68×10^{-6}	7.92×10^{-7}	2.84×10^{-6}		6.94×10^{-9}	6.94×10^{-9}	6.94×10^{-9}
SiO2(aq)	-	1.00×10^{-9}	2.75×10^{-6}	1.00×10^{-9}	2.75×10^{-6}	2.89×10^{-7}	2.37×10^{-5}	3.50×10^{-5}		6.44×10^{-6}	3.34×10^{-5}	6.48×10^{-6}		4.50×10^{-7}	4.50×10^{-7}	4.50×10^{-7}
O2(aq)	-	2.84×10^{-4}	2.84×10^{-4}	2.84×10^{-4}	2.84×10^{-4}	2.84×10^{-4}	2.84×10^{-4}	2.84×10^{-4}		2.84×10^{-4}	2.84×10^{-4}	2.84×10^{-4}		3.06×10^{-4}	3.06×10^{-4}	3.06×10^{-4}
pH (measured)	2.15/4.21	3.03	3.01	3.09	3.03	3.04	3.03	3.72		3.62	3.71	3.45		3.36	3.18	3.25
Minerals	***SI* (PhreeqC)**															
calcite	-17.9/-13.7	-11.6	-9.0	-11.6	-9.0	-12.7	-10.6	-7.0	-7.4	-3.5	-3.0	-3.0		-3.2	-3.3	-3.1
quartz	-5.0/-5.0	-5.0	-1.0	-5.0	-1.5	-2.5	-0.6	-0.4	-0.9	-1.2	-1.2	-1.9		-2.9	-2.9	-2.9
illite	-55.3/-38.3	-43.4	-30.9	-43.4	-32.3	-33.7	-28.8	-17.5	-16.8	-14.4	-17.6	-22.3		-26.0	-27.5	-27.2
albite	-41.4/-32.9	-35.5	-18.5	-35.5	-19.9	-28.3	-22.7	-10.6	-10.9	-10.7	-11.6	-14.9		-18.1	-18.7	-18.5
gypsum	-13.9/-13.4	-9.3	-0.1	-9.1	-0.3	-10.2	-3.7	0.0	0.0	0.0	0.0	0.0		-7.5	-7.5	0.0
clinochlore	-125.4/-91.3	-101.4	-66.0	-101.4	-67.4	-98.0	-89.0	-62.1	-53.2	-61.7	-58.2	-61.6		-67.6	-70.4	-69.7
anhydrite	-14.2/-13.9	-9.6	-0.4	-9.5	-0.6	-10.5	-4.0	-0.3	0.0	-0.3	0.0	0.0		-7.5	-7.5	0.0
pyrite	-32.5/-64.6	-244.0	-34.1	-244.0	-31.0	-243.9	-235.3	-231.4	-202.7	-229.6	-204.7	-202.8		-218.1	-218.2	-203.4
kaolinite	-31.2/-18.4	-24.5	-20.1	-24.5	-20.8	-19.9	-16.3	-11.8	-11.0	-7.9	-11.4	-14.4		-16.5	-17.8	-17.5
dolomite-dis	-35.7/-27.2	-24.0	-17.9	-23.9	-18.0	-3.8	-1.9	-1.7	-2.0	-2.5	-2.2	-6.2		-3.9	-3.9	-3.9
SiO2(am)						-26.2	-22.9	-14.5	-14.9	-7.5	-6.2	-3.0		-6.4	-6.7	-6.5
mesolite						-37.1	-30.2	-16.8	-16.0	-14.5	-16.7	-21.0		-24.5	-25.8	-25.4
stilbite						-46.1	-31.1	-20.2	-21.3	-20.5	-22.7	-30.2		-37.3	-38.9	-38.4
smectite						-39.7	-32.2	-19.7	-18.7	-20.3	-20.4	-24.4		-28.9	-30.1	-29.8
mordenite						-29.9	-19.7	-12.2	-13.5	-14.1	-14.7	-19.5		-24.6	-25.2	-25.0
Scolecite						-35.1	-27.5	-19.2	-17.9	-16.9	-18.6	-23.0		-26.3	-27.8	-27.3
Analcime						-25.2	-21.4	-10.0	-9.8	-9.4	-10.3	-12.8		-15.1	-15.7	-15.5
Wairakite						-43.9	-34.3	-25.8	-23.9	-24.3	-24.7	-29.9		-34.2	-35.6	-35.2
Laumontite						-39.5	-29.9	-21.3	-20.5	-19.9	-21.3	-26.5		-30.8	-32.2	-31.8
Gismondine						-67.2	-55.7	-39.6	-45.1	-33.4	-45.9	-53.1		-57.9	-60.8	-59.9
montmorillonite-Ca						-28.6	-20.4	-13.9	-13.9	-12.9	-14.8	-19.4		-23.5	-24.6	-24.3
montmorillonite-K						-29.3	-22.4	-14.0	-14.2	-13.0	-15.0	-19.7		-23.8	-24.8	-24.6
montmorillonite-Mg						-28.6	-20.5	-13.8	-13.8	-12.9	-14.7	-19.3		-23.3	-24.5	-24.2
montmorillonite-Na						-30.6	-22.8	-13.8	-13.9	-12.8	-14.8	-19.4		-23.5	-24.6	-24.3

K_{eq} values are from Phreeqc V.3 database except for gypsum which is from Garcia-Rios et al. (2014).

2.1.4 Experimental Setup and Methodology

Six experimental setups were used to carry out the different flow-through, column, percolation and batch experiments at atmospheric pressure (*atm*-CO_2), subcritical pressure (*subc.*-CO_2) and supercritical pressure (*supc.*-CO_2) (Table 2.7).

Table 2.7 Experimental conditions, experimental setups and types of samples used in the different experiments.

		experimental conditions							
sample type (description)	**experimental setup**	***T*** **[°C]**	***P*** $_{Total}$ **[bar]**			***p*** CO_2 **[bar]**			
powder and crushed rock (Chapter III)	Flow-though	25	1			$10^{-3.5}$			
	Column-*atm*-CO_2	25	1			$10^{-3.5}$			
	Column-*subc.*-CO_2	25	10			10			
	Column-*subc.*-CO_2	60	10			10			
	Column/Percolation-*supc.*-CO_2 ICARE Lab CSS II	60	150			37			
fracture core (chapter IV)		60	150			61			
	Percolation-*supc.*-CO_2 ICARE Lab CSS I	60	150			61			
powder (Chapter V)	Batch-*subc.*-CO_2	25	10	50	74	10	50	74	
	Batch-*supc.*-CO_2	70							
		90							

2.1.4.1 Flow-through experimental setup (*atm*-CO_2; *p*CO_2 = $10^{-3.5}$ bar)

Flow-through experiments were carried out in reaction cells that varied from 40 to 50 mL in volume, with two chambers separated by a fine mesh (0.45 µm). Powder (illite) or crushed rock (limestone and marl) samples (≈ 1 g) were placed onto the fine mesh (lower chamber). Input solution circulated through a tube of 0.76 mm in diameter. The flow rate was controlled by a peristaltic pump and ranged from 0.020 to 0.034 mL min^{-1}. Input and output solutions passed through 0.45 µm nylon membranes that were placed at the inlet and outlet of the lower and upper chambers, respectively (Fig. 2.7). Residence times ranged from approximately 24 to 32 h. Experiments had different time durations (*t*) until steady state was reached ($\partial C/\partial t = 0$). The steady state condition for each experiment was considered to be attained when differences in the Al and Si concentrations in output solutions were within ±10 % in consecutive solution output

samples for at least ≈ 800 h. After steady-state conditions were reached, steady-state illite dissolution rates were calculated.

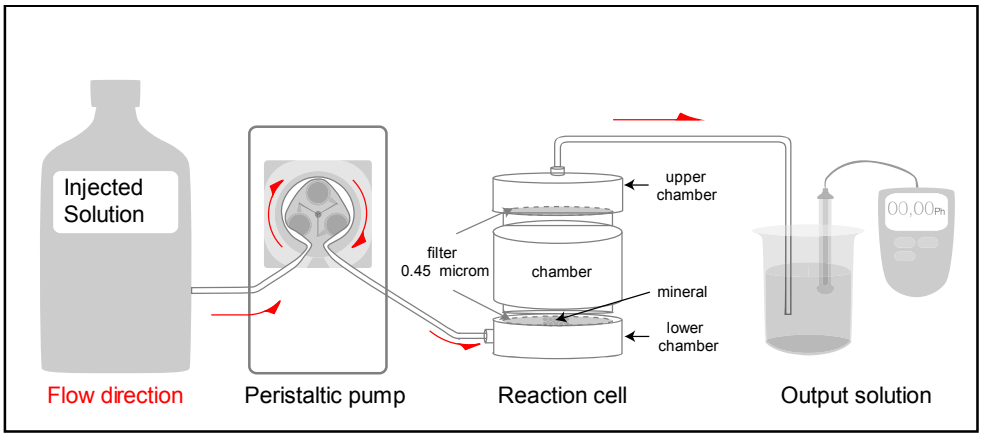

Figure 2.7 *Experimental setup used in flow-through experiments under atmospheric conditions.*

2.1.4.2 Column experimental setup (*atm*-CO_2; $pCO_2 = 10^{-3.5}$ bar)

Transparent methacrylate cylindrical columns of 2.6 cm in diameter (ℓ) and 2.5-3 cm in length (L) were filled in approximately 20 g of crushed rock fragments with a grain size of 1-2 mm. A bed of glass beads 0.7 mm in diameter was placed at the top and bottom of the cylinder to homogenize the inlet and outlet solutions. The thickness of the beds was about 0.8 cm, yielding an effective column volume (V_{bulk}) of 13.8 cm^3 (Fig. 2.8). A 0.22 µm filter was placed at the top of the column to prevent any particle release into the output solution. Column porosity was calculated using the mass of the rock sample, the density of the rock and the effective column volume. The density of the *S2.3* marl (ρ = 2.71 g cm^{-3}) was obtained from the weight fractions of the minerals [calcite (87.3 *wt.*%), quartz (4.2 *wt.*%), illite (7.6 *wt.*%) and albite (0.9 *wt.*%)] and the respective densities (2.71, 2.65, 2.80 and 2.61 g cm^{-3}; Downs, 2006). Initial porosities ranged from 0.42 to 0.56 (Table 2.8). Given the mineral mass, the rock density and the effective column volume, and assuming that the rock fragments were spheres of 1.5 mm in diameter, the geometric surface area of the *S2.3* marl fragments was approximately 2317 $m^2_{mineral}\ m^{-3}_{bulk}$.

Input solutions were injected from bottom to top of the column using a peristaltic pump under a constant flow rate of 0.021 ± 0.002 mL min^{-1} (Table 2.8). The outlet solution was periodically

collected. Darcy velocity and residence times are listed in Table 2.8. Collected samples were immediately acidified with 1% HNO_3 to avoid changes in chemical composition. For the experiments performed at 60 °C the columns were fully immersed in a thermostatic bath. Input and output pH at the desired temperature was measured with a conventional glass pH electrode (accuracy ± 0.02) that was calibrated using Crison buffer solutions of pH 2.02 and 7.00. Total input and output concentrations were measured by ICP-AES (see *Section 2.1.1*).

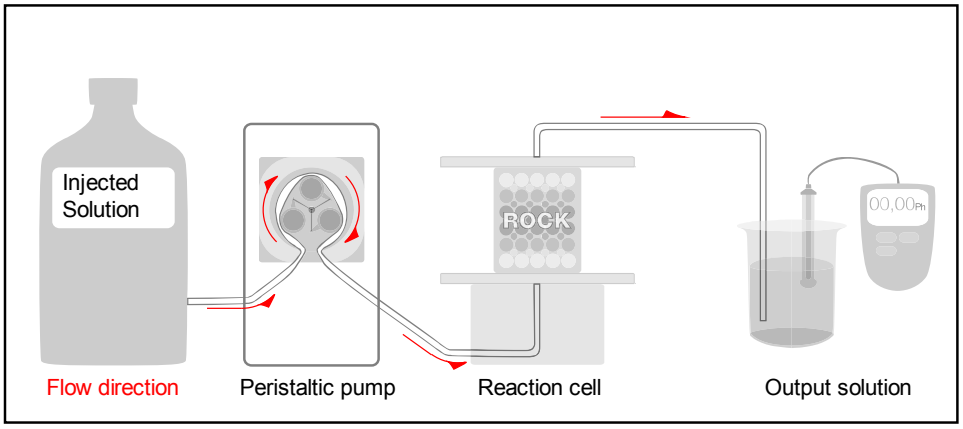

Figure 2.8 *Scheme of the experimental setup used in the column experiments under atmospheric conditions.*

2.1.4.3 Column experimental setup (*subc.*-CO_2 ; pCO_2 = 10 bar)

The experimental setup was completely designed and assembled at the Geosciences Department of the IDAEA-CSIC in collaboration with the GASLI company, a manufacturer of pressure gauges and measurement instruments located in Barcelona.

A 316 stainless steel column (3.2 cm in diameter (ℓ) and 6 cm in length (L)) was filled with approximately 60 g of crushed rock fragments with a grain size of 1-2 mm. The mass of the sample was weighed before and after the experiments. Two plastic filter screens of 1 mm thickness were placed at the top and bottom of the cylinder to homogenize the inlet and outlet solutions. Two pieces of 0.45 µm stainless steel mesh were likewise placed at the bottom and the top of the reaction cell to prevent any particle release into the output solution. The effective column volume (V_{bulk}) was 43.43 cm^3. Initial porosity ($\phi_{(i)}$) was calculated using the same approach as in the atmospheric pressure setup was approximately 49 %. Given the mineral mass,

the rock density and the effective column volume, and assuming that the fragments were spheres of 1.5 mm in diameter, the geometric surface area of the marl fragments was approximately 2000 $m^2_{mineral}\ m^{-3}_{bulk}$.

The input solution was poured into the Teflon-coated pressurized storage tank (V_{tank}) of 3 L capacity. Sufficient head space was left to inject CO_2 gas under the desired pressure (P_{Total} = 10 bar). To ensure that CO_2 was the only gas phase in contact with the solution, air was removed airing the head space with CO_2 gas for 15 min approximately. Thereafter, to guarantee that the input solution was equilibrated with CO_2 before injection, the valve that connects the CO_2 bottle with the storage tank was alternatively closed and opened until no pressure drop occurred in the tank with the valve closed. Once the pressure in the closed tank was constant (after *ca.* 12 h) the solution was considered to be in equilibrium with CO_2 and ready to be injected. The CO_2-equilibrated input solution was injected from bottom to top through the crushed sample by a dual-piston pump under a constant flow rate of 0.02 ± 0.005 mL min^{-1} (Fig. 2.9). Darcy velocities were 1.1 × 10^{-6} and 1.2 × 10^{-6} $m^3\ m^{-2}\ s^{-1}$ yielding residence times (τ) of 6 and 7 h for *exps. 18 and 19*, respectively (according to the different sections; Table 2.6). Solution pH and fluid pressure were measured in line before the solution reached the column and after the reaction cell. pH was measured using Hamilton Polilyte Plus XP 120 pH electrodes (accuracy ± 0.02), which allow measurements under conditions up to 60 °C and 50 bar. The electrodes were calibrated using Crison buffer solutions of pH 2.02 and 7.00. Fluid pressure was measured using Gasli pressure transducers with a pressure range from -1 to 24 bar and an accuracy of 0.5% full scale.

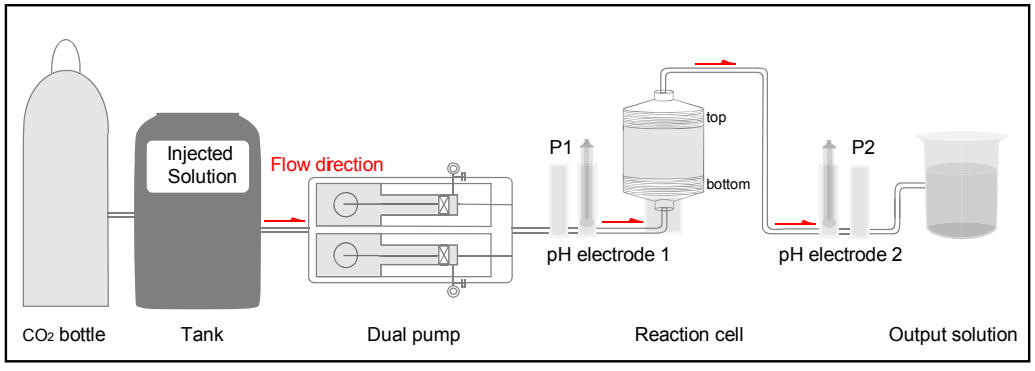

Figure 2.9 *Scheme that shows the experimental setup used to perform column experiments under 10 bar of pCO_2.*

The reacted solution was collected using two pressurized syringes of 250 mL, which worked as back-pressure system maintaining the whole setup under a total pressure of 10 bar. After filling one syringe, the solution was manually diverted to the other one. This sampling system allowed the collection of the output solution without any experimental interruption. Collected output solutions were extracted from the syringe and immediately acidified with 1% HNO_3 to avoid any potential precipitation during sample depressurization. The whole sampling operation lasted less than 2 min. Total concentrations were analyzed using ICP-AES (see *Section 2.1.1*). Column experiments were performed at 22-25 °C and 60 ± 0.1 °C. The storage tank and the column were adequately heated using a resistor and insulated for the experiment performed at 60 °C.

2.1.4.4 Column and percolation experimental setups (*supc.*-CO_2; pCO_2 = 150 bar)

Two flow-through apparatus (Icare Lab CSS I, Luquot and Gouze, 2009, and Icare Lab CSS II, Luquot et al., 2012), which belong to the Geosciences Department of Montpellier University (France), were used to reproduce the *in situ* reservoir conditions for CO_2 sequestration (Fig. 2.10). In both experimental devices, the CO_2-equilibrated solution was injected into the percolation cell using a monitorized piston-pump system. This system was equipped with displacement encoders to obtain an accurate control of the flow rate, ranging from 0.6 to 180 mL h^{-1} in Icare Lab CSS I and from 0.05 to 40 mL h^{-1} in Icare Lab CSS II. Radial confining pressure was applied to the silicon jacket that covered the sample in the percolation cell (112% of the inlet pressure). The piston pump motion and the pneumatically-controlled valves were operated by LabView-based software.

Two column experiments with crushed rock samples were performed using the ICARE Lab CSS I apparatus with a flow rate of 0.01 mL min^{-1} (0.6 mL h^{-1}), P = 150 bar and T = 60 ºC (Fig. 2.10a; *Chapter III)*. The CO_2 partial pressure of the inlet solution was set to be 37 bar (0.41 mol L^{-1} of CO_2) (Table 2.6). 0.8258 ± 0.001 g and 0.9962 ± 0.001 g of ground *S3.4 (exp. 20)* and *S4.3* (*exp. 21*) marl samples (grain size of 250-500 µm) were placed in Teflon cells of 0.7 cm in inner diameter (ℓ) and 1.7 cm length (L) with an effective column volume of 0.69 cm^3. Calculated initial volumes of solid were 0.3013 and 0.3691 cm^3 with an initial porosity of around 53.9 and 43.6 %, respectively. A 0.45 µm stainless steel filter was placed at the outlet (bottom) of the

Teflon cell to prevent particle escape into the output solution. Given the mineral mass, the rock density and the effective column volume, and assuming that the rock fragments were spheres of 0.375 µm in diameter, the geometric surface areas of the respective samples were 3684 and 4513 $m^2_{mineral}\ m^{-3}_{bulk}$ (*exps. 20 and 21)*. Test tubes of 10 mL were used to collect 0.5 mL of the output solution, which was acidified with 9.5 mL of 1% HNO_3 solution to avoid precipitation of carbonates during sample depressurization. Total concentrations were analyzed by ICP-AES (see *Section 2.1.1*). Darcy velocity was 4.33×10^{-6} $m^3\ m^{-2}\ s^{-1}$ in both experiments, yielding a residence time (τ) of 0.6 and 0.5 h for *exps. 20 and 21,* respectively (Table 2.8).

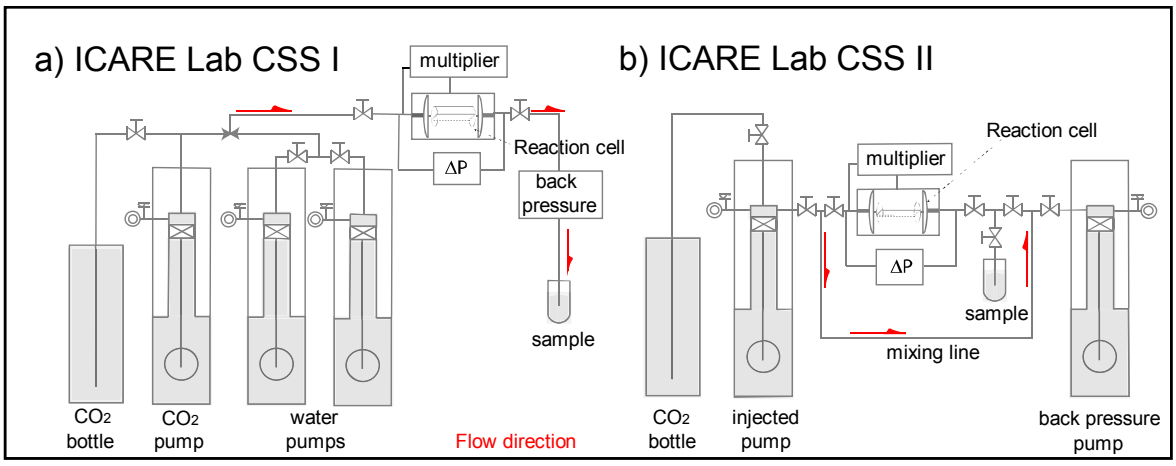

Figure 2.10 *Schemes showing: a) the ICARE Lab CSS I experimental setup and b) the ICARE Lab CSS II experimental setup. CO_2 is added from a liquid CO_2 reservoir.*

Seven percolation experiments with fractured cores were run using both experimental apparatus (Figs. 2.10a and b; Icare Lab CSS I and Icare Lab CSS II). The CO_2 partial pressure of the inlet solution was set to be 61 bar (0.61 mol/L of CO_2) and obtained by mixing the solutions with industrial-grade pure CO_2. CO_2-rich solutions were injected under a constant volumetric flow rate corresponding to Q = 60 mL h^{-1} for *exps. 24 and 28* using Icare Lab CSS I and Q = 0.2 and 1 mL h^{-1} for *exps. 22, 23, 25, 26 and 27* using Icare Lab CSS II (Table 2.8). The pressure difference (ΔP) between the inlet and the outlet of the sample was recorded continuously. As before periodically, 0.5 mL of the output solution was collected in 10 mL test tubes that contained 9.5 mL of 1% HNO_3 solution. The acid was used to prevent any carbonate precipitation due to sample depressurization. Total concentrations were analyzed by ICP-AES (see *Section 2.1.1*). The geometric areas of the minerals that form the marl rocks ($m^2_{mineral}\ m^{-3}_{rock}$)

calculated as explained above, are given in Table 2.9. The grain radii of quartz and clinochlore were measured from SEM images (23 µm and 30 µm, respectively). Since calcite matrix in the marl rocks was assumed to be formed of small aggregates with a radius of 2.5 µm, the geometric area of calcite was 2×10^5 $m^2_{mineral}$ m^{-3}_{bulk} (Table 2.9).

2.1.4.5 Batch experimental setup (pCO_2 > 10 bar)

Thirty-eight stirring batch experiments at 25, 70 and 90 °C and pCO_2 of 10, 50 and 74 bar were conducted in an autoclave system (Fig. 2.11). The experimental time spans varied from 5 to 97 hours. The solid/solution ratio was kept constant in all the experiments (5.3 g MgO/47.7 mL of Ca-rich water). Once solid and solution were placed in the autoclave, the desired pCO_2 and temperature were applied and maintained constant during the whole experimental run. In the experiments run at T > 25 °C, the desired temperature in the autoclave was reached one hour before the experimental run (before injecting the solution and the CO_2). The experiments were stirred at 500 rpm to guarantee homogeneous composition of the bulk solution. At the end of the experiment, 10 mL of solution were sampled with a syringe, immediately filtered and acidified in 10 mL of 2% HCl solution (pH = 1) to avoid precipitation of Ca and Mg-bearing carbonate phases as sample depressurized. Total concentrations of Mg and Ca were measured by ICP-AES in a Thermo Jarrel-Ash instrument with CID detector. The detection limits were 10 and 200 mg L^{-1}, respectively, and the analytical error was estimated to be 3%.

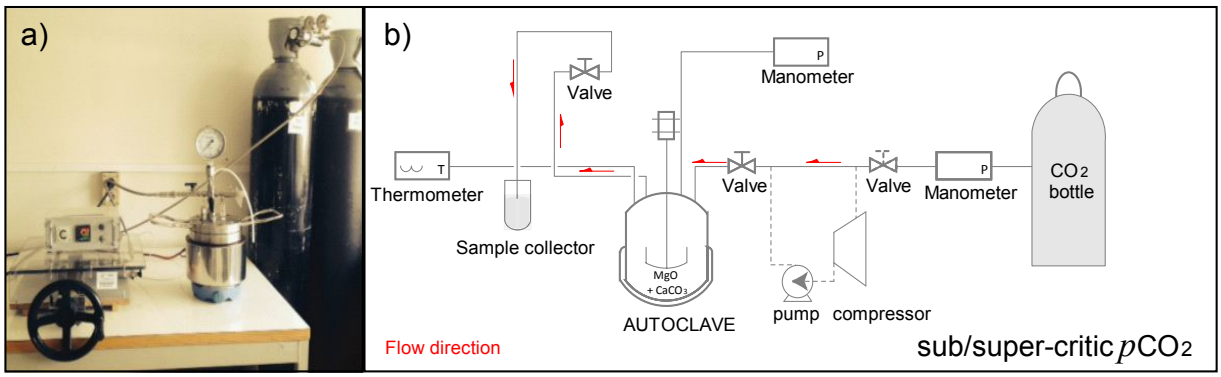

Figure 2.11 *Photography (a) and scheme (b) of the experimental setups to perform batch experiments under different* P_{Total}, pCO_2 and T *conditions.*

2.2Calculations

2.2.1 Calculation of the illite dissolution rate

In the flow-through experiments (*exps. 1-8*; *Chapter III*), the illite dissolution rate was calculated based on the temporal variation of the aqueous Si concentration in the output fluid. The illite dissolution rates (r_{Si}) obtained at different acid pH values were compared with the apparent illite dissolution rates obtained by Köhler et al. (2003). The authors used the term apparent illite dissolution rate because the rate was obtained from the net Si flux during closed system experiments, and may in some cases stem from a combination of illite dissolution and 1) the precipitation of potential Si bearing secondary phases; or 2) the effect of colloid retention. In the present study, when the output Si concentration reached steady state $\left(\frac{dC_{Si}}{dt}=0\right)$, the steady-state illite dissolution rate (r_{Si} in mol m^{-2} s^{-1}) was calculated as (Cama et al., 2000)

$$r_{Si}=\frac{Q}{v_{Si}M_{ilt}S_{ilt}}\left(C_{Si(o)}-C_{Si(i)}\right) \tag{2.18}$$

where Q is the flow rate (m^3 s^{-1}), M_{ilt} represents the mass of the sample, v_{Si} is the Si stoichiometric coefficient in the illite du Puy, S_{ilt} is the BET specific surface area of the sample (124 m^2 g^{-1}; Köhler et al. (2003)), and $C_{Si(i)}$ and $C_{Si(o)}$ are the input and output Si concentration (mol m^{-3}), respectively.

2.2.2 Calculation of parameters used in the reactive transport modeling

First estimation of the value of the mineral reactive surface area ($A_{geometric}$ in $m^2_{mineral}m^{-3}_{bulk}$) of the initial samples was done by assuming that the mineral grains were spheres. The diameter of the grains was estimated from the mineral grain sizes measured in the ESEM images of initial samples

$$A_{geometric}=\frac{A_g}{V_{bulk}} \tag{2.19}$$

where V_{bulk} is the effective volume of cell (m^3) and A_g is the grain surface area (m^2) calculated using Eq.(2.20)

$$A_g = \frac{3}{r_g}\frac{m_{Rock}}{\rho_{Rock}} \tag{2.20}$$

where m_{Rock} is the mass of rock (g) used in each experiment, r_g is the grain radii (m) and ρ_{Rock} is the rock density (kg m^{-3}) calculated as

$$\rho_{Rock} = \sum_{j=1}^{n} wt._j\% \cdot \rho_j \cdot \frac{1}{100} \tag{2.21}$$

where j is the number of minerals that compose the rock, $wt._j\%$ is the weight percent, ρ_j is the density of each mineral (kg m^{-3}). $A_{reactive}$ is used as an initial guess in the reactive transport modeling. Initial porosity ($\phi_{(i)}$) in each experiment was calculated as

$$\phi_{(i)} = \frac{V_p}{V_{bulk}} \tag{2.22}$$

where V_p is the pore volume (m^3) defined as

$$V_p = V_{bulk} - V_{Rock} \tag{2.23}$$

where V_{Rock}, the rock volume (m^3) in each experiment, was calculated as

$$V_{Rock} = \frac{m_{rock}}{\rho_{Rock}} \tag{2.24}$$

and V_{bulk} is the cell volume (m^3) defined as

$$V_{bulk} = \pi \cdot (r_{Cell})^2 \cdot L_{Cell} \tag{2.25}$$

where r_{Cell} and L_{Cell} are the radius and length of the cell in m, respectively.

The residence time (τ in s) in each experiment was obtained as

$$\tau = \frac{V_p}{Q} \tag{2.26}$$

Finally, Darcy velocity (v_D) in $m^3\ m^{-2}\ s^{-1}$ was calculated as

$$v_D = \frac{L_{Cell}}{\tau}\phi_{(i)} \tag{2.27}$$

2.2.3 Mass balance calculations

In the experiments in which the marl was the initial rock described in *Chapter III and IV*, based on the marl rock reactions (dissolution of calcite, clinochlore and albite and precipitation of gypsum) and assuming that kaolinite precipitation could take place, $C_{j(diss)}$ and $C_{j(ppt)}$ were calculated from the following mass balance equations

$$C_{j(out)} = C_{j(in)} + \sum_{1}^{N} C_{j(diss)} - \sum_{1}^{M} C_{j(ppt)} \tag{2.28}$$

where $C_{j(out)}$ is the total concentration of element j in the output solution, $C_{j(diss)}$ and $C_{j(ppt)}$ are concentrations and precipitation, respectively, and N and M are the numbers of dissolved and precipitated minerals, respectively. For each element, Eq. (2.28) is given as

$$C_{Ca(out)} = C_{Ca(in)} + C_{Ca\ (Cal\ -diss)} + C_{Ca\ (\ Gp\text{-}diss)} - C_{Ca(Gp\text{-}ppt)} \tag{2.29}$$

$$C_{Fe\ (out\ )} = C_{Fe\ (in\ )} + C_{Fe\ (Cln\ -diss)} \tag{2.30}$$

$$C_{S\ (out\ )} = C_{S\ (\ in)} + C_{S\ (Gp\ -diss)} - C_{S\ (\ Gp\text{-}ppt)} \tag{2.31}$$

$$C_{Si(out)} = C_{Si(in)} + C_{Si(Cln\text{-}diss)} + C_{Si(Ab\text{-}diss)} - C_{Si(Kln\text{-}ppt)} \quad (2.32)$$

where calcite, clinochlore, gypsum, albite and kaolinite are referred as *Cal, Cln*, *Gp*, *Ab* and *Kln*, respectively, and mineral dissolution or precipitation as *-diss* or *-ppt*, respectively. As an example, the calcite dissolution rate (R_{Cal} in mol s^{-1}) was calculated as

$$R_{Cal} = \frac{n_{Cal\text{-}diss}}{t} \quad (2.33)$$

where $n_{Cal\text{-}diss}$ is the total number of moles of dissolved calcite during the experiments

$$n_{Cal\text{-}diss} = \int_{t'=0}^{t'=t} C_{Ca(Cal-diss)} Q \Delta t' \quad (2.34)$$

where $\Delta t'$ is the sampling time interval, t is the total experimental time. This formulation can be used to calculate the total amount of dissolved and precipitated minerals using the different minerals composition.

ΔC_j accounts for the difference between the output and the input concentrations of element j ($\Delta C_j = C_{j(out)} - C_{j(in)}$). The error associated to ΔC_j ($\varepsilon(\Delta C_j)$) was estimated using the Gaussian error propagation method (Barrante, 1974) from the equation

$$\varepsilon(\Delta C_j) = \left[\varepsilon\left(C_{j(out)}\right)^2 + \varepsilon\left(C_{j(in)}\right)^2\right]^{\frac{1}{2}} \quad (2.35)$$

where $\varepsilon(C_{j(in)})$ and $\varepsilon(C_{j(out)})$ are the absolute errors associated with the input and output concentrations of element j, respectively, with an estimated uncertainly in the measured concentrations of 3% (ICP-AES). $\varepsilon(\Delta C_j)$ ranged from 10 to 40 % for Ca and was around 3% for S, Fe and Si.

The volume of dissolved or precipitated mineral ($V_{min\text{-}diss}$ and $V_{min\text{-}ppt}$) was calculated as

$$V_{\min} = v_{\min} Q \int_{t'=0}^{t'=t} \alpha^{-1} C_j(t') dt' \quad (2.36)$$

where $v_{\min}$ is the molar volume of the mineral in m^3 mol^{-1}, α is the stoichiometric coefficient of element j in the mineral, C_j is the concentration of the element j from dissolved or precipitated mineral ($C_{j(diss)}$ or $C_{j(ppt)}$) in mol m^{-3} and t is the total experimental time. The molar volumes of calcite, clinochlore, gypsum, albite and kaolinite were calculated from the respective molecular weights and densities Downs, 2006) to be 36.9, 226.0, 74.3, 100.0 and 98.2 cm^3 mol^{-1}, respectively.

In the core samples used in *Chapter IV*, the initial fracture volume ($V_{f\text{-}initial}$ in m^3) was calculated as

$$V_{f\text{-}final} = L \cdot \ell \cdot h \quad (2.37)$$

Where L is the core length (m), ℓ is the core diameter (m) and h is the fracture aperture in (m). The final pore volume ($V_{f\text{-}final}$ in m^3) associated to the reacted core (volume of the final fracture plus volume of pores in the altered zone along the fracture wall), was calculated as

$$V_{f\text{-}final} = V_{f\text{-}initial} + V_{Cal\text{-}diss} + V_{Gp\text{-}diss} + V_{Cln\text{-}diss} + V_{Ab\text{-}diss} - V_{Gp\text{-}ppt} - V_{Kln\text{-}ppt} \quad (2.38)$$

where $V_{Cal\text{-}diss}$ is the volume of dissolved calcite, $V_{Gp\text{-}diss}$ is the gypsum , $V_{Cln\text{-}diss}$ is the clinochlore and $V_{Ab\text{-}diss}$ is the albite and $V_{Gp\text{-}ppt}$ is the volume of precipitated gypsum and $V_{Kln\text{-}ppt}$ is the kaolinite.

In the experiments when the Ca concentration reached steady state (*exps. 24 and 27*), a penetration length (x), corresponding to the zone next to the fracture affected by calcite dissolution, was calculated using

$$x = \frac{V_{Cal\text{-}diss}}{\mathbf{2}\cdot L\cdot \ell \cdot vol._{Cal}} \tag{2.39}$$

where $V_{Cal\text{-}diss}$ is the volume of dissolved calcite, L is the length of the core and $vol._{Cal}$ is the volume fraction of calcite (0.66) in the fractured cores.

Apparent diffusion coefficients (D_a, $m^2\ s^{-1}$) were obtained in the experiments where the output Ca concentration reached steady state as

$$D_a = \frac{x^2}{2t} \tag{2.40}$$

where x (m) is the penetration length Eq. (2.21), and t is the total experimental time (s).

The porosity over the reacted zone was estimated as

$$\phi_{Vol} = \frac{V_{Cal-diss} + V_{Gp-diss} + V_{C\ln-diss} + V_{Ab-diss} - V_{Gp-ppt} - V_{K\ln-ppt}}{V_{reac-zone}} + \phi_{(i)} \tag{2.41}$$

where $V_{reac\text{-}zone}$ is the volume of reacted zone ($2L\cdot\ell\cdot x$).

2.2.4 Calculation of permeability

The pressure drop between the inlet and the outlet of the crushed and fractured cores described in *Chapters III and IV* was continuously measured over the entire time of the column and percolation experiments respectively, using a differential pressure sensor (Rosemount 3051).

Permeability k (m^2) in the crushed samples was calculated as

$$k = \frac{Q\cdot L\cdot \mu}{\Delta P\cdot S} \tag{2.42}$$

where Q is the volumetric flow rate in $m^3\ s^{-1}$, L is the column length in m, μ is the viscosity of the fluid in $Pa{\cdot}s^{-1}$ ($0.47\ 10^{-3}\ Pa{\cdot}s^{-1}$) and ΔP is the pressure gradient in $Pa\ m^{-1}$, S is the cross section area ($S = \pi{\cdot}\ r^2$) in m^2.

Fracture permeability k_f (m^2) in the fractured cores was calculated as

$$k_f = \frac{h^2}{12} \tag{2.43}$$

where h is the hydraulic aperture in m. Eq. (2.42) was derived by combining the cubic law for flow, assuming that the fracture walls are represented by two smooth parallel plates (Huitt, 1956; Snow, 1969),

$$Q = -\frac{Wh^3}{12\mu}\nabla P \tag{2.44}$$

and Darcy's law

$$Q = -\frac{Ak_f}{\mu}\nabla P \tag{2.45}$$

where W is the fracture width in m, ∇P is the pressure gradient in $Pa\ m^{-1}$ and A is the cross section area ($A = W{\cdot}h$) in m^2. The volume of the fractures was estimated assuming a parallelepiped with h, L and W dimensions (Fig. 2.5a).

2.3.1 Calculation of saturation index

The saturation indexes (*SI)* of all input solutions under all experimental conditions were calculated using PhreeqC (v.3) (Parkhurst and Appelo, 2013).

Table 2.8 Parameters used and calculated for each experiment described in *Chapter III*.

experimental setup	*Flow-through*									
label	***Ilt-25-1***	***Ilt-25-5***	***Ilt-25-2***	***Ilt-25-3***	***Ilt-Cal-25-1***		***Ilt-Cal-25-2***		***Mar-25-3***	***Mar-25-4***
N^0 exp.	***1***	***2***	***3***	***4***	***5***		***6***		***7***	***8***
rock or mineral	illite	illite	illite	illite	illite	calcite	illite	calcite	*S2.4*	*S2.4*
parameters										
w [g]	0.7600				0.5027	0.5018	0.5027	0.5018	1.0045	1.005
r_g [m]	1.88×10^{-5}				3.0×10^{-8}	7.5×10^{-4}	3.0×10^{-4}	7.5×10^{-4}	7.5×10^{-4}	
ρ [g cm^{-3}]	2.8				2.79	2.71	2.79	2.71	2.71	2.71
$V_{sol.}$ [cm^3]	0.271				0.18	0.19	0.18	0.19	0.37	0.37
A_g [m^2 g^{-1}]	4.3×10^{-2}				$1.8 \times 10^{+1}$	7.4×10^{-4}	$1.8 \times 10^{+1}$	7.4×10^{-4}	1.5×10^{-3}	
Q [mL min^{-1}]	0.036	0.035	0.037	0.018	0.0218		0.0236		0.0217	0.0239
t [h]	1053	1536	1487	1536	2628		2565		2559.5	2418.5
r_{cell} [cm]	2.4				2.1		2.1		2.1	2.1
L_{cell} [cm]	2.7				2.7					
V_{cell} [cm^3]	50.0				38.8		38.8		38.8	38.8
V_p [cm^3]	49.73				38.5		38.5		38.47	38.47
$\phi_{(t)}$ [%]	99.46				99.06		99.06		99.05	99.05
total vol.%	0.54				0.94		0.94		0.95	0.95
v_D [m s^{-1}]	8.00×10^{-7}			3.93×10^{-7}	5.39×10^{-7}		5.85×10^{-7}		5.39×10^{-7}	5.92×10^{-7}
τ [h]	23	24	22	46	29		27		29	27
$A_{geometric}$ [m$^2_{mineral}$ m$^{-3}_{bulk}$]	$9 \times 10^{+2}$				$2 \times 10^{+5}$		$2 \times 10^{+5}$		$4 \times 10^{+1}$	

Table 2.8 Parameters used and calculated for each experiment described in *Chapter III*-cont´d.

experimental setup	*Column*												
label	***Marc-25-1***	***Marc-25-2a***	***Marc-60-2a***	***Marc-25-6***	***Marc-25-6a***	***Marc-60-6a***	***Marc-25-3***	***Marc-25-4a***	***Marc-60-4a***	***Marc-25-8***	***Marc-60-8***	***s3.4b***	***s4.3b***
N^0 exp.	***9***	***10***	***11***	***12***	***13***	***14***	***15***	***16***	***17***	***18***	***19***	***20***	***21***
rock or mineral	*S2.4*	*S2.4*	*S2.4*	*S3.4*	*S3.4*	*S3.4*	*S4.3*	*S4.3*	*S4.3*	*S4.3*	*S4.3*	*S3.4*	*S4.3*
parameters													
w [g]	20.8	20.0	20.1	16.0	20.0	20.0	18.8	20.0	20.0	60.1	59.2	0.83	0.99
r_g [m]	7.5×10^{-4}	3.8×10^{-4}											
ρ [g cm^{-3}]	2.71	2.71	2.71	2.74	2.74	2.74	2.70	2.70	2.70	2.70	2.70	2.74	2.70
$V_{sol.}$ [cm^3]	7.68	7.39	7.41	5.84	7.30	7.30	6.97	7.41	7.41	22.27	21.97	0.30	0.37
A_g [m^2]	3.0×10^{-2}		3.0×10^{-2}	2.3×10^{-2}	2.9×10^{-2}	2.9×10^{-2}	2.8×10^{-2}	3.0×10^{-2}	3.0×10^{-2}	8.9×10^{-2}	8.8×10^{-2}	2.4×10^{-3}	3.0×10^{-3}
Q [mL min^{-1}]	0.022	0.021	0.021	0.023	0.021	0.021	0.024	0.024	0.024	0.022	0.02	0.01	
t [h]	1104.0	720.0		1512.0	720.0		1056.0	720.0		1104.0	1056.0	1742.4	987.1
r_{cell} [cm]	1.3									1.6		0.35	
L_{cell} [cm]	3.0	2.6		2.5	2.8		3.0	2.6		5.4		1.7	1.7
V_{cell} [cm^3]	15.9	13.8	13.8	13.3	14.9	14.9	15.9	13.8	13.8	43.4	43.4	0.654	
V_p [cm^3]	8.25	6.41	6.39	7.44	7.56	7.57	8.96	6.39	6.39	21.16	21.46	0.35	0.28
$\phi_{(t)}$ [%]	51.79	46.45	46.33	56.02	50.87	50.89	56.27	46.31	46.31	48.72	49.42	53.90	43.60
total vol.%	48.21	53.55	53.67	43.98	49.13	49.11	43.73	53.69	53.68	51.28	50.58	46.10	56.40
v_D [m s^{-1}]	8.98×10^{-7}	8.57×10^{-7}		9.39×10^{-7}	8.57×10^{-7}		9.79×10^{-7}			1.99×10^{-6}	1.79×10^{-6}	1.52×10^{-6}	
τ [h]	6	5			6		4			6	7	0.6	0.5
$A_{geometric}$ [m$^2_{mineral}$ m$^{-3}_{bulk}$]	$4 \times 10^{+4}$									$4 \times 10^{+5}$		$4 \times 10^{+3}$	

Table 2.9 Parameters used and calculated for each experiment described in *Chapter IV*.

experimental setup	***Percolation***						
N exp.	***22***	***23***	***24***	***25***	***26***	***27***	***28***
label	***S4.3a-4***	***S4.3a-3***	***S4.3a-6***	***S4.3a-5***	***S4.3a-2***	***S4.3a-1***	***S4.3a-10***
w [g]	3.1	3.1	2.9	2.9	3.1	3.0	3.0
h [µm]	3.24	3.46	14.28	4.07	3.84	16.25	
ρ [cm^3 g^{-1}]	2.7						
$V_{fracture}$ [cm^3]	5.71×10^{-4}	5.81×10^{-4}	2.41×10^{-3}	6.60×10^{-4}	6.63×10^{-4}	2.84×10^{-3}	2.41×10^{-3}
Q [mL h^{-1}]	0.2	1	60	1	0.2	1	60
Q [mL min^{-1}]	0.0033	0.020	1.000	0.020	0.003	0.017	1.000
t [h]	43	21	6	23	35	70	7
ℓ_{core} [cm]	0.9						
L_{core} [cm]	1.96	1.86	1.87	1.80	1.92	1.94	1.84
V_{core} [cm^3]	1.24	1.18	1.19	1.15	1.22	1.23	1.17
$V_{injected}$ [mL]	8.6	21.0	340.7	23.0	7.0	69.6	416.4
$\phi_{(i)}$ (%)	7						
total vol.%	93	93	93	93	93	93	93
Section [m^2]	2.92×10^{-8}	3.12×10^{-8}	1.29×10^{-7}	3.66×10^{-8}	3.46×10^{-8}	1.46×10^{-7}	
v_D [m s^{-1}]	1.90×10^{-3}	8.91×10^{-3}	1.30×10^{-1}	7.58×10^{-3}	1.61×10^{-3}	1.90×10^{-3}	1.14×10^{-1}
τ [h]	10.3	2.1	0.1	2.4	11.9	10.2	0.1
$A_{geometric}$ [$m^2_{mineral}$ m^{-3}_{bulk}]	3×10^5						
$k_{f\text{-}initial}$ [m^2]	0.9×10^{-12}	1.0×10^{-12}	17.0×10^{-12}	1.4×10^{-12}	1.2×10^{-12}	22.0×10^{-12}	22.0×10^{-12}
Pe	4	21	1267	21	4	21	1267

2.3 Reactive transport modeling

1D simulations of the flow-through and column experiments (*Chapter III*), 0D simulations of the batch experiments (*Chapter V) and* 2D simulations of the percolation experiments with fractured cores (*Chapter IV)* were performed using CrunchFlow (Steefel et al., 2015).

2.3.1 Description of the reactive transport code

The reactive transport modeling was performed using the CrunchFlow code (Steefel et al., 2015), which solves numerically the mass balance of solutes expressed as

$$\frac{\partial(\phi C_j)}{\partial t} = \nabla \cdot (D \nabla C_j) - \nabla (v_D C_j) + R_j \qquad (j = 1, 2, 3, \ldots, n) \qquad (2.46)$$

where ϕ is porosity, C_j is the concentration of component j (mol m^{-3}), v_D is the Darcy velocity (m^3 m^{-2} s^{-1}), R_j is the total reaction rate affecting component j (mol m^{-3} rock s^{-1}) and D is the combined dispersion-diffusion coefficient (m^2 s^{-1}).

The total reaction rate R_j is given by

$$R_j = -\sum_m \nu_{jm} R_m \tag{2.47}$$

where R_m is the rate of precipitation (R_m>0) or dissolution (R_m<0) of mineral m in mol m^{-3} rock s^{-1}, and ν_{jm} is the number of the moles of j in mineral m.

The reaction rate laws used in the calculations are of the form

$$R_m = A_m \sum_{terms} k_{m,T} a_{H+}^{n_{H+}} \left(\prod_i a_i^{n_i} \right) f_m(\Delta G_r) \tag{2.48}$$

where A_m is the mineral surface area in m^2 m^{-3} rock, $k_{m,T}$ is the reaction rate constant in mol m^{-2} s^{-1}, $a_{H+}^{n_{H+}}$ is the term describing the effect of pH on the rate, $a_i^{n_i}$ is the term describing a catalytic/inhibitory effect on the rate by another species, and $f_m(\Delta G_r)$ is the function describing the rate dependence on the solution saturation state. The summation term indicates that several parallel rate laws may be used to describe the dependence of the rate on pH or on other species. The $f_m(\Delta G_r)$ function is defined as

$$f_m(\Delta G_r) = \left(\left(\frac{IAP}{K_{eq}} \right)^{m_2} - 1 \right)^{m_1} \tag{2.49}$$

where ΔG_r is the Gibbs free energy of the reaction (J mol^{-1}), IAP is the ionic activity product of the solution with respect to the mineral, K_{eq} is the equilibrium constant for that mineral reaction (ionic activity product at equilibrium) and m_1 and m_2 exponents allow for nonlinear dependencies on the affinity term and are normally taken from experimental studies. The rate constant at temperature T (K) is calculated from

$$k_{m,T} = k_{m,25} \exp\left(\frac{Ea}{R} \left(\frac{1}{T_{25}} - \frac{1}{T} \right) \right) \tag{2.50}$$

where $k_{m,25}$ is the rate constant at 25 ^{o}C, E_a is the apparent activation energy of the overall reaction (J mol^{-1}) and R is the gas constant (J mol^{-1} K^{-1}).

Change in mineral surface area (A_m in m$^2_{mineral}$ m$^{-3}_{bulk}$) due to dissolution is given by

$$A_m = A^{initial}\left(\frac{\phi_m}{\phi_{m(i)}}\right)^{\frac{2}{3}}\left(\frac{\phi}{\phi_{(i)}}\right)^{\frac{2}{3}} \tag{2.51}$$

Change due to precipitation is given by

$$A_m = A^{initial}\left(\frac{\phi}{\phi_{(i)}}\right)^{\frac{2}{3}} \tag{2.52}$$

where $\phi_{m(i)}$ is the initial volume fraction of the mineral m and $\phi_{(i)}$ is the initial porosity of the medium. This formulation ensures that as the volume fraction of a mineral goes to 0, its surface area does too. Moreover, for both dissolving and precipitating minerals, the term $(\phi/\phi_{(i)})^{2/3}$ requires that the surface area of a mineral in contact with fluid goes to 0 when the porosity of the medium goes to 0. This formulation is used primarily for primary minerals (*i.e.*, minerals with initial volume fractions > 0). For secondary minerals which precipitate, the value of the initial bulk surface area specified is used as long as precipitation occurs. If this phase later dissolves, the above formulation is used with an arbitrary initial volume fraction of 0.01.

2.3.2 One and zero-dimensional model (Chapter III and V: flow-through, column and batch experiments).

1D and 0D reactive transport models were used to model of the flow-through and column, and batch experiments showed in *Chapter III and V*, respectively. The model parameters used in both simulations are given in the following sections.

2.3.2.1 Numerical discretization

In the flow-through, column and batch experiments the domain was respectively composed of 4, 40 and 1 elements. The spatial discretization for all experiments is shown in Table 2.10.

Table 2.10 Spatial discretization (number of nodes and grid spacing) described in *Chapter III and V*.

			along the cell	
sample type (description)	**experimental setup**	**N° nodes**	**spacing [m]**	**total distance [m]**
powder and crushed (Chapter III)	Flow-through *atm*-CO_2	4	6.75×10^{-3}	2.7×10^{-2}
	Column *atm*-CO_2	40	6.80×10^{-4}	3.0×10^{-3}
	Column *subc*- CO_2	40	1.35×10^{-3}	5.4×10^{-2}
	Column *supc.*- CO_2 ICARE Lab CSS I	40	4.25×10^{-4}	1.7×10^{-2}
powder (Chapter V)	Batch *subc./supc.*-CO_2	1	4.90×10^{-5}	

2.3.2.2 Rock and solution compositions

Rock composition and initial mineral volume fractions of the flow-through (*exps.7 and 8*) and column experiments (*exps. 9- 22*) are shown in Table 2.11. The table also shows secondary sulfate and aluminosilicate phases taken into account. However, the rock composition and initial mineral volume fractions of the batch experiments (*exps.29 to 66*) are shown in Table 2.12.

In all simulations, the rate laws for the reacting minerals were taken from the literature (Tables 2.14 and 2.15). The fit of the model to the experimental data (aqueous element concentrations and pH) was performed by adjusting the values of the reactive surface areas ($A_{reactive}$). A sensitivity analysis of the reactive surface areas was performed. As a result, ranges of values that could also fit the experimental concentrations within the ± 3% analytical error and experimental pH are provided.

In the flow-through and column experiments where gypsum precipitated, the initial value of the gypsum was calculated using the specific surface area ($A_{specific}$) option in CrunchFlow with which the evolution of the mineral volume fraction causes the bulk surface area (A_m) to evolve with time according to the following equation

$$A_m = \frac{\phi_m A_{specific} MW_m}{V_m} \quad (2.53)$$

where MW_m refers to the molecular weight of the phase and V_m is the molar volume of the solid phase.

The composition of the initial solution used in the simulations of the flow-through and column experiments was the same as the input solution in all experiments (Table 2.6). In the solutions, the initial concentration of CO_2 was 1.36-8.85 × 10^{-5} mol kgw^{-1} for pCO_2 = $10^{-3.5}$ bar, 2.87-1.47 × 10^{-1} mol kgw^{-1} for pCO_2 = 10 bar and 4.14 × 10^{-1} mol kgw^{-1} for pCO_2 = 37 bar using the Duan and Sun (2003) model considering P_{Total}, *T and I* depending of each case. Also, the initial concentration of O_2 was estimated to be 3.06 × 10^{-4} mol L^{-1} (atmospheric and CO_2-bottle concentrations).

Since the initial pore water composition of these samples was not known and it was also disturbed during sample preparation, it was assumed that the initial rock porewater was at equilibrium with respect to calcite, and gypsum for *S-rich* solution experiments at room *T* and atmospheric pCO_2 (concentration of CO_2 = 4.14 × 10^{-4} mol kgw^{-1}), yielding a pH ≈ 7.7.

The MgO solid (batch experiments) is composed of 2.43 *vol.%* brucite, 0.1 *vol.%* calcite, 0.18 *vol.%* quartz, 0.05 *vol.%* hydromagnesite, 0.02 *vol.%* dolomite and 0.12 *vol.%* portlandite. Porosity was calculated from the ratio between the volumes of water and water plus solid in the experiments and it is 97 %. For each experiment (*T*, pCO_2), only the most abundant secondary Mg carbonate phases were taken into account (Table 2.1). Otherwise, only the most stable phase (magnesite) would precipitate at 25 °C. Hence, nesquehonite was considered at 25 °C. At higher temperature hydromagnesite and magnesite were respectively considered at 70 and 90 °C (Table 2.12). Initial areas of the mineral were adjusted to fit the observed experimental data (aqueous Mg and Ca concentrations). The composition of the initial solution was the same as that of the input solution presented in *Section 2.1.3.4*.

Table 2.11 *Vol.*% and initial reactive surface areas used in simulations under atmospheric, 10 and 37 bar of pCO_2 conditions described in *Chapters III and IV*.

N⁰ exp.	**7**	**8**		**9**	**10**	**11**	**12**	**13**	**14**	**15**	**16**	**17**	**18**	**19**	**20**	**21**		
label	Mar-25-3	Mar-25-4		Marc-25-1	Marc-25-2a	Marc-60-2a	Marc-25-5	Marc-25-6a	Marc-60-6a	Marc-25-3	Marc-25-4a	Marc-60-4a	Marc-25-8	Marc-60-8	s3.4b	s4.3b		
Minerals	***vol.*%**		**$A_{geometric}$ (flow-through *exps.*)**	***vol.*%**													**d_g [µm]**	**$A_{geometric}$ (column exps.)**
Calcite	0.954	0.956	38.6	41.59	50.00	50.07	29.83	36.00	36.03	31.02	38.09	41.19	35.26	34.78	31.20	40.02	10	1.9×10^5
Quartz	0.047	0.048	1.9	2.07	2.50	2.49	2.87	3.50	3.47	4.34	5.32	5.76	4.75	4.67	3.00	5.59	23	1.0×10^4
Illite	0.081	0.081	3.4	3.54	4.30	4.27	6.79	8.20	8.19	2.99	3.67	3.97	3.62	3.57	7.10	3.86	10	2.0×10^4
Albite	0.010	0.010	0.4	0.45	0.54	0.54	1.45	1.70	1.73	2.90	3.57	3.51	3.99	3.86	1.50	3.76	30	6.0×10^3
Gypsum	0.013	0.013	0.4	0.01	0.01	0.01	0.85	0.02	0.02	0.03	0.04	0.39	0.00	0.01	0.02	0.04	68	9.5×10^2
Clinochlore				0.56	0.70	0.68	1.42	1.00	1.02	1.01	1.24	1.34	1.58	1.56	0.90	1.31	30	3.0×10^3
Anhydrite							0.29	0.00	0.00	0.00	0.00	0.00	0.00	0.00	0.00	0.00	68	1.5×10^2
pyrite							0.49	1.70	1.71	1.24	1.52	1.65	1.80	1.78	1.50	1.60	30	8.1×10^1
kaolinite	-									-							-	-
$SiO_{2(am)}$	-									-							-	-
dolomite	-									-							-	-
zeolites	-									-							-	-
Total *vol.*%	0.96	0.01		48.21	58.05	58.06	43.14	52.12	52.17	43.53	53.45	57.81	51.00	50.23	45.21	56.18		
% porosity (ϕ)	99.04	0.99		51.79	41.95	41.94	56.86	47.88	47.83	56.47	46.55	42.19	49.00	49.77	54.79	43.82		

$A_{geometric}$ in $m^2_{mineral}\ m^{-3}_{bulk}$; d_g refers to the diameter of the grain.

Table 2.12 Mineralogical composition and initial reactive surface areas used in the simulations for MgO-based cement experiments described in *Chapter V*.

N⁰ exp.		**29-33**	**34-38**	**39-42**	**43-48**	**49-53**	**54-58**	**59-61**	**62-66**
Label		**MgO-25-10**	**MgO-70-10**	**MgO-90-10**	**MgO-25-50**	**MgO-70-50**	**MgO-90-50**	**MgO-70-74**	**MgO-90-74**
pCO_2 [bar]		**10**	**10**	**10**	**50**	**50**	**50**	**74**	**74**
T [°C]		**25**	**70**	**90**	**25**	**70**	**90**	**70**	**90**
Mineral	***vol.*%**	**$A_{geometric}$ (batch exps.) [$m^2_{mineral}\ m^{-3}_{bulk}$]**							
Brucite	0.0247	4.4×10^5							
Calcite	0.0010	1.6×10^4							
Dolomite	0.0002	2.9×10^5							
Portlandite	0.0008	1.6×10^4							
Quartz	0.0018	2.7×10^4							
Nesquehonite	0.0	-	*	*	-	*	*	*	*
Hydromagnesite	0.0005	5.9×10^3							
Magnesite	0.0	*	-		*	-	-	-	-
Aragonite	0.0	-							

*minerals not included in the model

2.3.2.3 Flow and transport properties

The Darcy velocity (v_D) in the flow-through and column experiments was calculated according to Eq. 2.27. Darcy velocity used in the simulations is shown in Table 2.8. The effective diffusion coefficient (D_{eff}) was derived from

$$D_{eff} = \phi^m D_o \quad (2.54)$$

The diffusion coefficient in water at 25 ºC, D_0 and the cementation exponent m used in the simulations were 10^{-9} m^2 s^{-1} and 2.5, respectively. They are based on common values reported in the literature (*e.g.*, Ullman and Aller, 1982; Domenico and Schwartz, 1990).

In MgO experiments the effective diffusion coefficients in the model are calculated from

$$D_{eff} = \phi \alpha D_o \quad (2.55)$$

where ϕ is porosity, α is a lithology factor and D_o is the diffusion coefficient in water (4.5×10^{-9} m^{-2} s^{-1} at 90 °C; Samson et al. (2003)). The initial effective diffusion coefficient (D_{eff}) was assumed to be 1.13×10^{-11} m^2 s^{-1}, which is a value in the range for Portland cement grouts (Laurila et al., 2005; Soler et al., 2010; 2011).

2.3.2.4 Thermodynamic and kinetic data

To reproduce the flow-through and column experiments one hundred and seven aqueous species were taken into account in the simulations. The equilibrium constants were taken from the EQ3/6 thermodynamic database (Wolery et al., 1990) included in CrunchFlow and are listed in Table A1 (Appendix 1). The activity coefficients were calculated using the extended Debye-Hückel formulation (b-dot model) with parameters from the same database. Twenty solid phases [eight primary minerals (calcite, quartz, illite, albite, gypsum, clinochlore, anhydrite and pyrite) and twelve secondary minerals (kaolinite, $SiO_{2(am)}$, dolomite, mesolite, stilbite, smectite, mordenite, scolecite, analcime, wairakite, laumontite, gismondine) were considered in the calculations

(Table A2; Appendix 1). The equilibrium constant for the mineral reactions were also taken from de EQ3/6 data base.

In the MgO batch experiments, eleven species in solution and seven (25 °C) or eight minerals (70 and 90 °C) were considered in each calculation depending on the case (Table 2.12). The equilibrium constants for the reactions at 25, 70 and 90 °C are from the EQ3/6 thermodynamic database as well and are listed in Tables B1 and B2 (Appendix 2). Solubilities of CO_2 at high *P* were implemented by fixing the activities of $CO_{2(aq)}$ in the input solution to the solubility calculated from the model by Duan and Sun (2003) at each pCO_2 and *T* at zero ionic strength (Table 2.12). The activity coefficients were calculated using the extended Debye-Hückel formulation (b-dot model).

Table 2.13 Concentrations and log activities (fixed) of $CO_{2\,(aq)}$ (mol kgw^{-1}); *T* = 25, 70 and 90 °C; pCO_2= 10, 50 and 74 bar.

	pCO_2 = 10bar		pCO_2 = 50bar		pCO_2 = 74bar	
Temperature (°C)	**Concentration (mol kgw^{-1})**	***log (activity)***	**Concentration (mol kgw^{-1})**	***log (activity)***	**Concentration (mol kgw^{-1})**	***log (activity)***
25	3.16×10^{-1}	-0.501	1.20×10^{0}	0.078		-
70	1.39×10^{-1}	-0.858	5.95×10^{-1}	-0.226	7.88×10^{-1}	-0.103
90	1.09×10^{-1}	-0.965	4.95×10^{-1}	-0.306	6.70×10^{-1}	-0.174

2.3.2.5 Reaction rates

Kinetic rate laws used for primary minerals (calcite, quartz, illite, albite, gypsum, clinochlore, anhydrite and albite) are itemized in Table 2.14. Xu et al. (2012) proposed a calcite dissolution rate that improves the rate-ΔG dependence under close-to-equilibrium conditions ($-12 \leq \Delta G \leq 1.7$ kJ/mol) with respect to the simplest TST-based rate law ($m_1 = m_2 = 1$ in Eq. (2.49)). Hence, all simulations were run based on this rate law (*i.e.*, $m_1 = 3$ and $m_2 = 1$ in Eq. (2.49)). Rate parameters and apparent activation energies are listed in Table 2.14. The two parallel rate laws for each primary mineral describe the explicit dependence of the rates on pH. Rate constants at temperatures different from 25 ºC were calculated according to Eq. (2.50).

Table 2.14 Reaction rate constants ($k_{m,25}$), activation energies (E_a) and rate parameters (Eq. (2.48)) for the mineral reactions considered in the models. The parallel rate laws for minerals describe the pH dependencies under different pH ranges (a: acid, n: neutral and b: basic) for the flow-through and column experiments.

Mineral and Chemical composition	$k_{m,25}$ [mol m^{-2} s^{-1}]	n_{H+}	n_{O2}	*Ea* [kcal mol^{-1}]	m_1	m_2	*Reference*
	Primary phases						
Calcite ($CaCO_3$)	5.01×10^{-1} [a] 6.46×10^{5} [n]	1.000 [a]	-	3.44 [a] 5.62 [n]	3.0	1.0	Palandri and Kharaka, 2004; Xu et al., 2012
Quartz (SiO_2)	1.02×10^{-14} [n]	-	-	20.95 [n]	1.0	1.0	Palandri and Kharaka, 2004; Bandstra et al., 2008
Illite ($K_{0.6}Mg_{0.25}Al_{2.3}Si_{3.5}O_{10}(OH)_2$)	2.20×10^{-4} [a] 2.50×10^{-13} [n] 2.70×10^{-1} [b]	0.600 [a]	-	11.00 [a] 3.35 [n] 15.30 [b]	1.0	1.0	Bibi et al., 2011
Albite ($NaAlSi_3O_8$)	7.41×10^{-9} [a] 9.12×10^{-13} [n] 1.05×10^{-17} [b]	0.457 [a] -0.572 [b]	-	15.54 [a] 16.69 [b] 16.98 [n]	15.0	0.3	Palandri and Kharaka, 2004; Chou and Wollast, 1985; Hellmann et al., 2010
Gypsum ($CaSO_4{\cdot}2H_2O$)	1.62×10^{-3} [n]	-	-	15.00 [n]	1.0	1.0	Palandri and Kharaka, 2004
Clinochlore ($Mg_{2.9}Fe_{2.1}Si_3Al_2O_{10}(OH)_8$)	3.21×10^{-10} [a]	0.450 [a]	-	16.00 [a]	1.5.0	0.06	Hamer et al., 2003; Zhang et al., 2015
Anhydrite ($CaSO_4$)	1.55×10^{3} [n]	-	-	3.42 [n]	1.0	1.0	Palandri and Kharaka, 2004
Pyrite (FeS_2)	3.02×10^{-8} [a] 2.82×10^{-5} [n]	-0.500 [a]	0.500	13.61 [a] 13.61 [n]	1.0	1.0	Palandri and Kharaka, 2004; Domènech et al., 2002
	Secondary phases						
Kaolinite ($Al_2Si_2O_5(OH)_4$)	4.90×10^{-12} [a] 6.61×10^{-14} [b] 8.91×10^{-18} [n]	0.777 [a] -0.472 [b]	-	15.76 [a] 5.31 [b] 4.28 [n]	1.0	1.0	Palandri and Kharaka, 2004
$SiO_{2\,(am)}$	1.00×10^{-9}	-	-	0.00	1.0	1.0	*
Dolomite ($CaMg(CO_3)_2$)	6.46×10^{-4} [a] 2.95×10^{-8} [n]	0.500 [a]	-	8.63 [a] 12.48 [n]	1.0	1.0	Palandri and Kharaka, 2004
Mesolite ($Ca_{0.657}Na_{0.676}(Al_{0.663}Si_{1.003}O_{1.562})_3{\cdot}7.96H_2O$)	1.00×10^{-9}	-	-	0.00	1.0	1.0	*
Stilbite ($Na_{0.136}K_{0.006}Ca_{1.019}Al_{2.18}Si_{6.82}O_{16.61}{\cdot}8.72H_2O$)	1.00×10^{-9}	-	-	0.00	1.0	1.0	*
Smectite ($Ca_{0.025}Na_{0.10}Fe_{0.7}K_{0.2}Mg_{1.15}Al_{1.25}Si_{3.5}O_7{\cdot}H_2O$)	1.00×10^{-12}	-	-	0.00	1.0	1.0	Cama et al., 2000
Mordenite ($Ca_{0.2895}Na_{0.361}Al_{0.94}Si_{5.06}O_{12}{\cdot}3.468H_2O$)	1.00×10^{-9}	-	-	0.00	1.0	1.0	*
Scolecite ($CaAl_2Si_3O_{10}{\cdot}3H_2O$)	1.00×10^{-9}	-	-	0.00	1.0	1.0	*
Analcime ($Al_{0.96}Na_{0.96}(Si_{2.04}O_{3.92}){\cdot}H_2O$)	1.00×10^{-9}	-	-	0.00	1.0	1.0	*
Wairakite ($CaAl_2Si_4O_{12}{\cdot}2H_2O$)	1.00×10^{-9}	-	-	0.00	1.0	1.0	*
Laumontite ($Ca(AlSi_2O_6)_2{\cdot}4H_2O$)	1.00×10^{-9}	-	-	0.00	1.0	1.0	*
Gismondine ($Ca_2Al_4Si_4O_6{\cdot}9H_2O$)	1.00×10^{-9}	-	-	0.00	1.0	1.0	*

*Large value of $A{\cdot}k_{m,T}$ to allow local equilibrium conditions.

a,b and c means acid, neutral and basic, respectively.

The kinetic rate laws used in the simulations of batch experiments were obtained from Bullard et al. (2010) for portlandite and from Cubillas et al. (2005) for aragonite. The kinetic rate laws for nesquehonite and hydromagnesite were assumed to be the same as magnesite. Rate laws for the other minerals were from Palandri and Kharaka (2004) (Table 2.15). The crucial parameter to fit

the models to experimental data using reactive transport codes is the value of the reactive surface area of primary minerals. Based on the specific surface area ($A_{specific}$ from BET) of the initial solid, a resulting total surface area of 5.1×10^5 $m^2_{mineral}$ m^{-3}_{rock} was calculated. The reactive surface area calculated assuming spherical geometry was 6×10^3 $m^2_{mineral}$ m^{-3}_{rock} which differs in 2 orders of magnitude from the BET value. Surface areas of secondary minerals (except dolomite) had to be sufficiently large to facilitate their precipitation.

Table 2.15 Reaction rates and activation energies for the mineral reactions considered in the models. The 2 parallel rate laws for each mineral describe the pH dependencies under different pH ranges for MgO batch experiment.

Pressure		**atm**	**atm**		
Temperature		**25°C**	**25 °C**		
Mineral	$n(a_{H^+}{}^n)$	$k_{m,25}$ [mol m^{-2} s^{-1}]	Ea [kcal mol^{-1}]	m_1	m_2
Brucite	0.5	1.86×10^{-05} 5.75×10^{-09}	14.10 10.04		
Calcite	1.0	5.01×10^{-01} 1.55×10^{-06}	3.44 5.62	3.0	1.0
Dolomite	0.5	1.74×10^{-04} 2.51×10^{-09}	13.53 22.75		
Quartz	0.3	5.01×10^{-15}	15.00		
Portlandite	1.0	3.98×10^{-06}	15.0		
Nesquehonite	1.0	4.17×10^{-07} 4.57×10^{-10}	3.44 5.61	1.0	4.0
Hydromagnesite	1.0	4.17×10^{-07} 4.57×10^{-10}	3.44 5.61	1.0	4.0
Magnesite	1.0	4.17×10^{-07} 4.57×10^{-10}	3.44 5.61	1.0	4.0
Aragonite	1.0	7.94×10^{-09}	0.00		

magnesite affinity dependence (Pokrovsky and Schott, 1999)
calcite affinity dependence (Xu et al., 2012).
for the rest of the minerals (Palandri and Kharaka, 2004).

2.3.3 Two-dimensional model (Chapter IV: percolation experiments)

2D reactive transport modeling was used in the interpretation of the percolation experiments that are presented in *Chapter IV*. The model parameters used in 2D simulation are given in the following sections.

2.3.3.1 Numerical discretization

The 3D cylindrical core sample used for the laboratory experiments was converted to a 2D rectangular symmetry. First, half of the circular section of the core was transformed into a rectangle. The area of this rectangle is equal to the area of the half circle (area = $x \cdot \ell = \frac{1}{2} \cdot \pi \cdot (\ell/2)^2$; where ℓ is the diameter of the core and x is the width of the rectangle). A 2D longitudinal section

of the resulting prism was used as the calculation domain (Fig. 2.12). The domain was composed of a fracture (high permeability zone) and rock matrix (low permeability zone; Fig. 2.11b). The domain was divided into 36 and 30 nodes from the inlet to the outlet (L) and from the center of the fracture to 3.5 mm in the model, respectively (see Table 2.16). Fracture corresponds only to the first node in the x direction. The model considers advection and dispersion only along the fracture. Solute transport in the rock matrix is only by diffusion.

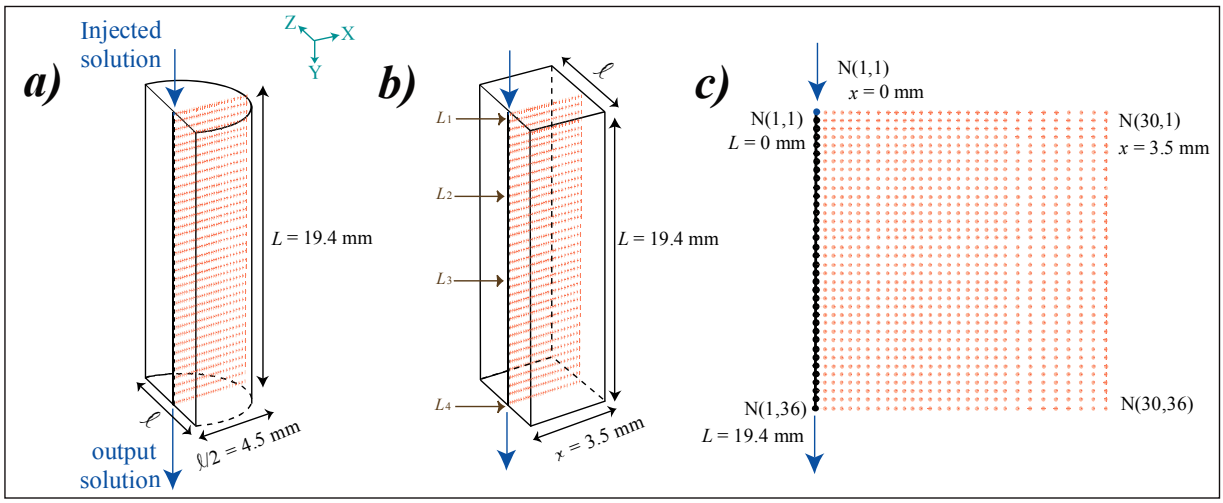

Figure 2.12 *Schemes showing: the spatial discretization corresponding to the fractured marl cores a) cylindrical coordinates and b) rectangular coordinates, and c) mesh distribution along the core sample.*

Table 2.16 Experimental conditions, flow and transport properties, mineralogical composition, initial effective diffusion coefficients and reactive surface areas used in the experimental simulations described in *Chapter III and V*.

perpendicular to fracture			along fracture		
N Nodes in X	**spacing [µm]**	**accumulated distance [µm]**	**N Nodes in Y**	**spacing [mm]**	**accumulated distance [mm]**
1	8.0	8.0	10	3.9×10^{-1}	3.9
2	1.0	10.0	9	4.3×10^{-1}	7.8
3	12.7	48.1	8	4.9×10^{-1}	11.7
7	16.2	161.5	6	6.5×10^{-1}	15.6
10	32.4	485.5	3	1.29×10^{0}	19.4
7	435.0	3530.5			

2.3.3.2 Rock and solution compositions

The rock considered in the models was the marl described in *Section 2.1.2* composed of calcite (≈ 71 *wt.*%), quartz (≈ 10 *wt.*%), illite (≈ 7 *wt.*%), albite (≈ 7 *wt.*%), gypsum (≈ 2 *wt.*%),

clinochlore (≈ 3 *wt.*%), anhydrite (≈ 1 *wt.*%), and pyrite (≈ 0.2 *wt.*%). The initial porosity of the rock matrix was estimated by image segmentation processing applied to ESEM images, which allowed separation of rock and voids. The estimated porosity was 6.7 % and hence the initial mineral volume fractions (Table 2.17). An analysis of the selection of the secondary minerals was performed based on equilibrium batch modeling as described by Gaus et al. (2010), Soler et al. (2011) and Tian et al. (2014). Initial estimation of the reactive surface areas of the primary minerals was calculated by assuming spheres with radii estimated from the ESEM images (Table 2.17). The secondary minerals were allowed to start precipitating when the solution reached supersaturation. The initial reactive surface areas for all the secondary minerals were assumed to be the same and also were sufficiently large (1.0×10^4 $m^2_{mineral}$ m^{-3}_{rock}) to allow fast precipitation (local equilibrium).

Table 2.17 Experimental conditions, flow and transport properties, mineralogical composition, effective diffusion coefficient and initial reactive surface areas used in the experimental simulations.

	Conditions		
P_{Total} [bar]	150		
pCO_2 [bar]	61		
T [°C]	60		
initial porosity ($\phi_{(i)}$)	0.067		
cementation exponent (m)	2.5		
longitudinal dispersivity (α_L) [m]	1.0×10^{-3}		
transversal dispersivity (α_T) [m]	0.0		
Mineral	***vol.%***	$A_{reactive}$ $[m^2_{mineral}\ m^{-3}_{rock}]$	d_g [μm]
calcite	66.2	1.9×10^5	10
quartz	9.2	1.0×10^4	23
illite	6.4	2.0×10^4	10
albite	6.3	6.0×10^3	30
gypsum	2.2	9.5×10^2	68
clinochlore	2.6	3.0×10^3	30
anhydrite	0.3	1.5×10^2	68
pyrite	0.1	8.1×10^1	30
kaolinite	-	-	-
$SiO_{2(am)}$	-	-	-
dolomite	-	-	-
zeolites	-	-	-

The two solutions used in the models were the experimental ones (Table 2.6). In both solutions, the initial concentration of CO_2 was 6.52×10^{-1} mol kgw^{-1} using the Duan and Sun (2003) model considering P_{Total} = 150 bar, T = 60 °C and I = 0.6 M. Also, the initial concentration of O_2 was estimated to be 3.06×10^{-4} mol L^{-1} (atmospheric and CO_2-bottle concentrations). The *S-rich(4)* solution was undersaturated with respect to calcite (SI_{Cal} = -3.20) and near equilibrium with respect to gypsum (SI_{Gp} = -0.02) at 60 °C. The *S-free(1)* injected solution was undersaturated with respect to calcite (SI_{Cal} = -3.50) at 60 °C. The calculated initial pH values were 3.26 and

3.29 for the *S-rich(4)* and *S-free(1)* solutions, respectively. The initial rock porewater was equilibrated with respect to calcite and gypsum at room *T* and atmospheric pCO_2 (concentration of $CO_2 = 4.14 \times 10^{-4}$ mol kgw^{-1}), yielding concentrations of Ca and S equal to 1.07×10^{-2} and 1.05×10^{-2} mol kgw^{-1} and pH = 7.71 (Table 2.18).

Table 2.18 Chemical composition, pH and saturation indexes (*SI*) of the injected and porewater solutions used in the simulations.

		Initial rock porewater
Component	**Constraints**	**Concentration [mol kgw^{-1}] or pH**
Ca^{2+}	calcite	1.07×10^{-2}
Mg^{2+}	fixed	1.00×10^{-6}
HCO_3^-	known	4.14×10^{-4}
pH	charge balance	7.71
SO_4^{2-}	gypsum	1.05×10^{-2}
Na^+	fixed	1.00×10^{-6}
K^+	fixed	1.00×10^{-6}
Al^{3+}	fixed	1.00×10^{-6}
Cl^-	fixed	1.00×10^{-6}
Br^-	fixed	1.00×10^{-6}
Fe^{2+}	fixed	1.00×10^{-6}
$SiO_{2(aq)}$	fixed	1.00×10^{-6}
$O_{2(aq)}$	fixed	2.84×10^{-4}
Minerals	**abbreviation**	
calcite	Cal	0.00
quartz	Qtz	-2.00
Illite	Ilt	-5.92
Albite	Ab	-10.06
gypsum	Gp	0.00
clinochlore	Cln	-37.18
anhydrite	Anh	-0.44
pyrite	Py	-242.24
kaolinite	Kln	-0.65
$SiO_{2(am)}$		-3.28
dolomite	Dol	-4.46
mesolite	Ms	-3.93
stilbite	Stl	-8.62
smectite	Smc	-12.81
mordenite		-12.25
scolecite	Scl	-2.65
analcime	Anc	-8.10
waikerite		-10.84
laumontite		-6.44
gismondine	Gsm	-3.29

Since the initial pore water composition of these samples was not known and was also disturbed during sample preparation, it was assumed that the initial rock porewater was at equilibrium with respect to calcite, and gypsum for *S-rich(4)* solution experiments at room *T* and atmospheric pCO_2 (concentration of $CO_2 = 4.14 \times 10^{-4}$ mol kgw^{-1}), yielding a pH ≈ 7.7 (Table 2.6). A very small concentration (10^{-6} mol kgw^{-1}) was assumed for Na^+, K^+, Al^{3+}, Cl^-, Br^-, Fe^{2+} and $SiO_{2(aq)}$.

The reactive surface areas ($A_{reactive}$) of the secondary phases were initially calculated considering the geometric surface area. Thereafter, the reactive surface area was fitted to reproduce the variation in Ca, K, S, Fe, Mg and Si concentrations. The reactive surface area for all the

secondary minerals were adjusted with the same value. Calculated values of saturation index, ionic strength and pH of the injected solutions are listed in Table 2.6. In all simulations, the initial rock porewater solution was considered to be in equilibrium with calcite and gypsum and is described in Table 2.18.

2.3.3.3 Flow and Transport parameters

Darcy velocity (v_D), initial effective diffusion coefficients ($D_{eff(i)}$), and longitudinal dispersivity (α_L) used in the simulations are show in Table 2.9. The flow field used in the reactive transport simulations prescribed the Darcy velocity (v_D) along the fracture. The effective diffusion coefficient (D_{eff}) at 60 °C was calculated using Eq. (2.54), where m is the cementation exponent (m = 2.5; Revil and Glover, 1997) and D_o is the diffusion coefficient in water.

2.3.3.4 Thermodynamic and kinetic data

One hundred and seven aqueous species were considered in the simulations. The equilibrium constants were taken from the EQ3/6 thermodynamic database (Wolery et al., 1990) included in CrunchFlow and are listed in Table A1 (Appendix 1). The activity coefficients were calculated using the extended Debye-Hückel formulation (b-dot model) with parameters from the same database. Twenty solid phases [eight primary minerals (calcite, quartz, illite, albite, gypsum, clinochlore, anhydrite and pyrite) and twelve secondary minerals (kaolinite, $SiO_{2(am)}$, dolomite, mesolite, stilbite, smectite, mordenite, scolecite, analcime, wairakite, laumontite, gismondine) were considered in the calculations. Equilibrium constant for the mineral dissolution reactions (CrunchFlow, EQ3/6) are given in Table A2 (Appendix 1).

2.3.3.5 Reaction rates

Kinetic rate laws for the primary and secondary minerals, rate parameters and activation energies are listed in Table 2.14. The parallel rate laws for minerals describe the explicit dependence of the rates on pH. Rate constants at temperature different from 25 °C were calculated according to Eq. (2.50).

Chapter III

Dissolution of illite and marl caprocks under subcritical and supercritical CO_2 conditions at 25 and 60 °C: flow-through, column experiments and 1D reactive transport modeling

3.1 Introduction

This chapter presents the experimental and modeling results of two sets of experiments: (*1*) flow-through experiments (*i*) to calculate the illite dissolution rate under acidic pH, atmospheric pressure and room temperature (P_{Total} = 1 bar and T = 25 ºC) and (*ii*) to study the reactivity of the marl (e.g., marly limestone; *S2.4*) and (*2*) column experiments to study the reactivity of the caprock (marly limestone (*S2.4*), bituminous black shale (*S3.4*) and marl (*S4.3*)) by varying P_{Total}, pCO$_2$ and T conditions (P_{Total} = 1, 10 and 150 bar; pCO$_2$ = $10^{-3.5}$, 10 and 37 bar, respectively and T = 25 and 60 ºC). The experimental conditions of the performed experiments are listed in Table 3.1. The illite flow-through experiments were carried out using powder samples, whereas the marly limestone flow-through and all column experiments were performed using crushed samples. The experimental results of the marl flow-through and column experiments were reproduced by 1D reactive transport simulations using CrunchFlow (Steefel et al., 2015) in order to interpret the processes and to quantify porosity variation.

Table 3.1 Number, label, experimental setup, injected solution and experimental conditions of the experiments studied in this chapter.

					conditions		
Nº exp.	**label**	**experimental setup**	**injected solution**	**sample**	**P_{Total} [bar]**	**pCO$_2$ [bar]**	**T [ºC]**
1	*Ilt-25-1*	Flow-through (*atm-CO$_2$*)	HCl	illite	1	10-3.5	25
2	*Ilt-25-5*		HCl	Illite			
3	*Ilt-25-2*		HCl	illite			
4	*Ilt-25-3*		HCl	illite			
5	*Ilt-Cal-25-1*		HCl	illite + limestone			
6	*Ilt-Cal-25-2*		*S-rich(a1)*	illite + limestone			
7	*Mar-25-3*		HCl	marly limestone (*S2.4*)			
8	*Mar-25-4*		*S-rich(a2)*				
9	*Marc-25-1*	Column *atm-CO$_2$*	HCl				
10	*Marc-25-2a*		*S-rich(a3)*				
11	*Marc-60-2a*						60
12	*Marc-25-5*		HCl	bituminous black shale (*S3.4*)			25
13	*Marc-25-6a*		*S-rich(a3)*				
14	*Marc-60-6a*						60
15	*Marc-25-3*		HCl	marl (*S4.3*)			25
16	*Marc-25-4a*		*S-rich(a3)*				
17	*Marc-60-4a*						60
18	*Marc-25-8*	Column *subc.-CO$_2$*	*S-rich(1)*		10	10	25
19	*Marc-60-8*		*S-rich(2)*			10	60
20	*S3.4b*	Column *supc.-CO$_2$* ICARE Lab CSS I	*S-rich(3)*	bituminous black shale (*S3.4*)	150	37	60
21	*S4.3b*			marl (*S4.3*)		37	60

3.2 Flow-through experiments

3.2.1 Illite

Four flow-through experiments using HCl solutions (pH ranging from 2.15 to4.21) were performed to calculate the illite dissolution rates at different pH and compare them with those reported by Köhler et al. (2003) under $P_{Total} = 10^{-3.5}$ bar and $T = 25$ °C conditions. 0.76 g of illite du Puy were placed into the flow-through reaction cells. The flow rate of the injected solutions was kept constant at 0.032 mL min^{-1} throughout the experiments, which lasted for ≈ 1000 h. The Cl concentrations of the injected solutions were 6.8 × 10^{-3}, 7.1 × 10^{-3}, 8.6 × 10^{-4} and 6.1 × 10^{-5} mol L^{-1} for *exps. 1, 2, 3 and 4*, respectively. Variation of the output Si and Al concentrations at different pH is illustrated in Fig. 3.1.

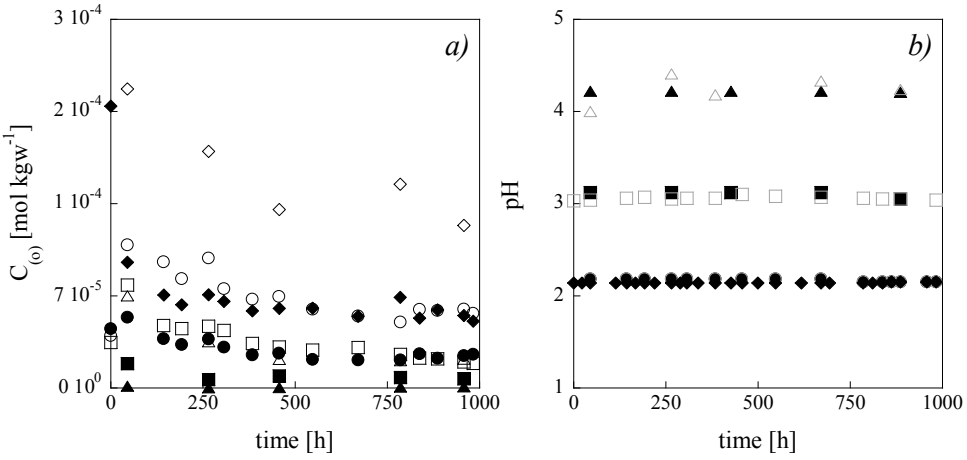

Figure 3.1 *Temporal variation of output Si and Al concentrations (a) and pH (b) during the illite du Puy dissolution experiments at atmospheric pressure and 25 °C. Si =empty and Al =fill symbols; exp.1 = ○, exp 2 = ◊, exp. 3 = □ and exp4 = Δ. Black and gray color indicates input and output solution, respectively.*

As the illite du Puy started to dissolve, the output concentration of Si and Al increased to thereafter gradually decrease and achieve steady state (Table 3.2 and Fig. 3.1a). The output pH was similar to the input one throughout all experiments (Fig. 3.1b; Table 3.2). At pH ≤ 3.05 the steady-state Al/Si ratio was nearly similar, within error, to that of the illite du Puy structural formula (Al/Si ≈ 0.47), whereas at pH ≈ 4.21 an Al deficit was observed, yielding a low ratio of

Al/Si of 0.02 (Table 3.2). This indicates a possible precipitation of an Al-bearing secondary phase and/or Al adsorption on illite surfaces (Columbera et al., 1971). The steady-state illite dissolution rates (r_{Si}) at different pH were calculated using Eq. (2.18). The obtained variation of r_{Si} with pH exhibited the expected decrease in dissolution rate with pH in the acidic range (Fig. 3.2).

Table 3.2 Input (i) and output (o) Al and Si concentrations, *ex-situ* input (i) and output (o) pH, output Al/Si ratio and illite dissolution rate.

Nº exp.	label	sample	injected solution	Q [mL min^{-1}]	$pH_{(i)}$	$pH_{(o)}$	$Al_{(i)}$ [μM]	$Al_{(o)}$ [μM]	$Si_{(i)}$ [μM]	$Si_{(o)}$ [μM]	Al/Si	r_{Si} [mol m^{-2} s^{-1}]
1	ilt-25-1	illite	HCl	0.04	2.15	2.00	0.00	27.01	0.91	63.76	0.43	-1.13×10^{-13}
2	ilt-25-5	illite	HCl	0.03	2.15	-	0.16	76.69	0.00	129.77	0.42	-2.31×10^{-13}
3	ilt-25-2	illite	HCl	0.04	3.05	3.05	0.00	8.30	0.29	21.38	0.38	-3.88×10^{-14}
4	ilt-25-3	illite	HCl	0.02	4.21	4.31	0.00	0.49	0.00	21.99	0.02	-2.00×10^{-14}

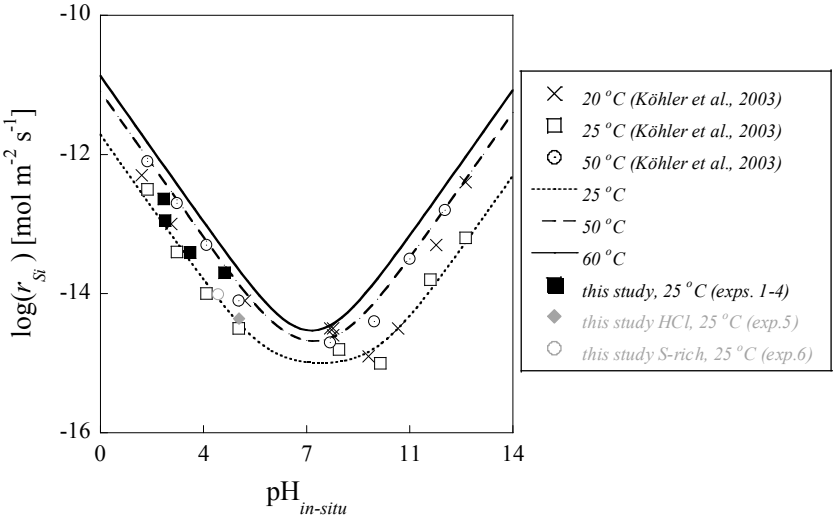

Figure 3.2 *Rates of illite dissolution as a function of pH and temperature: 20, 25 and 50 °C. The open symbols represent experimental rates of Köhler et al. (2003) and solid lines the calculated rates using the parameters from Oelkers et al. (2001). Black fill and gray symbols represent the dissolution rate obtained in this study (r_{Si}) using illite and mixtures illite and calcite, respectively.*

Two experiments with a mixture of 50 *wt.*% illite powder (fraction size < 63 μm) and 50 *wt.*% limestone (fragments size of 1-2 mm) were performed to evaluate any possible effect of calcite dissolution and gypsum precipitation on the illite dissolution rate. HCl solutions with (*S-rich(a1); exp. 6*) and without sulfate (HCl; *exp. 5*) were used (Table 2.6).

Fig. 3.3 shows the temporal variation of pH for the two experiments. The output pH rapidly increased in both solutions to reach steady state (pH ≈ 4.70 (HCl) and 4.10 (*S-rich(a1)* at ≈ 1000 h).

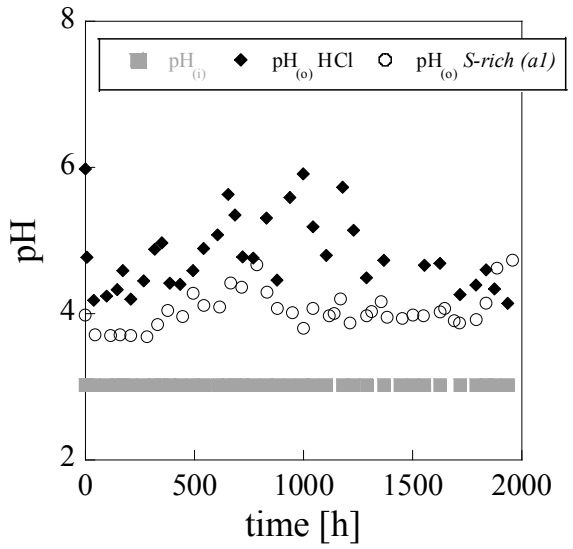

Figure 3.3 *Variation of pH with time during the illite-calcite experiments with the HCl (exp. 5) and S-rich(a1) (exp. 6) injected solutions.*

In both experiments, the increase in the output concentration of Ca was fairly small and within analytical error compared to the respective initial concentration (Fig. 3.4). The increase in Ca concentration was due to calcite dissolution (Fig. 3.4a). ΔS was zero within error (Fig. 3.4b). In the *S-rich(a1)* experiment, the saturation index of the output solution showed equilibrium with respect to gypsum. However, no precipitated crystals of gypsum were observed in the SEM images of the reacted sample (*exp. 6*).

The increase in Mg, K and Si concentrations was due to illite dissolution (Fig. 3.4c, d and e). The increment in the output concentrations (ΔMg, ΔK and ΔSi) was slightly higher in the experiment with lower pH (*S-rich(a1)* solution), yielding a slightly faster illite dissolution rate (r_{Si}) compared to than that obtained with HCl solution (Fig. 3.2). Nonetheless, since the saturation index of the steady-state solution showed a slightly supersaturated solution with respect to kaolinite (suggesting possible kaolinite precipitation), r_{Si} values were slightly slower than expected.

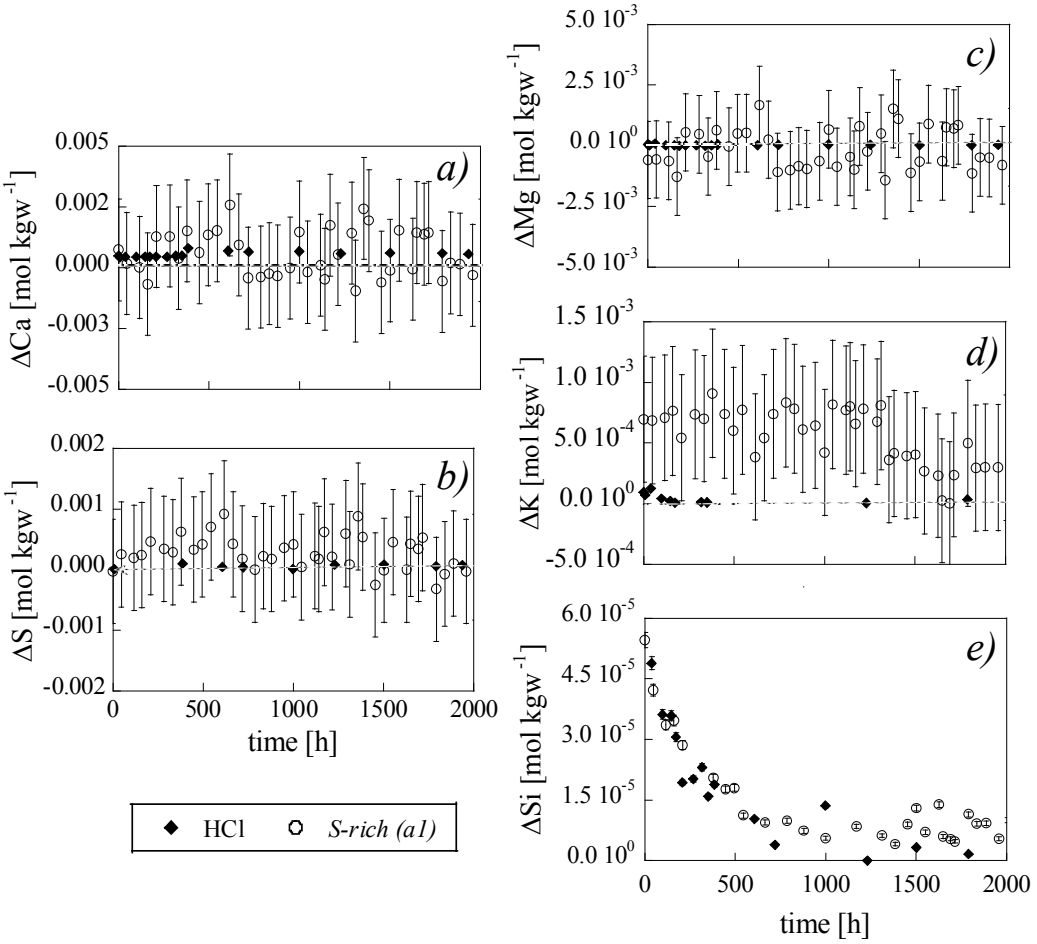

Figure 3.4 *Variation of the increase in the output concentrations with time in HCl and S-rich(a1) solutions (exps. 5 and 6): (a) ΔCa, (b) ΔS, (c) ΔMg, (d) ΔK and (e) ΔSi.*

Therefore, based on the previous experimental results, the obtained illite dissolution rates were similar to those reported by Köhler et al. (2003) (Fig. 3.2). Thus, the illite dissolution rate law that relates illite dissolution with pH, reported by these authors, was used in all reactive transport simulations of this study. Calcite dissolution and gypsum precipitation showed no influence on illite dissolution.

3.2.2 Marly limestone

Two flow-through experiments with HCl and *S-rich(a2)* solutions and *S2.4* marl rock were performed at $pCO_2 = 10^{-3.5}$ bar and $T = 25$ °C. Fig. 3.5a shows an increase in the output pH in

both experiments (*exps. 7 and 8*), due to calcite dissolution, and immediate steady-state achievement (pH ≈ 7.60 and 6.50, respectively).

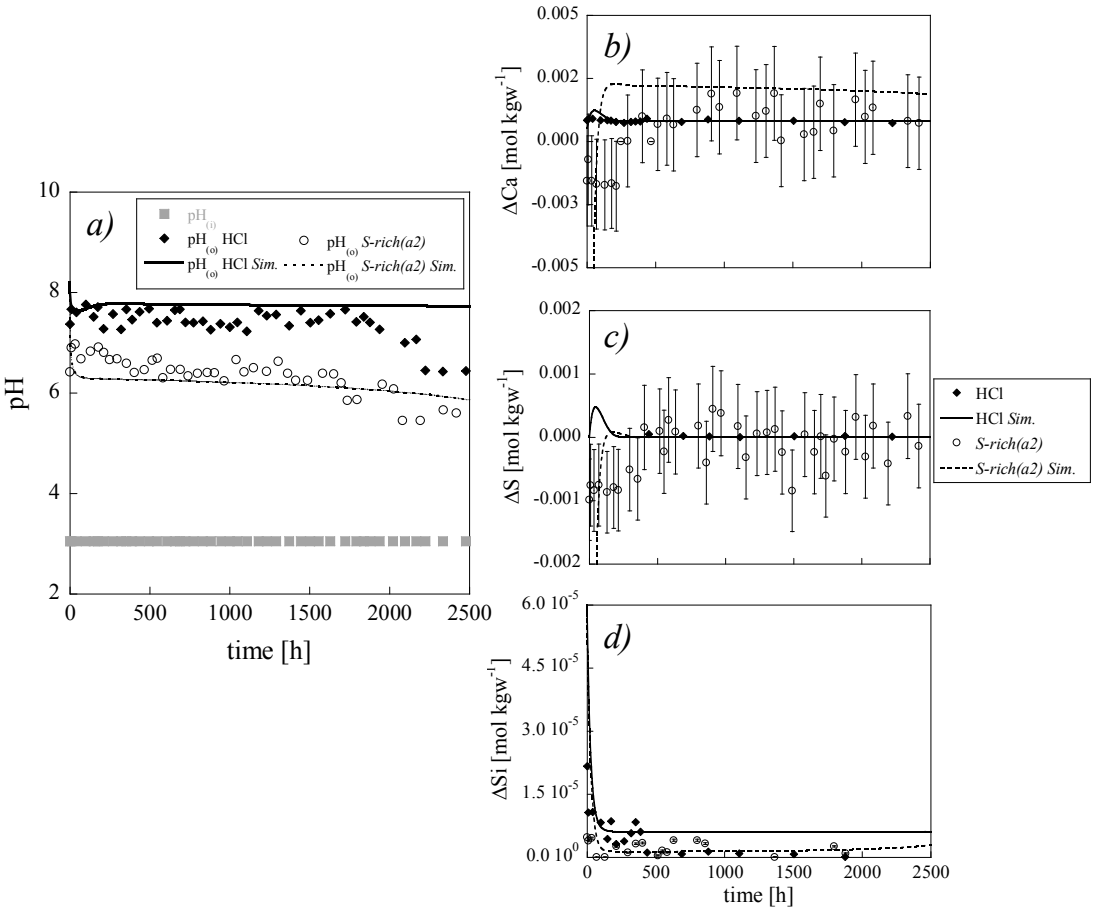

Figure 3.5 *Variation of the measured (symbols) and simulated (lines) a) output and input pH and b) ΔCa, c) ΔS, and d)ΔSi concentrations with time in HCl (exp. 7) and S-rich(a3) (exp. 8) experiments.*

The ΔCa concentration slightly increased with time, whereas ΔS slightly decreased likely due to gypsum precipitation (Fig. 3.5b and c). Dissolution of aluminosilicates contributed to the initial increase and steady-state Si concentrations, with a ΔSi slightly lower in the HCl experiment (Fig. 3.5d).

Regarding simulations, the model fit was achieved by adjusting the values of the reactive surface areas of the primary minerals, using values smaller than the calculated geometric surface area for

calcite ($A_{geometric}$ = 38.6 $m^2_{mineral}$ m^{-3}_{bulk}) and higher values for illite and albite ($A_{geometric}$ = 3.4 and 0.4 $m^2_{mineral}$ m^{-3}_{bulk}, respectively; Table 2.11) for both experiments. 1D reactive transport simulations using $A_{reactive}$ = 25, 5 and 1 $m^2_{mineral}$ m^{-3}_{bulk} for calcite, illite and albite, respectively, provided a good fit to the experimental data in the two experiments (Fig. 3.5a, b, c and d). The smaller value of the calcite reactive surface area may account for the transport (diffusion) control of the calcite dissolution (Sjöberg and Rickard, 1984). Quartz dissolution is negligible in acidic pH. The quartz surface area was not adjusted ($A_{geometric}$ = 1.9 $m^2_{mineral}$ m^{-3}_{bulk}).

In the HCl solution experiment, the pH increase was originated by the proton consumption from calcite dissolution forming HCO_3^-. In the *S-rich(a2)* solution experiment, the deprotonation of the initial HSO_4^- in solution (about 1 % of the total sulfate in the input solution) causes a smaller increase in pH after calcite dissolution. In addition, temporal variation in the calcite saturation state (*SI*) from the simulations indicates that calcite is further from equilibrium in the *S-rich(a2)* solution experiment (from -0.7 to -1.2) than in the HCl solution experiment (from -0.3 to -0.4). As a consequence, in the *S-rich(a2)* solution experiment, calcite dissolution rate was faster than that in the HCl solution experiment (Fig.3.6). Therefore, in the HCl injected solution experiment, ΔCa concentration was lower.

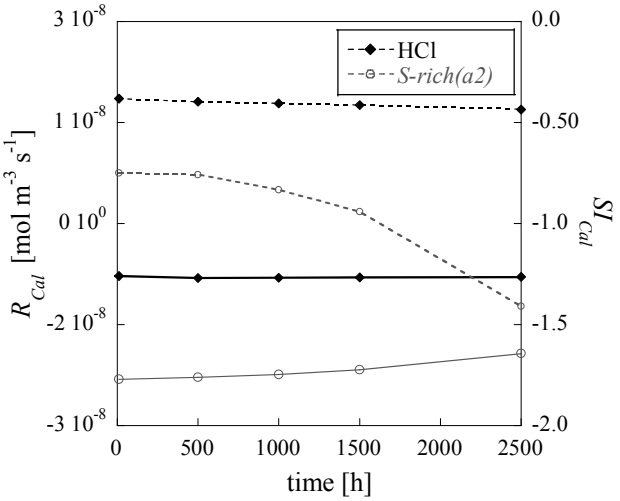

Figure 3.6 *Temporal variation of calcite dissolution rate (R_{Cal}; solid lines) and saturation index (SI; dashed lines) in HCl (exp. 7) and S-rich(a2) (exp. 8) solutions.*

In the *S-rich(a2)* experiments, simulation showed that solution was near in equilibrium with respect to gypsum suggesting that gypsum could precipitates. Gypsum needles were observed in the SEM images of the reacted sample (Fig.3.7).

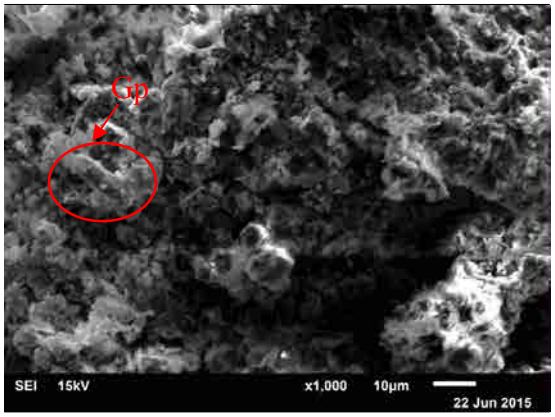

Figure 3.7 *SEM image from the reacted sample with S-rich(a2) injected solution (exp. 8).*

Simulations show that as pH increased from 3 to 6.5-7.6, dissolution of illite contributed to the initial increase in the ΔSi concentration. Thereafter, dissolution illite coupled with precipitation of Si-bearing minerals (stilbite and scolecite in the HCl experiment, and mesolite and kaolinite in the S-rich experiment; Fig. 3.8a and b) produce a decrease in Si concentration and achievement of steady state (Fig. 3.5d).

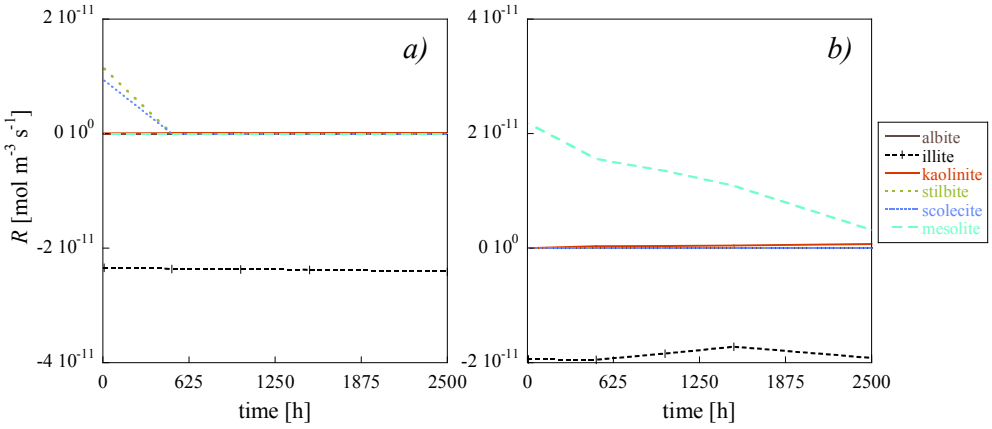

Figure 3.8 *Temporal variation in dissolution (albite and illite) and precipitation (kaolinite, stilbite, scolecite and mesolite) rates in a) the HCl (exp. 7) and b) the S-rich(a2) (exp. 8).*

3.3 Column experiments

Thirteen experiments were performed under different experimental conditions (Table 3.1): nine at atmospheric pressure (*atm*-CO_2 experiments*:* P_{Total} = 1 bar, $pCO_2 = 10^{-3.5}$ bar and T = 25 and 60 °C), two at subcritical pressure (*subc*.-CO_2 experiments: $P_{Total} = pCO_2$= 10 bar and T = 25 and 60 °C) and two at supercritical pressure (*supc*.-CO_2 experiments: P_{Total} = 150 bar and pCO_2 = 37 bar and T = 60 °C). The sulfate content was different in the injected solutions (sulfate free, gypsum-undersaturated and gypsum-equilibrated; Table 3.1). pH was measured *ex situ* in the *atm*-CO_2 experiments, *in situ* in the *subc*.-CO_2 and not measured in the *supc*.-CO_2 experiments (due to design of the experimental setup). Permeability was calculated in the *supc*.-CO_2 experiments. The mineral composition of the three caprock samples used in the experiments is shown in Fig. 3.9 (as described in *Chapter II*).

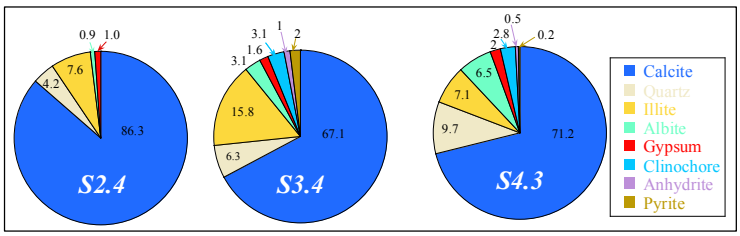

Figure 3.9 *Cycle charts showing the mineral composition of the Hontomín caprock: S2.4 (marly limestone) and S4.3 marl rocks are $CaCO_3$ richer than S3.4 (bituminous black shale) with a higher presence of aluminosilicates.*

1D reactive transport simulations were performed to reproduce the experimental results and interpret the ongoing processes by adjusting the values of the reactive surface areas of the primary minerals (calcite, clinochlore, albite and illite ; Table 3.3). It was necessary to consider a 1 *vol.*% fraction of highly reactive microparticles of albite in order to match the initially high Si concentration, even when the samples were previously washed (see *Section 2.1.2*). Also, a second gypsum phase was included in the simulations to account for gypsum precipitation with reactive surface area values that ranged from 0.01 to 20 $m^2_{min}\ m^{-3}_{bulk}$ in different experiments (Table 3.3). For Si-bearing secondary minerals, the values of the reactive surface areas were 100 $m^2_{mineral}\ m^3_{bulk}$ in column experiments under atmospheric and subcritical CO_2 conditions and 500 $m^2_{mineral}\ m^3_{bulk}$ under supercritical CO_2 conditions.

Table 3.3 Initial volumetric fraction (*vol.*%), porosity and adjusted mineral reactive surface area ($m^2_{min}\ m^{-3}_{bulk}$) in the column experiments.

label	**Marc-25-1**		**Marc-25-4**		**Marc-25-3**		**Marc-25-2a**	**Marc-60-2a**	**Marc-25-6a**	**Marc-60-6a**	**Marc-25-4a**	**Marc-60-4a**		**Marc-25-8**	**Marc-60-8**		**s3.4b**	**s4.3b**	
Nº exp.	**9**		**12**		**15**		**10**	**11**	**13**	**14**	**16**	**17**		**18**	**19**		**20**	**21**	
P_{Total} [bar]	1													10			150		
pCO_2 [bar]	$10^{-3.5}$													10			37		
T [°C]	25						60	25	60	25	60			25	60		60		
minerals	***vol.*%**	**area**	***vol.*%**	**area**	***vol.*%**	**area**	***vol.*%**	***vol.*%**	***vol.*%**	***vol.*%**	***vol.*%**	***vol.*%**	**area**	***vol.*%**	***vol.*%**	**area**	***vol.*%**	***vol.*%**	**area**
calcite	41.59	18	29.83	3	31.02	30	50.00	50.07	36.00	36.03	38.09	41.19	6 ± 2	35.26	34.74	170	31.20	40.00	90 ± 10
quartz	2.07	36	2.87	36	4.34	36	2.50	2.49	3.50	3.47	5.32	5.78	36	4.75	4.67	36	3.00	5.60	36
illite	3.54	$5 \times 10^{+2}$	6.79	$1 \times 10^{+7}$	2.99	$1 \times 10^{+7}$	4.30	4.27	8.20	8.19	3.67	3.97	$1 \times 10^{+7}$	3.62	3.57	49	7.10	3.90	$1 \times 10^{+7}$
albite	0.45	$4 \times 10^{+5}$	1.42	$1 \times 10^{+5}$	2.90	$2 \times 10^{+5}$	0.54	0.54	1.70	1.73	3.57	3.51	$2 \pm 0.2 \times 10^{+7}$	3.99	3.86	41	1.50	3.80	$3 \times 10^{+7}$
albite*	0.01	$3 \times 10^{+7}$	0.01	$4 \times 10^{+7}$		$4 \times 10^{+9}$	0.01	0.01	0.02	0.02	0.04	0.39	$1 \pm 0.9 \times 10^{+9}$	0.00	0.01	$9 \times 10^{+8}$	1.50	3.80	$3 \times 10^{+7}$
gypsum	0.56	-	0.85	-	0.03	-	0.70	0.68	1.00	1.02	1.24	1.34	-	1.58	1.56	-	0.90	1.30	-
gypsum**	0.01	$2 \times 10^{+1}$		$2 \times 10^{+1}$	0.00	$2 \times 10^{+1}$	1.00	7.00	1.00	1.00	1.00	1.00	$2 \pm 1 \times 10^{-2}$	0.01	0.01	9×10^{-2}	0.00	0.00	$9 \times 10^{+-2}$
clinochore		5	1.42	$2 \times 10^{+4}$	1.01	$2 \times 10^{+4}$							$3 \pm 2 \times 10^{+5}$			$2 \times 10^{+5}$			$3 \times 10^{+5}$
Anhydrite		5	0.29	0	0.00	0							5			5			3
Pyrite		5	0.49	5	1.24	5							5			5			1
Total *vol.*	48.21		43.93		43.73		58.01	58.06	53.11	53.11	53.70	58.07		51.30	50.50		46.00	56.40	
ϕ	51.76		56.07		56.27		41.95	41.94	46.89	46.89	46.30	41.93		48.70	49.50		54.00	43.60	

* stands for the second small volume fraction of albite (1 *vol.*% of total albite) included in the simulation (see text).
** stands for the second gypsum included in the simulations (see text).

Table 3.4 Volume of dissolved and precipitated minerals and $\Delta\phi$ in the column experiments calculated from the simulations.

		$V_{m\text{-}diss}$ [cm^3]				$V_{m\text{-}ppt}$ [cm^3]					$\Delta\phi$
Nº exp.	**label**	**Cal**	**Cln**	**Ab**	**Ilt**	**Gp**	**Kln**	**Ms**	**Stl**	**Scl**	
9	Marc-25-1	0.053	0.00E+00	0.003	6.77×10^{-7}	-	3.93×10^{-4}	2.86×10^{-4}	4.21×10^{-4}	9.56×10^{-4}	0.34
12	Marc-25-5	0.039	2.52×10^{-4}	0.002	1.57×10^{-3}	-	1.96×10^{-3}	7.64×10^{-8}	1.15×10^{-3}	0.00E+00	0.36
15	Marc-25-3	0.048	1.27×10^{-5}	0.006	4.90×10^{-3}	-	6.51×10^{-4}	1.57×10^{-3}	6.63×10^{-3}	2.41×10^{-3}	0.28
10	Marc-25-2a	0.025	0.000	0.002	4.49×10^{-3}	0.001	2.27×10^{-6}	7.85×10^{-3}	-	1.70×10^{-5}	0.05
11	Marc-60-2a	0.021	0.000	0.007	3.78×10^{-3}	0.005	8.42×10^{-5}	1.14×10^{-2}	-	6.70×10^{-5}	0.11
13	Marc-25-6a	0.022	0.001	0.002	1.29×10^{-3}	0.012	6.84×10^{-6}	4.20×10^{-3}	-	1.50×10^{-5}	0.10
14	Marc-60-6a	0.015	0.011	0.006	9.27×10^{-3}	0.005	6.51×10^{-5}	2.68×10^{-2}	-	8.97×10^{-5}	0.08
16	Marc-25-4a	0.019	0.003	0.003	7.17×10^{-4}	0.010	7.84×10^{-6}	5.47×10^{-3}	-	1.93×10^{-5}	0.06
17	Marc-60-4a	0.015	0.010	0.010	5.38×10^{-3}	0.005	6.53×10^{-5}	2.47×10^{-2}	-	8.84×10^{-5}	0.09
18	Marc-25-8	2.635	0.000	0.010	0.003	1.234	1.12×10^{-3}	4.74×10^{-3}	0.0	2.28×10^{-8}	3.33
19	Marc-60-8	1.558	0.009	0.018	0.057	1.303	4.31×10^{-3}	2.26×10^{-3}	0.0	0.0	0.18
20	S3.4b	0.021	0.000	0.002	9.88×10^{-5}	0.008	3.90×10^{-5}	2.29×10^{-7}	0.0	3.79×10^{-7}	2.01
21	S4.3b	0.012	0.000	0.001	1.96×10^{-4}	0.003	6.37×10^{-5}	1.81×10^{-6}	0.0	3.68×10^{7}	1.4

Cal: calcite, Cln: clinochlore, Ab: albite, Ilt: illite, Gp: gypsum, Kln: kaolinite, Ms: mesolite, Stl: stilbite, Scl: scolecite and Gs: gismondime.
$\Delta\phi = \phi_{(f)} - \phi_{(i)}$

For all experiments, the volumes of dissolved minerals ($V_{Cal\text{-}diss}$ (calcite), $V_{Ilt\text{-}diss}$ (illite), $V_{Cln\text{-}diss}$ (clinochlore) and $V_{Ab\text{-}diss}$ (albite)) and precipitated minerals ($V_{Gp\text{-}ppt}$ (gypsum), $V_{Kln\text{-}ppt}$ (kaolinite), $V_{Stl\text{-}ppt}$ (stilbite), $V_{Scl\text{-}ppt}$ (scolecite) and $V_{Gs\text{-}ppt}$ (gismondine)), as well as final porosity, were calculated from the modeling results (Table 3.4).

3.3.1 *S-free solution experiments,* $p\mathrm{CO_2} = 10^{-3.5}$ bar

Three column experiments, each column filled with a different caprock sample (*S2.4* in *exp. 9*; *S3.4* in *exp. 12* and *S4.3* in *exp. 15*; Table 2.6), were performed to study the caprock reactivity in the absence of sulfate (HCl solutions) at atmospheric pressure (P_{Total} = 1 bar, $p\mathrm{CO_2} = 10^{-3.5}$ bar and T = 25 °C).

The measured and simulated pH is shown in Fig.3.10. The output measured pH rapidly increased from 3.0 to 7.5 in the *S3.4* experiment and to 8.0 in both the *S2.4* and *S4.3* experiments and reach steady state throughout the experiments. The output simulated pH matched the measured ones in the experiments with *S2.4* and *S4.3* samples (*exps. 9 and 15*), but was lower than the measured in the experiment with *S3.4* (*exp. 12;* Table 2.6 and Fig.3.10). This mismatch was attributed to CO_2 degassing while measuring the output pH under atmospheric conditions.

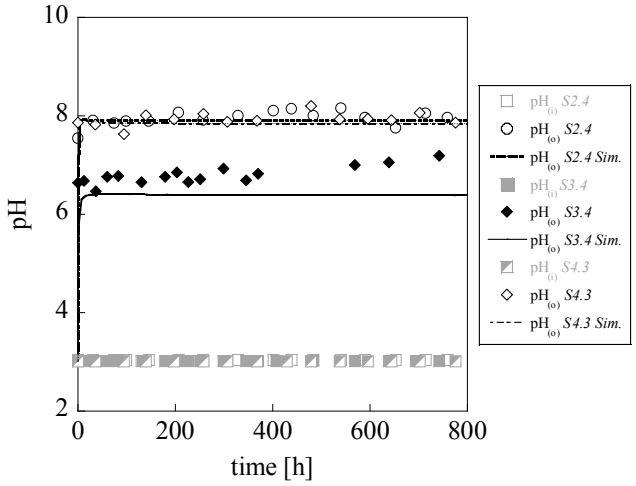

Figure 3.10 *pH variation with time at* P_{Total} *= 1 bar,* $pCO_2 = 10^{-3.5}$ *bar and T = 25 °C in the three experiments with S-free solution (HCl solution).*

The lower output pH, observed in the experiment with *S3.4* sample, was consistent with a smaller increase in ΔCa, which was readily associated to less calcite dissolution (Fig.3.11a) since the *SI* of the input solution with respect to calcite was smaller than that of the other two input solutions (i.e., -10.6 instead of -12.7; Table 2.6).

Match between the simulated and experimental change of pH and Ca concentration with time (Fig. 3.11a) was achieved by adjusting the calcite reactive surface area (Table 3.3). The fitted values of the calcite reactive surface areas (A_{Cal}) were 18, 3 and 30 m^2_{min} m^{-3}_{bulk} in *S2.4*, *S3.4* and *S4.3* experiments, respectively, becoming between one and two orders of magnitude smaller than the calculated geometric values ($A_{geometric}$ = 740, 530 and 552 m^2_{min} m^{-3}_{bulk} in *S2.4*, *S3.4* and *S4.3* experiments). An explanation for the smaller value of calcite reactive surface area (A_{Cal}) could be given by the transport (diffusion) control of the net reactions at pH < 5 (e.g., Sjöberg and Rickard, 1984). Additionally, the difference in A_{Cal} between the different marls could be related to rock heterogeneity (Noiriel et al., 2009).

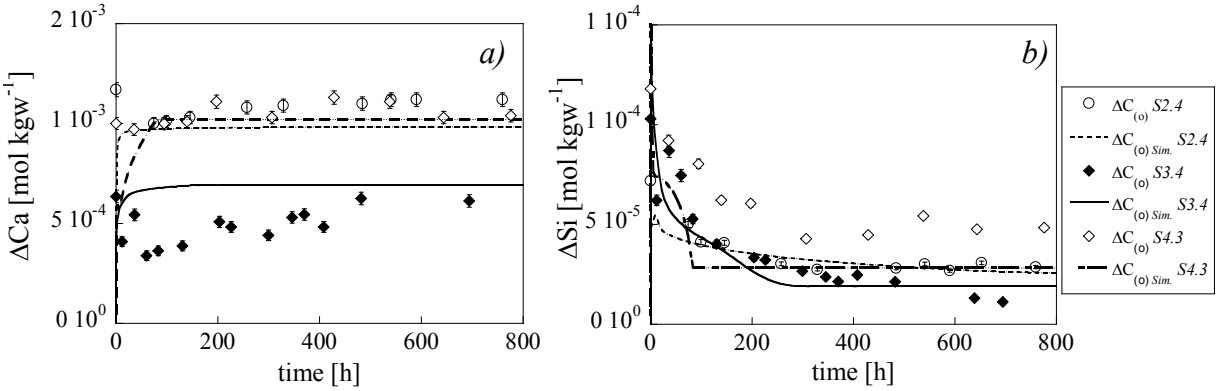

Figure 3.11 *Variation in the measured and simulated (Sim.) a) ΔCa and b) ΔSi concentrations with time in the three experiments with S-free solution (HCl solution): exps. 9, 12 and 15.*

Fig. 3.11b shows the variation of ΔSi concentration with time. ΔSi initially increased due to dissolution of Si-bearing minerals (albite (Ab), clinochlore (Cln) and illite (Ilt)). Thereafter, the ΔSi concentration decreased to reach a steady state. This was attributed to dissolution of the primary minerals (Ab, Cln and Ilt) and, probably, precipitation of secondary Si-phases (e.g., aluminosilicates). However, precipitated phases were not detected by SEM. The reactive surface

areas of the Si-bearing minerals were also larger than the geometric values, ranging from 2×10^5 to 9×10^8 m^2_{min} m^{-3}_{bulk}, in order to match the measured Si concentrations.

Variations in the Na, K, S and Mg concentrations could not be determined because the small differences between the large input and output concentrations were within analytical error.

Fig. 3.12 shows the variations of mineral volume ($\Delta vol.\%$) and porosity ($\Delta\phi$) along the columns in the three experiments. Calculations show that calcite dissolution mainly occurred at the very inlet of the column. The volume of dissolved calcite increased with the initial amount of calcite in the samples ($V_{Cal\text{-}diss}$ = 0.053, 0.048 and 0.039 cm^3 in the *S2.4*, *S4.3* and *S3.4* experiments, respectively). Albite dissolution was noticeable at the inlet and also occurred along the column, but in a lesser extent. The volume of dissolved albite also increased with the initial amount of albite in the samples ($V_{Ab\text{-}diss}$ = 0.006 cm^3 (*S4.3*), 0.003 cm^3 (*S2.4*) and 0.002 cm^3 (*S3.4*) Fig. 3.12). In comparison to albite, in the *S3.4* and *S4.3* samples, clinochlore dissolution was very minor, mainly occurring at the inlet. The illite behavior was related to dissolution of albite and chlinochlore: precipitation of illite occurred initially (for 10 h approximately) and near the inlet as albite dissolved (Fig. 3.13). In the *S3.4* and *S4.3* samples, chlinochlore dissolution also contributed to illite precipitation (Fig. 3.13). Thereafter, a decrease in dissolution of albite and clinochlore due to a pH increase, yielded a solution subsaturated with respect to illite and promoted its dissolution (Fig. 3.13). In the samples with pyrite, its dissolution was negligible.

Regarding the secondary phases, kaolinite, mesolite, scolecite and stilbite can precipitated as long as aqueous Si was supplied by dissolution of albite, clinochlore and illite. Overall, kaolinite precipitation occurred near the inlet, being highly related to albite dissolution (Fig. 3.13). In the *S3.4* rock sample, kaolinite precipitation is also predicted along the column as albite dissolved. The volume of precipitated kaolinite increased with the content of albite in the rock samples, being greater in the bituminous black shale (*S3.4*) than in the marl (*S4.3*) and in marly limestone (*S3.4*; Table 3.4). Zeolites (mesolite, scolecite and stilbite) showed similar precipitated volume among them but in a lesser excess than kaolinite. Their precipitation took place mostly along the column (Fig. 3.12), being subject to dissolution of albite near the inlet and illite dissolution along the column (Fig. 3.13).

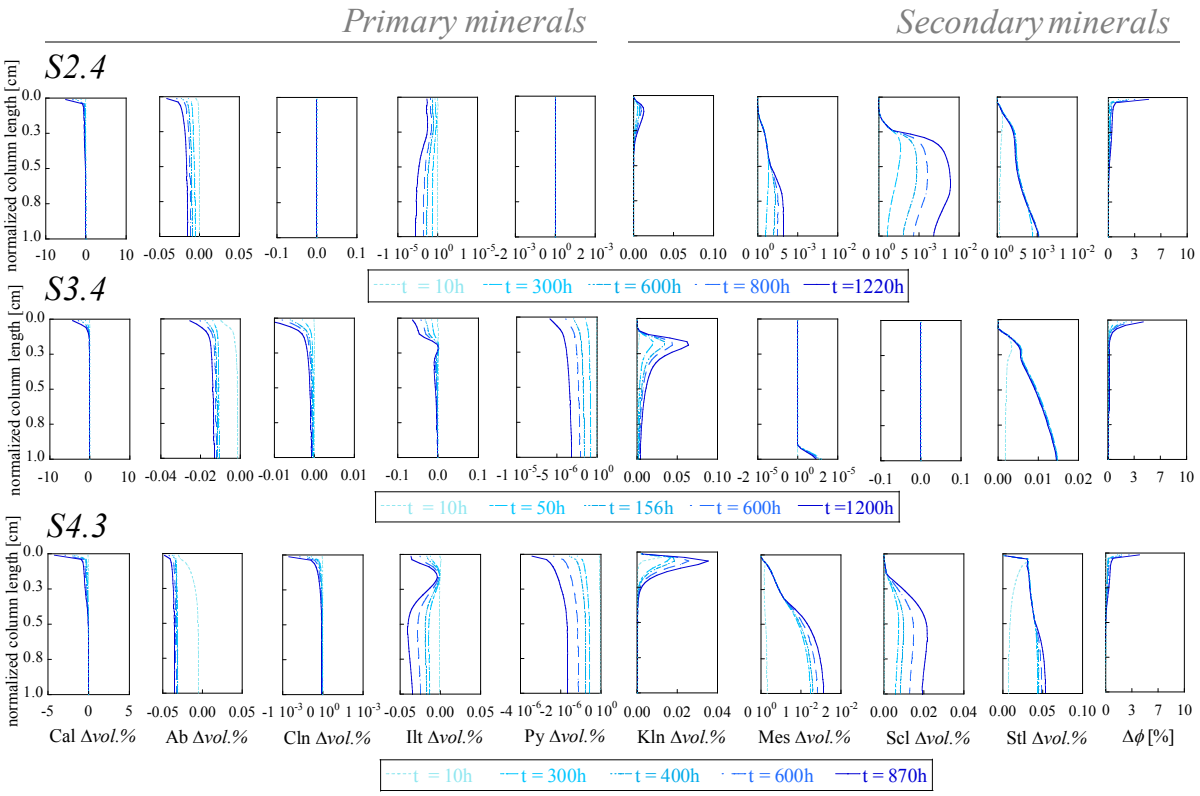

Figure 3.12 *Variation of the simulated volume fraction of the primary minerals (calcite (Cal), albite (Ab), clinochlore (Cln) and illite (Ilt)) and secondary minerals (kaolinite (Kln), mesolite (Ms), scolecite (Scl) and stilbite (Stl)) and porosity along the normalized column length (0.0 = inlet) under atmospheric CO_2 conditions at the end of the experiments: S2.4 = marly limestone, S3.4 = bituminous black shale and S4.3 = marl.*

In the three experiments, porosity increased near the inlet, yielding $\Delta\phi$ = 0.34, 0.37 and 0.30 in the *S2.4*, *S3.4* and *S4.3* experiments, respectively (Table 3.4). Along the column, porosity remained fairly the same. It is noted that the increase in porosity was mainly controlled by a larger dissolution of calcite compared to those of albite, illite, and clinochlore, together with little precipitation of kaolinite, mesolite, scolecite and stilbite. Maximum total volume of precipitated mineral is only 0.21 *vol.*%. Therefore detection of secondary minerals by SEM is practically impossible.

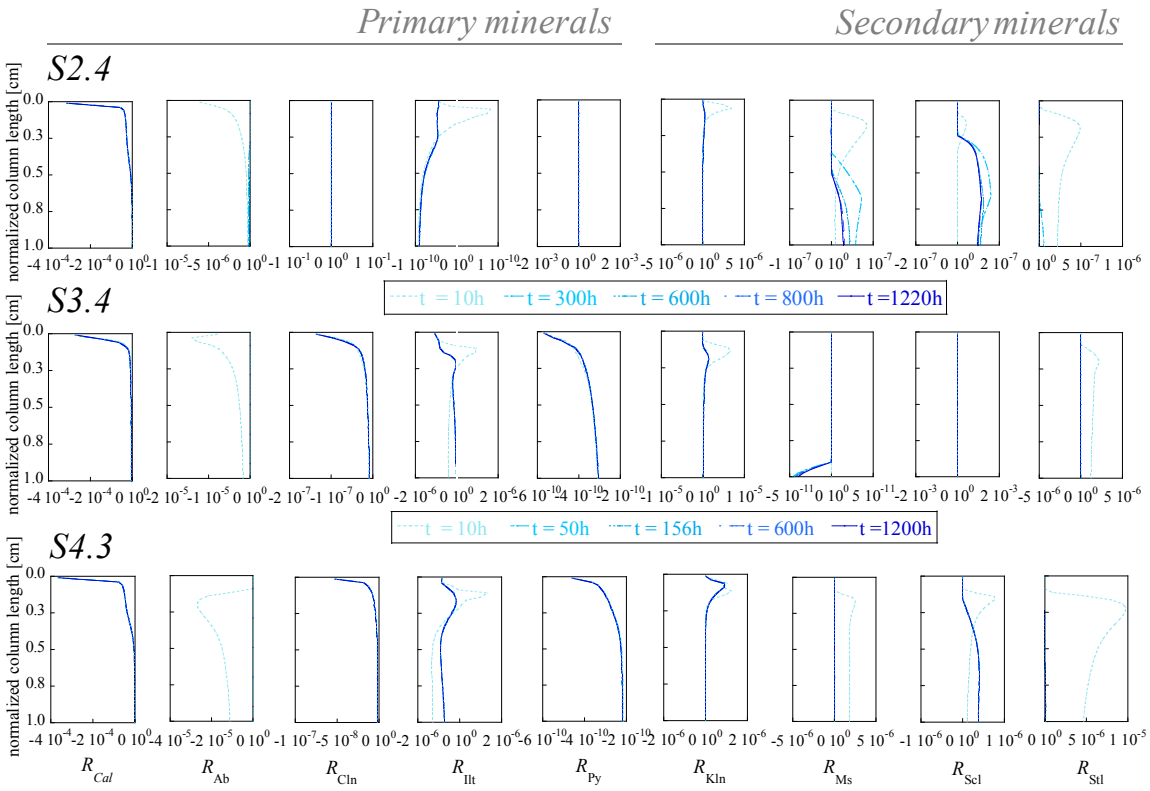

Figure 3.13 *Variation of the dissolution and precipitations rates of primary (albite (Ab), clinochlore (Cln) and illite (Ilt)) and secondary (kaolinite (Kln), mesolite (Ms), scolecite (Scl) and stilbite (Stl)) Si-bearing phases (R in mol m^{-3} s^{-1}) along the normalized column length (0.0 = inlet) in the experiments run under atmospheric CO_2 conditions. S2.4 = marly limestone, S3.4 = bituminous black shale and S4.3 = marl.*

3.3.2 *S-rich solution experiments,* $pCO_2 = 10^{-3.5}$ bar

Six column experiments were performed to study the caprock reactivity in the presence of sulfate (*S-rich(a3)* solution) at atmospheric pressure (P_{Total} = 1 bar and $pCO_2 = 10^{-3.5}$ bar) and T = 25 °C (*exps. 10(S2.4), 13 (S3.4) and 16 (S4.3)*) and T = 60 °C (*exps. 11(S2.4), 14 (S3.4) and 17 (S4.3)*).

The measured and simulated pH variation with time at 25 and 60 ºC is shown in Fig. 3.14. The *ex-situ* measured pH was higher than the input one and, for approximately 200 h, slightly higher at 60 ºC than at 25 ºC (pH = 6.82 at 60 ºC and pH = 6.75 at 25 ºC). Thereafter, at both temperatures, pH reached steady state. Overall, the simulated output pH matched the measured output pH.

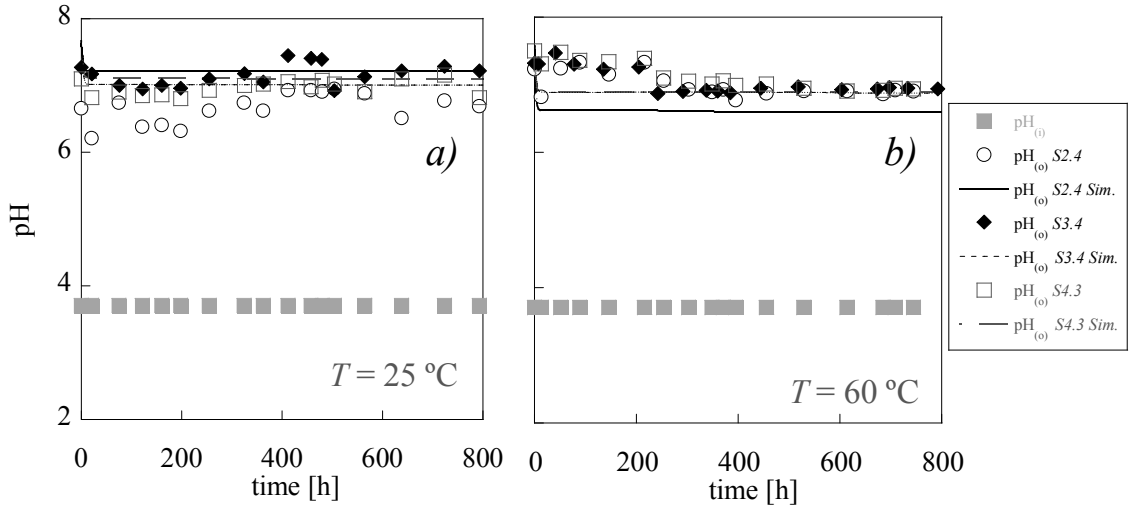

Figure 3.14 *pH variation with time at P_{Total} = 1 bar, $pCO_2 = 10^{-3.5}$ bar and 25 °C (a) and 60 °C (b) in the six experiments with S-rich solution (S-rich(a3) solution).*

The measured and simulated variation of ΔCa, ΔS and ΔSi concentrations with time is illustrated in Fig. 3.15. In all experiments, ΔCa and ΔS concentrations were close to zero within error. ΔCa variation indicates that dissolution of calcite occurred, followed by a likely precipitation of Ca-bearing phases at both temperatures (ΔCa < 0). This behavior is more evident at 25 ºC than at 60 ºC (Fig. 3.15a,b). According to S, gypsum precipitation was likely occurring when ΔS was negative (S deficit in Fig. 3.15c,d). The good agreement between the simulated and experimental variation of pH and Ca concentration with time was achieved by adjusting the calcite reactive surface area (Table 3.3). The fitted value of the calcite reactive surface area (A_{Cal}) in all experiments was 6 ± 2 m^2_{min} m^{-3}_{bulk}, which is of the same order of magnitude as the ones used in the S-free (HCl) experiments. Although the simulations suggest some gypsum precipitation, gypsum was not observed by SEM.

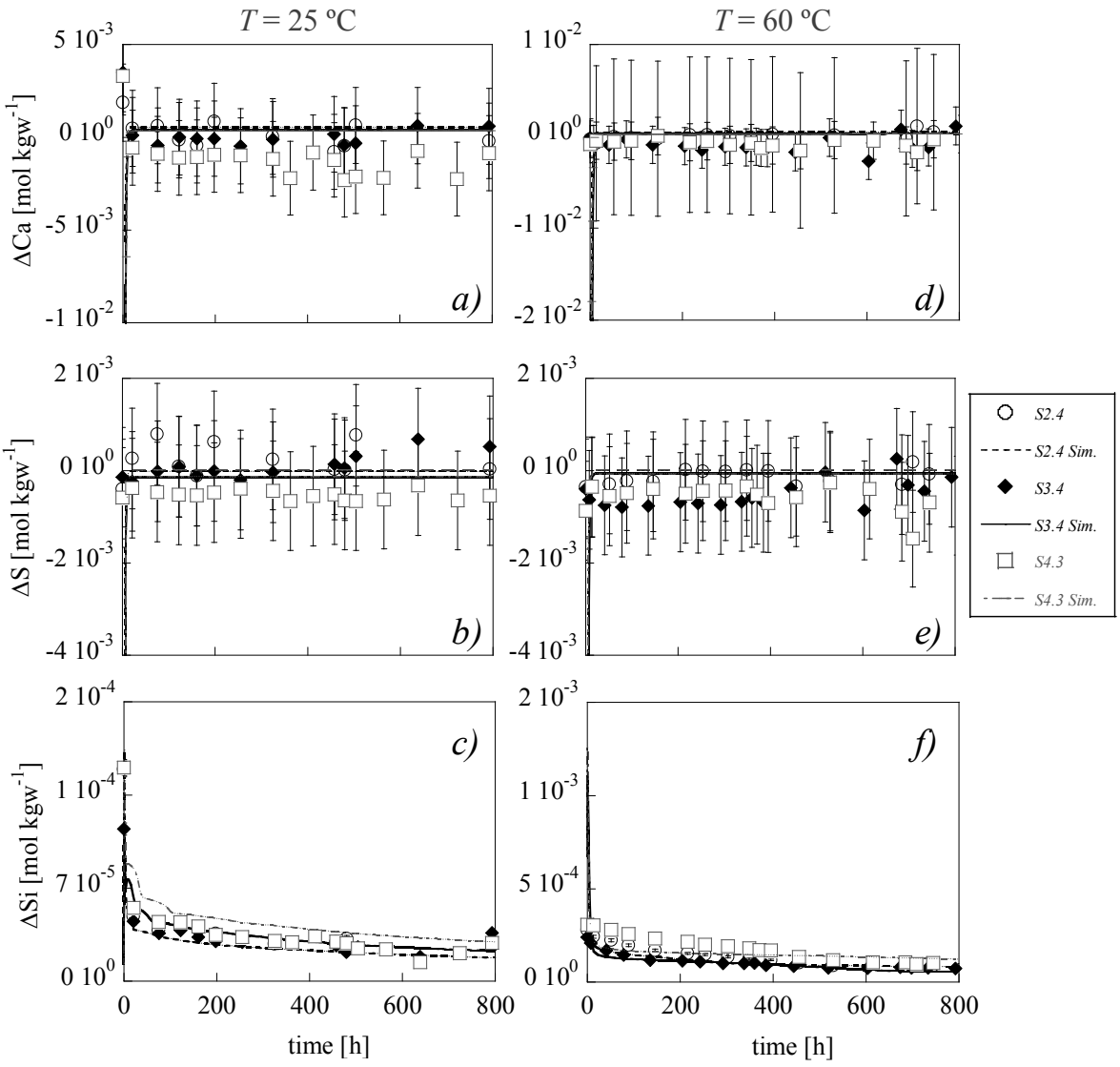

Figure 3.15 *Variation of the increase in concentration with time in exps. 10 and 11 (S2.4), 13 and 14 (S3.4), and 16 and 17(S4.3) with S-rich solution (S-rich(a3)) and atmospheric CO_2 pressure: a) ΔCa, b) ΔS and c) ΔSi at T = 25 °C and d) ΔCa,e) ΔS and f) ΔSi at T = 60 °C.*

Fig. 3.15e,f shows a positive ΔSi variation with time caused by dissolution of albite, illite and clinochlore, which was higher at 60 ºC. The consequent ΔSi decrease and achievement of steady state was also related to precipitation of three aluminosilicates (kaolinite, mesolite and scolecite), which is evidenced by their respective precipitation rates (Fig. 3.16). As in the case of the *S-free* experiments, the reactive surface areas of the primary Si-bearing minerals also needed to be larger than the geometric values, ranging from 1×10^5 m^2_{min} m^{-3}_{bulk} to 3×10^9 m^2_{min} m^{-3}_{bulk}, in

order to match the measured Si concentration. Fig. 3.16 shows that albite and clinochlore dissolution favored illite precipitation at the inlet. Thereafter, along the column, dissolution of albite was less and hence the solution became undersaturated with respect to illite, allowing its dissolution. This reaction originated precipitation of mesolite and in a lesser extent that of kaolinite and scolecite. At 60 ºC, near the inlet, dissolution of albite instantaneously contributed to illite precipitation, which contrasts with the slower illite precipitation at 25 ºC (Fig. 3.16). Variations in the Na, K and Mg concentrations could not be determined because the small differences between the large input and output concentrations were within analytical error.

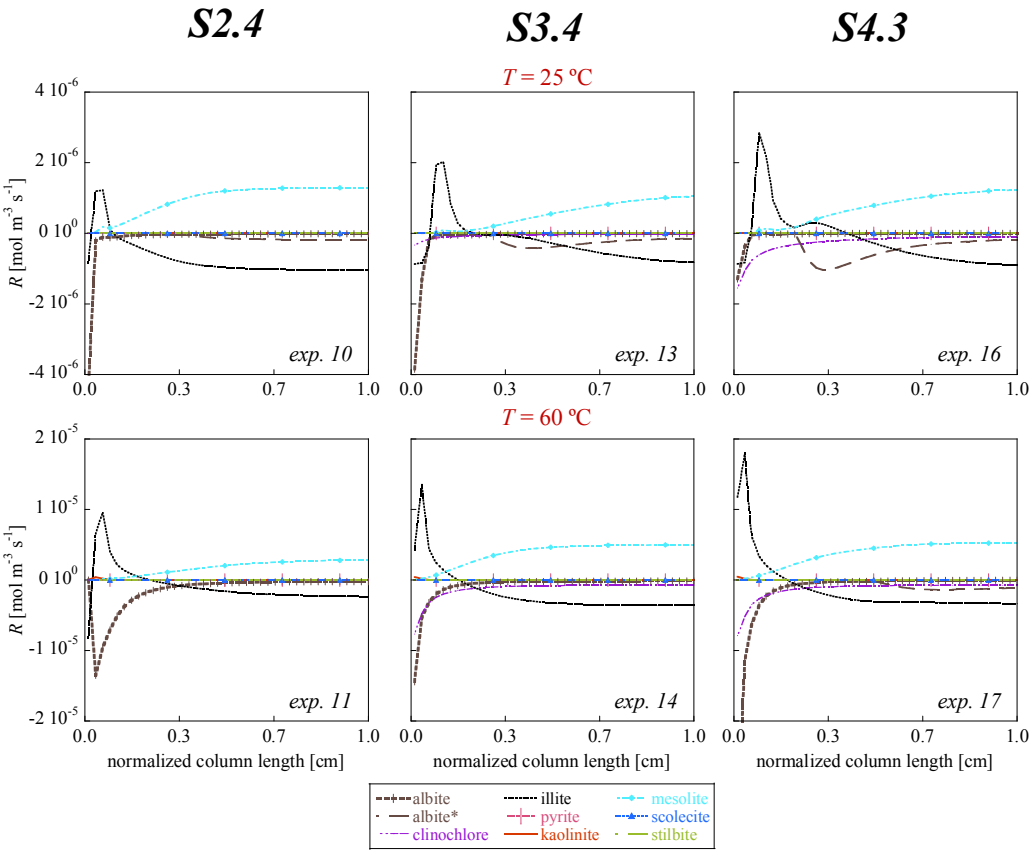

Figure 3.16 *Variation of dissolution and precipitation rates of albite, clinochlore, illite and pyrite and kaolinite, mesolite, scolecite and stilbite with normalized column length in the exps. 10 and 11 (S2.3), exps. 13 and 14 (S3.4) and exps.16 and 17 (S4.3) at 25 °C (top) and 60 °C (bottom).*

Variation of the volumes of dissolved calcite, albite, clinochlore and illite and volumes of precipitated gypsum, kaolinite, mesolite and scolecite yields variation of porosity along the columns (Fig. 3.17 and Table 3.4). Calculations showed that the volume of dissolved calcite increased with the initial calcite content in the rocks ($V_{Cal\text{-}diss}$ in *S2.4* > $V_{Cal\text{-}diss}$ in *S3.4 and S4.3*) and decreased with temperature. Overall, volume of precipitated gypsum ($V_{Gp\text{-}ppt}$) was always smaller than $V_{Cal\text{-}diss}$. In all experiments, calcite dissolution and gypsum precipitation occurred mainly at the inlet (Fig. 3.17). Volumes of dissolved albite ($V_{Ab\text{-}diss}$), clinochlore ($V_{Cln\text{-}diss}$) and illite ($V_{Ilt\text{-}diss}$) were greater than volumes of precipitated kaolinite ($V_{Kln\text{-}ppt}$), mesolite ($V_{Ms\text{-}ppt}$) and scolecite ($V_{Scl\text{-}ppt}$) (Table 3.4). Like calcite dissolution and gypsum precipitation, dissolution and precipitation of primary and secondary Si-bearing minerals occurred near the inlet, yielding a porosity increase in this zone. The increase in porosity was calculated to be $\Delta\phi_{25\,°C} = 0.05$ (*S2.4*), 0.10 (*S3.4*) and 0.06 (*S4.3*) and $\Delta\phi_{60\,°C} = 0.11$ (*S2.4*), 0.08 (*S3.4*) and 0.09 (*S4.3*). These values showed that at 25 ºC the presence of sulfate decreased $\Delta\phi$ by 15-30% compared to $\Delta\phi$ in the absence of sulfate (Table 3.4) and $\Delta\phi$ was slightly affected by a temperature increase.

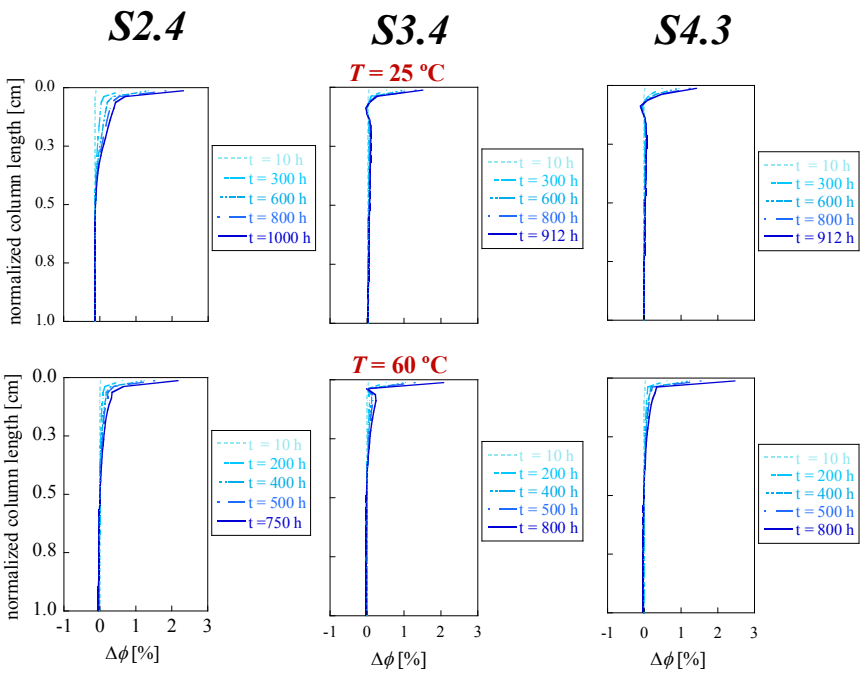

Figure 3.17 *Variation of porosity (Δϕ) with normalized column length in the exps. 10 and 11 (S2.3), exps. 13 and 14 (S3.4) and exps.16 and 17 (S4.3) at 25 °C (left) and 60 °C (right).*

3.3.3 *T* effect on marl reactivity, pCO_2 = 10 bar

Two column experiments filled with the same marl rock (*S4.3*) were performed in sulfate rich solutions (*S-rich(1)* and *S-rich(2)*) at the same pressure ($P_{Total} = pCO_2$ = 10 bar; Table 2.6) and one at 25 ºC (*exp. 18*) and the other at 60 ºC (*exp. 19*).

The measured and simulated pH variation with time is shown in Fig. 3.18. The *in-situ* measured output pH immediately increased up to 5.21 (25 ºC) and 5.26 (60 ºC) and thereafter reached steady state (Fig. 3.18). A good match was achieved between the measured and simulated output pH.

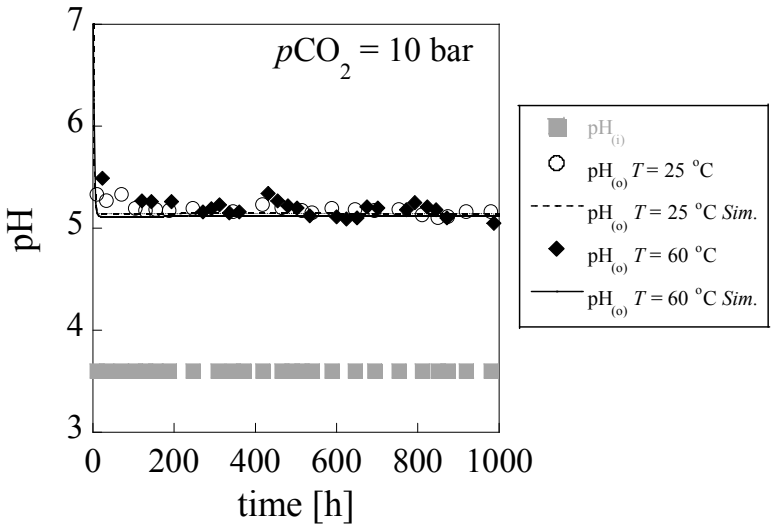

Figure 3.18 *Variation of pH with time in exps. 18 and 19 at* $P_{Total} = pCO_2$ *= 10 bar and 25 and 60 °C.*

The measured and simulated variation of ΔCa, ΔS, ΔFe and ΔSi concentration with time are shown in Fig. 3.19. As the injected solutions were undersaturated with respect to calcite (Table 2.6), allowing calcite to dissolve, the output Ca concentration exceeded that of the input solution. A sharp increase occurred initially due to exclusive calcite dissolution. Thereafter, while calcite dissolved, ΔCa gradually decreased, together with ΔS (Fig. 3.19a,b). The S deficit was related to gypsum and/or anhydrite precipitation depending on *T*. Finally, steady state was reached in the two experiments. ΔCa was smaller at high temperature, indicating that calcite dissolution was favored by decreasing temperature ($\Delta Ca_{25\ ^oC} > \Delta Ca_{60\ ^oC}$), since undersaturation increased by

decreasing temperature all over the columns (e.g. -1.5 < SI_{Cal-25} < -0.2 and -0.8 < SI_{Cal-60} < -0.1 after 1000 h). At 60 ºC, the S deficit was larger for the first 300 h. Thereafter, at both temperatures, steady state was achieved with same ΔS. SEM of the reacted samples showed only the presence of gypsum at both temperatures, which was confirmed by XRD patterns (Fig. 3.20). A good match was achieved between the measured and simulated output Ca and S concentrations by fitting the value of the calcite reactive surface area (A_{Cal}) to 170 $m^2_{mineral}\ m^{-3}_{bulk}$ and gypsum reactive surface area (A_{Gp}) to 0.02 ± 0.01 $m^2_{mineral}\ m^{-3}_{bulk}$ in both experiments (Table 3.3).

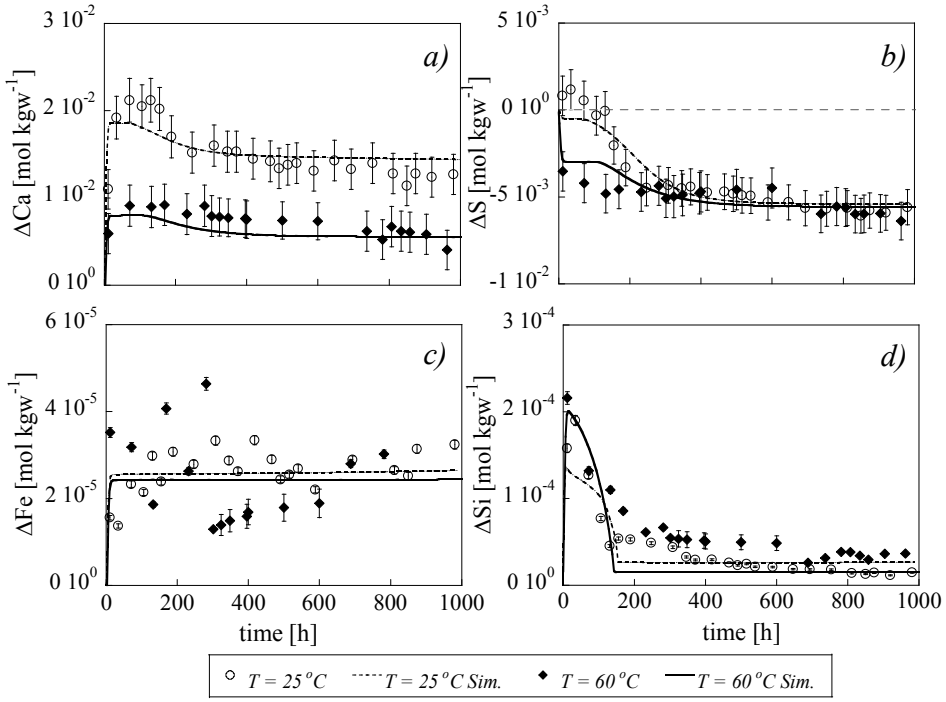

Figure 3.19 *Variation in a) ΔCa, b) ΔS, c) ΔSi and d) ΔFe concentrations with time at P_{Total} = 10 bar= 10 bar and 25 °C (exp. 18) and 60 °C (exp. 19).*

A slight Fe increase was observed in both experiments indicating that clinochlore dissolution occurred at both temperatures (Fig. 3.19c). The output Si concentration exceeded that of the input one. Initially, at both temperatures, a sharp increase in Si concentration took place, followed by a fast decrease to thereafter reach steady state (Fig. 3.19d). The initial sharp increase was associated to a fast dissolution of 1 *vol.*% fraction of highly reactive albite microparticles. The decrease was related to coupled dissolution and precipitation of Si-bearing phases (albite,

clinbochlore, illite, kaolinite and mesolite). A reasonable match between the experimental and simulated Si and Fe concentrations was achieved. The values of reactive surface area for the primary Si-bearing minerals, as in the case of S-free experiments, were also larger than the geometric ones, ranging from 2×10^{1} to 9×10^{8} m^2_{min} m^{-3}_{bulk}. Variations in the Na, K and Mg concentrations could not be determined because the small differences between the large input and output concentrations were within analytical error.

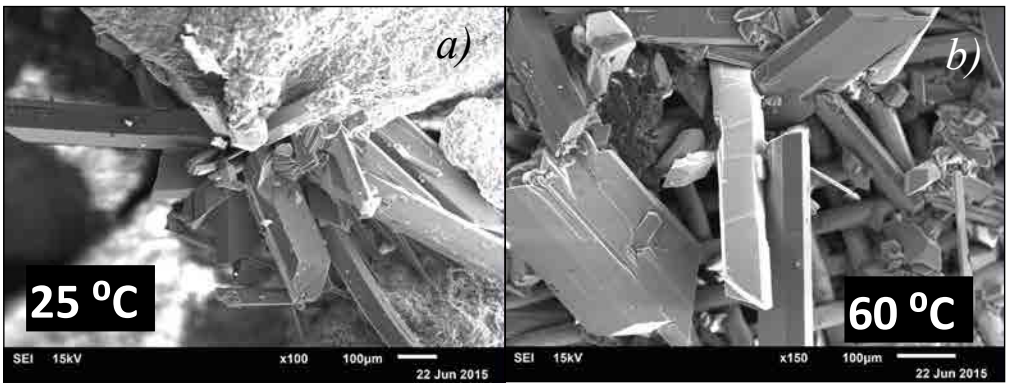

Figure 3.20 *SEM images of the reacted samples show gypsum needles at 25 °C (exp. 18) (a) and 60 °C (exp. 19) (b).*

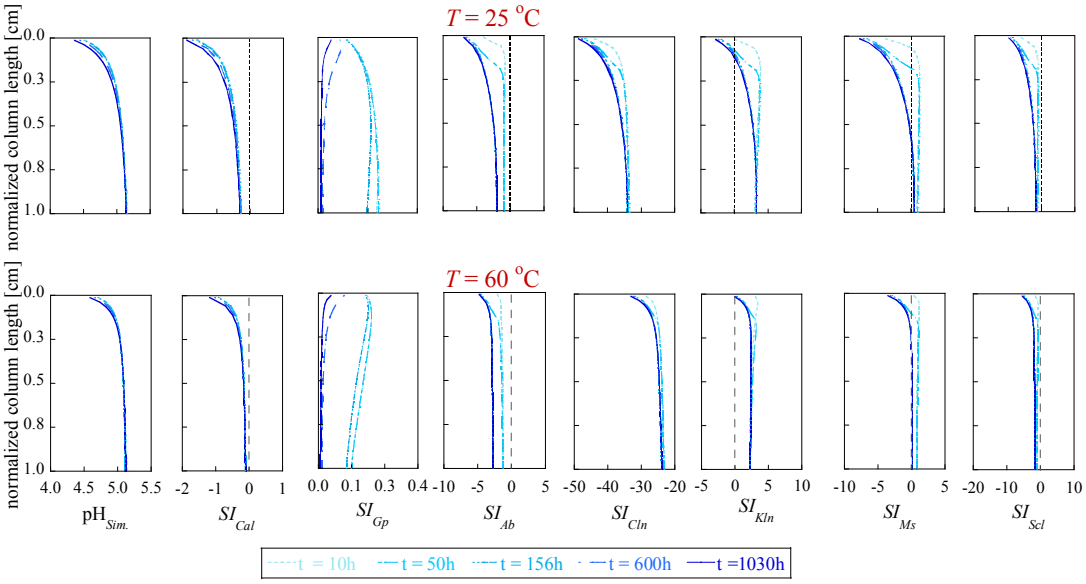

Figure 3.21 *Simulated variation of (a) pH and mineral saturation index and (b) mineral dissolution and precipitation rates along the normalized column length in the S4.3 rock experiments at P_{Total} = pCO_2= 10 bar and 25 and 60 °C. Cal: calcite, Gp: gypsum, Cln: clinochlore, Kln: kaolinite and Ms: mesolite.*

Simulations show that pH near the inlet was lower than in the rest of the column causing smaller SI_{Cal} values near the inlet (Fig.3.21). As calcite dissolution at 25 ºC took place in more undersaturated conditions than at 60 ºC (Fig.3. 22), the dissolution front went farther along the column at lower temperature (25 ºC; Fig.3. 21). SI_{Gp} indicates that the solution became initially supersaturated as calcite started to dissolve. With time solution supersaturation decreased and reached steady state (near equilibrium) at both temperatures (Fig.3. 21). Initially, the solution was undersaturated with respect to clinochlore and albite (Fig. 3.22). With time, solution gained undersaturation in both temperatures (Fig. 3.21). Regarding secondary Si-bearing phases, supersaturation was lower near the inlet than in the rest of the column yielding a higher dissolution of clinochlore and in a lesser extent of albite (Figs. 3.21 and 3.22). At 25 ºC, solution was undersaturated ($SI_{Kln} < 0$; $SI_{Ms} < 0$; $SI_{Stl} < 0$) near the inlet (Figs.3. 21). Thereafter it was supersaturated with respect to kaolinite and mesolite, allowing their precipitation (Fig. 3.22).

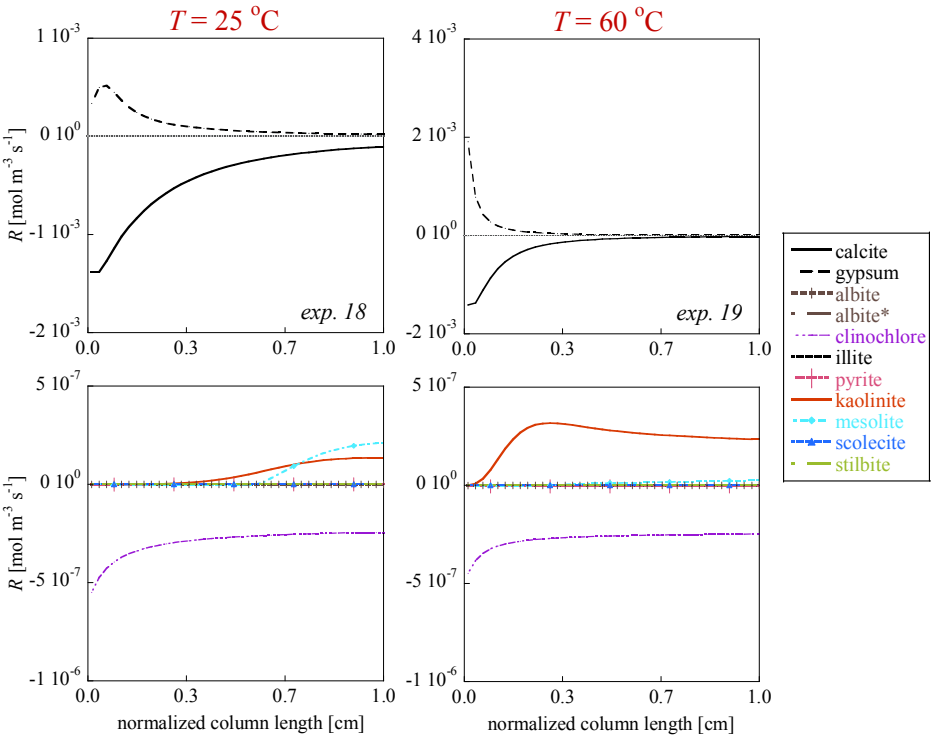

Figure 3.22 *Simulated variation of calcite dissolution and gypsum precipitation and Si-bearing minerals precipitation (albite, albite*, clinochlore, illite, pyrite, kaolinite, mesolite, scolecite and stilbite) rates along the normalized column length in the S4.3 rock experiments at* $P_{Total} = pCO_2 = 10$ *bar and 25(left) and 60 ºC (right).*

Fig. 3.23 illustrates the variation of mineral volumetric fraction along the column. At both temperatures, significant calcite dissolution took place near the inlet. Nonetheless, at 25 ºC, dissolution still occurred along the column. Consequently, the amount of dissolved calcite increased when lowering temperature. Accordingly, gypsum precipitation mainly occurred near the inlet and it was greater at 60 ºC. Regarding Si-bearing minerals, the volume of dissolved clinochlore and albite was very small compared to that of calcite, yielding a small volume of precipitated kaolinite, mesolite and scolecite (Table 3.4). At 60 ºC, the solution was unsaturated with respect to scolecite.

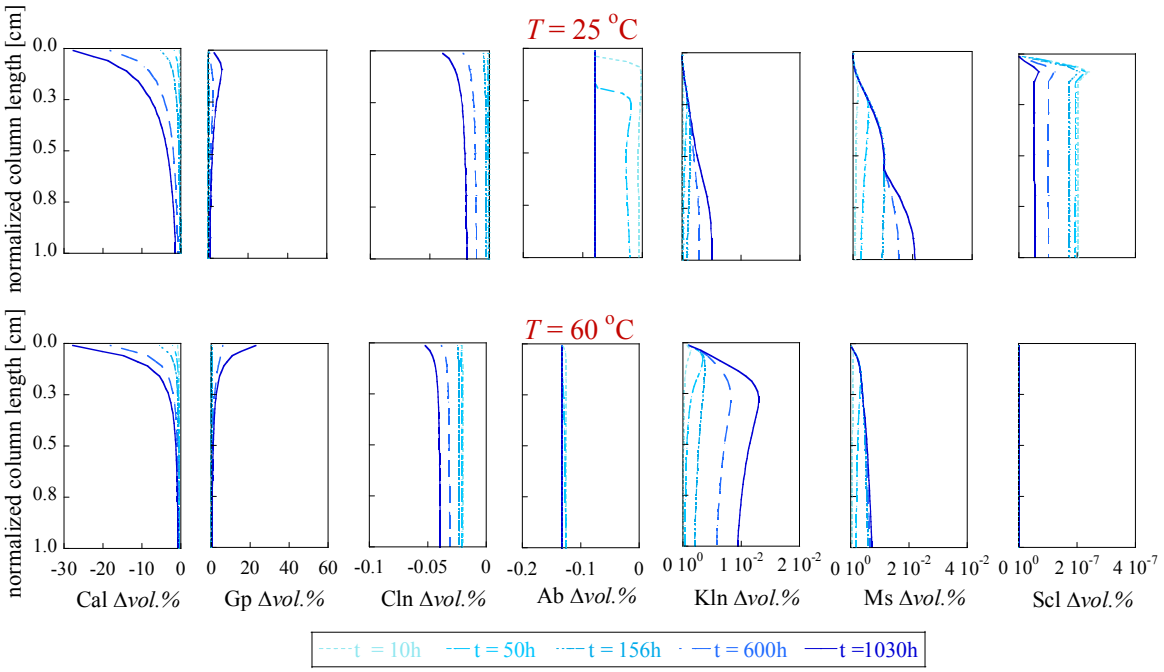

Figure 3.23 *Simulated variation of the primary and secondary minerals vol.% with the normalized column length in the S4.3 rock experiments at pCO_2 of 10 bar and a) 25 °C and b) 60 °C. Dashed lines indicate equilibrium. Cal: calcite, Gp: gypsum, Cln: clinochlore, Kln: kaolinite, Ms: mesolite and Scl: scolecite.*

Variation of mineral volume fraction along the column controlled variation of porosity, which increased significantly near the inlet, and more at 25 ºC than at 60 ºC (Fig. 3.23). At low temperature (25 ºC), the extension of porosity was larger. Creation of porosity was mainly ruled by calcite dissolution and gypsum precipitation and, in a lesser extent, by dissolution and precipitation of Si-bearing phases. A sensitivity analysis using suitable values of A_{Cal} (160-500

$m^2_{mineral}\ m^{-3}_{bulk}$) and A_{Gp} (0.01-0.04 $m^2_{mineral}\ m^{-3}_{bulk}$) to match the resulting uncertainty of Ca and S output concentrations was carried out (Fig. 3.23). Within the uncertainty, porosity was favored at 25 ºC. The larger uncertainty at 25 ºC was caused by using a larger range of A_{cal} values, which allowed a good match of the variation in the output Ca and S concentration with time, since calcite dissolution at 25 ºC was taken place at higher undersaturation than at 60 ºC.

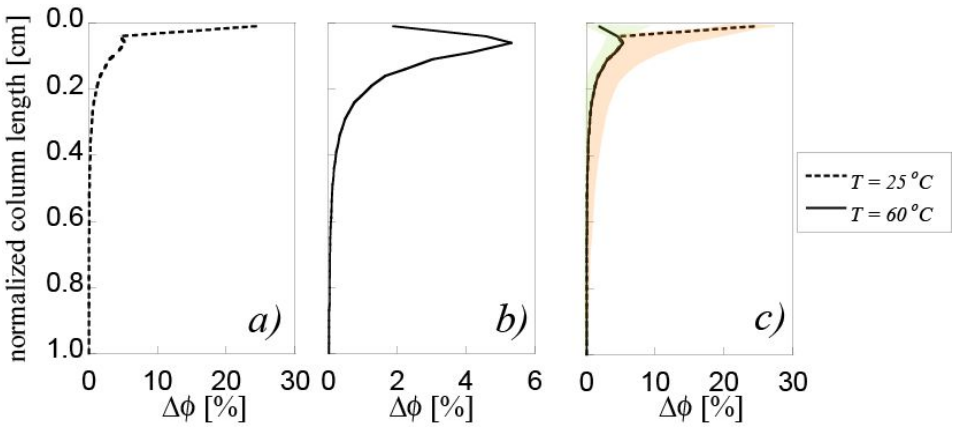

Figure 3.24 *Variation of porosity (Δϕ) with normalized column length in the S4.3 experiment at 10 bar of pCO_2 and 25 °C (a) and 60 °C (b). Shaded areas (green = 25 °C and orange = 60 °C) show the results of the sensibility analyses (c).*

The temperature effect on marl reactivity was investigated under atmospheric pCO_2 and 25 and 60 ºC. Like in the experiments run under P_{Total} = pCO_2 = 10 bar, the calcite dissolution rate increased by decreasing temperature and the gypsum precipitation rate was not favored. In general, the coupled process of calcite dissolution and gypsum precipitation, together with Si-bearing minerals precipitation, always increased porosity (under both pCO_2), the increase being higher at the lowest temperature. Simulations showed that an increase in temperature affected the trend of porosity variation along the column and reduced porosity creation under this two CO_2 conditions (Figs. 3.17 and 3.24).

3.3.4 pCO_2 effect on marl reactivity

Two column experiments using the bituminous black shale (*S3.4*) and marly limestone (*S4.3*) with a sulfate-rich solution (*S-rich(3))* were performed at P_{Total} = 150 bar, pCO_2 = 37 bar and T =

60 ºC (*exps. 20 and 21*; Table 2.6). The results obtained with the *S3.4* sample were compared with those obtained at $pCO_2 = 10^{-3.5}$ bar (*exp. 14*) and the results obtained with the *S4.3* sample were compared with those at 10 bar (*exp. 19*) and $10^{-3.5}$ bar (*exp. 17*) of pCO_2.

Simulated output pH increased from 3.45 to 4.64 (*S3.4*) and 4.98 (*S4.3*) (Fig. 3.25). These values were lower than those obtained at 10 bar (pH = 5.19) and atmospheric pressure (pH = 6.95 ± 0.02; Fig. 3.25).

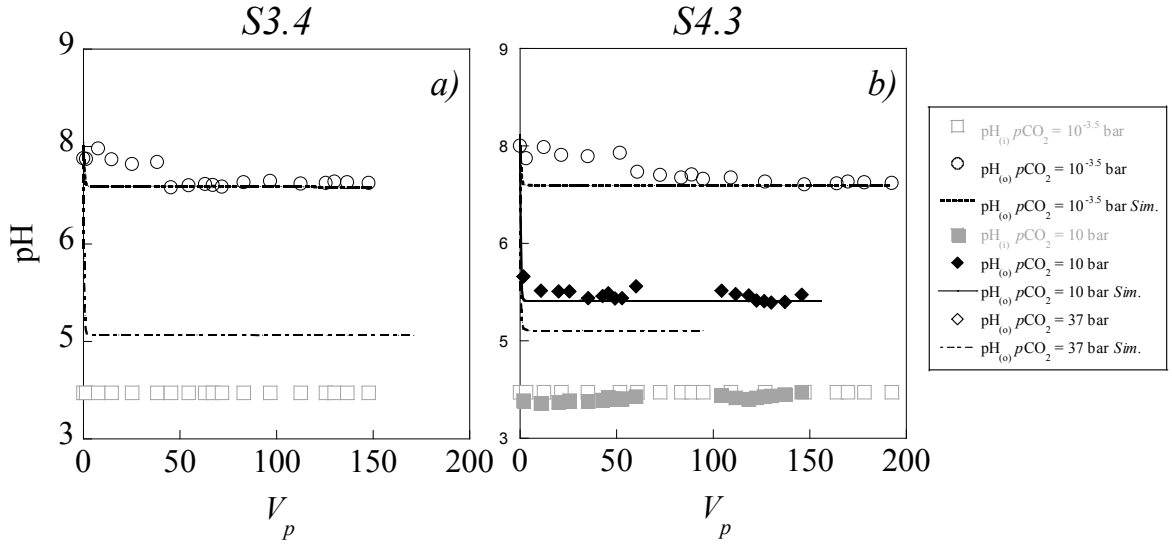

Figure 3.25 *Variation of measured and simulated pH with number of pore volumes in the bituminous black shale (S3.4) experiment (a) and the marl (S4.3) experiment (b) at P_{Total} = 150 bar, pCO_2 = 37 bar and T = 60 °C. Comparison with experiment performed at pCO_2 = 10 bar and $10^{-3.5}$ bar. Note that at pCO_2 = 37 bar pH was not measured due to design of the experimental setup.*

In the *S3.4* experiments (Fig. 3.26a), ΔCa and ΔS variation with number of pore volumes ($V_p = t/\tau$ where t = total experimental time and τ = residence time) shows that dissolution of calcite and precipitation of gypsum were larger at pCO_2 = 37 bar than at atmospheric pressure. ΔSi variation with V_p shows that release of silicon was similar at both pressures, whereas that of Fe was higher at high pressure. ΔSi and ΔFe variation was associated to dissolution of albite, clinochlore and illite, and precipitation of kaolinite and mesolite.

In the *S4.3* experiments (Fig. 3.26b), ΔCa variation with V_p shows that dissolution of calcite at pCO_2 = 10 and 37 bar was similar and larger than that at $pCO_2 = 10^{-3.5}$ bar. ΔS variation shows

that precipitation of gypsum was larger at pCO_2 = 10 bar than those at pCO_2 = 37 and $10^{-3.5}$ bar. ΔSi variation shows that Si released was higher at $pCO_2 = 10^{-3.5}$ bar than at 37 and 10 bar. ΔFe variation shows that Fe release was higher at pCO_2 = 37 bar than at 10 bar. ΔSi and ΔFe variation was associated to dissolution of albite, clinochlore and illite, and precipitation of kaolinite and mesolite. It is noticed that small differences in rock mineralogy barely influenced the reactivity of the two rocks.

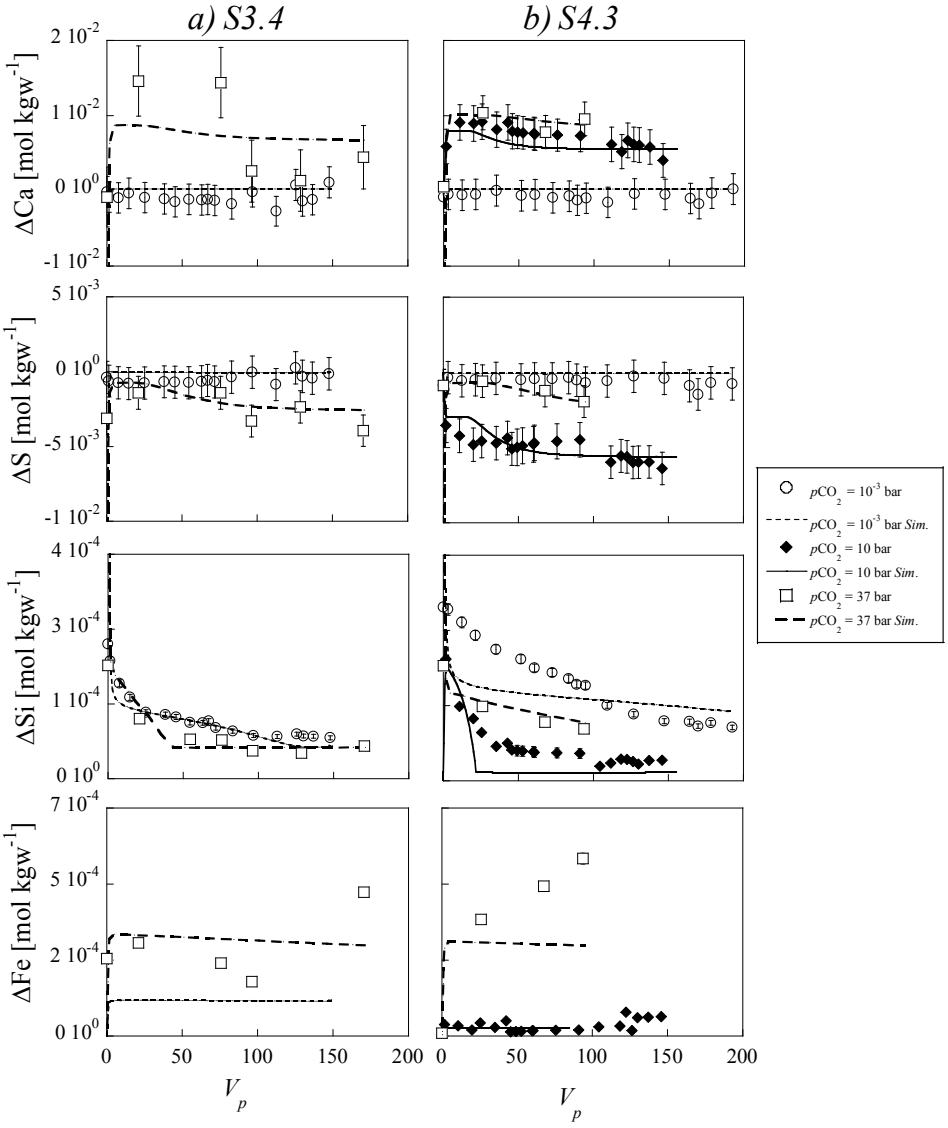

Figure 3.26 *Variation of the measured and simulated ΔCa, ΔS, Δ Si and ΔFe with number of pore volumes in the columns filled with a) bituminous black shale (S3.4) and b) marly limestone (S4.3) under different pCO_2 conditions (atmospheric, 10 and 37 bar) and 60 °C. Note that at $pCO_2 = 10^{-3.5}$ bar Fe concentration was not measured.*

The calcite dissolution rate was faster along the column at higher pCO_2 (Fig. 3.27). Given that the input pH is around 3.45 in the three experiments, the faster calcite dissolution rate at high pCO_2 (10 and 37 bar) is related to the weak character of the H_2CO_3 acid in contrast to the strong nature of the HCl acid used under atmospheric pCO_2. As a weak acid, H_2CO_3 acts as a pH buffer and dissociates partially yielding lower solution pH all over the column.

A good match was achieved between the measured and simulated output Ca and S concentrations by fitting the value of the calcite reactive surface area (A_{Cal}) to 90 ± 10 $m^2_{mineral}$ m^{-3}_{bulk} and gypsum reactive surface area (A_{Gp}) to 0.09 $m^2_{mineral}$ m^{-3}_{bulk} in both experiments (Table 3.3). The reactive surface areas of the primary Si-bearing minerals, as in all previous cases, were also larger than the geometric values to be 1-3 × 10^7 m^2_{min} m^{-3}_{bulk}, in order to match the measured Si and Fe concentrations.

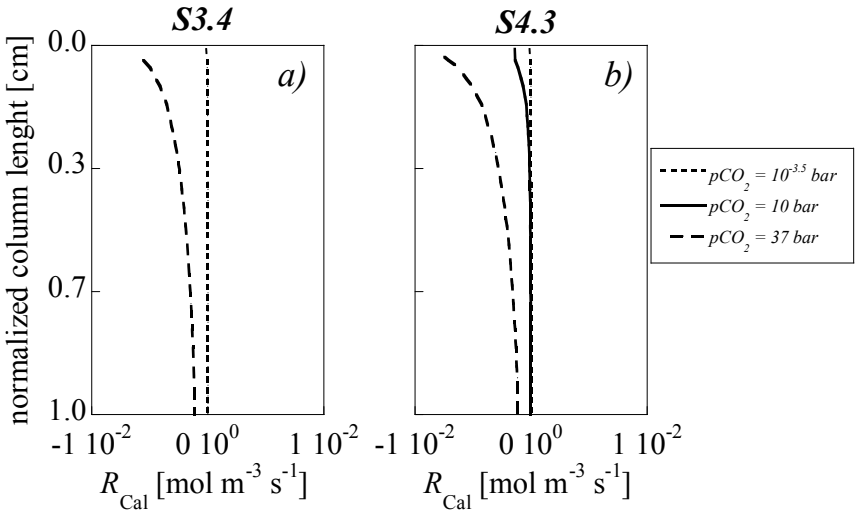

Figure 3.27 *Variation in calcite dissolution rate along the normalized column length at different pCO_2 ($10^{-3.5}$, 10 and 37 bar) and 60 °C: a) bituminous black shale (S3.4) and b) marly limestone (S4.3).*

Variation of dissolved volume of calcite (and in a lesser extent of albite, clinochlore and illite) together with precipitated volume of gypsum (and kaoline, mesolite and scolecite) yielded variation of the initial porosity. Porosity variation along the column shows that an increase in pCO_2 enhances noticeably the porosity near the inlet, as well as creation of porosity along the column (Fig. 3.28).

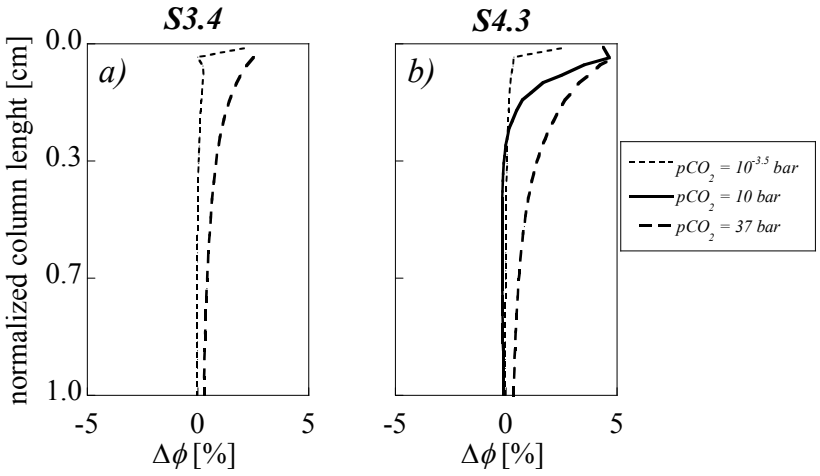

Figure 3.28 *Porosity variation with respect to the normalized column length at different pCO_2 ($10^{-3.5}$, 10 and 37 bar) and 60 °C: a) bituminous black shale (S3.4) and b) marly limestone (S4.3).*

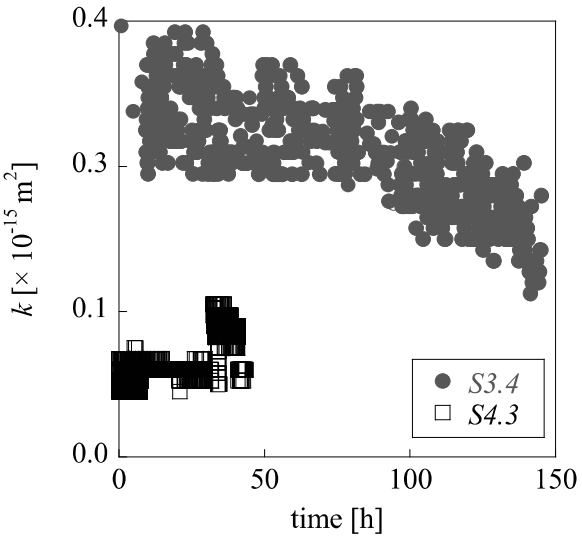

Figure 3.29 *Variation of permeability with time in the S3.4 and S4.3 rock experiments at P_{Total} = 150 bar, pCO_2 = 37 bar and 60 °C.*

The calculated permeability (k) based on the measured pressure drop between the inlet and the outlet of the column according to Eq.(2.42) showed a k decrease with time in both experiments (Fig. 3.29), from 4.0×10^{-16} to 1.1×10^{-16} m^2 (*S3.4; exp. 20*) and from 8.5×10^{-17} to 7.4×10^{-17}

m^2 (*S4.3; exp. 21*). This trend of slight permeability decrease contrasts with porosity creation in both rocks. k decrease was somehow larger in the *S3.4* rock experiment ($\Delta k = 2.9 \times 10^{-16}$ m^2 (*S3.4*) and $\Delta k = 1.1 \times 10^{-17}$ m^2 (*S4.3*)). An explanation of this behavior could be that precipitation of gypsum and a lesser extent of kaolinite and mesolite, together with the remaining Si-bearing minerals, contributed to obstruct the solution circulation through the column. This fact is corroborated by larger gypsum precipitation in the *S3.4* rock experiment (V_{Gp} = 0.008 cm^3 (*S3.4*) and 0.003 cm^3 (*S4.3*)). Also the shape of the precipitated minerals (e.g. gypsum as needles) in the direction perpendicular to the flux can contribute to reduce the final permeability.

3.4 Summary and conclusions

Illite dissolution rates were obtained by conducting flow-through experiments at P_{Total} = 1 bar, $pCO_2 = 10^{-3.5}$ bar and 25 °C at the acidic pH range of 2.15-4.21. The illite dissolution rate decreased with pH such that the obtained pH-rate dependence was similar to that reported by Köhler et al. (2003). Moreover, it was observed that ongoing calcite dissolution was not affecting illite dissolution rates.

Columns filled with crushed Hontomín caprock samples (*S2.4*, *S3.4* and *S4.3*), with an initial porosity of ca. 50%, proved to be useful to investigate the effects that the mineral composition, sulfate content, temperature and pCO_2 exert on the Hontomín caprock reactivity. Overall, calcite dissolution was larger than that of albite, illite, and clinochlore, and precipitation of gypsum was larger than that of kaolinite, mesolite, scolecite and stilbite. Coupled reactions of dissolution and precipitation yielded larger volume of dissolved calcite and Si-bearing minerals (illite, albite and clinochlore) than volume of secondary gypsum and Si-bearing minerals (kaolinite, mesolite, scolecite and stilbite), yielding a porosity increase in all experiments.

Regarding the mineral composition, it was observed that the increase in initial calcite content (67.1 *wt.%* (*S3.4*), 71.2 *wt.%* (*S4.3*) and 87.3 *wt.%* (*S2.4*)) leads to small differences in porosity increase ($\Delta\phi$= 0.36 (*S3.4*), 0.28 (*S4.3*) and 0.34 (*S2.4*)), yet considering that the volume of dissolved calcite was larger with larger calcite content in the rocks (V_{Cal} = 0.053 cm^3 (*S2.4*), 0.048 cm^3 (*S4.3*) and 0.039 cm^3 (*S3.4*)). The small differences in the content of illite, albite and

chlinochlore among the three marl samples barely affect their reactivity, resulting in similar variation of porosity near the inlet and along the column.

Regarding the effect of sulfate content, it was observed that the increase in porosity ($\Delta\phi_{25\,^{o}C}$ = 0.05 (*S2.4*), 0.10 (*S3.4*) and 0.06 (*S4.3*)) was 15-30% lower in the presence of sulfate, and $\Delta\phi$ was slightly varied by the temperature increase ($\Delta\phi_{60\,^{o}C}$ =0.11 (*S2.4*), 0.08 (*S3.4*) and 0.09 (*S4.3*)).

Regarding the temperature effect, it was demonstrated that the volume of dissolved calcite increased by decreasing temperature, whereas the volume of precipitated gypsum was barely influenced by temperature variation. In general, the increase in porosity under any pCO_2 was higher at the lowest temperature. Simulations showed that an increase in temperature reduced creation of porosity near the inlet when pCO_2 increased (e.g., pCO_2 = 10 bar).

Regarding the pCO_2 effect on the Hontomín caprock reactivity, when rising pCO_2, the calcite dissolution rate increased along the column because of the direct pH effect on it. Dissolution of the clinochlore, albite and illite was always minor in acidic pH and is controlled, under atmospheric pressure, by the protons provided by the strong acid (HCl), whereas under high pCO_2, H_2CO_3 partial dissociation controls the dissolution. Modeling results show that if the solution acidity is controlled by a strong acid, dissolution occurs exclusively at the first rock-solution contact, raising the pH at ≈ 7 and limiting the calcite dissolution further away. In contrast, simulations under high pCO_2 conditions show that pH remains acidic (≈ 5) and the solution is permanently undersaturated with respect to calcite, clinochlore, albite, illite and pyrite (due to the carbonic acid buffer capacity), yielding a higher increase in porosity all over the rock-solution contact.

Calculated permeability (k) under CO_2 supercritical conditions slightly decreased in both the bituminous black shale and marl rocks, contrasting with porosity creation. This enhancement could be due to an obstruction of flux circulation through the columns, being generated by precipitation of gypsum and to a lesser extent of kaolinite and mesolite, together with the remaining Si-bearing minerals.

A good match of the output concentrations in solution was obtained using CrunchFlow reactive transport calculations. Rate laws including the values of the rate constants were taken from literature (Table 2.14). The fit of the model to the experimental data was performed by adjusting the values of the reactive surface areas. The calcite reactive surface area values were diminished by one and two orders of magnitude from the initially calculated geometric surface areas. The adjusted values of the reactive surface areas were small probably due to transport control of the reaction. It should be noted that the values for the reactive surface area for calcite ranged from 3 to 6 $m^2_{min}\ m^{-3}_{bulk}$ in the simulations under atmospheric pCO_2, whereas under higher pCO_2 (10-37 bar) the values ranged from 90 $m^2_{min}\ m^{-3}_{bulk}$ to 170 $m^2_{min}\ m^{-3}_{bulk}$. This increase could be associated to higher transport control of the reaction at lower pH at higher pCO_2. A single value for illite (1 $m^2_{min}\ m^{-3}_{bulk} \times 10^7\ m^2_{min}\ m^{-3}_{bulk}$) provided a good fit of the model to all experimental results, supporting the applicability of this modeling approach. For the rest of primary Si-bearing minerals with lower content in the rocks, the range was between $2 \times 10^5\ m^2_{min}\ m^{-3}_{bulk}$ and $3 \times 10^9\ m^2_{min}\ m^{-3}_{bulk}$.

Chapter IV

Interaction between a fractured marl caprock and CO_2-rich sulfate solution under supercritical CO_2 conditions and 2D reactive transport modeling

4.1 Introduction

In this chapter the experimental and modeling results from percolation experiments performed at P_{Total} = 150 bar, pCO_2 = 61 bar and T = 60 °C are presented. The experiments consisted of fractured cores of marl (*S4.3*) through which *S-free* and *S-rich* solutions were injected at different flow rates. The effects that the sulfate content and the flow rate exert on the variation of the hydrodynamic and geochemical evolution of the reacted fractured cores were studied. Fracture permeability was calculated based on the difference between the inlet and outlet pressures. The aqueous chemistry results were obtained from the variation of the chemical composition of the input and output solutions, being measured by ICP-AES. The core samples were examined before and after reaction using XRD, XRF, SEM, XMT and MicroRaman. 2D reactive transport modeling was used to reproduce the variation in the outflow composition with time, quantify the processes and match the observed alteration zones along the fracture.

4.2 Results

The initial mineral composition of the *S4.3* marl rock used to conduct the experiments is described in *Section 2.1.2* (Table 2.1). The percolation experiments, labeled from *exp. 22* to *28*, are listed in Table 4.1. The injected solutions were a sulfate-rich and sulfate-free solutions with different ionic strengths (*S-rich(4) I* = 0.6 M, *S-free(2) I* = 0.6 M and *S-free(1) I* = 0.3 M) and likewise are described in *Section 2.1.3* (Table 2.6). As mentioned before, these experiments were carried out in the ICARE Lab CSS I and the ICARE Lab CSS II apparatus depending of the flow rate used. Only one experiment with *S-free(2) I* = 0.6 M injected solution was executed in order to compare with the *S-free(1) I* = 0.3 M injected solution at the same flow rate (1 mL h^{-1}) to examine the ionic strength effect. Three experiments using the same injected solution (*S-rich(4) I* = 0.6 M and *S-free(1) I* = 0.3 M) were conducted at different flow rates (0.2, 1 and 60 mL h^{-1}).

4.2.1 Experimental results

The initial fracture permeability ($k_{f\text{-initial}}$) was calculated according to Eq. (2.43) (*Section 2.2.4*) based on the initial fracture aperture. In *exp. 26*, fracture permeability could not be measured because ΔP was lower than the measurable one in the used equipment. In this case, the fracture

aperture was estimated from the ESEM image of the fractured core. Experimental duration (t) varied from 6 to 70 h (Table 4.1). The residence time (τ) was calculated for each experiment using Eq. (2.26) since each experiment involved a sample with slightly different dimensions. Table 4.1 shows the experimental conditions in the percolation experiments.

Table 4.1 Experimental conditions of the experiments. *S-rich* experiments in bold.

exp.	Injected solutions	Q [mL h^{-1}]	t [h]	$h_{initial}$ [m]	τ [s]	$k_{f\text{-initial}}$ [m^2]
22	*S-free I* = 0.3	0.2	43	3.2×10^{-6}	10.0	8.8×10^{-13}
23	*S-free I* = 0.3	1	21	3.5×10^{-6}	2.0	1.0×10^{-12}
24	*S-free I* = 0.3	60	6	1.4×10^{-5}	0.1	1.7×10^{-11}
25	*S-free I* = 0.6	1	23	4.1×10^{-6}*	2.0	-
26	***S-rich I* = 0.6**	**0.2**	**35**	$\mathbf{3.8 \times 10^{-6}}$	**12.0**	$\mathbf{1.2 \times 10^{-12}}$
27	***S-rich I* = 0.6**	**1**	**70**	$\mathbf{1.6 \times 10^{-5}}$	**10.0**	$\mathbf{2.2 \times 10^{-11}}$
28	***S-rich I* = 0.6**	**60**	**7**	$\mathbf{1.6 \times 10^{-5}}$	**0.1**	$\mathbf{2.2 \times 10^{-11}}$

t experimental duration.
$h_{initial}$ and $k_{f\text{-initial}}$ stand for initial fracture aperture and fracture permeability, respectively.
τ residence time.
*Permeability could not be measured. Aperture estimated from the ESEM image.

4.2.1.1 *Dissolution and precipitation processes*

4.2.1.1.1 Output concentrations

Figs. 4.1 shows the variations in the aqueous chemistry with time in the sulfate-free (I = 0.3 and 0.6 M) and sulfate-rich (I = 0.6 M) experiments. ΔC_j accounts for the difference between the output and the input concentrations of element j ($\Delta C_j = C_{j(out)} - C_{j(in)}$). The error associated with ΔC_j ($\varepsilon(\Delta C_j)$) was estimated using the Gaussian error propagation method (*Chapter II Section 2.2.3*), and, as mentioned before, with an estimated uncertainty in the measured concentrations of 3% (ICP-AES). $\varepsilon(\Delta C_j)$ ranged from 10 to 40 % for Ca and was around 3% for S, Fe and Si.

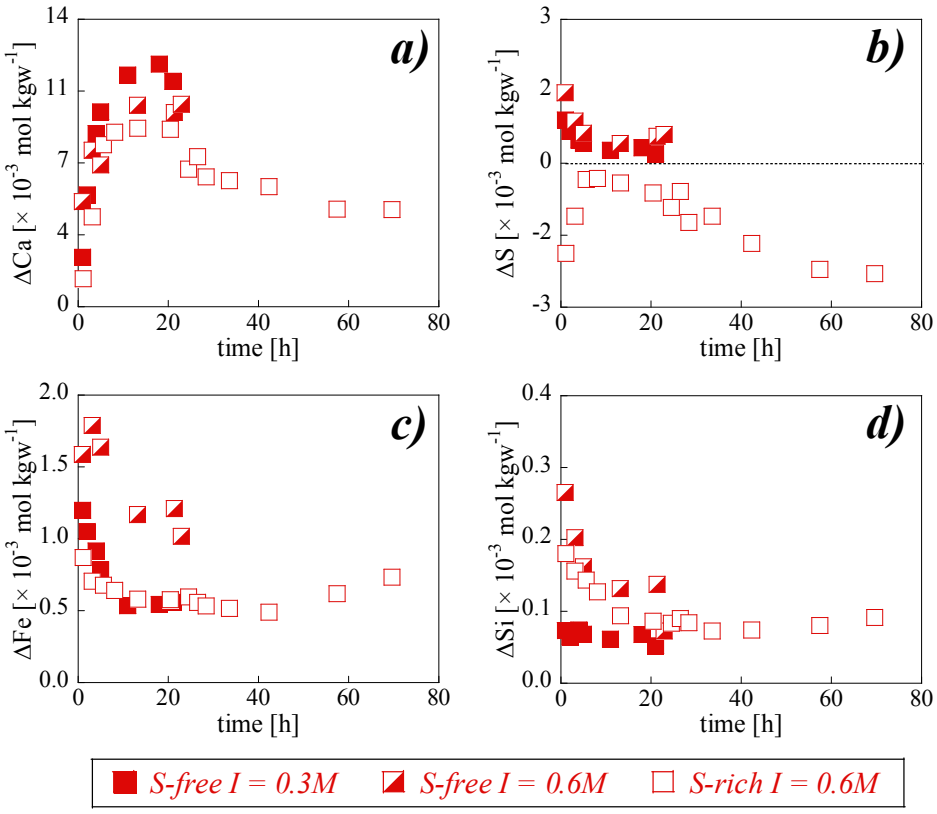

Figure 4.1 *Variation of the increment in the output S-free and S-rich solutions concentration vs. time in three experiments at 1 mL h^{-1} with S-free injected solutions (I = 0.3 and 0.6 M; exp. 23 and 25, respectively) and with S-rich injected solution (I = 0.6 M; exp. 27): (a) ΔCa, (b) ΔS, (c) ΔFe and (d) ΔSi.*

In *S-free* experiments and ionic strength of 0.3 and 0.6 M (*exps. 23 and 25*; *Chapter II* Table 2.3), similar temporal variations in the Ca concentration, as well as very small changes in the S, Si and Fe output concentrations, were observed (Fig. 4.1). Slight differences in concentrations can be attributed to different distributions of the primary iron- and silicon-bearing minerals (quartz, pyrite, illite, clinochlore and albite) along the fractures. The results suggest that in the *I* range of 0.3-0.6, the ionic strength effect on the mineral dissolution rates was negligible. This is in agreement with the small or negligible effect of ionic strength on gypsum and illite dissolution rates reported by Raines and Dewers (1997) and Bibi et al. (2011).

The excess of Ca concentration was attributed to calcite dissolution (Fig. 4.1a). All input solutions were strongly undersaturated with respect to calcite. The calculated input pH was 3.23 ± 0.03

(*Chapter II*; *Section 2.1.3*, Table 2.6). Fig. 4.1b shows ΔS variation with time. Dissolution of both gypsum and pyrite was expected in the *S-free* solution experiments (*Chapter II Section 2.1.3*Table 2.6). However, since the pyrite dissolution rate (ca. 10^{-10} mol m^{-2} s^{-1} in acidic pH from 3 to 5 and O_2 concentration of 3×10^{-4} mol L^{-1}; Domènech et al., 2002) was approximately six to seven orders of magnitude slower than that of gypsum (10^{-3} mol m^{-2} s^{-1}; Palandri and Kharaka, 2004), it was assumed that most of the released S was from gypsum dissolution. As the gypsum dissolution rate was not affected by dissolved CO_2 (Jeschke et al., 2001) nor by pH, the ΔS decrease was probably caused by a decrease in the gypsum reactive surface area as gypsum dissolved (Fig. 4.1b). In the *S-rich* solution experiment the solution was in equilibrium with gypsum (Table 2.6). The early negative ΔS values indicated precipitation of a S-bearing phase (Fig. 4.1b). MicroRaman spectra of the reacted solid samples (*exp. 27*; Fig. 4.2) showed that the precipitated S-bearing phase was gypsum, ruling out anhydrite precipitation. This observation is in accordance with precipitation of gypsum in limestone column experiments that were run under the same *P*, *T* and pCO_2 conditions (Singurindy and Berkowitz, 2005; Garcia-Rios et al., 2014).

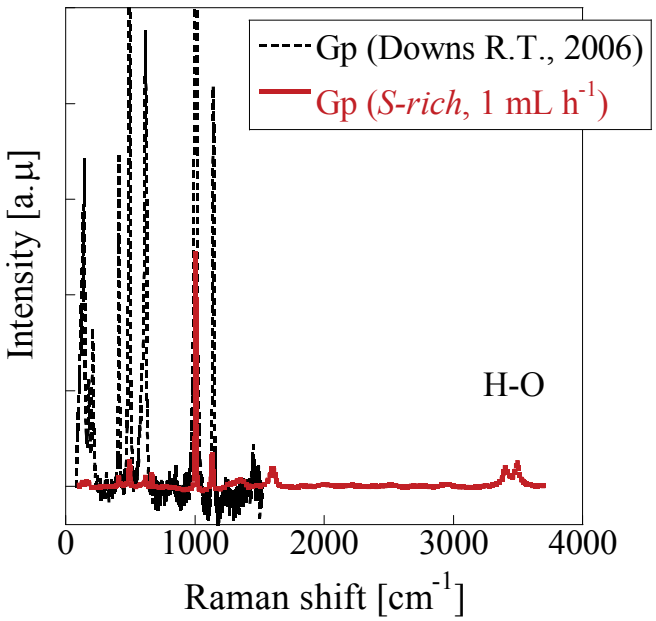

Figure 4.2 *MicroRaman spectrum (black solid line) of a thin section prepared from exp. 27 (S-rich solution, Q = 1 mL h^{-1}) showing the presence of gypsum. The dashed line shows the gypsum spectrum acquired from the RRUFF database (Downs, 2006).*

The ΔFe and ΔSi concentrations tended to decrease with time in the two experiments (*S-free* and *S-rich* solutions; Figs. 4.1c,d). It was assumed that the Fe was mainly released from clinochlore dissolution. Although the pyrite dissolution rate is much faster than that of clinochlore (1-6 × 10^{-12} mol m^{-2} s^{-1} at pH of 3.2-5; Lowson et al., 2007), the content of pyrite was one orders of magnitude smaller than that of clinochlore, resulting in a small pyrite reactive surface area that limited its dissolution. As for the Si concentration (Figs. 4.1d), since the injected solution was undersaturated with respect to illite, chlinochlore, albite and quartz, dissolution of the aluminosilicates and quartz could take place (*Chapter II Section 2.1.3;* Table 2.6). However, illite dissolution was unexpected or regarded as negligible because at pH of 3, the illite rate constant (3 × 10^{-14} mol m^{-2} s^{-1}; Köhler et al., 2003) was two orders of magnitude smaller than those of clinochlore (7 × 10^{-12} mol m^{-2} s^{-1}; Lowson et al., 2007) and albite (8 × 10^{-12} mol m^{-2} s^{-1}; Chou and Wollast, 1985). Given that the quartz dissolution rate constant (≈3 × 10^{-13} mol m^{-2} s^{-1} at pH= 3.2; Bandstra et al., 2008) was also lower than those of chlinochlore and albite, Si was likely released from chlinochlore and albite. Accordingly, quartz, illite and pyrite dissolutions were omitted from the following mass balance calculation.

ΔSi was about one order of magnitude lower than ΔFe in all experiments. The aqueous Si/Fe ratio was around 0.1, which based on the clinochlore stoichiometric ratio (Si/Fe = 1.4; Figs. 4.1c,d), indicated a Si deficit. Moreover, since albite dissolution would increase the aqueous Si/Fe ratio, it was assumed that some Si-bearing minerals could precipitate during the experiments. However, kaolinite precipitation was observed in reported experiments where sandstone rocks interacted with CO_2-rich brines (Ketzer et al., 2009; Luquot et al., 2012; Yu et al., 2012; Tutolo et al., 2015). In the current study, the calculated *SI* values of the output solutions indicated undersaturation with respect to kaolinite, smectite and muscovite. In fact, this was expected since the measured Al concentrations were always low (close to the ICP-AES detection limit (≈1.85 × 10^{-6} mol L^{-1})) probably because of precipitation of Al-bearing phases.

Although precipitation of kaolinite in the low-porosity rock matrix must not be ruled out, inspection of the thin sections of the reacted samples with ESEM and microRaman spectroscopy showed no presence of kaolinite. Note that, as shown below, the volume of precipitated kaolinite associated with the Si deficit along the fracture would be ~1 mm^3, making kaolinite detection

difficult. At this point, it is important to highlight that the observed Si deficit could also be associated with precipitation of less crystallized SiO_2 (amorphous silica gel).

Variations in the Na, K and Mg concentrations could not be determined because the small differences between the large input and output concentrations were within analytical error.

4.2.1.1.2 Influence of the flow rate

On the basis of the reactions described in *Section 2.2.3* (dissolution of calcite, clinochlore and albite and precipitation of gypsum) and on the assumption that kaolinite precipitation took place, $C_{j(diss)}$ and $C_{j(ppt)}$ were calculated from the following mass balance equations (Eq. (2.28-2.32)).

The effect of the flow rate on the chemical processes was deduced from the variation in aqueous chemistry as a function of the number of equivalent water fracture volumes ($V_f = t/\tau$) that circulated through the fracture. V_f was defined as the ratio between the experimental duration (t) and the residence time (τ, where $\tau = V_{f\text{-}initial}/Q$; Table 4.1). V_f increased by increasing Q for the same duration of the experiment. Figs. 4.3 and 4.4 compare the variations in ΔCa, ΔS, ΔFe and ΔSi between experiments with *S-free* and *S-rich* injected solutions with different flow rates (0.2, 1 and 60 mL h^{-1}).

In the *S-free* experiments, Ca released from calcite dissolution at Q = 60 mL h^{-1} was similar to those in the experiments run with slow flow rates (Fig. 4.3a). At 60 mL h^{-1}, ΔCa was lower and, in this case, it reached steady state before the end of the experiment. Under slow flow rate conditions, R_{Cal} increased by speeding up the flow rate (4.4×10^{-10} mol s^{-1} at 0.2 mL h^{-1} and 1.6×10^{-9} mol s^{-1} at 1 mL h^{-1}, Table 4.2). At the highest flow rate (60 mL h^{-1}), the calcite dissolution rate (9.1×10^{-8} mol s^{-1}; Table 4.2) was one order of magnitude higher than that at 1 mL h^{-1}. ΔS was only measured in the experiments at 0.2 and 1 mL h^{-1} (Table 4.2), and the increase in the flow rate favored early gypsum dissolution (Fig. 4.3b).

In *S-rich* experiments, ΔCa was higher in the experiments run under slow flow rate conditions and nearly zero at the fastest flow rate (Fig. 4.4a). Reproducibility of the experimental results was verified by performing the 60 mL h^{-1} experiment twice. The short residence time of the solution

prevented the Ca concentration from increasing. ΔS was negative in the experiments run under slow flow rates (Fig. 4.4b). Likewise, at 60 mL h^{-1}, the short residence time of the solution prevented the S concentration from decreasing (Fig. 4.4b).

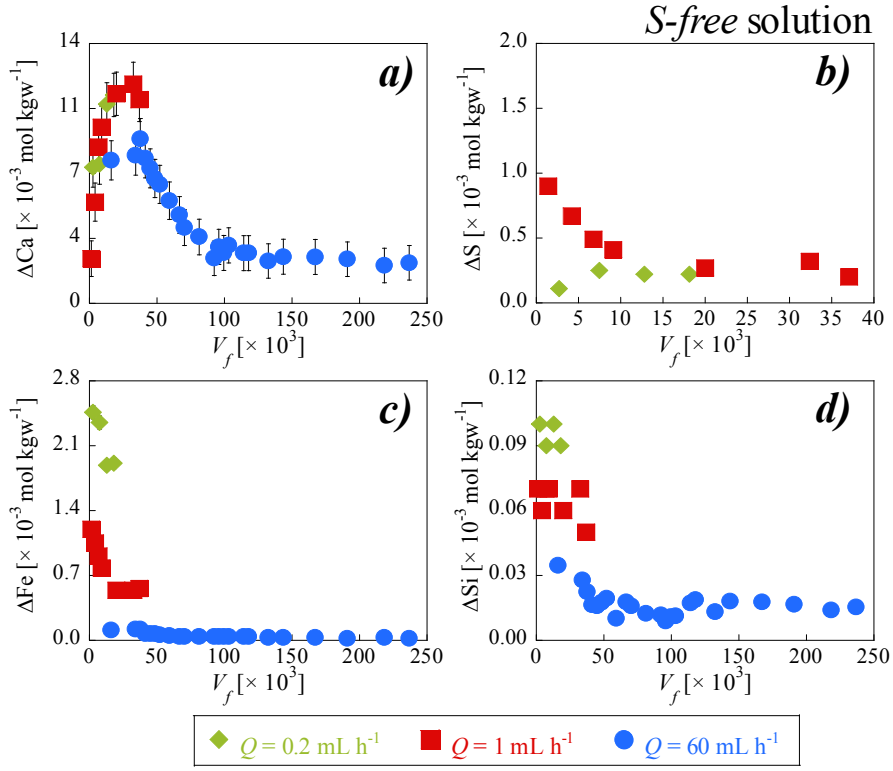

Figure 4.3 *Variation of solution composition with number of equivalent water fracture volumes (V_f) under different flow rates [Q (mL h^{-1}) = 0.2 (exp. 1), 1 (exp. 3) and 60 (exp. 6)] in S-free injected solution (I = 0.3 M): (a) ΔCa, (b) ΔS, (c) ΔFe and (d) ΔSi. pCO_2 = 61 bar, T = 60 °C.*

Like *S-free* solution experiments, under slow flow rate conditions, calcite dissolution rate increased by speeding up the flow rate (from 2.3 × 10^{-10} mol s^{-1} at 0.2 mL h^{-1} to 1.6 × 10^{-9} mol s^{-1} at 1 mL h^{-1}, Table 4.2). At 60 mL h^{-1}, calcite dissolution rate (8.3 × 10^{-9} mol s^{-1}) was about one order of magnitude higher than that at 1 mL h^{-1}. Therefore, regardless of the composition of the injected solution, an increase in the flow rate led to an increase in the calcite dissolution rate, which was, a factor of two higher in *S-free* than in *S-rich* solutions. Slower calcite dissolution rates in the presence of sulfate could be favored by the formation of gypsum coatings on the surface of calcite grains, promoting calcite passivation (Offeddu et al., 2014).

Regarding Fe and Si concentrations, in the two types of injected solution, an increase in flow rate resulted in a decrease in ΔFe and ΔSi (Figs. 4.3c,d and 4.4c,d), and steady state was achieved in the experiment under the highest flow rate.

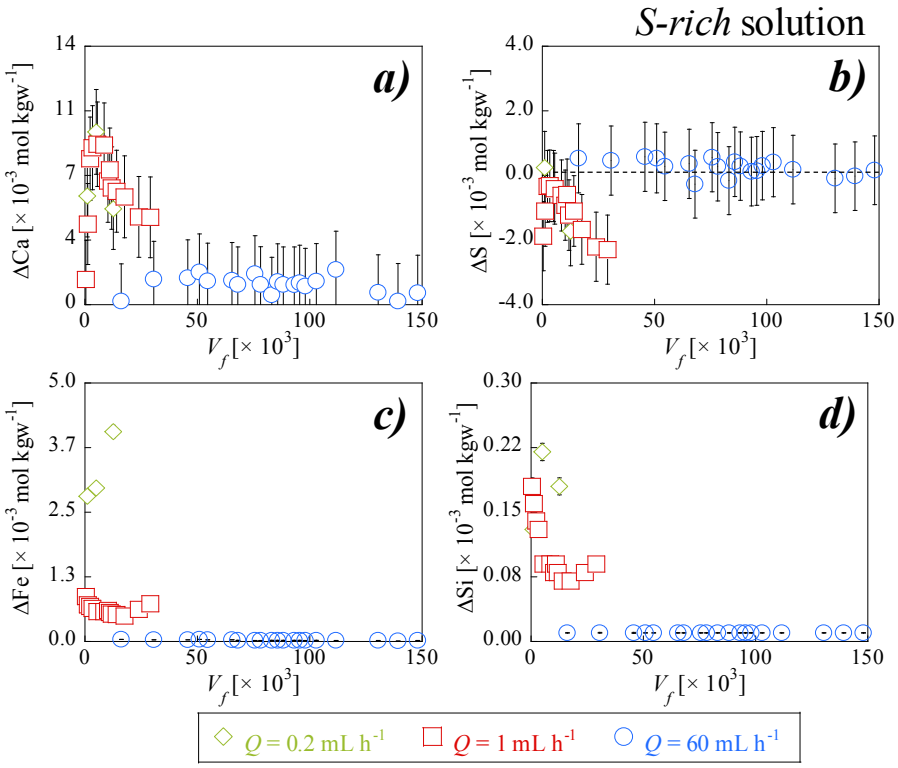

Figure 4.4 *Variation of solution composition with number of equivalent water fracture volumes (V_f) under different flow rates [Q (mL h^{-1}) = 0.2 (exp. 2), 1 (exp. 4) and 60 (exp. 7)] in S-rich injected solution (I = 0.6 M): (a) ΔCa, (b) ΔS, (c) ΔFe and (d) ΔSi. pCO_2 = 61 bar, T = 60 °C. Horizontal lines indicate zero increase in concentration.*

The effect of the flow rate on the chemical processes was also deduced from the variation in the calculated volumes of dissolved and precipitated minerals ($V_{min\text{-}diss}$ and $V_{min\text{-}ppt}$) as described in *Section 2.2.3* (Eq. (2.36)).

As mentioned above, the measured Al concentrations were always close to the detection limit (≈1.85 × 10^{-6} mol L^{-1}), preventing the calculation of the amount of dissolved albite and consequently the amount of precipitated kaolinite. Therefore, two mass balance calculations were

performed in order to estimate the volumes of dissolved albite and precipitated kaolinite: in the first calculation, albite dissolution was not considered (Si was only released from clinochore dissolution), whereas in the second calculation, equal dissolution of albite and clinochlore was assumed. In the former case, Si was only released from clinochore dissolution, and in the latter, Si was released from both minerals. Comparing the results in both cases, it was observed that inclusion of albite dissolution in the calculation barely affected the final volume associated with the reacted fracture. This resulted from the low albite content (< 6 %).

In *S-free* solution experiments, the volume of dissolved calcite ($V_{Cal\text{-}diss}$) increased with flow rate (Table 4.2) as did the volume of dissolved gypsum ($V_{Gp\text{-}diss}$). Note that S concentration was not measured in the experiment performed at the highest flow rate (Fig. 4.3b). The volumes of dissolved clinochlore ($V_{Cln\text{-}diss}$) and albite ($V_{Ab\text{-}diss}$) and precipitated kaolinite ($V_{Kln\text{-}ppt}$) were almost the same under all flow rates. In *S-rich* solution experiments under slow flow rate conditions (0.2-1 mL h^{-1}), $V_{Cal\text{-}diss}$ and $V_{Gp\text{-}ppt}$ increased by speeding up the flow rate (Table 4.2), and the $V_{Cal\text{-}diss}/V_{Gp\text{-}ppt}$ ratio was always greater than one (Table 4.2), indicating dominancy of calcite dissolution over gypsum precipitation. At 60 mL h^{-1}, although $V_{Cal\text{-}diss}$ and $V_{Gp\text{-}ppt}$ were of the same order of magnitude as those at 1 mL h^{-1}, $V_{Gp\text{-}ppt} > V_{Cal\text{-}diss}$, yielding a slightly lower $V_{Cal\text{-}diss}/V_{Gp\text{-}ppt}$ ratio. $V_{Gp\text{-}ppt}$ tended to increase with the flow rate. $V_{Cln\text{-}diss}$, $V_{Ab\text{-}diss}$ and $V_{Kln\text{-}ppt}$ were almost the same at low flow rates but slightly lower at 60 mL h^{-1}.

Thus, based on the variation in the calculated volumes of dissolved and precipitated minerals and type of solution, it was observed that: *(1)* $V_{Cal\text{-}diss}$ tended to increase with flow rate regardless of the injected solution, except at 60 mL h^{-1} in the *S-rich* solution experiment; *(2)* $V_{Cln\text{-}diss}$ and $V_{Ab\text{-}diss}$ in *S-rich* solution were larger than those in *S-free* solution at 0.2 and 1 mL h^{-1} experiments, but not at 60 mL h^{-1} (Table 4.2); *(3)* as for $V_{Cln\text{-}diss}$ and $V_{Ab\text{-}diss}$, $V_{Kln\text{-}ppt}$ in *S-rich* solution was greater than that in *S-free* solution at 0.2 and 1 mL h^{-1}, showing an opposite trend at 60 mL h^{-1}. In all cases, regardless of the solution, the final pore volume associated with the reacted core (volume of the final fracture plus volume of pores in the altered zone along the fracture wall), calculated as $V_{f\text{-}final} = V_{f\text{-}initial} + V_{Cal\text{-}diss} + V_{Gp\text{-}diss} + V_{Cln\text{-}diss} + V_{Ab\text{-}diss} - V_{Gp\text{-}ppt} - V_{Kln\text{-}ppt}$, was always larger than the initial fracture volume ($V_{f\text{-}initial}$), even if gypsum precipitated in the *S-rich* solution experiments (Table 4.2).

Table 4.2 Volume of initial fracture, volumes of dissolved calcite, gypsum, clinochlore and albite, volumes of precipitated kaolinite and gypsum, final volume of the fracture plus altered zone (pores), Cal-diss/Gp-ppt volume ratio, and calcite dissolution rate in mol s^{-1}. *S-rich* experiments in bold.

exp.	injected solution	Q [mL h^{-1}]	t [h]	$V_{Cal\text{-}diss}$ [mm^3]	$\varepsilon V_{Cal\text{-}dis}$ (%)	$V_{Gp\text{-}diss}$ or $V_{Gp\text{-}ppt}$ [mm^3]	$\varepsilon V_{Gp\text{-}diss}$ or $V_{Gp\text{-}ppt}$ (%)	$V_{Cln\text{-}diss}$ [mm^3]	$V_{Ab\text{-}diss}$ [mm^3]	$V_{Kln\text{-}ppt}$ [mm^3]	$\varepsilon V_{Cln\text{-}diss}$, $V_{Ab\text{-}diss}$ and $V_{Kln\text{-}ppt}$ (%)	$V_{f\text{-}initial}$ [mm^3]	$V_{diss\text{-}tot}$ [mm^3]	$V_{ppt\text{-}tot}$ [mm^3]	$V_{f\text{-}final}$ [mm^3]	$V_{Cal\text{-}diss}$/ $V_{Gp\text{-}ppt}$	R_{Cal} [mol s^{-1}]
22	*S-free*	0.2	43	3.1	3	0.1	1	2.3	0-1.1	1.5-3.0*	1	0.6	5.4-6.4	1.6-3.2*	3.5-4.0	-	4.4×10^{-10}
23	*S-free*	1	21	7.3	2	0.6	1	1.5	0-0.7	1.0-2.0*	1	0.6	8.8-9.5	1.6-2.6*	8.2-9.1	-	1.6×10^{-9}
24	*S-free*	60	7	45.8	2	-	-	2.0	0-0.9	1.0-2.3	1	2.4	47.8-48.7	19.0-20.3*	48.8-46.8	-	9.1×10^{-8}
26	***S-rich***	**0.2**	**35**	**2.8**	**10**	**0.4***	**39**	**3.3**	**0-1.5**	**2.1-4.3***	**2**	**0.7**	**6.1-7.6**	**1.5-2.7***	**3.6-4.4**	**7.2**	$\mathbf{2.3 \times 10^{-10}}$
27	***S-rich***	**1**	**70**	**20.3**	**2**	**7.2***	**9**	**4.5**	**0-2.1**	**2.7-5.7***	**1**	**2.8**	**24.9-26.9**	**9.9-12.9***	**14.0-15.0**	**2.8**	$\mathbf{1.6 \times 10^{-9}}$
28	***S-rich***	**60**	**7**	**9.1**	**12**	**14.0***	**32**	**1.2**	**0-0.5**	**0.6-1.4***	**1**	**2.7**	**10.3-10.8**	**14.6-15.4***	**12.1-13.4**	**0.7**	$\mathbf{8.3 \times 10^{-9}}$

t: experimental time; diss: dissolved mineral; ppt: precipitated mineral.
Cal: calcite, Gp: gypsum, Cln: clinochlore, Ab: albite, Kln: kaolinite
$V_{f\text{-}initial}$: initial fracture volume, $V_{f\text{-}final}$: final fracture volume and R_{Cal}: calcite dissolution rate.
* indicates mineral precipitation.

4.2.1.2 *Alteration of the rock*

In the two *S-free* and *S-rich* solutions, a porous zone with a width (distance normal to fracture) up to ≈ 300 μm formed along the fracture walls during the experiments (Fig. 4.5). This was the result of significant calcite dissolution, and to a lesser extent, dissolution of clinochlore and albite (Fig. 4.6). The partially dissolved silicate grains and non-dissolved grains of quartz, pyrite and illite were still visible in the altered zone (Fig. 4.5a-d). The initial increase in ΔCa with time depicted in Figs. 4.3a and 4.4a indicated that calcite dissolution was favored by a high reactive surface area of the calcite grains. As calcite dissolution progressed, the calcite reactive surface area close to the fracture diminished, leading to a decrease in ΔCa until steady state was achieved. Diffusion through the remaining porous matrix of the altered zone limited further calcite dissolution (transport control of the reaction; see *exps. 24 and 27* in Figs. 4.3a and 4.4a).

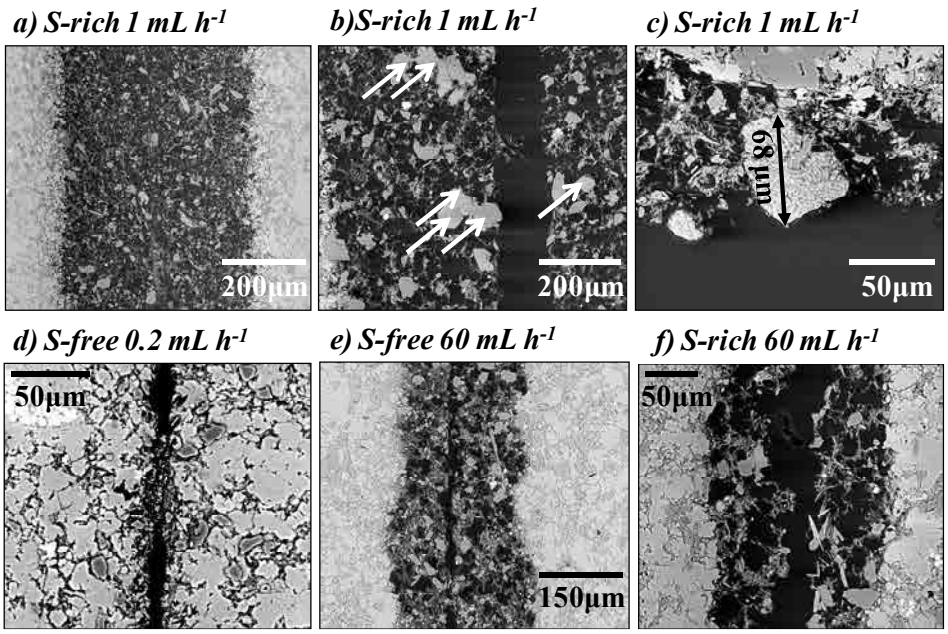

Figure 4.5 *ESEM images of several regions of the thin sections of the cores run in S-free and S-rich solution experiments under different flow rates. Top row: exp. 27; a) fracture alteration at 8 mm from the inlet, b) gypsum precipitation (indicated by arrows) and alteration at 12 mm from the inlet and c) gypsum precipitate at 15 mm from the inlet. Bottom row: d) fracture clogging (exp. 22); e) altered zone along the fracture wall (exp. 24) and f) altered zone along the fracture wall (exp. 28).*

In the experiments where the Ca concentration reached steady state (*exps. 24 and 27*), a penetration length (x) corresponding to the zone next to the fracture affected by calcite dissolution was calculated using Eq. (2.39) described in *Chapter II Section 2.2.2*. Comparison of the calculated and measured (ESEM and XMT) penetration lengths was made in the two experiments. In the *S-free* solution *exp. 24* (60 mL h^{-1}), x was 249 μm, which was only 11% smaller than the measured one (280 μm; Fig. 4.7a,b). In the *S-rich* solution *exp. 27* (1 mL h^{-1}), x was 176 μm, which was only 1% smaller than the observed one (180 μm; Fig. 4.7c).

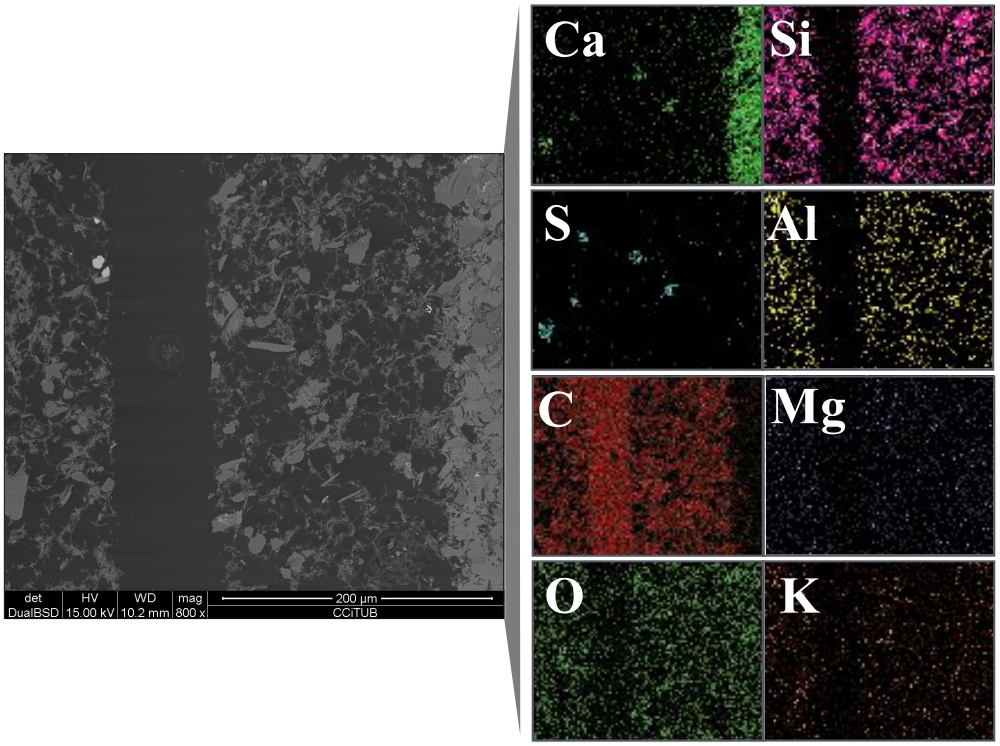

Figure 4.6 *Spot from the ESEM image showing the altered zone and elements (EDS maps) present in exp. 27.*

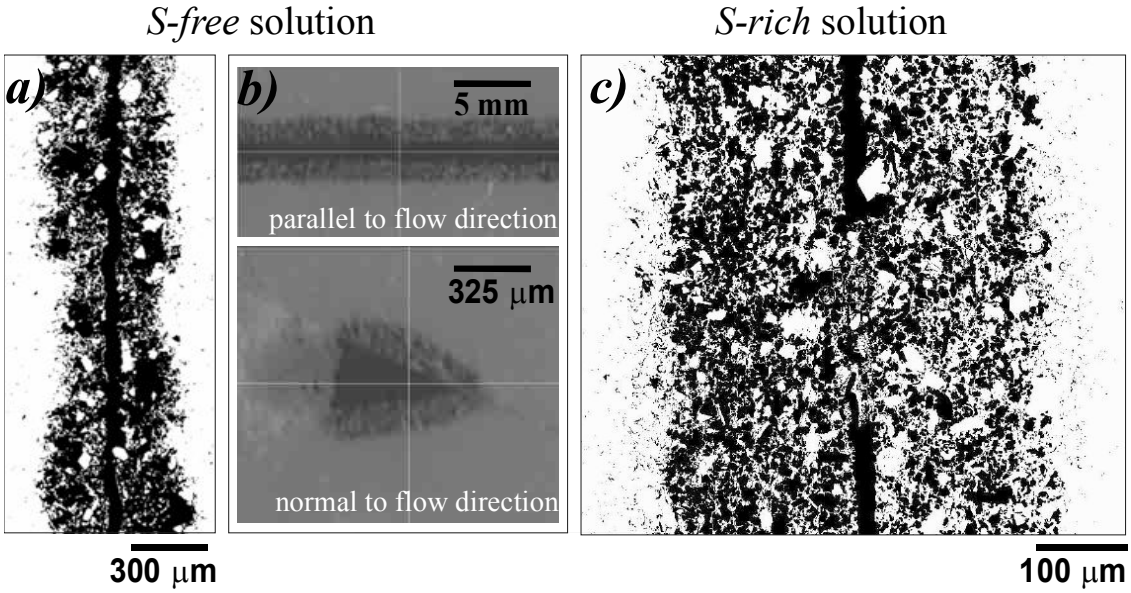

Figure 4.7 *Processed images: a) ESEM image and b) XMT image showing the altered zone along the fracture; the black background corresponds to pore space. c) ESEM image showing the altered zone from where the pore space volume was calculated.*

Apparent diffusion coefficients (D_a, $m^2\ s^{-1}$) at 60 °C were obtained in the experiments where the output Ca concentration reached steady state (*exp. 24*: *S-free* solution and 60 mL h^{-1} and *exp. 27*: *S-rich* and 1 mL h^{-1}; Figs. 4.3a and 4.4a). D_a values were calculated according to Eq. (2.40) (*Section 2.2.3*). By plotting x^2 as a function of time, D_a was calculated from the slope ($2D_a$) of the linear regression to be 2×10^{-12} $m^2\ s^{-1}$ (*exp. 24*; $R^2 = 0.999$) and 1×10^{-13} $m^2\ s^{-1}$ (*exp. 27*; $R^2 = 0.975$). One fact that could contribute to the obtainment of a larger D_a in the *S-free* solution (*exp. 24*) was a possible increase in tortuosity generated by gypsum precipitation.

The increase in porosity over the reacted zone was estimated in two ways: *(1)* from a specific region of the fracture by ESEM and XMT images (ϕ_{ESEM} and ϕ_{XMT}) and *(2)* from the calculated volumes of dissolved and precipitated minerals of the core, expressed as $\phi_{VOL} = ((V_{Cal\text{-}diss} + V_{Gp\text{-}diss} + V_{Cln\text{-}diss} + V_{Ab\text{-}diss} - V_{Gp\text{-}ppt} - V_{Kln\text{-}ppt})/V_{total\text{-}cal}) + \phi_i$, where $V_{total\text{-}cal}$ is the volume of calcite if the core was composed of 100 % of calcite. In *exp. 24* (*S-free* solution), ϕ_{ESEM}, ϕ_{XMT} and ϕ_{VOL} were 65%, 48% and 67%, respectively. The difference between ϕ_{ESEM} and ϕ_{XMT} was attributed to the inherent lower resolution of the XMT images (7.5 μm $pixel^{-1}$) compared with the ESEM (1 μm $pixel^{-1}$).

Therefore, porosity in the reacted zone increased from 7 % to ≈ 65 %, which was similar to the volumetric fraction of calcite in the marl (≈ 66 %). Dissolution of the calcite grains played a major role in the increase in porosity. In *exp. 27* (*S-rich* solution), the porosity was only calculated from the ESEM image and volume variation. $\phi_{ESEM} = \phi_{VOL} = \approx 56$ %, which was much larger than the initial value, but smaller than 65%. In this case, secondary gypsum contributed to a smaller increase.

4.2.1.3 *Dissolution patterns*

The adimensional Peclet number relates the diffusive and advective characteristic time scales ($Pe = h \cdot v / D_o$, where h is the fracture aperture (m), v is the linear velocity (m s^{-1}), and D_o is the molecular diffusion coefficient of the solutes). To evaluate the role of solute transport in the mineral dissolution and precipitation processes along the fracture, the *Pe* values of the experiments were calculated considering that D_o at 60 °C was 2×10^{-9} m^2 s^{-1} (Samson et al., 2003), fracture apertures ranged from 3 to 10 μm and flow rates were 0.2, 1 and 60 mL h^{-1} (Table 4.3). Since the three obtained *Pe* values (4, 21 and 1267) were > 1, solute transport in the fracture was controlled by advection in all experiments (e.g., Detwiler et al., 2000), regardless of the composition of the solutions.

Table 4.3 Variation of the calculated fracture permeability and *Pe* number. *S-rich* experiments in bold.

exp.	Q [mL h^{-1}]	*Pe*	$h_{initial}$ [m]	$k_{f\text{-initial}}$ [m^2]	$k_{f\text{-final}}$ [m^2]	$k_{f\text{-final}}/k_{f\text{-initial}}$
22	0.2	4	3.2×10^{-6}	0.9×10^{-12}	0.7×10^{-12}	0.7
23	**0.2**	**4**	$\mathbf{3.8 \times 10^{-6}}$	$\mathbf{1.2 \times 10^{-12}}$	$\mathbf{0.04 \times 10^{-12}}$	**0.03**
24	1	21	3.5×10^{-6}	1.0×10^{-12}	0.8×10^{-12}	0.8
25	**1**	**21**	$\mathbf{1.6 \times 10^{-5}}$	$\mathbf{22.0 \times 10^{-12}}$	$\mathbf{0.2 \times 10^{-12}}$	**0.07**
26	60	1267	1.4×10^{-5}	17.0×10^{-12}	21.0×10^{-12}	1.2
27	**60**	**1267**	$\mathbf{1.6 \times 10^{-5}}$	$\mathbf{22.0 \times 10^{-12}}$	$\mathbf{84.0 \times 10^{-12}}$	**3.8**

$h_{fracture}$ stands for fracture aperture.

Earlier studies showed a certain correlation between distinct dissolution patterns in fractured cores and *Pe* numbers (Detwiler et al., 2003; Szymczak and Ladd, 2009; Elkhourly et al., 2013; Garcia-Rios et al., 2015). Elkhourly et al. (2013) showed that at low *Pe*, development of dissolution instabilities in fractured vuggy limestone cores led to face dissolution, intermediate *Pe* gave rise to large-scale channels, and a high *Pe* regime led to uniform dissolution along the fracture.

The respective ESEM and XMT images of the thin sections parallel and perpendicular to the flow direction (Figs. 4.8), taken at different positions along the fracture (Fig. 4.9), show the geometry of the dissolution patterns throughout the experiments. In *S-free* solution experiments, while fracture dissolution at 0.2 mL h^{-1} took place only near the inlet (Fig. 4.8a), larger dissolved region formed at 1 mL h^{-1} along the fracture (Fig. 4.8b). Therefore, face dissolution was observed at low *Pe* values (4 and 21). At the highest flow rate (60 mL h^{-1}) and high *Pe* (1267), dissolution occurred all along the entire fracture (Fig. 4.8c), resulting in a wormhole that probably originated from an existing local heterogeneity in the fracture (Figs. 4.8c and 4.9a).

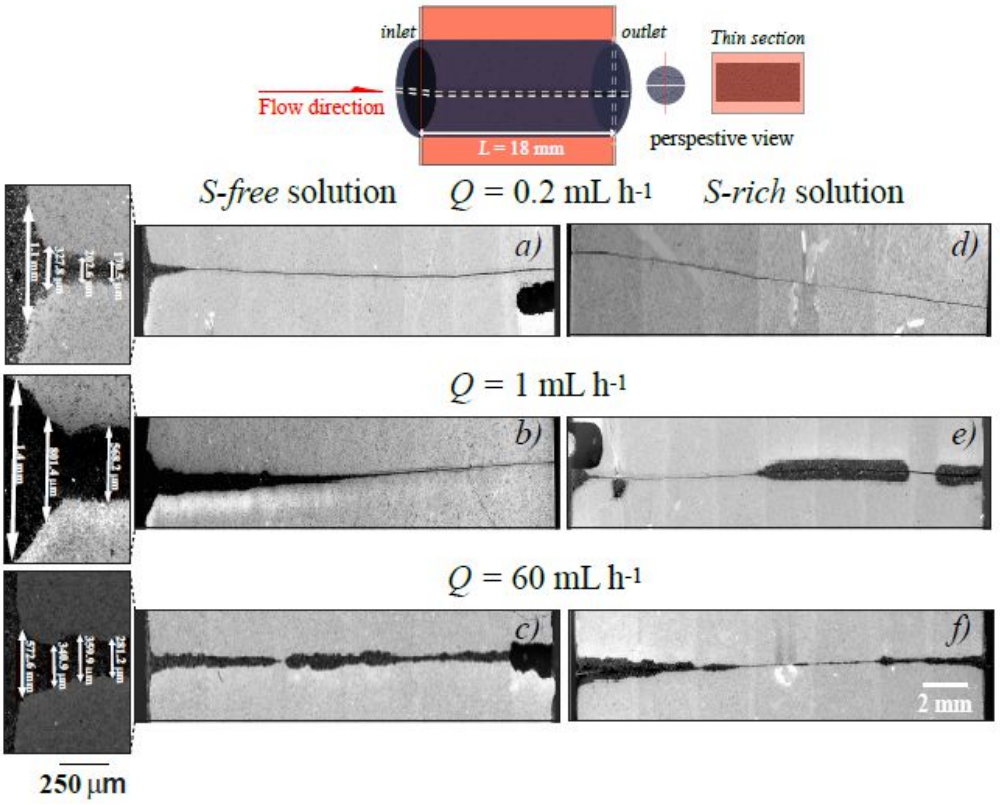

Figure 4.8 *ESEM images of thin sections parallel to flow direction of samples run under different flow rates: with S-free injected solution (a, b, c) and with S-rich injected solution (d, e, f). Note that the thin sections of b), c) and f) were cut through the most altered zone, shown by the arrows in Fig. 4.9.*

In the *S-rich* solution experiments, at the lowest *Pe*, face dissolution initiated near the inlet (Fig. 4.8d). At *Pe* = 21, uniform dissolution developed in the first 16 mm of the fracture (Figs. 4.8e and 4.9b). From this point to the outlet, a combination of wormhole and uniform dissolution occurred

(Figs. 4.8e and 4.9b). For *Pe* = 1267, uniform dissolution predominated all along the fracture (Figs. 4.8f and 4.9c).

The result show that, as predicted by Elkhourly et al. (2013) and observed by Garcia-Rios et al. (2015), a *Pe* increase resulted in an evolution of the dissolution pattern from face dissolution to wormhole formation and finally uniform dissolution. Nonetheless, it is important to highlight that local heterogeneities may control the overall dissolution pattern along the fractures, altering the predictions based on *Pe*.

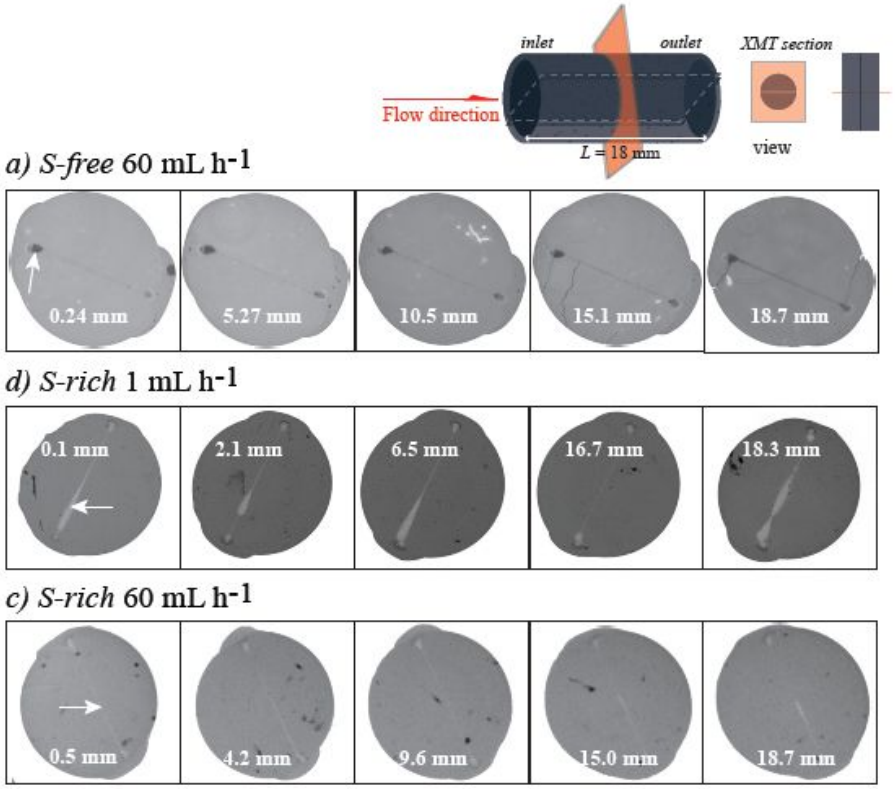

Figure 4.9 *XMT images normal to the flow direction showing the evolution of the dissolution pathways along the core length a) S-free (exp. 24), b) S-rich (exp. 27) and c) S-rich (exp. 28). The arrows indicate the altered zone where the thin sections were made (Fig. 4.8).*

4.2.1.4 *Fracture permeability*

Table 4.3 lists the calculated values of the initial fracture permeability ($k_{f\text{-}initial}$) of the fractures that ranged from 0.9×10^{-12} to 22×10^{-12} m^2 (see *Section 2.2.4;* Eq. (2.43)). Variations in fracture

permeability with time are depicted in Fig. 4.10. In the *S-free* solution experiments, final fracture permeability ($k_{f\text{-}final}$) was similar to the initial one in the three experiments, yielding $k_{f\text{-}final}/k_{f\text{-}initial}$ ratios of 0.74, 0.81 and 1.24 at 0.2, 1 and 60 mL h^{-1}, respectively (Table 4.3 and Fig. 4.10a,b,c). A higher variation in k_f was expected given the considerable increase in pore volume during the experiments ($V_{f\text{-}initial}$ and $V_{f\text{-}final}$; Table 4.2). This suggests that flow moved mainly through the initial fracture, with only diffusion in the reacted rock matrix. Under slow flow rates (*exps. 22 and 23*), face dissolution resulted in about 85 % of the fracture with negligible variations in the aperture (Fig. 4.8a,d), which could promote slight changes in k_f. Also, partial blocking of flow paths caused by (moving) grains may explain the small k_f changes, as shown in Figs. 4.5a,d,e and 4.7c. Noiriel et al. (2007) and Andreani et al. (2008) also reported minor changes in permeability in similar experiments with marls due to reorganization of clay minerals in the fracture.

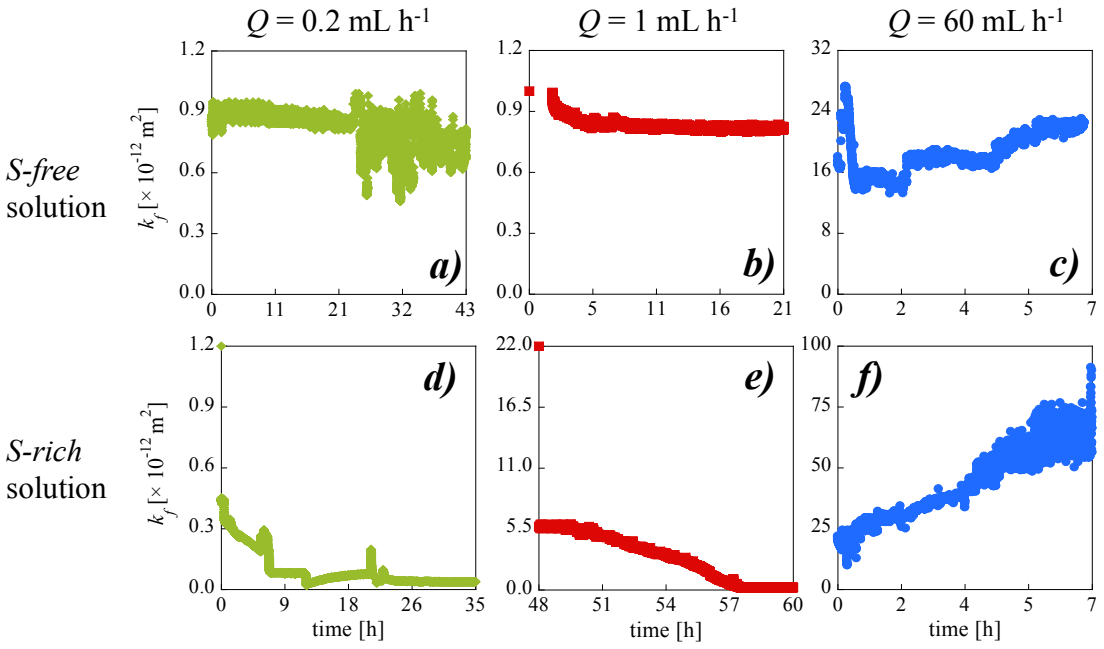

Figure 4.10 *Variation of fracture permeability, k_f, with time under different flow rates and solution compositions. In S-free solution experiments: a) exp. 22; b) exp. 23 and c) exp.24. In S-rich solution experiments: d) exp. 26; e) exp. 27 and f) exp. 28.*

In the *S-rich* solution experiments, $V_{f\text{-}final}$ increased by a factor that ranged from 4 to 5 (Table 4.2). In these experiments, in contrast to the small changes in k_f values obtained in the *S-free*

experiments, a dramatic k_f decrease was measured at the low flow rate rang, yielding $k_{f\text{-}final}/k_{f\text{-}initial}$ ratios of 0.03 and 0.07 (Table 4.3 and Fig. 4.10d,e). This behavior was attributed to fracture sealing caused by gypsum precipitation along the fracture (Fig. 4.5a,b,c). Conversely, at the highest flow rate, k_f increased, yielding $k_{f\text{-}final}/k_{f\text{-}initial} \approx 4$ (Table 4.3 and Fig. 4.10f). In this experiment, gypsum precipitation was not observed.

Therefore, the experimental results showed that under slow flow rates, k_f barely changed in *S-free* experiments but decreased in *S-rich* experiments, whereas it increased under fast flow rate in both types of solution. Nonetheless, k_f is greater in the *S-rich* solution experiments. The observed k_f variability could depend on: *i)* small differences in composition and/or structure among samples affecting the reproducibility of the results (Chen et al., 2014), *ii)* calcite passivation cause by gypsum coating or inhibition of calcite dissolution by the presence of sulfate (Garcia-Rios et al., 2014; Offeddu et al., 2015) and *iii)* movement of grains to block the flow paths, as illustrated in Fig. 4.5d.

4.2.2 Modeling results

This part of the Chapter presents the 2D reactive transport simulations to reproduce the experimental results obtained in the percolation experiments. The initial conditions and injected solutions used in the simulations were the same as the experimental ones. In all cases, the initial pore water was a solution in equilibrium with respect to calcite and gypsum at 25 °C.

4.2.2.1 *Dissolution and precipitation processes*

4.2.2.1.1 *S-rich* injected solution

Adjusted values of the mineral reactive surface areas (A_m) and initial effective diffusion coefficients (D_{eff}) was used to match the experimental variation in Ca, S, Mg, K, Si and Fe concentrations with time (Table 4.4).

Fig. 4.11 shows the match between the experimental and modeled variation in the output concentrations with time in the *S-rich* injected solution experiment at 1 mL h^{-1} (*exp. 27*). The adjusted surface area of calcite was decreased by one order of magnitude from the calculated

geometric surface value calculated to match the output Ca concentration, which due to calcite dissolution was higher than the input one (Fig. 4.11). The initial increase in the output Ca concentration was associated to an initially large reactive surface area of calcite, resulting in significant calcite dissolution, which caused a decrease in calcite content and surface area close to the fracture. Reaction became controlled by diffusion through the rock matrix and slows down.

Table 4.4 Mineralogical composition, effective diffusion coefficient and reactive surface areas used in the experimental simulations.

Parameters				**Experiments**					
injected solution				***S-rich***			***S-free***		
experiment label				**exp 26**	**exp 27**	**exp 28**	**exp 22**	**exp 23**	**exp 24**
model (see text)				**B**	**A**	**C**	**B**	**A**	**C**
core length (L) [mm]				19.2	19.4	18.4	19.6	18.6	18.7
Q [mL h^{-1}]				0.2	1	60	0.2	1	60
h [µm]				3.8	16.3	16.3	3.2	3.5	14.3
v_D [m^3_{rock} m^{-2}_{cell} s^{-1}]				1.6×10^{-3}	1.9×10^{-3}	1.1×10^{-1}	1.9×10^{-3}	8.9×10^{-3}	1.3×10^{-1}
$D_{eff(i)}$ [m^2 s^{-1}]				1×10^{-13}	3×10^{-13}	6×10^{-12}	1×10^{-13}	3×10^{-13}	6×10^{-12}
Primary Mineral	***vol.%***	**geometric surface area** [$m^2_{mineral}$ m^{-3}_{rock}]	**grain size (radius in µm)**	**adjusted surface area** [$m^2_{mineral}$ m^{-3}_{rock}]					
calcite	66.2	1.9×10^5	10	$1.9 \pm 1.5 \times 10^4$		$8.5 \pm \times 10^4$	$1.9 \pm 1.5 \times 10^4$		$2.5 \pm \times 10^5$
quartz	9.2	1.0×10^4	23	1.0×10^6					
illite	6.4	2.0×10^4	10	2.0×10^6					
albite	6.3	6.0×10^3	30	3.5×10^8					
gypsum	2.2	9.5×10^2	68	$1.0 \pm 0.5 \times 10^1$					
clinochlore	2.6	3.0×10^3	30	$3.9 \pm 3.6 \times 10^9$					
anhydrite	0.3	1.5×10^2	68	1.5×10^2					
pyrite	0.1	8.1×10^1	30	1.0×10^6					
kaolinite	-	-	-	1.0×10^4					
$SiO_{2(am)}$	-	-	-	1.0×10^4					
dolomite	-	-	-	1.0×10^4					
zeolites	-	-	-	1.0×10^4					

The experimental and simulated output S concentrations were always lower than the input one (Fig. 4.11). Considering the excess of Ca concentration and the positive values of the gypsum saturation index ($0 < SI \leq 0.17$) of the solution at the outlet of the core during the experiment, the deficit of S was attributed to gypsum precipitation. The calculated and measured Mg and K concentrations coincided within error with their respectively input concentrations (Fig. 4.11).

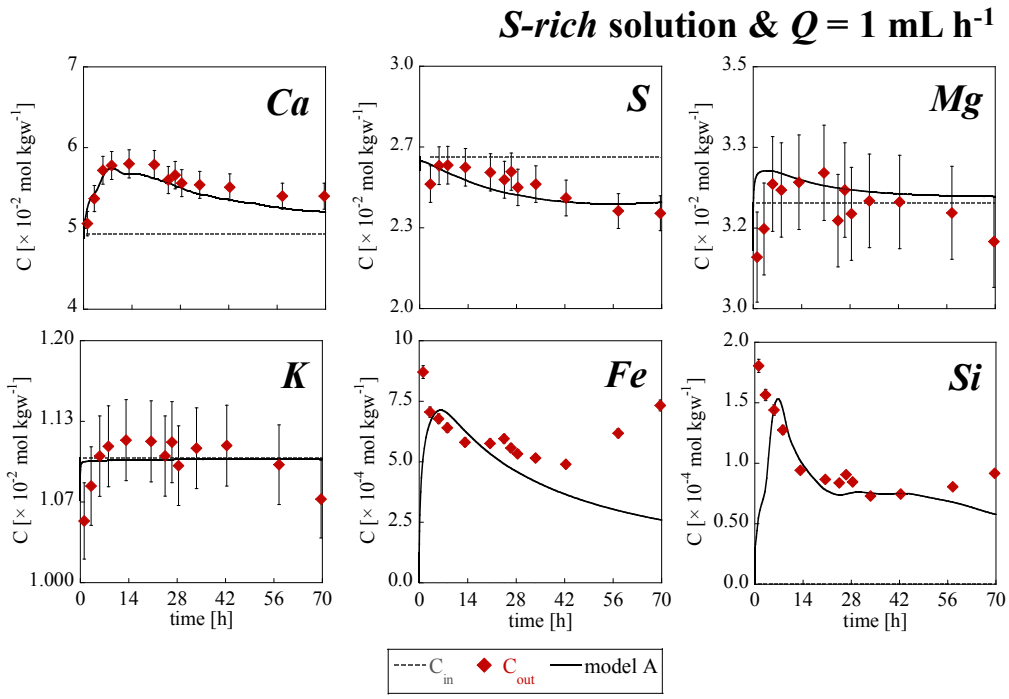

Figure 4.11 *Variation of the output concentrations with time under pCO_2 of 61 bar and 60 °C in S-rich injected solution at 1 mL h^{-1} (exp. 27) for Ca, S, Mg, K, Fe and Si. Solid symbols and solid line represent the experimental and calculated variations, respectively. The dotted line represents the input solution concentration.*

The excess of Fe concentration indicated dissolution of the primary Fe-bearing minerals (clinochlore and pyrite). The main Fe source was clinochlore dissolution. Although the output solutions were highly undersaturead with respect to both minerals at the outlet of the core (-36.2 < SI_{Cln} < -29.8 and SI_{Py} = -200), the amount of pyrite in the cores was very small compared to that of clinochlore. The adjusted value of the surface area of clinochlore was significantly larger than that calculated geometric area in order to match the measured Fe concentration (Table 4.4). This value is not unreasonable for a clay mineral and is similar to that used in previous studies (4.4×10^8 $m^2_{mineral}$ m^{-3}_{rock}; Gaus et al., 2005).

The excess of the output Si concentration (Fig. 4.11) was related to the dissolution of the Si-bearing minerals (albite, clinochlore, illite and quartz). A good match was achieved by using significantly larger values of the surface area of the Si-bearing phases than the geometrical surface areas values. Dissolution of albite and clinochlore was linked to precipitation of clay minerals (smectite and kaolinite) and zeolites (mesolite, stilbite, scolecite and gismondine; Table 4.5).

Dissolution of quartz and illite was negligible. Using the same reactive surface area value for all the secondary minerals, calculations showed that precipitation of kaolinite, mesolite and stilbite was the most important. The late decrease in Si concentration was due to the decrease in reactive surface areas of albite and clinochlore while dissolving.

Table 4.5 Volumes of dissolved calcite, gypsum, clinochlore and albite, and volumes of precipitated secondary minerals. Calculated from mass balance and from the simulations.

	Primary phases					***Secondary phases***					
Minerals	**Cal**	**Ilt**	**Gp**	**Cln**	**Ab**	**Kln**	**Dol**	**Ms**	**Slb**	$\Delta V_{Total\text{-}diss}$ [mm^3]	$\Delta V_{Total\text{-}ppt}$ [mm^3]
***S-rich* solution**	***exp 26*; Q = 0.2 mL h^{-1}**										
ΔV_{model} [mm^3]	-2.97	0.03	0.45	-1.55	-0.01	0.06	0.79	1.04	0.54	-4.53	2.87
$\Delta V_{balance}$ [mm^3]	-2.80	-	0.39	-3.29	-(0-1.50)	2.13-4.34	-	-	-	-(6.09-7.59)	2.51-4.72
$\Delta V_{model}/\Delta V_{balance}$ [%]	6	-	13	112							
	***exp 27*; Q = 1 mL h^{-1}**										
ΔV_{model} [mm^3]	-19.30	-0.03	7.24	-3.85	-0.18	0.13	2.04	2.51	0.40	-23.33	12.31
$\Delta V_{balance}$ [mm^3]	-20.34	-	7.17	-4.51	-(0-2.06)	2.69-5.73	-	-	-	-(24.85-26.91)	9.87-12.90
$\Delta V_{model}/\Delta V_{balance}$ [%]	5	-	1	17							
	***exp 28*; Q = 60 mL h^{-1}**										
ΔV_{model} [mm^3]	-7.85	-0.13	4.76	-1.18	-0.16	0.05	0.43	-	0.76	-9.20	6.04
$\Delta V_{balance}$ [mm^3]	-9.09	-	13.98	-1.17	-(0-0.53)	0.59-1.38	-	-	-	-(10.25-10.79)	14.57-15.36
$\Delta V_{model}/\Delta V_{balance}$ [%]	16	-	194	1							
***S-free* solution**	***exp 22*; Q = 0.2 mL h^{-1}**										
ΔV_{model} [mm^3]	-3.18	0.07	-0.13	-1.83	-0.02	0.09	0.97	1.17	0.39	-5.02	2.51
$\Delta V_{balance}$ [mm^3]	-3.07	-	-0.14	-2.29	-(0-1.05)	1.49-3.03	-	-	-	-(5.36-6.41)	1.63-3.17
$\Delta V_{model}/\Delta V_{balance}$ [%]	3	-	5	26							
	***exp 23*; Q = 1 mL h^{-1}**										
ΔV_{model} [mm^3]	-7.37	0.05	-0.80	-1.98	-0.02	0.11	0.86	1.15	0.32	-9.37	1.65
$\Delta V_{balance}$ [mm^3]	-7.30	-	-0.62	-1.53	-(0-0.70)	0.96-1.99	-	-	-	-(8.83-9.53)	1.58-2.61
$\Delta V_{model}/\Delta V_{balance}$ [%]	1	-	22	23							
	***exp 24*; Q = 60 mL h^{-1}**										
ΔV_{model} [mm^3]	-44.30	-0.10	-2.47	-1.85	-0.15	0.09	0.52	0.83	0.09	-46.30	0.94
$\Delta V_{balance}$ [mm^3]	-45.82	-	-	-1.98	-(0-0.90)	(0.98-2.31)	-	-	-	-(47.80-48.70)	19.00-20.33
$\Delta V_{model}/\Delta V_{balance}$ [%]	3	-	-	7							

Dissolution and precipitation processes occurred during the experiments and affected the outlet pH. Fig. 4.12a shows the temporal variation of the outlet pH in the experiment with *S-rich* injected solution at Q = 1 mL h^{-1} (*exp. 27*). A pH increase up to 4.4 was calculated to occur within the first 9 h. Thereafter, pH remained fairly constant for 14 h to thereafter decrease smoothly to 4.2 (Fig. 4.12a). The evolution of pH with respect to the distance normal to fracture and several positions along the sample is shown in Fig. 4.12b. At the contact between the fracture wall and the injected

solution, pH was low, increasing towards the rock matrix. Differences in pH between the inlet and the outlet of the core were minor due to the slow residence time of the reacting solution. The pH was higher under slow flow rates (4.5, 4.2 and 3.7 at 0.2, 1 and 60 mL h^{-1}; Fig. A1; Appendix 1).

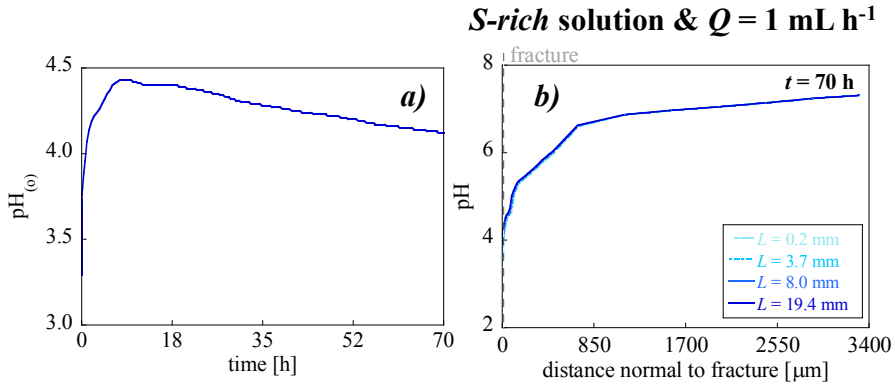

Figure 4.12 *Simulated pH variation of the outlet solution with respect to time (left) and with distance normal to fracture in μm and at various positions along the fracture (right) in exp. 27 at Q = 1 mL h^{-1} and S-rich injected solution.*

A first prediction of the experimental concentrations in the experiments run at 0.2 and 60 mL h^{-1} was performed using fitted values of D_{eff} and A_m for the primary and secondary minerals in *exp. 27* (Fig. 4.13). This model configuration is labeled model A. Either an overestimation or underestimation of the experimental output concentrations was obtained for these two experiments using model A. An improved match between the experimental and the calculated data was obtained by slightly diminishing D_{eff} in the experiment run under slow flow rate (0.2 mL h^{-1}) and by increasing D_{eff} by a factor of 20 in the high flow rate experiment (Table 2). These new model configurations are designated model B at 0.2 mL h^{-1} and model C at 60 mL h^{-1}. Model B leads to an approximate fit of solution composition at 0.2 mL h^{-1}. The fit from model C (60 mL h^{-1}) is poorer and not much better than model A. In models B and C, the A_m values for the primary and secondary species were the same as in model A, independently of the flow rate, except for calcite (Table 4.4). Based on the results, an increase in the apparent diffusion coefficient by a factor of 20 was obtained by increasing the flow rate from 1 to 60 mL h^{-1}. This correlation could be associated to two facts: *(1)* fast flow rate implies less transport control, which is reproduced by the model using a large initial $D_{eff(i)}$, and *(2)* fast flow rates lead to larger alteration and porosities at late times, leading also to larger diffusion coefficient.

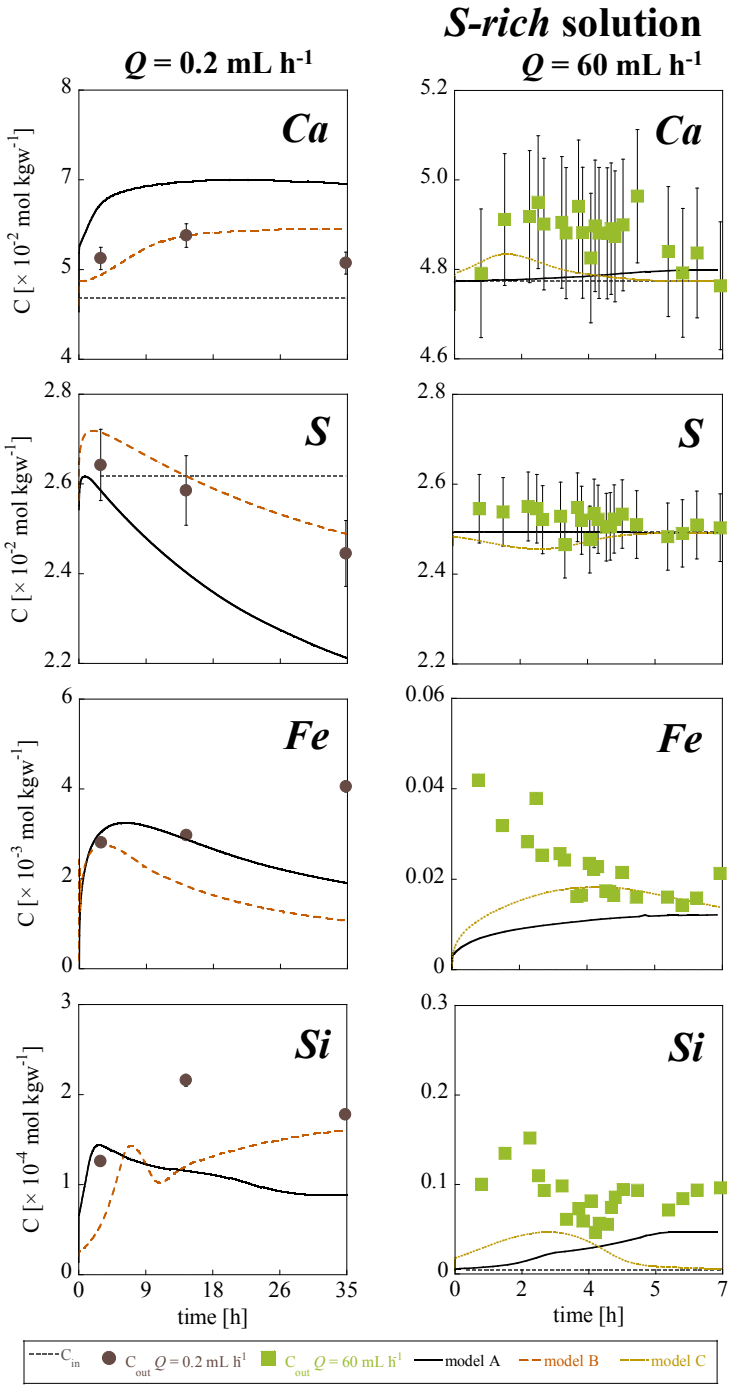

Figure 4.13 *Variation in the output Ca, S, Fe and Si concentrations with time under pCO_2 of 61 bar and 60 °C and S-rich injected solution at Q = 0.2 mL h^{-1} (exp. 26;left), and Q = 60 mL h^{-1} (exp. 28; right). Symbols and lines represent the experimental and calculated (model A (solid line), B and C (dashed lines)) variations, respectively. The dotted line represents the input solution concentration.*

4.2.2.1.2 *S-free* injected solution

In the *S-free* injected solution experiments, gypsum did not precipitate because of the lack of S in the input solution. Therefore, sulfate in solution was originated from dissolution of primary gypsum and/or anhydrite. A reasonable match between the measured and the calculated output concentrations was obtained for the experiments run at 0.2 and 1 mL h^{-1} (Fig. 4.14) by using the respective D_{eff} values obtained in the *S-rich* solution experiment (Table 4.4), and slightly different reactive surface areas of calcite (modified by factors of 0.5 and 3; Table 4.4). However, in the experiment run at 60 mL h^{-1}, a wormhole dissolution pattern formed. The rectangular geometry of the model domain could not suitably account for the evolution of the cylindrical geometry related to wormholing. Therefore, discrepancies between the calculated and measured concentrations were to be expected (Fig. 4.14). The temporal evolution of the outlet pH in the experiment with *S-free* injected solution was similar than those in the *S-rich* solution experiments (pH ≈ 4.6 at all flow rates; Fig. A1; Appendix 1).

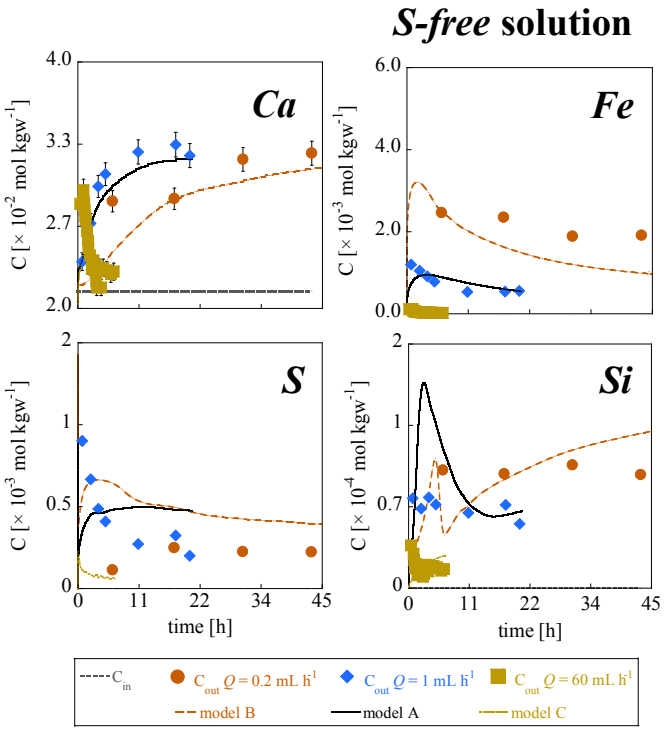

Figure 4.14 *Variation in the output Ca, S, Fe and Si concentrations with time under pCO_2 of 61 bar and 60 °C in S-free injected solution at 0.2, 1 and 60 mL h^{-1} (exps. 22, 23 and 24).*

4.2.2.2 *Mineral dissolution and precipitation rates*

a) Primary Minerals

Fig. 4.15 shows the variation of the instantaneous mineral reaction rates (R_i) in the model with respect to distance normal to fracture at the outlet of the core and at different experimental times in *exp. 27* (*S-rich* injected solution and Q = 1 mL h^{-1}). Negative and positive values of reaction rates represent mineral dissolution and precipitation, respectively. Fig. 4.15 shows that the maximum calcite dissolution rate (R_{Cal}) decreased with time and with distance normal to fracture. Calcite totally dissolved at the fracture-matrix interface with the advance of the reaction front (Fig. 15). The decrease in magnitude of R_{Cal} is directly related to the transport control changing from advective to diffusive through the rock matrix. At the same time, the gypsum precipitation rate (R_{Gp}; Fig. 4.15) at the contact between the fracture and rock matrix increased within the first ≈ 20 h. This was controlled by Ca supply from calcite dissolution and SO_4^{-2} supply from the injected solution. Thereafter R_{Gp} decreased in magnitude because calcite dissolution slowed down diminishing the Ca release. The front of gypsum precipitation followed the calcite dissolution front.

Clinochlore dissolution rate (R_{Cln}) decreased with time and with the distance normal to fracture. The release of Si from clinochlore dissolution made the solution closer to equilibrium with respect to albite ($-4 < SI < -3$), which caused a decrease in the albite dissolution rate (R_{Ab}; Table 2.14). R_{Ab} also decreased with time and distance normal to fracture. Otherwise, the calculated quartz dissolution and precipitation rates (R_{Qtz}) were negligible as expected considering the acidity of the solution. Pyrite reaction was negligible in the model (see R_{Py}; Fig. 4.15), as it was two orders of magnitude slower than that of clinochlore, which is consistent with clinochlore being the main Fe source. The anhydrite dissolution rate also decreased with time and with the distance normal to fracture. The illite precipitation rate increased initially at the contact between the solution and the fracture wall and decreased with distance normal to fracture, being controlled by Al and Si supply from clinochlore (and albite) dissolution. R_{Ilt} decreased with time.

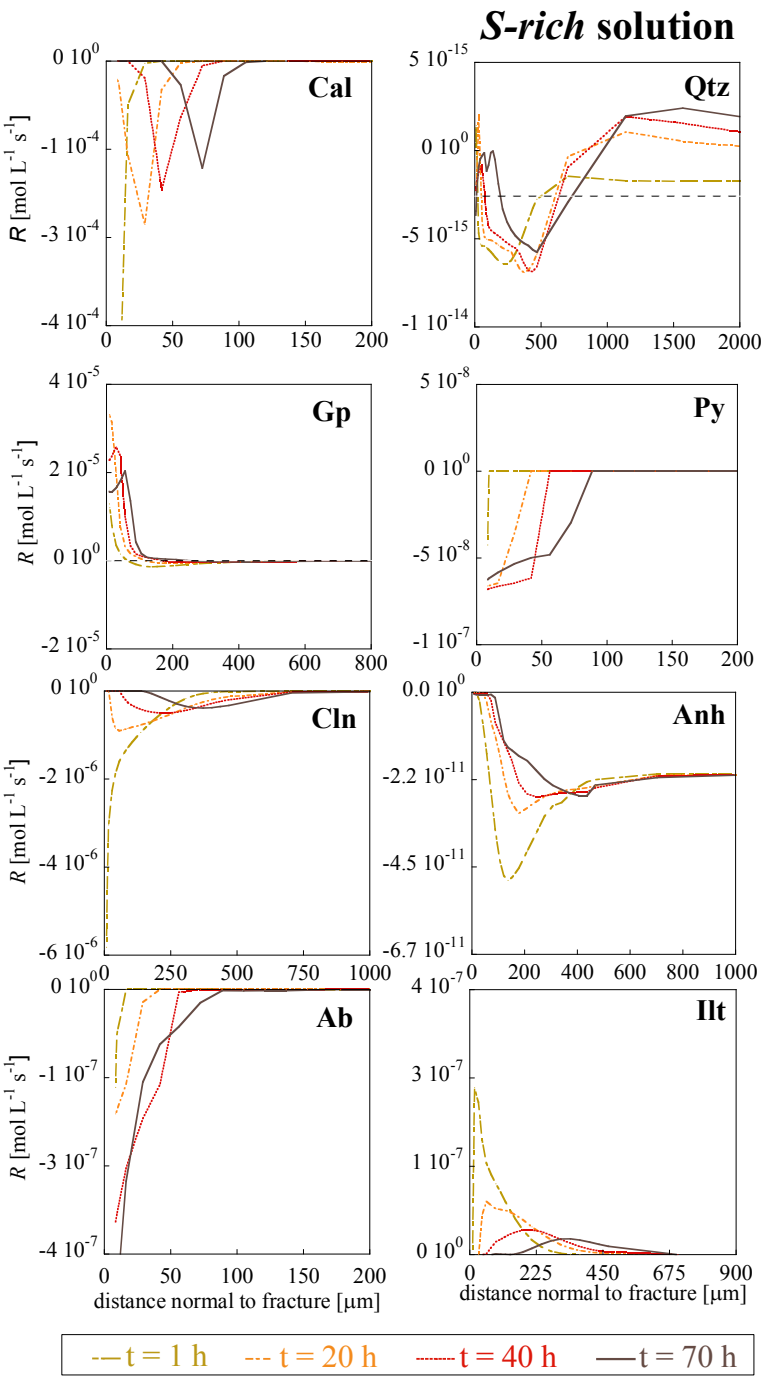

Figure 4.15 *Variation of the simulated dissolution and precipitation rates of the primary minerals (mol L^{-1} s^{-1}) with respect to the distance normal to fracture at different times at the outlet of the core sample for the 1 mL h^{-1} experiment (S-rich): calcite (Cal), gypsum (Gp), clinochlore (Cln), albite (Ab), quartz (Qtz), pyrite (Py), anhydrite (Anh) and illite (Ilt).*

b) *Secondary Minerals*

XRD and MicroRaman spectroscopy analysis did not reveal the presence of any Si secondary phases. The measured Al concentrations were always close to the ICP-AES detection limit (approximately 1.85 x 10^{-6} mol L^{-1}), indicating that precipitation of some Al-bearing phases could be possible. In previous studies with percolation experiments with similar S content, pCO_2, T and ionic strength, kaolinite precipitation was reported (Ketzer et al., 2009; Luquot et al., 2012; Yu et al., 2012; Tutolo et al., 2015). In the present study, potential secondary minerals included in the model were dolomite, $SiO_{2(am)}$, kaolinite, smectite, mesolite, stilbite, mordenite, scolecite, analcime, wairakite, laumontite and gismondine. In fact, the dolomite rate (R_{Dol}) greater than zero after 1 h indicated dolomite precipitation, although thereafter, $R_{Dol} < 0$ (Fig. 4.16). These rates suggest dolomite dissolution close to the fracture wall, due to the acidic injected solution, and precipitation further into the rock matrix due to Mg supplied by the dissolving clinochlore. Since Luquot et al. (2012) observed precipitation of poorly crystalized SiO_2 ($SiO_{2(am)}$) at P_{total} = 100 bar, pCO_2 = 60 bar and T = 95 °C in a dissolving rich Si-sandstone, $SiO_{2(am)}$ was included in the calculations. However, $SiO_{2(am)}$ did not precipitate in the model.

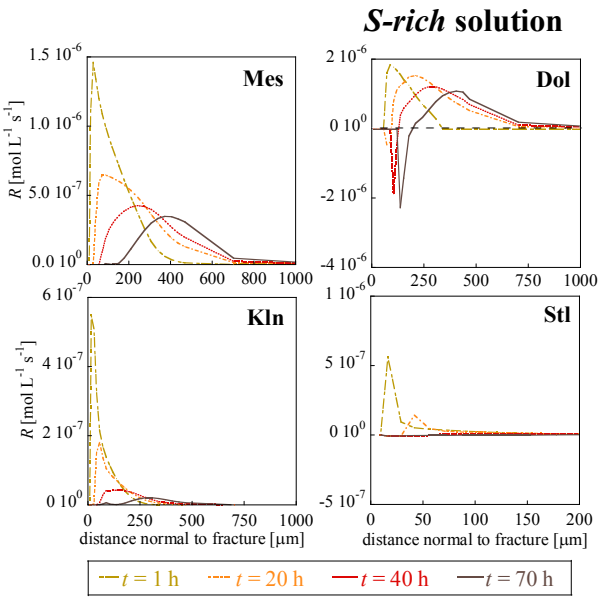

Figure 4.16 *Variation of the simulated precipitation rates of the secondary minerals (mol L^{-1} s^{-1}) with respect to the distance normal to fracture at different times in a 1 mL h^{-1} experiment (S-rich): dolomite (Dol), kaolinite (Kln), mesolite (Mes) and stilbite (Stl).*

The calculated precipitation rates of kaolinite, mesolite and stilbite were between 5 and 6 orders of magnitude higher than those of smectite (Fig. 4.16). The precipitation fronts showed that mesolite (R_{Ms}), kaolinite (R_{Kln}), and stilbite (R_{Stl}) rates increased initially at the contact between the solution and the fracture wall and decreased with distance normal to fracture, as well as with time. This is mainly controlled by the Ca, Al and Si supply from dissolution of calcite and clinochlore.

4.2.2.3 *Variation in mineral volume*

Fig. 4.17 shows the calculated variation in mineral volume fraction (*vol.*%) as a function of the distance normal to fracture at four different positions along the core in *exp. 27* (*S-rich* solution and Q = 1 mL h^{-1}). Calculations show that calcite dissolved totally within the first ≈ 80 μm from the fracture near the inlet (L = 0.2 mm; Fig. 4.17) and to a lesser extent further downstream along the column. This led to the formation of a reacted zone that in the model reached a distance of ≈ 154 μm, which was similar to what was measured in the ESEM images (≈ 176 μm; Fig. 4.5a). The calculated dimensions of the altered zone reasonably matched those of the observed dissolution patterns (mostly uniform dissolution) in the ESEM and XMT images. Gypsum precipitation was significant in the reacted zone reaching at the fracture-rock matrix interface up to 33 *vol.*% (Fig. 4.17). The amount of gypsum decreased with distance normal to fracture and along the fracture following calcite dissolution. The change between the initial and final volume of anhydrite was negligible. Besides, clinochlore dissolved totally over the reacted zone near the inlet. In comparison to clinochlore, albite dissolution was minor, as it was that of pyrite and illite.

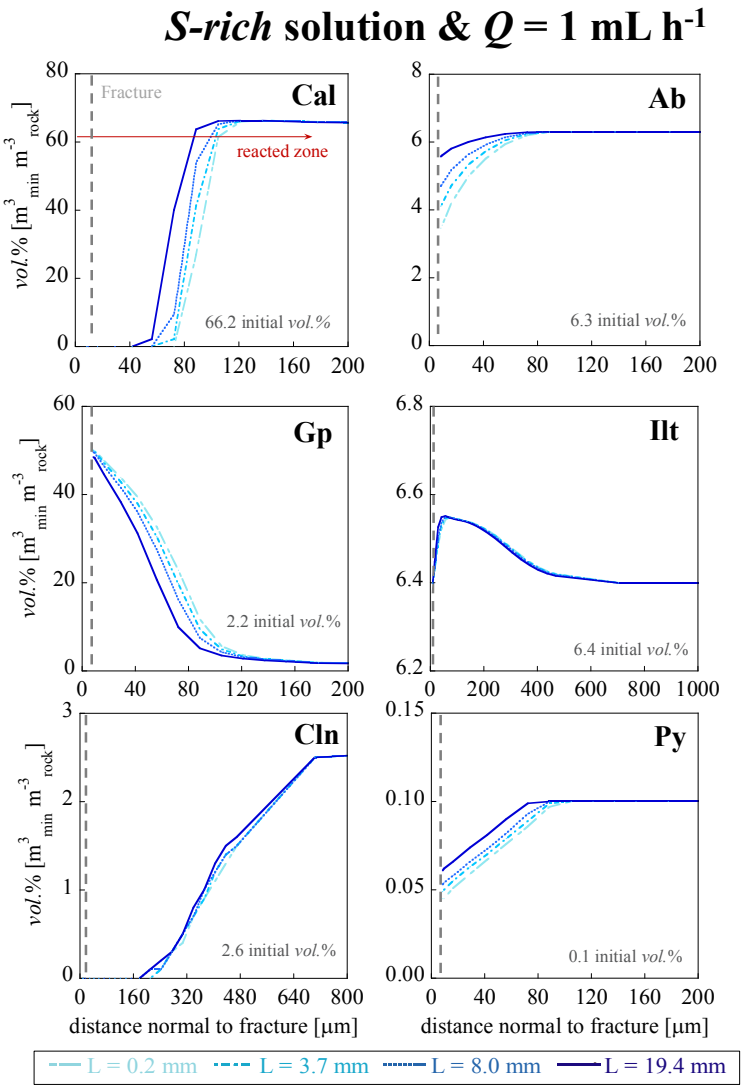

Figure 4.17 *Variation of the simulated volumes of the primary minerals with the distance normal to fracture at different distances from the inlet: calcite (Cal), gypsum (Gp), clinochlore (Cln), albite (Ab), illite (Ilt) and pyrite (Py).*

Regarding the secondary phases, dolomite precipitated as long as aqueous Mg from the dissolution of clinochlore was sufficient to supersaturate the solution (Fig.4.18). Fig.4.18 shows that the volume of precipitated kaolinite was rather small (up to 0.22 *vol.*%). Regarding zeolites, the volume of precipitated mesolite (≈ 1.8 *vol.*%) was greater than that of stilbite (≈ 0.6 *vol.*%). However, the small amounts of these secondary minerals would make the identification of the secondary phases in the ESEM and XMT images very difficult.

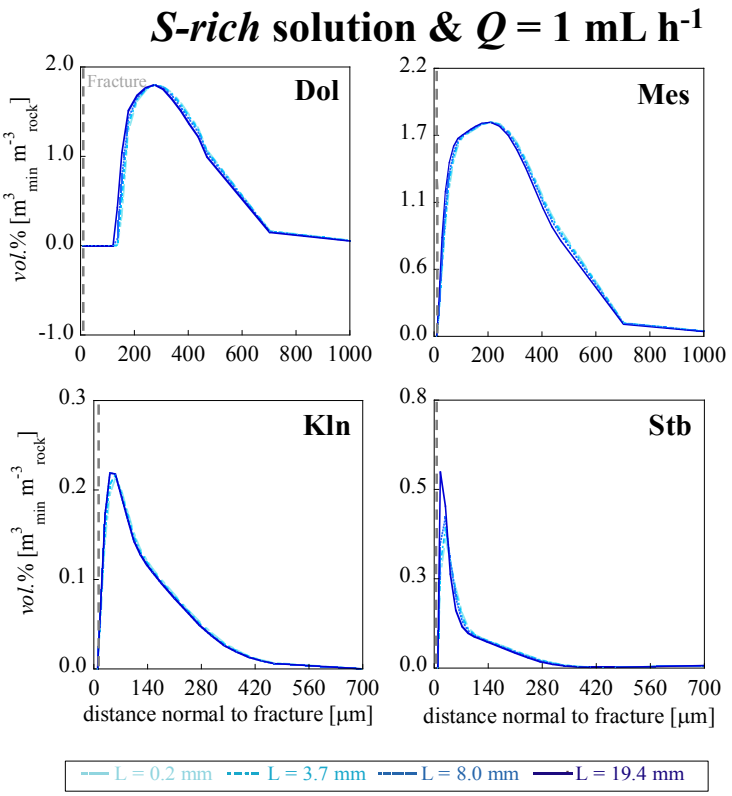

Figure 4.18 *Variation of the simulated volumes of the secondary minerals with distance normal to fracture at different distances from the inlet: dolomite (Dol), kaolinite (Kln), mesolite (Mes) and stilbite (Stl).*

Fig. 4.19a illustrates the effect of the flow rate on the variation in calcite volume fraction in the *S-rich* experiments. Calculations show that an increase in the flow rate tended to reduce differences between the inlet and the outlet and to increase the penetration length. Regarding the variation in volume fraction of calcite with the distance normal to fracture in the *S-free* solution experiments, an increase in the flow rate (from 0.2 to 1 mL h^{-1}) also tended to reduce the differences between the inlet and the outlet and to increase the penetration length. This tendency coincides with the type of dissolution pattern, i.e., face dissolution, formed under slow flow rates (0.2 mL h^{-1} in the *S-rich* solution experiment and 0.2 and 1 mL h^{-1} in the *S-free* solution experiments). In the *S-free* solution experiment at 60 mL h^{-1}, the difference in the volume of dissolved calcite between the inlet and the outlet was not representative of that formed during wormhole formation (Fig. 4.19b).

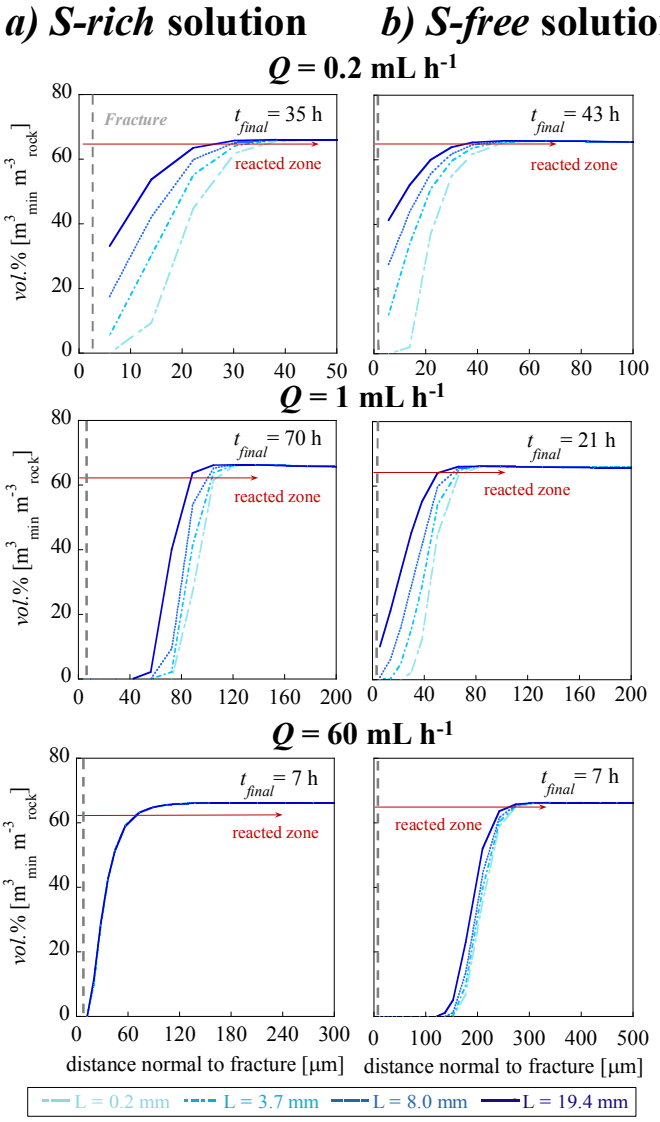

Figure 4.19 *Variation of the simulated calcite volume fraction (vol.%) with respect to distance normal to fracture in S-free (a) and S-rich (b) injected solution experiments at different flow rates (Q). The dashed vertical lines indicate the fracture-rock matrix interface.*

A reasonable match between the volumes of dissolved calcite, gypsum and clinochlore calculated from the simulations and those calculated from the mass balance equations was achieved with only a few exceptions (Table 4.5; see $V_{model}/V_{balance}$ ratio). In the *S-rich* solution experiments, except in the wormholing formation experiment (*exp. 24*), the model under or overestimated the volume of dissolved calcite. This difference in V_{Cal} is related by the fact that a change in A_{Cal} was very sensitive to the calculated calcite *vol.*%, even into the uncertainty range of the Ca concentrations.

For example, $V_{Cal\text{-}diss}$ in the model was greater than those calculated from the mass balance for the experiments at 0.2 and 1 mL h^{-1} using the same A_{Cal}. This could be related to the fact that experimentally less calcite was accessible to react than in the simulation (Noiriel et al., 2009). At high flow rate (*exp. 28*), the model did not reach the amount of precipitated gypsum calculated from mass balance but this difference could be linked with the analytical error between the measured input and output S concentrations.

In *S-free* solution experiment at 0.2 mL h^{-1}, the model underestimated the volume of dissolved gypsum calculated from mass balance. Possibly this was related to the heterogeneities of the samples in which A_{Gp} was considered to be the same. In the case of clinochlore in a *S-free* solution experiment at 1 mL h^{-1}, the model underestimated the volume of dissolved clinochlore calculated from mass balance.

4.2.2.4 *Variation in porosity*

Fig. 4.20 shows the calculated variation in porosity (ϕ) with respect to distance normal to fracture at the outlet of the core at the end of each experiment. ϕ increased up to 75 % in the altered zone at the contact between fracture and the rock matrix (*S-free* solution experiment). Porosity decreases with distance normal to fracture, and overall, its variation is similar to that obtained from the ESEM images of the thin section (ϕ = 60 %; *exp 27*; Fig. 4.20). In both types of solution, an increase in the flow rate led to an increase in porosity, which was higher in the *S-free* solution experiments than in the *S-rich* solution experiments (Fig. 4.20). In the *S-free* solution experiment, the largest increase in porosity is readily related to wormhole formation.

The resulting increase in porosity contrasts with the variation in fracture permeability, which tended to decrease in the *S-rich* experiments at 0.2 and 1 mL h^{-1} and slightly change in the *S-free* experiments at these low flow rates. This behavior suggests that at low flow rate, k_f was not strictly related to the dissolution and precipitation reactions occurring over the fracture evolution, but it could be influenced by partial blocking of flow paths caused by (moving) grains in the fracture causing changes in pore structure (Fig. 4.6). At high flow rate (60 mL h^{-1}), in both injected solutions, the calculated porosity was higher than that at low flow rate. Under these conditions, k_f increased, and the increase was larger in the *S-free* injected solutions. This behavior is expected in

a porous media, in which an increase in porosity yields an increase in permeability (Chen et al., 2014). However, the simulations show that the flow through the reacted zone (which is not included in the model) is not significant in the calculated porosity changes, but it could be representative in the permeability calculation.

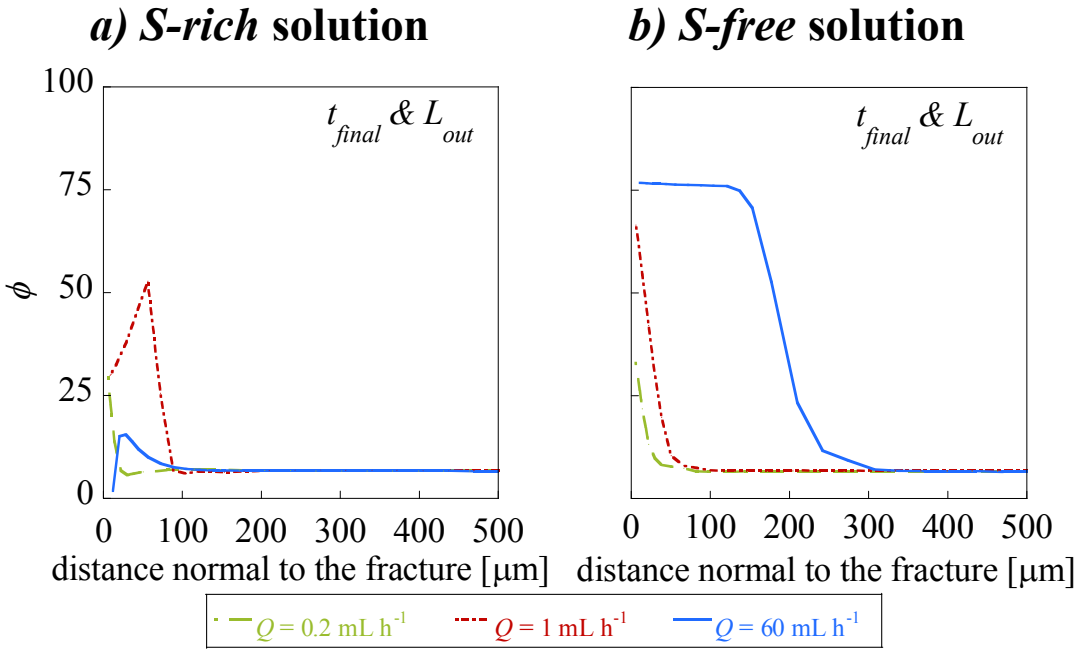

Figure 4.20 *Modeled porosity (ϕ) variation along the normalized distance normal to fracture at different flow rates (0.2, 1 and 60 mL h^{-1}) at the outlet of the core and at the end of the experiments under different solution compositions: a) S-rich injected solution and b) S-free injected solution.*

4.3 Summary and conclusion

Regarding experimental results:

Percolation experiments using fractured marl cores under P_{Total} = 150 bar, pCO_2 = 61 bar and T = 60 °C (supercritical CO_2 conditions) with *S-free* and *S-rich* injected solutions at different flow rates (0.2, 1 and 60 mL h^{-1}) were run to better understand the reactivity of the Hontomín marl caprock.

Calcite dissolution was the main reaction because of the acidic character of the injected solutions under supercritical pCO_2. Results based on the experimental aqueous chemistry showed that the overall process was not affected by changing the ionic strength from 0.3 to 0.6 M. In *S-free* solutions, dissolution of calcite, primary gypsum, clinochlore and albite took place. In *S-rich* solutions in equilibrium with gypsum, dissolution of clinochlore and albite took place as did that of calcite, which promoted gypsum precipitation. A Si deficit suggests that dissolution of the silicate minerals triggers precipitation of Si-bearing secondary minerals (e.g., kaolinite and amorphous SiO_2 gel).

The dissolution and precipitation reactions controlled the variations in the final pore volume associated with the reacted core. In all experiments, an increase in the flow rate from 0.2 to 60 mL h^{-1} led to an increase in the calcite dissolution rate and in the final pore volume associated with the reacted core. In the *S-rich* solution, the volume of dissolved calcite was always larger than the volume of precipitated gypsum (except at 60 mL h^{-1}). The dissolution of calcite grains and, to a lesser extent, the dissolution of clinochlore and albite, created a high porosity zone (ϕ ranged from 48 to 67 %) along the fracture walls. This porosity zone was composed of non-dissolved quartz, pyrite and illite grains, precipitated gypsum (in *S-rich* solutions) and precipitated Si-bearing phases (e.g., kaolinite or amorphous SiO_2).

As for dissolution patterns, in the *S-free* solution experiments face dissolution occurred at slow flow rates (*Pe* of 4 and 21). At high flow rate (*Pe* = 1267), wormhole formation was observed. However, in *S-rich* solution experiments, face dissolution occurred only at the slowest flow rate. At an intermediate flow rate range, both uniform dissolution and wormhole took place. At high flow rate, a combination of wormhole formation and uniform dissolution similarly occurred, although the latter dominated. In both types of solutions, local heterogeneities controlled mineral dissolution along the fracture, which could led to unexpected dissolution patterns associated with *Pe* values.

As for fracture permeability, at slow flow rate (low *Pe*), in *S-free* solutions, k_f did not significantly change since face dissolution did not cause the fracture aperture to vary. Moreover, detached grains along the fracture could lead to the obstruction of the fluid flow, preventing a k_f increase. In *S-rich* solutions, a marked decrease in k_f was attributed to gypsum precipitation. At fast flow rate

(high *Pe*), k_f slightly increased with slight variations in aperture in the *S-free* solution. In the *S-rich* solution, the increase in k_f was attributed to the absence of gypsum precipitates. This suggests the existence of flow through the altered rock matrix.

Nevertheless, small differences in composition and/or structure exist between different samples. These differences exert a considerable influence on the reproducibility of the experimental results, passivation of gypsum or inhibition of calcite dissolution in the presence of sulfate, movement of grains, and on the obstruction of flow paths. These phenomena play a central role in fracture permeability.

In the light of our findings, CO_2-rich solutions in contact with a fractured marl caprock favor CO_2 migration pathways if *(1)* groundwater has a low content of sulfate that prevents gypsum precipitation and/or if *(2)* the fluid flow is fast. By contrast, sealing of the fractures takes place if gypsum precipitates and the flow rates are slow.

Regarding modeling results:

Two dimensional reactive transport modeling has been applied to interpret the results from the experiments with fractured marl cores during the injection of CO_2-rich solutions under supercritical conditions (P_{Total} = 150 bar, pCO_2 = 61 bar T = 60 °C). Calculated solution composition of the outlet compares reasonably well with the variation in the measured concentrations under slow flow rates, whereas at fast flow rate experiments poor match was obtained. Likewise, the simulations reproduced the dimensions of the dissolution patterns observed in the ESEM and XMT images, except for the experiment run at high flow rate (60 mL h^{-1}) and *S-free* solution in which a wormhole formed due to local heterogeneity. The fraction of a porous, altered zone was also predicted by the simulation. These results help us to understand the different dissolution and precipitation processes observed or suggested during the flow-through percolation experiments.

A successful match (except for fast flow rate) between the experimental and calculated output concentrations was achieved by using a D_{eff} between 1×10^{-13} and 3×10^{-13} m^2 s^{-1} at low flow rate, whereas a larger value (6×10^{-12} m^2 s^{-1}) was used at high flow rate. Regarding the mineral surface

area values, a single value for calcite was used in the *S-rich* solution experiments ($1.2 \pm 0.7 \times 10^4$ $m^2_{mineral}$ m^{-3}_{rock}), whereas in *S-free* solution experiments the area was slightly increased in the faster flow rate experiments (1 and 60 mL h^{-1}). The surface areas for the rest of the minerals were not changed.

Different compositions of the injected solutions produced different effects on the dissolution and precipitation processes in the Hontomín caprock. The main reaction that occurred was dissolution of calcite in both types of injected solutions. For the same experimental time and under the same flow rate, the volume of dissolved calcite was always larger in the *S-free* solution experiments than in the *S-rich* ones. In *S-rich* solution experiments, gypsum precipitated and in a larger amount in the experiment run at 1 mL h^{-1}. Dissolution of clinochlore, albite and pyrite, and precipitation of dolomite, illite, kaolinite, mesolite and stilbite took also place. Precipitation of secondary Al and Si rich minerals was expected by the mass balance calculated from the laboratory experiments, but it was never observed by the ESEM images.

During the experiments, the mineral reaction rates increased larger in the fracture-rock matrix interface as a result of the interaction with the acidic solution. Inside the rock matrix solute transport was controlled by diffusion, which could not happen under fast flow rate.

In both types of solution, the calculated porosity in the reacted zone was higher at the fracture wall contact and decreased with distance normal to fracture. An increase in the flow rate caused an increase in porosity. The increase in porosity was higher at the inlet of the core than at the outlet, but the difference between the inlet and the outlet lowered by increasing the flow rate. The increase in porosity from 6 % to ≈ 60 % was similar to the volume of calcite dissolved (≈ 60 %).

Chapter V

Efficiency of magnesium hydroxide as engineering seal in the geological sequestration of CO_2

5.1 Introduction

In this chapter the reactivity of MgO in a Ca–rich solution under subcritic (pCO_2 of 10 and 50 bar and T of 25, 70 and 90 °C) and supercritic (pCO_2 of 74 bar and T of 70 and 90 °C) CO_2 conditions is evaluated in order to examine the efficiency of a MgO-based cement as a potential material with seal capacity. MgO quickly hydrates to brucite ($Mg(OH)_2$), which dissolves causing the precipitation of magnesium carbonate phases (magnesite and/or metastable phases such as nesquehonite ($MgCO_3 \cdot 3H_2O$) or hydromagnesite ($Mg_5(CO_3)_4(OH)_2 \cdot 4(H_2O)$) that depends on pCO_2, temperature and solid/water content.

The solid and solution samples were analyzed by XRD-Rietveld and SEM and ICP-AES, respectively. The evolution of the experimental variation of Mg and Ca concentrations and pH at different T and pCO_2 was simulated using the CrunchFlow reactive transport code. These results were used in the simulation of an application case with a deep borehole surrounded by MgO cement under 150 bar and 90 °C conditions.

5.2 Results

5.2.1 Experimental results

Thirty-eight stirring batch experiments were performed at different duration ranging from 5 to 97 h. The solid/water ratio was maintained constant the (5.3 g MgO/47.7 mL of water equilibrated with respect to calcite). In these experiments, total pressure was the same as the CO_2 partial pressure (pCO_2; Table 5.1).

Table 5.1 Experimental conditions used in the batch experiments performed under subcritical and supercritical CO_2 conditions. The experimental time spans varied from 5 to 97 h (see *Chapter II*).

N° exp.	amount of exp. (different durations)	label	P_{Total} [bar]	T [°C]
29-33	5	MgO-25-10	10	25
34-38	5	MgO-70-10		70
39-42	4	MgO-90-10		90
43-48	6	MgO-25-50	50	25
49-53	5	MgO-70-50		70
54-58	5	MgO-90-50		90
59-61	3	MgO-70-74	74	70
62-66	5	MgO-90-74		90

XRD-Rietveld analyses of the solids in the different experiments showed that with increasing temperature the secondary Mg carbonate phases that tended to precipitate were less hydrated (Table 5.2). Bénézeth et al. (2011) reported the chemical composition of the different phases crystallizing in the $MgO–CO_2–H_2O$ system. The results of the present study coincide with their results. The less stable Mg-carbonate phases were those with a higher content of water and tended to form at low temperature. Hänchen et al. (2008) and Kristova et al. (2014) reported that metastable Mg-carbonate phases are progressively replaced by more stable one.

Table 5.2 XRD (Rietveld analyses) of the initial and reacted samples at different *T* and pCO_2.

Sample	**Initial**	**1**	**2**	**3**	**4**	**5**	**6**	**7**	**8**
pCO_2 [bar]	atmospheric	10	10	10	50	50	50	74	74
Temperature [°C]	25	25	70	90	25	70	90	70	90
time [h]	-	74	72	72	72	72	72	72	72
Minerals	***wt.%***								
Brucite	**86.9**	20.0	3.0	20.0	18.0	0.0	9.0	13.0	0.0
Calcite	3.1	17.0	12.0	6.0	5.0	12.0	3.0	8.0	4.0
Quartz	5.3	4.0	2.0	4.0	6.0	3.0	4.0	4.0	3.0
Nesquehonite		**57.0**		0.0	**68.0**				
Hydromagnesite	1.2		**29.0**	**42.0**		**4.0**	**10.0**	**19.0**	
Magnesite			**46.0**	**20.0**	2.0	**74.0**	**66.0**	**50.0**	**91.0**
Dolomite	0.6				1.0	1.0	3.0	4.0	1.0
Aragonite		2.0	7.0	2.0		1.0		2.0	
Portlandite	3.1			6.0		4.0	5.0		
Others			1.0			1.0			1.0

SEM images of the initial sample showed the common morphology of MgO grains (Fig 5.1a). At 25 °C, based on crystal morphology, precipitation of nesquehonite (well-formed needles) was observed in the samples reacted at pCO_2 of 10 and 50 bar (Fig. 5.1b). At 70 °C, precipitation of hydromagnesite (thin platelets) dominated (Fig. 5.1c), and precipitation of magnesite (hexagonal prisms) was enhanced by temperature and pCO_2 (Fig. 5.1d). Transformation from nesquehonite to hydromagnesite and magnesite with temperature was reported at 50 and 70 °C and pCO_2 of 82 bar (Schaef et al., 2011) and at 120 °C and pCO_2 of 3 bar (Hänchen et al., 2008). Also, formation of minor amounts of aragonite was measured by XRD-Rietveld analysis (*wt.*% < 7; Table 5.2). Nonetheless, this phase could not be observed by SEM.

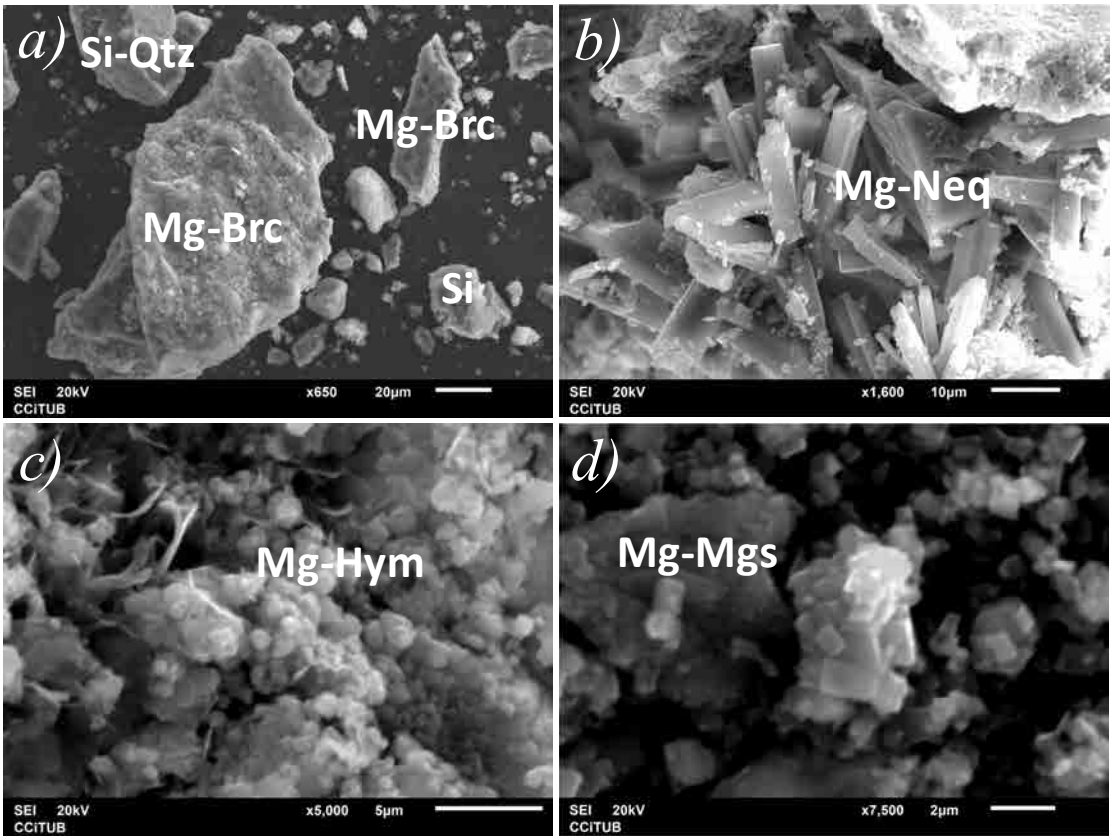

Figure 5.1 *SEM images of the initial and reacted samples: (a) initial MgO; (b) nesquehonite (Neq), after 72 h at 50 bar and 25 °C; (c) hydromagnesite (Hym), after 31 h at 74 bar and 70 °C and (d) magnesite (Mgs), after 72 h at 50 bar and 90 °C.*

The variation of Mg and Ca concentrations with time in the experiments performed at subcritical pCO_2 of 10 and 50 bar and 25, 70 and 90 °C is shown in Fig. 5.2a-d. Note that Mg concentration was more than one order of magnitude higher than that of calcium because of the higher $Mg(OH)_2$ content compared to that of $CaCO_3$ and $Ca(OH)_2$. Variation in Mg concentration was similar for both pCO_2 (10 and 50 bar). At 25°C and 10 and 50 bar, the simulated Mg concentration could not match a faster precipitation of the secondary phases observed in the experiments. For both values of pCO_2, Mg and Ca release tended to be higher at 25 than at 70 and 90 °C. With time Mg and Ca concentration tended to reach steady state at high temperature but not at 25 °C. The increase in Mg concentration was assumed to be due to dissolution of brucite, whereas the increase in Ca concentration was possibly related to the dissolution of calcite and portlandite. The decrease in both concentrations (Mg and Ca) was assumed to be caused by precipitation of Mg and/or Ca carbonates.

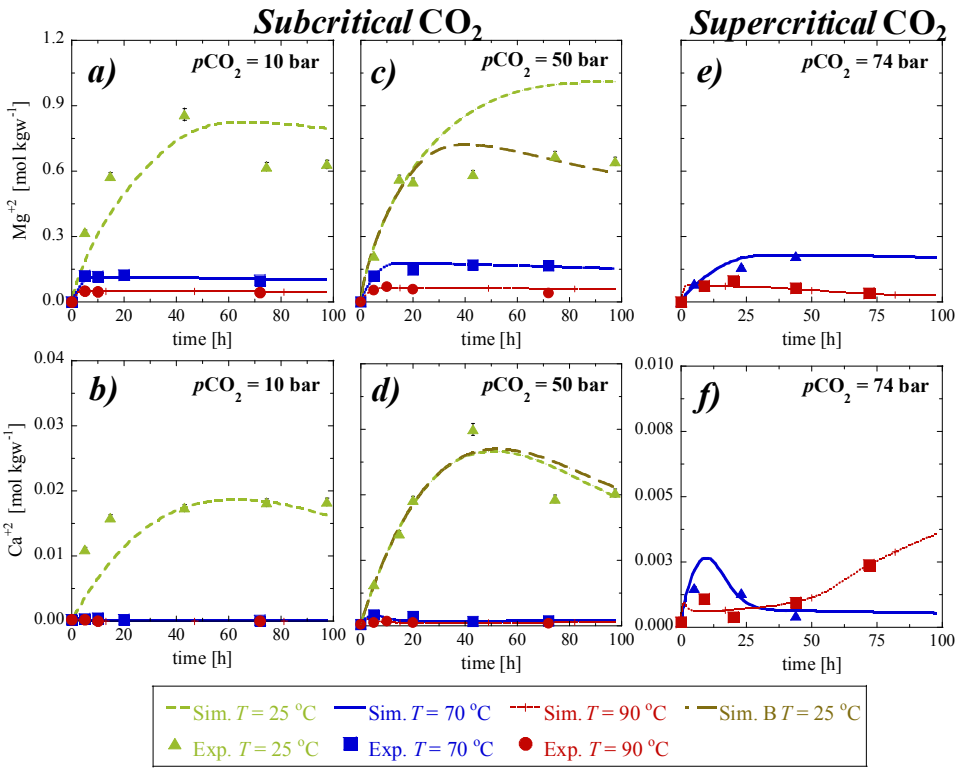

Figure 5.2 *Variation of solution composition with time at different temperatures and subcritical pCO_2 of 10 bar (a) [Mg^{+2}] and (b) [Ca^{+2}], 50 bar (c) [Mg^{+2}] and (d) [Ca^{+2}] and 74 bar (e) [Mg^{+2}] and (f) [Ca^{+2}]. Symbols are experimental data and lines correspond to model results.*

Fig. 5.2e,f shows the temporal evolution of the Mg and Ca concentrations for the supercritical CO_2 experiments (pCO_2 = 74 bar and 70 and 90 °C). A behavior similar as the one reported for the subcritical CO_2 experiments was observed for Mg concentration, with similar values of the Mg concentration. Mg and Ca release tended to be higher at 70 than at 90 °C. Likewise, increase in Mg and Ca concentrations was due to dissolution of brucite, calcite and portlandite, whereas the decrease in their concentrations was caused by precipitation of Mg and/or Ca carbonates. At 90°C, the Ca concentration started to increase after reaching an early plateau, probably caused by a faster dissolution of the Ca-bearing phases in the absence of Mg. The experimental results were compared under subcritical and supercritical CO_2 conditions at 70 °C were compared. An increase in pCO_2 resulted in a very slight increase in Mg concentrations. At 90 °C, Mg concentrations were similar ($\approx 4.0 \times 10^{-2}$ mol kgw^{-1}). The Ca concentration increased to reach a maximum value at around 60 h after the start, tending to be reduced thereafter. An increase in the Ca concentration was noted during the whole stage by increasing the pressure from 10 to 50 bar. Then, an increase in pressure and Ca concentration occurred.

5.2.2 *Modeling results*

Reasonable fits for the aqueous Mg and Ca concentrations were achieved under the different pCO_2 and temperature conditions (Fig. 5.2), allowing an explanation for the evolution of the overall MgO carbonation process. Table 5.2 lists the minerals considered in the modelling under the different pCO_2 and T conditions. Fig. 5.2a,b shows the simulated variation in Mg and Ca concentration at pCO_2 of 10 bar. To match the Mg experimental variation with time, dissolution of brucite, precipitation of dolomite (25, 70 and 90 °C), nesquehonite (25 °C) and both hydromagnesite and magnesite (70 and 90 °C) were considered. The Ca experimental variation was matched by considering dissolution of portlandite and precipitation of calcite (25 °C) and dolomite (25, 70 and 90 °C). Likewise, at pCO_2 of 50 bar, the same processes occurred. However, magnesite precipitation ought to be considered to match the Mg experimental variation at 25 °C (Sim. B; Fig. 5.2c,d). Dissolution of portlandite and calcite (70 and 90 °C) and precipitation of calcite (25 °C) and dolomite (25, 70 and 90 °C) were taken into account to match the experimental Ca variation (Fig. 5.2c,d).

Under supercritical pCO_2 conditions, the same processes as those reported at 50 bar were also taken into account to match the Mg experimental variation at 70 and 90 °C. Dissolution of brucite and precipitation of dolomite, hydromagnesite and magnesite were considered to match the Mg experimental variation. With respect to Ca experimental variation, dissolution of portlandite and calcite was considered (Fig. 5.2e,f).

To match the experimental variation in Mg concentrations with time and the final mineral volume fractions at 10, 50 and 74 bar, the reactive surface area of brucite was decreased with temperature from $3.8 \pm 0.3 \times 10^5$ (25 °C) to $3.5 \pm 2.5 \times 10^3$ $m^2_{mineral}$ m^{-3}_{rock} (70 and 90 °C; Tables 6 and 7). This decrease was likely caused by the formation of Mg-carbonate coatings over the $Mg(OH)_2$ grains (Fig. 5.1), causing passivation. In the case of Ca variation, the reactive surface area of calcite was $6.0 \pm 0.1 \times 10^3$ $m^2_{mineral}$ m^{-3}_{rock} at 10 bar and smaller at 50 and 74 bar ($2.7 \pm 1.2 \times 10^2$ $m^2_{mineral}$ m^{-3}_{rock}). The ΔG_r dependence of the calcite dissolution rate in the model was taken from Xu et al. (2012), but they did not have experimental data in this range of ΔG_r values in their study (see *chapter II,* Eqs. (2.47 and 2.48)). As a consequence, the calcite dissolution rate law might overestimate the dissolution rate in this ΔG_r range, and hence a lower surface area was necessary. The reactive surface area of dolomite was rather small, ranging from $3.0 \pm 2.0 \times 10^{-5}$ to $7.0 \pm 2.0 \times 10^{-3}$ $m^2_{mineral}$ m^{-3}_{rock}.

Table 5.3 Mineralogical compositions and associated surface areas that were used in the simulations.

pCO_2 [bar]		10	10	10	50	50	50	74	74
T [°C]		25	70	90	25	70	90	70	90
Mineral	***vol.%***	**Surface Area ($m^2_{mineral}\ m^{-3}_{rock}$)**							
Brucite	0.0247	$3.8 \pm 0.3 \times 10^5$	1.0×10^4	$3.5 \pm 2.5 \times 10^3$	$3.8 \pm 0.3 \times 10^5$	$3.5 \pm 2.5 \times 10^3$			
Calcite	0.0010	$6.0 \pm 0.1 \times 10^3$			$2.7 \pm 1.2 \times 10^2$				
Dolomite	0.0002	$3.0 \pm 2.0 \times 10^{-5}$	$7.0 \pm 2.0 \times 10^{-3}$		$3.0 \pm 2.0 \times 10^{-5}$	$7.0 \pm 2.0 \times 10^{-3}$			
Portlandite	0.0008	$6.5 \pm 1.5 \times 10^1$	$4.2 \pm 0.1 \times 10^{-1}$	$3.0 \pm 0.1 \times 10^{-2}$	$6.5 \pm 1.5 \times 10^1$	$5.0 \pm 4.0 \times 10^{-1}$			
Quartz	0.0018	5.5×10^2							
Nesquehonite	0.0	$6.1 \pm 0.1 \times 10^6$	*	*	$6.1 \pm 0.1 \times 10^6$	*	*	*	*
Hydromagnesite	0.0005	$3.0 \pm 2.0 \times 10^{-1}$							
Magnesite	0.0	*	$2.0 \pm 0.1 \times 10^{-1}$		*	$3.0 \pm 2.0 \times 10^0$	$9.9 \pm 0.1 \times 10^1$	$3.0 \pm 2.0 \times 10^0$	$2.9 \pm 0.1 \times 10^2$
Aragonite	0.0	$5.0 \pm 0.1 \times 10^0$							

*not included in the model

Table 5.4 Mineralogical compositions and associated surface areas that were used in the simulations.

Samples	**1**		**2**		**3**		**4**		**5**		**6**		**7**		**8**	
pCO_2 [bar]	10		10		10		50		50		50		74		74	
T [°C]	25		70		90		25		70		90		70		90	
time [h]	74		72		72		72		72		72		72		72	
	vol.%															
Minerals	Exp.	Sim.	Exp.	Sim.	Exp.	Sim.	Exp.	Sim.	Exp.	Sim.	Exp.	Sim.	Exp.	Sim.	Exp.	Sim.
Brucite	15.1	3.0	2.3	8.0	17.4	20.7	11.7	0.0	0.0	9.5	7.5	24.3	13.0	35.3	0.0	0.0
Calcite	13.6	9.4	12.1	1.5	5.6	0.0	3.9	38.7	12.8	3.1	3.2	2.5	8.0	3.6	4.4	1.0
Quartz	3.3	10.4	2.1	5.6	3.8	5.2	4.8	43.4	3.3	6.4	4.3	6.0	4.0	7.0	3.4	5.7
Nesquehonite	**66.6**	**64.8**	0.0	0.0	0.0	0.0	**77.5**	**0.0**	0.0	0.0	0.0	0.0	0.0	0.0	0.0	0.0
Hydromagnesite	0.0	10.9	**35.1**	**33.3**	**47.5**	**45.7**	0.0	12.1	**5.1**	**1.8**	**12.7**	**1.7**	**19.0**	**2.0**	**0.0**	**1.6**
Magnesite	0.0	0.0	**42.0**	**43.0**	**17.1**	**19.0**	1.4	0.0	**71.7**	**71.9**	**63.1**	**58.8**	**50.0**	**43.9**	**91.2**	**83.0**
Dolomite	0.0	1.8	0.0	6.3	0.0	6.3	0.7	5.7	1.0	4.5	3.0	3.2	4.0	6.0	1.1	6.1
Aragonite	1.5	0.1	6.5	0.0	1.7	0.0	0.0	0.1	1.0	0.0	0.0	0.0	2.0	0.0	0.0	0.0
Portlandite	0.0	0.4	0.0	2.3	6.8	3.1	0.0	0.0	5.1	2.7	6.3	3.5	0.0	2.3	0.0	2.6

This variability was associated to the very small content of dolomite in the samples (*vol.*% < 0.6). Also, variability in the reactive surface of portlandite ($3.0 \pm 0.1 \times 10^{-2}$ to $6.5 \pm 1.5 \times 10^{1}$ $m^2_{mineral}$ m^{-3}_{rock}) was attributed to its small content (*vol.*% <3). The reactive surface of quartz was the same over the whole temperature range because its dissolution was very little. Regarding the secondary Mg-bearing minerals, the reactive surface area of nesquehonite was the same in all the experiments at 25 °C (Table 5.2). In the case of hydromagnesite, the reactive surface area was $3.0 \pm 2.0 \times 10^{-1}$ $m^2_{mineral}$ m^{-3}_{rock} over the pCO_2 and temperature ranges of this study. As for magnesite, at 10 bar and 70-90 °C the reactive surface area was merely a factor of 1.5 lower than that of hydromagnesite.

By increasing pCO_2 and temperature (50 and 74 bar and 70-90 °C), magnesite was the most stable Mg-carbonate phase, thus dominating the overall precipitation. In this case, the reactive surface area was increased in order to match the variation in Mg concentration and Mg-mineral volumetric fraction (Tables 5.3 and 5.4). This suggests that the increase in reactive surface area with increasing temperature was related to distinct growth and nucleation of magnesite, which are difficult to predict. The large surface area for nesquehonite at 25 °C indicates that this phase precipitated under or near local equilibrium conditions (only limited by the dissolution rate of the primary minerals). The small amount of precipitated aragonite (*vol.*% between 2 and 7 %) could not be reproduced by the model.

Fig. 5.3 shows the calculated variation of pH throughout the experiments. Overall, pH increased as brucite dissolved. Thereafter steady state is achieved under both subcritical and supercritical pCO_2 conditions. pH is higher at 25 °C than at 70 and 90 °C because brucite dissolution rate is greater at the lowest temperature, independently of pCO_2. Also as expected pH decreases by increasing pCO_2.

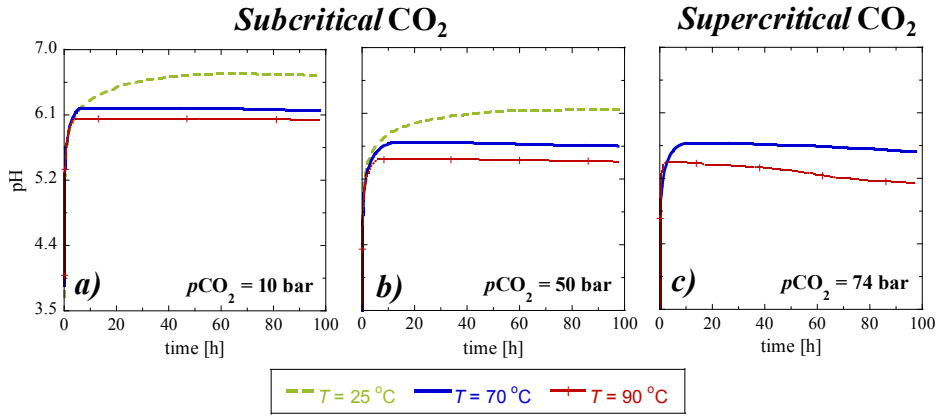

Figure 5.3 *Simulated pH variation with time at different pCO_2 and temperature. a) 10 bar, b) 50 bar, and c) 74 bar.*

At pCO_2 of 10 bar, the calculated saturation index (*SI*) with respect to nesquehonite showed that supersaturation is reached at 25 °C after 40 h. At higher temperatures, the nesquehonite *SI* showed undersaturation during the experiments. Solution was always supersaturated with respect to hydromagnesite and magnesite over the whole temperature range. At pCO_2 of 50 bar, the solution was always undersaturated with respect to nesquehonite and hydromagnesite, while it became quickly supersaturated with respect to magnesite.

Variation of the mineral volume fractions with time under the different pCO_2 conditions is displayed in Figs. 5.4, 5.5 and 5.6. At 10 bar (Fig. 5.4), brucite dissolved with time at all temperatures (e.g., 95 % at 25 °C; Fig. 5.4a). The temperature increase reduced brucite dissolution. Precipitation of calcite only took place at 25 °C, (Fig. 5.4b). Portlandite dissolution occurred at all temperatures, being greater at 25 °C (Fig. 5.4c). Quartz dissolution was negligible (Fig. 5.4d). Dolomite precipitation occurred at high temperature, becoming greater at 70 °C than at 90 °C (Fig. 5.4e). Regarding the Mg-carbonates, nesquehonite precipitated at 25 °C and precipitation of hydromagnesite and magnesite took place at 70 and 90 °C (Fig. 5.4f).

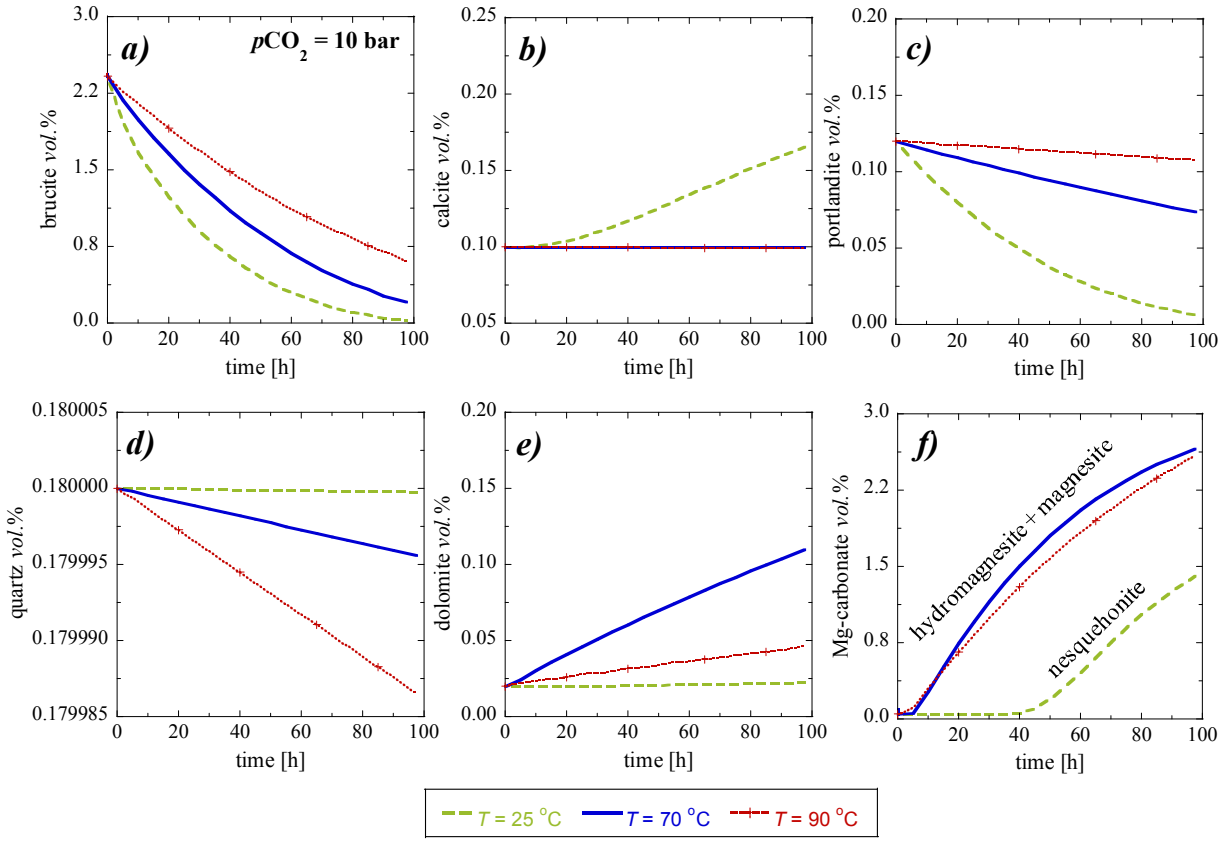

Figure 5.4 *Calculated variation of the mineral volume fraction (vol.%) with respect to time and T at pCO_2 of 10 bar. a) brucite, b) calcite, c) portlandite, d) dolomite e) Mg-carbonates.*

At pCO_2 of 50 and 74 bar, brucite and portlandite also tended to dissolve, and quartz dissolution was also insignificant. Dolomite precipitation also occurred at high temperature. Calcite precipitated at 25 °C and pCO_2 of 50 bar but dissolved at higher temperature (Fig. 5.5a,b). At pCO_2 of 50 bar, nesquehonite did not precipitate at 25 °C. At higher temperature hydromagnesite and magnesite precipitation was favored (Fig. 5.5c). At pCO_2 of 74 bar, precipitation of hydromagnesite and magnesite also occurred but the volume of Mg-carbonate was higher at 90 °C than at 70 °C (Fig. 5.5d).

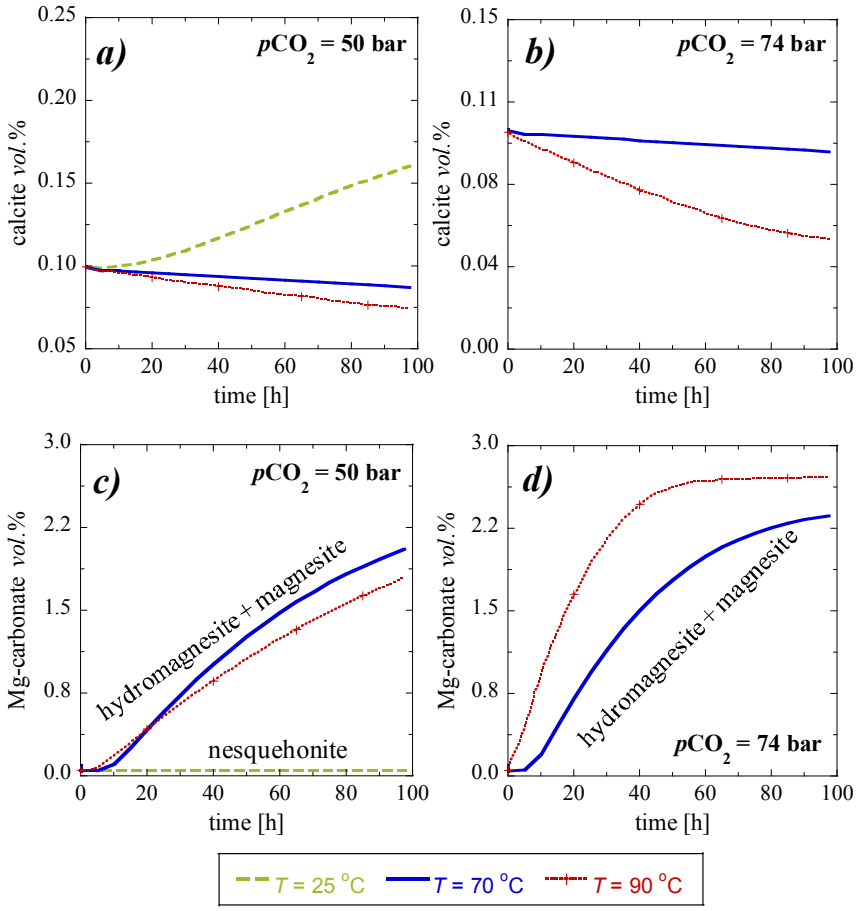

Figure 5.5 *Calculated variation of the mineral volume fraction (vol.%) with respect to time and T at pCO_2 of 50 bar. a) calcite, b) Mg-carbonates, and at pCO_2 of 74 bar c) calcite and d) Mg-carbonates.*

Variation in porosity normalized with respect to the initial total mineral *vol.*% is shown in Fig. 5.6. At pCO_2 of 10 and 50 bar, porosity was higher at 25 °C than at higher temperature. At 10 bar and 25 °C, porosity gradually increased to thereafter decrease because nesquehonite precipitation took place. On the contrary, porosity gradually increased at pCO_2 of 50 bar owing to the lack of nesquehonite precipitation. At pCO_2 of 74 bar (supercritical CO_2 conditions), porosity was higher at 70 than at 90 °C. A final overall decrease in porosity occurred at 90 °C.

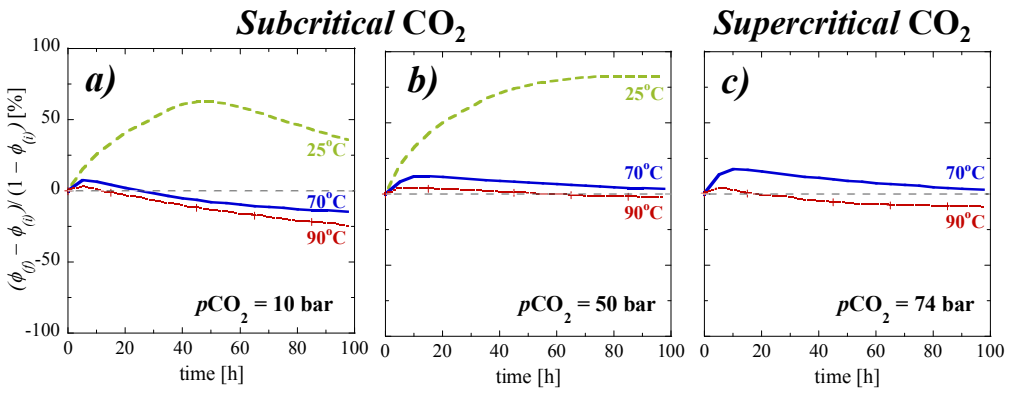

Figure 5.6 *Calculated porosity variation with time at different pCO_2 and T. a) 10 bar, (b) 50 bar and (c) 74 bar.*

The variation in mineral volume fraction under all pCO_2 conditions and 90 °C is shown in Fig. 5.7. Dissolution of brucite was favored by a pCO_2 increase (Fig. 5.7a). Likewise, dissolution of calcite and portlandite and precipitation of dolomite were favored by the increase in pCO_2 (Fig. 5.8b,c,d). Precipitation of hydromagnesite and magnesite was also favored by the increase in pCO_2 (Fig. 5.8e). The balance between these reaction led to an initial increase in porosity, followed by a gradual decrease, being greater at lower pCO_2 (Fig . 5.7).

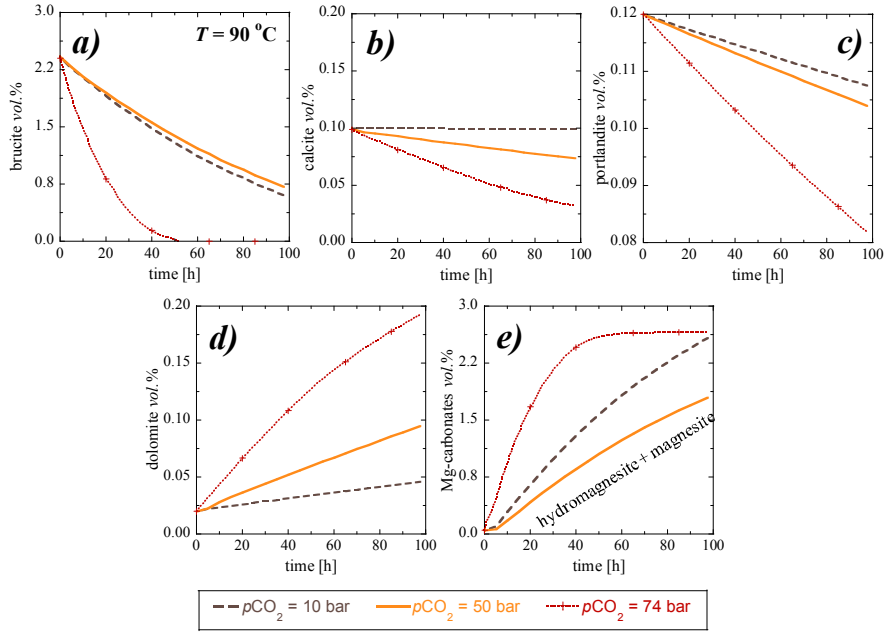

Figure 5.7 *Variation of the simulated volume (vol.%) of minerals with respect to time at different sub- and sc-pCO_2 at constant temperature of 90 °C a) brucite, b) calcite, c) portlandite, d) dolomite and e) Mg-carbonates.*

The measured (Exp.) and calculated (Sim.) variation in volume fractions are given in Table 5.4. Considering the low values of measured concentrations and the uncertainty associated to the Rietveld analysis, a good match between the calculated and measured values can be assumed when the differences are ≤ 7 *vol.*%. In general, the calculated mineral volume fractions were in a good agreement with the measured ones, although some discrepancies were found (Table 5.4): at 10 bar (25-70 °C), there was a mismatch about 10-12 *vol.*% between the calculated volume fraction and the measured one of brucite, hydromagnesite and calcite. At high pCO_2 (50 and 74 bar), the calculated brucite volumetric fraction was always greater than the simulated one, except for the experiment at 74 bar and 90 °C, where brucite was exhausted. At 50 bar, the calculated volume fractions of calcite (70 °C) and hydromagnesite (90 °C) were lower than the measured ones (10-11 *vol.* %). At 74 bar, the calculated volume fractions of hydromagnesite (70 °C) and magnesite (90 °C) were lower than the measured ones (9-17 *vol.*%).

It is suggested that discrepancies were to be expected since experimental nucleation of precipitated Mg-bearing minerals was hardly quantifiable, and small changes in reactive surface area might generate large variation in the mineral volumetric fraction. In addition, it is highlighted that at 50 bar and 25 °C the measured nesquehonite volume fraction could not be reproduced at all, suggesting possible uncertainly in the log K_{eq} for nesquehonite and its dependence on *P*.

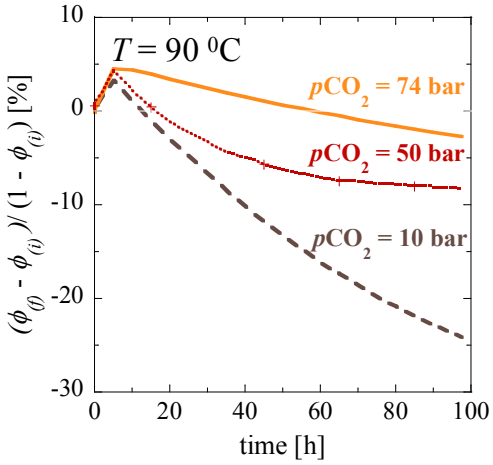

Figure 5.8 *Simulated normalized porosity [%] variation with time at different sub- and sc- pCO_2 and T = 90 °C.*

5.2.3 Application case: borehole-cement-reservoir rock interface

The geological sequestration of CO_2 involves injection through wells. Boreholes are usually surrounded by a layer of Portland cement mortar (Carey et al., 2007; Duguid et al., 2011; Scherer et al., 2011). In this work, MgO-based cement is studied as an alternative to Portland cement. This section intends to illustrate how the interaction between CO_2-rich water and the Mg-based cement surrounding the well at depth could occur. This scenario assumes a leak in the well casing causing diffusive exchange between the CO_2-rich water in the borehole, the Mg-based cement and eventually the limestone reservoir rock (Fig. 5.9). This process could induce changes in the composition of the original MgO-based cement mainly due to brucite dissolution and magnesite precipitation and cause variation in its porosity and sealing capacity.

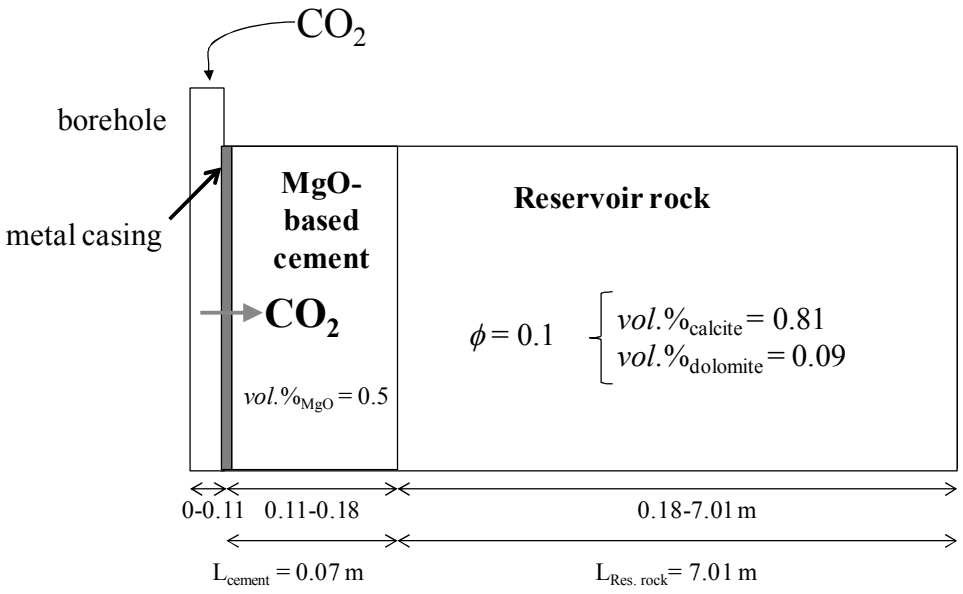

Figure 5.9 *Schematic representation of the modeled scenario in which CO_2-rich water diffuses through the MgO cement and the reservoir rock. Distances are from the center of the borehole.*

1-D modeling with symmetry around the borehole axis was performed considering that solute transport is dominated by diffusion perpendicular from the well to the reservoir rock. Effective diffusion coefficients in the model were calculated from $D_{eff} = \phi\alpha D_o$, where ϕ is porosity, α is a lithology factor and D_o is the diffusion coefficient in water (4.5×10^{-9} m^{-2} s^{-1} at 90 °C; Samson et al. (2003)). The initial effective diffusion coefficient (D_{eff}) was assumed to be 1.13×10^{-11} m^2 s^{-1}, which is a value in the range for Portland cement grouts (Laurila et al., 2005; Soler et al., 2010; 2011). Nonetheless, a sensitivity analysis was carried out

considering that the initial effective diffusion coefficient in the cement ranged from 1.13×10^{-12} to 1.13×10^{-10} m^2s^{-1} (Table 5.5). D_{eff} in the model changed linearly with porosity.

Table 5.5 Initial effective diffusion coefficients used for the sensitivity analysis in the simulations.

	Initial Porosity	Effective diffusion coefficient *Deff** (m^2 s^{-1})
well boundary conditions	1	4.5×10^{-9}
MgO-based cement (fast)	0.5	1.1×10^{-10}
MgO-based cement (reference)	0.5	1.1×10^{-11}
MgO-based cement (low)	0.5	1.1×10^{-12}
Limestone rock	0.1	4.5×10^{-11}

Details of the spatial discretization are given in Table 5.6. Initial porosities of the MgO-based cement and the reservoir rock are 0.5 (50%) and 0.1 (10%), respectively. The initial water in the MgO-based cement is water at atmospheric conditions with pH of 5.82 (Table 5.7). The initial composition of porewater in the reservoir rock is at equilibrium with respect to calcite and dolomite with a pH of 7.5 (Table 5.7). The CO_2-rich water is considered to be at 150 bar and 90 °C (e.g., at supercritical CO_2 conditions), yielding a pH of 3.17 (Table 5.7). The values of the mineral surface areas of the MgO-based cement are those obtained from the laboratory simulations (see *Section 5.2.1.1;*Table 5.2), and the values in the rock are considered large enough close to local equilibrium to allow dissolution (8.6×10^6 $m^2_{mineral}$ m^{-3}_{rock}).

Table 5.6 Spatial discretization (number of nodes and grid spacing).

Zones	N nodes	grid spacing (m)
well	11	0.010
MgO-based cement	13	0.005
	05	0.001
reservoir rock	05	0.001
	10	0.005
	10	0.020
	15	0.050
	20	0.050
	16	0.250
	04	0.250

The pH variation with distance from the borehole to the reservoir rock is shown in Fig. 5.10a. In the borehole, the CO_2-rich water at pCO_2 of 150 bar and 90 °C has a constant pH of 3.17. Fast equilibration of the cement porewater with brucite causes a fast initial increase in pH to values close to 9. Diffusive exchange with the CO_2-rich water in the borehole causes a gradual decrease in the pH of the cement porewater (Fig. 5.10b). The composition of the reservoir rock porewater is disturbed up to a distance of 7 m from the borehole after 300 y (Fig. 5.10b).

Table 5.7 Chemical composition (total concentrations and pH) of the initial waters used in the simulations.

	well (boundary conditions)		MgO-based cement		reservoir rock	
Component	**Constraint**	**Concentration (mol kgw^{-1}) or pH**	**Constraint**	**concentration (mol kgw^{-1}) or pH**	**constraint**	**concentration (mol kgw^{-1}) or pH**
HCO_3^-	pCO_2=150bar, 90°C	1.01×10^{0}	atm pCO_2 & 90°C	3.8×10^{-4}	charge balance	5.6×10^{-3}
Ca^{+2}	fixed	1.0×10^{-9}	fixed	1.0×10^{-9}	calcite	4.1×10^{-4}
pH	charge balance	3.17	charge balance	5.82	fixed	7.50
Mg^{+2}	fixed	1.0×10^{-9}	fixed	1.0×10^{-9}	dolomite	1.5×10^{-5}
$SiO_{2(aq)}$	fixed	1.0×10^{-9}	fixed	1.0×10^{-9}	fixed	1.0×10^{-9}

As the CO_2-rich water interacts with the cement, a front originates in which porosity decreases from 50 % to ca. 41 % (Fig. 5.10c) as a result of magnesite precipitation induced by the dissolution of brucite. Notice also the advance of a high-porosity front starting at the borehole-cement interface (Fig. 5.10c). The advance of this front is caused by the dissolution of magnesite in contact with the CO_2-rich water in the borehole.

At longer times, precipitation of dolomite at the cement-rock interface results in the complete sealing of porosity at the interface (t ca. 200 y; Fig. 5.10d). Dolomite precipitation is caused by the dissolution of magnesite (cement side of the interface) and calcite (rock side of the interface). The sealing of porosity would be beneficial for the isolating properties of the cement. In the rock side of the interface porosity increases from 10 to 18 % (~ 0.18 m), due to the dissolution of calcite.

A limited sensitivity analysis was performed by changing the initial effective diffusion coefficient (D_{eff}) of the cement to one order of magnitude smaller (1.13×10^{-12} m^2 s^{-1}) and larger (1.13×10^{-10} m^2 s^{-1}) values (Fig. 5.11). It is inferred that with the larger value of D_{eff}, pH along the distance is lower (Fig. 5.11a). As a consequence, brucite dissolution enhances, originating a fast advance of the high-porosity front (Fig. 5.11b), which would be highly detrimental for the performance of the cement.

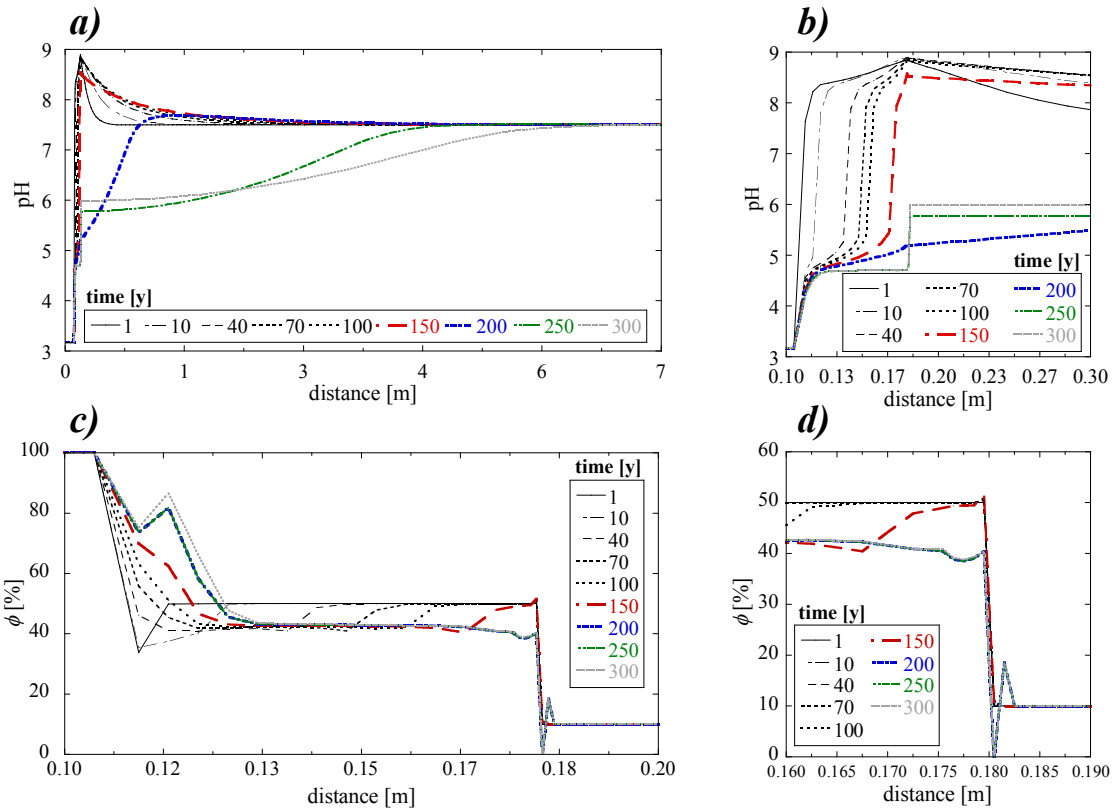

Figure 5.10 *Simulations of a) pH variation along the domain (wellbore from 0-0.11 m, MgO plug cement from 0.11-0.18 m and reservoir rock from 0.18-7.01 m); b) detailed variation of porosity at the cement/rock interface zones; c) porosity variation from 0.10 to 0.20 m and d) detailed variation of porosity at the interface MgO layer/reservoir rock. Time spans from 1 to 300 years.*

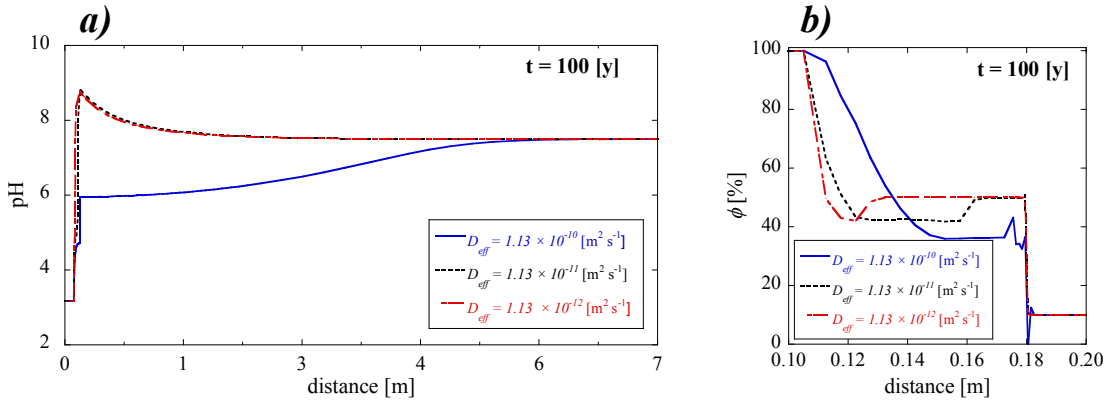

Figure 5.11 *Sensitivity analysis on simulations: variation of pH (a) and porosity (b) with distance by changing the effective diffusion coefficient (D_{eff}).*

5.3 Summary and conclusions

Batch experiments conducted at different pCO_2 and temperature (10, 50 and 74 bar and 25, 70 and 90 °C) were useful to study the evolution of MgO carbonation, which involves the fast hydration of MgO to brucite, the dissolution of brucite and the precipitation of magnesium carbonates. Numerical simulations of the experimental results allow quantification of the overall process. Altogether sheds light on the potential application of MgO-based cement as alternative cement in a context of CO_2 sequestration.

An increase in pCO_2 favors brucite dissolution, promoting formation of magnesium carbonates. At 10, 50 and 74 bar, increasing temperature hydrated Mg-carbonates (nesquehonite) transformed into those that are less hydrated (hydromagnesite and magnesite). Calcite, portlandite and quartz dissolution and dolomite and calcite precipitation are only minor. The balance between these reaction leads to a decrease in porosity by increasing temperature and decreasing pCO_2.

Initial values of the reactive surface areas of primary and secondary minerals were adjusted in order to numerically reproduce the experimental results. However, at 25 °C and 50 bar, nesquehonite (observed by XRD in the precipitates) was not calculated to precipitate. Fitting of the model aqueous Mg concentration and mineral volume fractions involved the use of large surface area for nesquehonite (25 °C) indicating that this phase precipitates under or near local equilibrium conditions (only limited by the dissolution rate of the primary minerals). Dolomite precipitation is always strongly inhibited.

Simulations over 300 years of an application case in a borehole in a limestone reservoir rock, show that brucite dissolution and magnesite precipitation lead to a decrease of the initial porosity of the cement from 50 to 42 %. Additionally, magnesite precipitation at the cement-rock interface leads to the sealing of porosity. These decreases in porosity would be beneficial for the performance of the cement. However, fast dissolution of magnesite at the contact with the borehole was calculated for the case with a large effective diffusion coefficient, which would be detrimental for performance under those conditions.

Chapter VI

Conclusions

The main conclusions of this thesis are:

1) From **the flow-through experiments** run to obtain illite dissolution rates at P_{Total} = 1 bar, $p\mathrm{CO_2}$ = $10^{-3.5}$ bar and 25 °C at the acidic pH range of 2.1-4.2:

- The illite dissolution rate decreased with pH, such that the obtained pH-rate dependence was similar to that reported by Köhler et al. (2003).

- It was observed that ongoing calcite dissolution and gypsum precipitation did not affect the illite dissolution rates.

2) From **the column experiments** performed to study the effect of P_{Total}, $p\mathrm{CO_2}$, T, mineralogy and sulfate content on the coupled dissolution and precipitation reactions (crushed rock):

- Columns experiments filled with crushed Hontomín caprock samples (*S2.4*, *S3.4* and *S4.3*), with an initial porosity of ca. 50%, proved to be useful to investigate the effects that the mineral composition, sulfate content, temperature, and $p\mathrm{CO_2}$ exert on the Hontomín caprock reactivity.

- Overall, dissolution of calcite was larger than that of albite, illite and clinochlore, and precipitation of gypsum was larger than that of kaolinite, mesolite, scolecite and stilbite. Hence, coupled reactions of mineral dissolution and precipitation yielded larger volume of dissolved calcite and Si-bearing minerals (illite, albite and clinochlore) than volume of precipitated gypsum and Si-bearing minerals (kaolinite, mesolite, scolecite and stilbite), yielding a porosity increase in all experiments.

- Regarding the mineral composition, it was observed that an increase in initial calcite content in the rock (67.1 *wt.%* (*S3.4*), 71.2 *wt.%* (*S4.3*) and 87.3 *wt.%* (*S2.4*)) leads to small differences in porosity increase ($\Delta\phi$ = 0.36 (*S3.4*), 0.28 (*S4.3*) and 0.34 (*S2.4*)), yet considering that the volume of dissolved calcite was larger with larger calcite content (V_{Cal} = 0.053 cm^3

(*S2.4*), 0.048 cm^3 (*S4.3*) and 0.039 cm^3 (*S3.4*)). The discrete differences in the content of illite, albite and chlinochlore among the three marl samples barely affect their reactivity, resulting in similar variation of porosity near the inlet and along the column.

- Regarding the sulfate content, it was observed that the increase in porosity ($\Delta\phi_{25\,°C}$ = 0.05 (*S2.4*), 0.10 (*S3.4*) and 0.06 (*S4.3*)) was 15-30% lower in the presence of sulfate, and $\Delta\phi$ slightly varied with temperature ($\Delta\phi_{60\,°C}$ =0.11 (*S2.4*), 0.08 (*S3.4*) and 0.09 (*S4.3*)).

- Regarding the overall temperature effect, it was demonstrated that the volume of dissolved calcite increased by decreasing temperature, whereas the volume of precipitated gypsum was barely influenced by temperature variation. In general, the increase in porosity under any pCO_2 was higher at the lowest temperature. Simulations showed that an increase in temperature reduced creation of porosity near the inlet when pCO_2 increased (e.g., pCO_2 = 10 bar).

- Regarding the pCO_2 effect on the Hontomín caprock reactivity. When rising pCO_2, the calcite dissolution rate increased along the column because of the direct correlation between pCO_2 and pH. Dissolution of the clinochlore, albite and illite was always minor in acidic pH and is controlled, under atmospheric pressure, by the protons provided by the strong acid (HCl), whereas under high pCO_2, H_2CO_3 partial dissociation controls the dissolution. Modeling results show that if the solution acidity is controlled by a strong acid, dissolution occurs exclusively at the first rock-solution contact, raising the pH at ≈ 7 and limiting the calcite dissolution further away. In contrast, simulations under high pCO_2 conditions show that pH remains acidic (≈ 5) and the solution is permanently undersaturated with respect to calcite, clinochlore, albite, illite and pyrite (due to the carbonic acid buffer capacity), yielding a higher increase in porosity all over the rock-solution contact.

- Match of the output concentrations in solution was obtained using CrunchFlow reactive transport calculations. The fit of the model to the experimental data was performed by adjusting the values of the reactive surface areas. The calcite reactive surface area values were diminished by one and two orders of magnitude from the initially calculated geometric surface areas. The adjusted values of the reactive surface areas were small probably due to transport control of the

reaction. It should be noted that the values for the reactive surface area for calcite ranged from 3 to 6 m^2_{min} m^{-3}_{bulk} in the simulations under atmospheric pCO_2, whereas under higher pCO_2 (10-37 bar) the values ranged from 90 to 170 m^2_{min} m^{-3}_{bulk}. This increase could be associated to higher transport control of the reaction at lower pH at higher pCO_2. A single value for illite (1×10^7 m^2_{min} m^{-3}_{bulk}) provided a good fit of the model to all experimental results, supporting the applicability of this modeling approach. For the rest of primary Si-bearing minerals with lower content in the rocks, the range was between 2×10^5 m^2_{min} m^{-3}_{bulk} and 3×10^9 m^2_{min} m^{-3}_{bulk}.

- In the light of our findings, CO_2-rich solutions in contact with a fractured marl caprock favor CO_2 migration pathways if *(1)* groundwater has a low content of sulfate that prevents gypsum precipitation and/or if *(2)* the fluid flow is fast. By contrast, sealing of the fractures takes place if gypsum precipitates and the flow rates are slow.

3) From **the percolation experiments** run under P_{Total} = 150 bar, pCO_2 = 61 bar and T = 60 °C (supercritical CO_2 conditions) with *S-free* and *S-rich* solutions injected at different flow rates (0.2, 1 and 60 mL h^{-1}) to better understand the reactivity of the Hontomín marl caprock (fractured cores):

- Calcite dissolution was the main reaction because of the acidic character of the injected solutions under supercritical pCO_2. Results based on the experimental aqueous chemistry showed that the overall process was not affected by changing the ionic strength from 0.3 to 0.6 M. In *S-free* solutions, dissolution of calcite, primary gypsum, clinochlore and albite took place. In *S-rich* solutions in equilibrium with gypsum, dissolution of clinochlore and albite took place as did that of calcite, which promoted gypsum precipitation. A Si deficit suggests that dissolution of the silicate minerals triggers precipitation of Si-bearing secondary minerals (e.g., kaolinite and amorphous SiO_2 gel).

- The dissolution and precipitation reactions controlled the variations in the final pore volume associated with the reacted core. In all experiments, an increase in the flow rate led to an increase in the calcite dissolution rate and in the final pore volume associated with the reacted core. In the *S-rich* solution, the volume of dissolved calcite was always larger than the volume of

precipitated gypsum. The dissolution of calcite grains and, to a lesser extent, the dissolution of clinochlore and albite, created a high porosity zone (ϕ ranged from 48 to 67 %) along the fracture walls. This porosity zone was composed of non-dissolved quartz, pyrite and illite grains, precipitated gypsum (in *S-rich* solutions) and precipitated Si-bearing phases (e.g., kaolinite or amorphous SiO_2).

- As for the dissolution patterns, in the *S-free* solution experiments, face dissolution occurred at slow flow rates (*Pe* of 4 and 21), whereas at the highest flow rate (*Pe* = 1267), wormhole formation was observed. However, in *S-rich* solution experiments, face dissolution occurred only at the slowest flow rate. At an intermediate flow rate range, both uniform dissolution and wormhole took place. A combination of wormhole formation and uniform dissolution dominated at the highest flow rate. In both types of solution, local heterogeneities controlled mineral dissolution along the fracture, which could lead to unexpected dissolution patterns associated with different *Pe* values.

- As for the fracture permeability, at slow flow rate (low *Pe*), in *S-free* solutions, k_f did not significantly change since face dissolution did not cause the fracture aperture to vary. Moreover, detached grains along the fracture could lead to the obstruction of the fluid flow, preventing a k_f increase. In *S-rich* solutions, a marked decrease in k_f was attributed to gypsum precipitation. At fast flow rate (high *Pe*), k_f slightly increased with slight variations in aperture with the *S-free* solution. In the *S-rich* solution, the increase in k_f was attributed to the absence of gypsum precipitates. This suggests the existence of flow through the altered rock matrix. Nevertheless, the small differences in composition and/or structure between different samples may exert a considerable influence on the reproducibility of the experimental results, passivation of gypsum or inhibition of calcite dissolution in the presence of sulfate, movement of grains, and on the obstruction of flow paths. These phenomena play a central role in fracture permeability.

- Two dimensional reactive transport modeling has been applied to interpret the results from the experiments with marl fractured cores during the injection of CO_2-rich solutions under supercritical conditions. Calculated solution composition of the outlet compares reasonably well with the variation in the measured concentrations under slow flow rates, whereas at fast flow rate experiments poor match was obtained. Likewise, the simulations reproduced the dimensions of

the dissolution patterns observed in the ESEM and XMT images, except for the experiment run at high flow rate (60 mL h^{-1}) and *S-free* solution in which a wormhole formed due to local heterogeneity. The fraction of a porous, altered zone was also predicted by the simulation.

- A successful match (except for fast flow rate) between the experimental and calculated output concentrations was achieved by using a D_{eff} between 1×10^{-13} and 3×10^{-13} m^2 s^{-1} at low flow rate, whereas a larger value (6×10^{-12} m^2 s^{-1}) was used at high flow rate. Regarding the mineral surface area values, a single value for calcite was used in the *S-rich* solution experiments ($1.2 \pm 0.7 \times 10^4$ $m^2_{mineral}$ m^{-3}_{rock}), whereas in *S-free* solution experiments the area was slightly increased in the faster flow rate experiments (1 and 60 mL h^{-1}). The surface areas for the rest of the minerals were not changed.

- Different compositions of the injected solutions produced different effects on the dissolution and precipitation processes in the Hontomín caprock. The main reaction that occurred was dissolution of calcite in both types of injected solutions. For the same experimental time and under the same flow rate, the volume of dissolved calcite was always larger in the *S-free* solution experiments than in the *S-rich* ones. In *S-rich* solution experiments, gypsum precipitated and in a larger amount in the experiment run at 1 mL h^{-1}. Dissolution of clinochlore, albite and pyrite, and precipitation of dolomite, illite, kaolinite, mesolite and stilbite took also place. Precipitation of secondary Al and Si rich minerals was expected by the mass balance calculated from the laboratory experiments, but it was never observed by the ESEM images.

- During the experiments, the mineral reaction rates increased larger in the fracture-rock matrix interface as a result of the interaction with the acidic solution. Inside the rock matrix solute transport was controlled by diffusion, which could not happen under fast flow rate.

- In both types of solution, the calculated porosity in the reacted zone was higher at the fracture wall contact and decreased with distance normal to fracture. An increase in the flow rate caused an increase in porosity. The increase in porosity was higher at the inlet of the core than at the outlet, but the difference between the inlet and the outlet lowered by increasing the flow rate. The increase in porosity from 6 % to ≈ 60 % was similar to the volume of calcite dissolved (≈ 60 %).

➢ In the light of our findings, CO_2-rich solutions in contact with a fractured marl caprock favor CO_2 migration pathways if *(1)* groundwater has a low content of sulfate that prevents gypsum precipitation and/or if *(2)* the fluid flow is fast. By contrast, sealing of the fractures takes place if gypsum precipitates -as it could happen in the Hontomín site- and the flow rates are slow.

4) From the **batch experiments** conducted at different pCO_2 and temperature (10, 50 and 74 bar and 25, 70 and 90 °C) to study the evolution of MgO carbonation:

➢ MgO carbonation involves the fast hydration of MgO to brucite, the dissolution of brucite and the precipitation of magnesium carbonates. An increase in pCO_2 favors brucite dissolution, promoting formation of magnesium carbonates. At 10, 50 and 74 bar, increasing temperature hydrated Mg-carbonates (nesquehonite) transformed into those that are less hydrated (hydromagnesite and magnesite). Calcite, portlandite and quartz dissolution and dolomite and calcite precipitation are only minor. The balance between these reaction leads to a decrease in porosity by increasing temperature and decreasing pCO_2.

➢ Initial values of the reactive surface areas of primary and secondary minerals were adjusted in order to numerically reproduce the experimental results. However, at 25 °C and 50 bar, nesquehonite (observed by XRD in the precipitates) was not calculated to precipitate. Fitting of the model aqueous Mg concentration and mineral volume fractions involved the use of large surface area for nesquehonite (25 °C) indicating that this phase precipitates under or near local equilibrium conditions (only limited by the dissolution rate of the primary minerals). Dolomite precipitation is always strongly inhibited.

➢ Simulations over 300 years of an application case in a borehole in a limestone reservoir rock, show that brucite dissolution and magnesite precipitation lead to a decrease of the initial porosity of the cement from 50 to 42 %. Additionally, magnesite precipitation at the cement-rock interface leads to the sealing of porosity. These decreases in porosity would be beneficial for the performance of the cement. However, fast dissolution of magnesite at the contact with the

borehole was calculated for the case with a large effective diffusion coefficient, which would be detrimental for performance under those conditions.

- The obtained reduction of porosity related to the interaction between MgO and CO_2-rich solutions (25 °C < T ≤ 90 °C) suggests that a MgO-based cement could become a suitable material to seal porosity. From this seal capacity it is inferred that MgO-based cement could represent an alternative to Portland cement.

Appendix 1

Table A1 Equilibrium constants (log K_{eq}) for the homogeneous reactions considered in the reactive transport model. Reactions are written as the destruction of 1 mol of the species in the table and in terms of Ca^{2+}, Mg^{2+}, HCO_3^-, H^+, SO_4^{2-}, Na^+, K^+, Al^{3+}, Cl^-, Br^-, Fe^{2+}, $SiO_{2(aq)}$ and $O_{2(aq)}$.

Species	log $K_{T=60°C}$
$Al(OH)_2^+$	8.75
$Al(SO4)_2^-$	-4.90
AlO_2^-	19.60
$AlOH^{++}$	4.00
$AlSO_4^+$	-3.01
$CO_{2(aq)}$	-6.27
CO_3^{--}	10.10
$CaCO_{3(aq)}$	6.45
$CaCl^+$	0.59
$CaCl_{2(aq)}$	0.62
$CaHCO_3^+$	-1.16
$CaOH^+$	12.90
$CaSO_{4(aq)}$	-2.27
$Fe(OH)_{2(aq)}$	20.60
$Fe(OH)_3^-$	31.00
$Fe(OH)_4^{--}$	46.00
$FeCO_{3(aq)}$	5.60
$FeCl^+$	0.03
$FeCl_{2(aq)}$	2.21
$FeCl_4^{--}$	-1.55
$FeHCO_3^+$	-2.72
$FeOH^+$	9.50
$FeSO_{4(aq)}$	-2.20
$H_2SO_{4(aq)}$	1.02
$H_2SiO_4^{--}$	23.00
$HAlO_{2(aq)}$	13.70
$HCl_{(aq)}$	-0.67
HSO_4^-	-2.44
$HSiO_3^-$	9.48
$KBr_{(aq)}$	1.45
$KCl_{(aq)}$	1.21

$KHSO_{4(aq)}$	-1.48
$KOH_{(aq)}$	14.50
KSO_4^-	-0.99
$Mg_4(OH)_4^{++++}$	39.80
$MgCO_{3(aq)}$	6.92
$MgCl^+$	0.05
$MgHCO_3^+$	-1.16
$MgSO_{4(aq)}$	-2.84
$NaAlO_{2(aq)}$	20.10
$NaBr_{(aq)}$	1.17
$NaCO_3^-$	10.10
$NaCl_{(aq)}$	0.65
$NaHCO_{3(aq)}$	0.11
$NaHSiO_{3(aq)}$	8.06
$NaOH_{(aq)}$	13.80
$NaSO_4^-$	-0.82
OH^-	13.00
HS^-	122.00
$S_2O_3^{--}$	118.00
Br_3^-	-6.34
BrO^-	10.30
BrO_3^-	15.90
BrO_4^-	30.30
$CO_{(aq)}$	36.50
ClO^-	14.00
ClO_2^-	21.10
ClO_3^-	15.80
ClO_4^-	14.70
Fe^{+++}	-6.66
$H_{2(aq)}$	41.00
HSO_5^-	14.60
SO_3^{--}	41.70
$Br_{2(aq)}$	-4.77
HO_2^-	26.00
$HS_2O_3^-$	133.00
S_2^{--}	215.00
$S_2O_4^{--}$	104.00
$S_2O_6^{--}$	44.70
$S_2O_8^{--}$	18.80
$S_3O_6^{--}$	128.00
$S_4O_6^{--}$	196.00
$S_5O_6^{--}$	292.00
$Fe(OH)_2^+$	-0.99

$Fe(OH)_{3(aq)}$	5.34
$Fe(OH)_4^-$	14.90
$Fe(SO_4)_2^-$	-9.88
$Fe_2(OH)_2^{++++}$	-10.40
$Fe_3(OH)_4^{(5+)}$	-13.70
$FeCO_3^+$	-5.25
$FeCl^{++}$	-6.61
$FeCl_2^+$	-8.79
$FeCl_4^-$	-5.87
$FeOH^{++}$	-4.47
$FeSO_4^+$	-9.25
$H_2S_{(aq)}$	115.00
$H_2SO_{3(aq)}$	32.50
$HBrO_{(aq)}$	2.96
$HClO_{(aq)}$	6.38
$HClO_{2(aq)}$	17.90
HSO_3^-	34.20
S^{--}	134.00
$S_2O_5^{--}$	73.30
$SO_{2(aq)}$	32.00

Table A2 Mineral and gas equilibrium constants (log K_{eq}) considered in the reactive transport model. Reactions are written as the destruction of 1 mol of the species Ca^{2+}, Mg^{2+}, HCO_3^-, H^+, SO_4^{2-}, Na^+, K^+, Al^{3+}, Cl^-, Br^-, Fe^{2+}, $SiO_{2(aq)}$ and $O_{2(aq)}$.

Mineral reactions	
Species	**log $K_{T=60°C}$**
calcite	1.33
quartz	1.33
illite	-3.47
albite	5.58
gypsum	5.58
clinochlore	5.58
anhydrite	1.59
pyrite	1.59
kaolinite	1.59
SiO2(am)	-4.74
dolomite-dis	50.23
mesolite	-4.76
stilbite	190.98
smectite	3.86
mordenite	3.86
scolecite	3.86
analcime	-2.40
wairakite	2.65
laumontite	2.65
gismondine	10.09
Gas reactions	
Species	**log $K_{T=60°C}$**
$CO_{2(g)}$	-8.05
$O_{2(g)}$	-3.06

Figure A1 Simulated pH variation with respect to time in the *S-rich* (left) and in the *S-free* (right) injected solutions at the different flow rates (0.2, 1 and 60 mL h^{-1}).

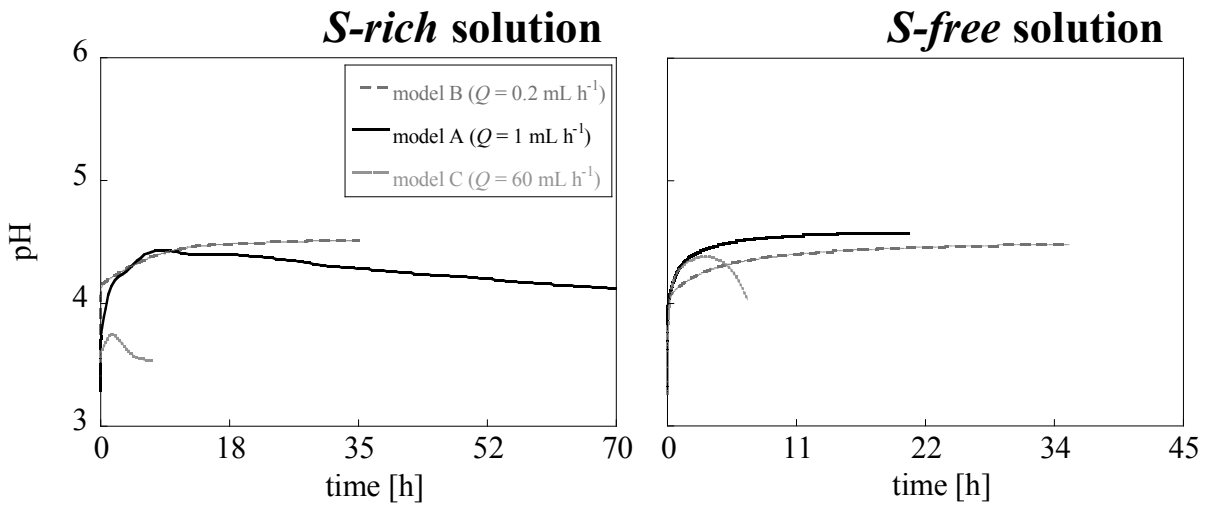

Appendix 2

Table B1 Homogeneous reactions (speciation) considered in the reactive transport model. Reactions are written as the destruction of 1 mole of the species in the first column.

				Stoichiometric coefficients					
species	**Log $K_{T=25°C}$**	**Log $K_{T=70°C}$**	**Log $K_{T=90°C}$**	**Ca^{+2}**	**Mg^{+2}**	**$SiO_{2\,(aq)}$**	**HCO_3^-**	**H^+**	**H_2O**
$CO_{2(aq)}$	-6.34	-6.28	-6.35	0	0	0	1	1	-1
CO_3^{--}	10.33	10.11	10.09	0	0	0	1	-1	0
$CaCO_{3(aq)}$	7.01	6.31	6.07	1	0	0	1	-1	0
$CaHCO_3^+$	-1.04	-1.22	-1.35	1	0	0	1	0	0
$CaOH^+$	12.85	12.85	12.85	1	0	0	0	-1	1
$H_2SiO_4^{--}$	22.96	22.96	22.96	0	0	1	0	-2	2
$HSiO_3^-$	9.94	9.36	9.17	0	0	1	0	-1	1
$Mg_4(OH)_4^{++++}$	39.75	39.75	39.75	0	4	0	0	-4	4
$MgCO_{3(aq)}$	7.36	6.82	6.64	0	1	0	1	-1	0
$MgHCO_3^+$	-1.03	-1.22	-1.36	0	1	0	1	0	0
OH^-	13.99	12.81	12.43	0	0	0	0	-1	1

Table B2 Mineral reactions considered in the reactive transport model. Reactions are written as the dissolution of 1 mole of mineral.

Minerals	log $K_{T=25°C}$	log $K_{T=70°C}$	log $K_{T=90°C}$	Ca^{+2}	Mg^{+2}	$SiO_{2\,(aq)}$	HCO_3^-	H^+	H_2O
Brucite	16.30	13.77	12.86	0	1	0	0	-2	2
Calcite	1.85	1.19	0.91	1	0	0	1	-1	0
Dolomite	2.52	1.00	0.38	1	1	0	2	-2	0
Quartz	-4.01	-3.35	-3.16	0	0	1	0	0	0
Portlandite	22.56	19.61	18.55	1	0	0	0	-2	2
Nesquehonite	5.14	4.67	4.68	0	1	0	1	-1	3
Hydromagnesite	30.87	23.78	21.13	0	5	0	4	-6	6
Magnesite	2.30	1.21	0.78	0	1	0	1	-1	0
Aragonite	2.00	1.33	1.05	1	0	0	1	-1	0

References

Abdoulghafour, H., Luquot, L., Gouze, P., 2013. Characterization of the Mechanisms Controlling the Permeability Changes of Fractured Cements Flowed Through by CO_2-Rich Brine. Environ. Sci. Technol. 47, 10332–10338.

Adams, E.E., Caldeira, K., 2008. Ocean storage of CO_2. Elements 4, 319–324.

Alemu, B.L., Aagaard, P., Munz I.A., Skurtveit, E., 2011. Caprock interaction with CO_2: A laboratory study of reactivity of shale with supercritical CO_2 and brine. Appl. Geochem. 26, 1975–1989.

Andreani, M., Gouze, P., Luquot, L., Jouanna, P., 2008. Changes in seal capacity of fractured claystone caprocks induced by dissolved and gaseous CO_2 seepage. Geophys. Res. Lett. 35, L14404.

Angeli, M., Soldal, M., Skurtveit, E., Aker, E., 2009. Experimental percolation of supercritical CO_2 through a caprock. Energy Procedia 1, 3351–3358.

Bachu, S., Bennion, D.B., 2009. Experimental assessment of brine and/or CO_2 leakage through well cements at reservoir conditions. Int. J. Greenh. Gas Con. 3, 494–501.

Bandstra, J.Z., Buss, H.L., Campen, R.K., Liermann, L.J., Moore, J., Hausrath, E.M., Navarre-Sitchler, A.K., Jang, J-H., Brantley, S.L., 2008. Appendix: Compilation of Mineral Dissolution Rates, in: Brantley, S.L., Kubicki, J.D., White, A.F. (Eds.), Kinetics of Water Rock Interactions, Springer, pp. 737–823.

Bardot, F., 1998. Les minéraux argileux et leur hétérogénéité superficielle: influence de la nature des cations compensateurs de l'illite sur les mécanismes d'adsorption de gaz. PhD Thesis, Institut National Polytechnique de Lorraine.

Barrante, J.R., 1974. Applied Mathematics for Physical Chemistry. Prentice-Hall.

Bénézeth, P., Saldi, G.D., Dandurand, J.L., Schott, J., 2011. Experimental determination of the solubility product of magnesite at 50 to 200 °C. Chem. Geol. 286, 21–31.

Benson, S.M., Cole, D.R., 2008. CO_2 sequestration in deep sedimentary formations. Elements, 4, 325–331.

Berrezueta, E., González-Menéndez, L., Breitner, D., Luquot, L., 2013. Pore system changes during experimental CO_2 injection into detritic rocks: Studies of potential storage rocks from some sedimentary basins of Spain. Int. J. Greenh. Gas Con. 17, 411–422.

Bertier, P., Swennen, R., Laenen, D., Dreesen, R., 2006. Experimental identification of CO_2-water-rock interactions caused by sequestration of CO_2 in Westphalia and Buntsandstein sandstones of the Campine Basin (NE-Belgium). J. of Geochem. Exploration 89, 10-14.

Bibi, I., Singh, B., Silvester, E., 2011. Dissolution of illite in saline–acidic solutions at 25°C. Geochim. Cosmochim. Acta 75, 3237–3249.

Brady, P.V., Carroll, S.A., 1994. Direct effects of CO_2 and temperature on silicate weathering: Possible implications for climate control. Geochim. Cosmochim. Acta 58, 1853–1856.

Broecker, W.S., 2005. Global warming: take action or wait? Jökull 55, 1–16.

Bullard, J.W., Enjolras, E., George, W.L., Satterfield, S.G., Terrill., J.E., 2010. A parallel reaction-transport model applied to cement hydration and microstructure development. Modelling Simul. Mater. Sci. Eng., 18, 16.

Busch, A., Alles, S., Gensterblum, Y., Prinz, D., Dewhurst D.N., Raven, M.D., Stanjek, H., Krooss, B.M., 2008. Carbon dioxide storage potential of shales. Int. J. Greenh. Gas Con. 2, 297–308.

Cama, J., Ganor, J., Ayora, C., Lasaga, C.A., 2000. Smectite dissolution kinetics at 80 °C and pH 8.8. Geochim. Cosmochim. Acta 64, 2701-2717.

Carey, J.W., Wigand, M., Chipera, S.J., Wolde, G., Pawar, R., Lichtner, P.C., Wehner, S.C., Raines, M.A., Guthrie Jr., G.D., 2007. Analysis and performance of oil well cement with 30 years of CO2 exposure from the SACROC Unit, West Texas, USA. Int. J. Greenh. Gas Con. 1, 75–85.

Carroll, S.A., McNab, W.W., Torres, S.C., 2011. Experimental Study of Cement−Sandstone/Shale−Brine−CO_2 Interactions. Geochemical Transactions 12, 9.

Celia, M.A., Bachu, S., Nordbotten, J.M., Gasda, S.E., Dahle, H.K., 2005. Quantitative estimation of CO_2 leakage from geological storage: analytical models, numerical models,

and data needs, in: Rubin, E.S., Keith, D.W., Gilboy, C.F. (Eds.), Greenhouse Gas Control Technologies, Vol. I, Elsevier, pp. 663–671.

Chen, L., Kang, Q., Viswanathan, H.S., Tao, W.Q., 2014. Pore-scale study of dissolution-induced changes in hydrologic properties of rocks with binary minerals. Water Resour. Res. 50, 9343–9365.

Chou, L., Wollast, R., 1985. Steady-State kinetics and dissolution mechanisms of albite. Am. J. Sci. 285, 963–993.

CO2CRC, 2015. CO_2 Cooperative Research Centers, http://www.co2crc.com.au/aboutccs/climatechange.html.

Columbera, P.M., Posner, A.M., Quirk, J.P., 1971. The adsorption of aluminum from hydroxy-aluminum solutions on to Fithian illite. Soil. Sci. Soc. Am. Proc. 22, 118–128.

Credoz, A., Bildstein, O., Jullien, M., Raynal, J., Trotignon, L., Pokrovsky, O., 2011. Mixed-layer illite-smectite reactivity in acidified solutions: Implications for clayey caprock stability in CO_2 geological storage. Appl. Clay Sci. 53, 402–408.

Cubillas, P., Prieto, M., ChaRrat, C., Oelkers, E.H., Kfhler, S., 2005. Experimental determination of the dissolution rates of calcite, aragonite, and bivalves. Chem. Geol. 216, 59–77.

Deng, H., Ellis, B.R., Peters, C.A., Fitts, J.P., Crandall, D., Bromhal, G.S., 2013. Modifications of carbonate fracture hydrodynamic properties by CO_2-acidified brine flow. Energy & Fuels 27, 4221-4231.

Detwiler, R.L., Glass, R.J., Bourcier, W.L., 2003. Experimental observations of fracture dissolution: The role of Peclet number on evolving aperture variability. Geophys. Res. Lett. 30, 1648.

Detwiler, R.L., Rajaram, H., Glass, R.J., 2000. Solute transport in variable-aperture fractures: An investigation of the relative importance of Taylor dispersion and macrodispersion. Water Resour. Res. 36, 1611–1625.

Dewaele, P.J., Reardon, E.J., Dayal, R., 1991. Permeability and porosity changes associated with cement grout carbonation. Cem. Con. Res. 21, 441–454.

Domènech, C., Ayora, C., De Pablo, J., 2002. Oxidative dissolution of pyritic sludge from the Aznalcóllar mine (SW Spain). Chem. Geol. 190, 339–353.

Domenico, P.A., Schwartz, F.W., 1990. Physical and Chemical Hydrogeology. John Wiley and Sons, New York.

Downs, R.T., 2006. The RRUFF Project: an integrated study of the chemistry, crystallography, Raman and infrared spectroscopy of minerals. Program and Abstracts of the 19th General Meeting of the International Mineralogical Association in Kobe, Japan. O03-13.

Duan, Z., Sun, R., 2003. An improved model calculating CO_2 solubility in pure water and aqueous NaCl solutions from 273 to 533 K and from 0 to 2000 bar. Chem. Geol. 193, 257–271.

Duguid, A., 2009. An estimate of the time to degrade the cement sheath in a well exposed to carbonated brine. Energy Procedia 1, 3181–3188.

Duguid, A., Radonjic, M., Scherer, G.W., 2011. Degradation of cement at the reservoir/cement interface from exposure to carbonated brine. Int. J. Greenh. Gas Con. 5, 1413–1428.

Elkhoury, J.E., Ameli, P., Detwiler, R.L., 2013. Dissolution and deformation in fractured carbonates caused by flow of CO_2-rich brine under reservoir conditions. Int. J. Greenh. Gas Control 16, S203–S215.

Ellis, B., Peters, C., Fitts, J., Bromhal, G., Mcintyre, D., Warzinski, R., Rosenbaum, E., 2011. Deterioration of a fractured carbonate caprock exposed to CO_2-acidified solution flow. Greenh. Gases Sci. and Technol. 1, 248–260.

Emberley, S., Hutcheon, I., Shevalier, M., Durocher, K., Mayer, B., Gunter, W.D., Perkins, E.H., 2005. Monitoring of fluid–rock interaction and CO_2 storage through produced fluid sampling at the Weyburn CO_2-injection enhanced oil recovery site, Saskatchewan, Canada. Appl. Geochem. 20, 1131–1157.

European Enviroment Agency (EEA), 2012. Greenhouse gas emission trends and projections in Europe 2012. ISSN 1725-9177. EEA, Copenhagen.

Fisher, S., Liebscher, A., Wandrey, M., the CO_2 SINK Group, 2010. CO_2-brine-rock interaction – first results of long-term exposure experiments at in situ P-T conditions of the Ketzin CO_2 reservoir. Chemie der Erde 70, 155-164.

Friedmann, S.J., 2007. Geological carbon dioxide sequestration. Elements, 3, 179–184.

Gabis, V., 1958. Etude préliminaire des argiles oligocènes du Puy-en-Velay (Haute-Loire). Bull. Soc. Franç. Minéral. Cristallog. 81, 183-185.

Garcia-Rios, M., Cama, J., Luquot, L., Soler, J.M., 2014. Interaction between CO_2-rich sulfate solutions and carbonate reservoir rocks from atmospheric to supercritical CO_2 conditions: Experiments and modeling. Chem. Geol. 383, 107–122.

Garcia-Rios, M., Luquot, L., Soler J.M., Cama, J., 2015. Influence of the flow rate on dissolution and precipitation features during percolation of CO_2-rich sulfate solutions through fractured limestone samples. Chem. Geol. 414, 95–108.

Garrido, D.R., Lafortune, S., Souli, H., Dubujet, P., 2013. Impact of supercritical CO_2/water interaction on the caprock nanoporous structure. Procedia Earth and Planetary Science 7, 738–741.

Gasda S.E., Bachu, S., Celia, M.A., 2004. Spatial characterization of the location of potentially leaky wells penetrating a deep saline aquifer in a mature sedimentary basin. Environ. Geol. 46, 707-720.

Gaus, I., 2010. Role and impact of CO_2–rock interactions during CO_2 storage in sedimentary rocks. Int. J. Greenh. Gas Control 4, 73–89.

Gaus, I., Azaroual, M., Czernichowski-Lauriol, I., 2005. Reactive transport modelling of the impact of CO_2 injection on the clayey caprock at Sleipner (North Sea). Chem. Geol. 217, 319–337.

Gherardi, F., Xu, T., Pruess, K., 2007. Numerical modeling of self-limiting and self-enhancing caprock alteration induced by CO_2 storage in a depleted gas reservoir. Chem. Geol. 244, 103–129.

Hamer, M., Graham, R.C., Amrhein, C., Bozhilov, K.N., 2003. Dissolution of Ripidolite (Mg, Fe-Chlorite) in Organic and Inorganic Acid Solutions. Soil Sci. Soc. Am. J. 67, 654–661.

Hänchen, M., Prigiobbe, V., Baciocchi, R., Mazzotti, M., 2008. Precipitation in the Mg-carbonate system-effects of temperature and CO_2 pressure. Chem. Eng. Sci. 63, 1012–1028.

Hangx, S.J.T., Spiers, C.J., Peach, C.J., 2010. The effect of deformation on permeability development in anhydrite and implications for caprock integrity during geological storage of CO_2. Geofluids 10, 369–387.

Harrison, J., 2001. Reactive magnesium oxide cements. In: W.I.P. Organisation (Ed.), Australia.

Haugan, P.M., Drange, H., 1996. Effects of CO_2 on the ocean environment. Energy conversion and management 37, 1019-1022.

Hellmann, R., Daval, D., Tisserand, D., 2010. The dependence of albite feldspar dissolution kinetics on fluid saturation state at acid and basic pH: Progress towards a universal relation, C. R. Geoscience, 342, 676–684.

Hesse, M., Orr, F., Tchelepi, H., 2008. Gravity currents with residual trapping .J. Fluid Mech. 611, 35–60.

Holloway S., 2001. Storage of fossil fuels-derived carbon dioxide beneath the surface of the earth, Annu. Rev. Energ. Env. 26, 145–166.

Huerta, N.J., Bryant, S.L., Strazisar, B.R., Hesse M., 2011. Dynamic alteration along a fractured cement/cement interface: Implications for long term leakage risk along a well with an annulus defect. Energy Procedia 4, 5398–5405.

Huitt, J.L., 1956. Fluid flow in simulated fractures, Am. Inst. Chem. Eng. 2, 259–264.

Intergovernmental Panel on Climate Change (IPCC), 2014. Climate Change 2014: Mitigation of Climate Change. Contribution of Working Group III to the Fifth Assessment Report of the Intergovernmental Panel on Climate Change [Edenhofer, O., R. Pichs-Madruga, Y. Sokona, E. Farahani, S. Kadner, K. Seyboth, A. Adler, I. Baum, S. Brunner, P. Eickemeier, B. Kriemann, J. Savolainen, S. Schlömer, C. von Stechow, T. Zwickel and J.C. Minx (eds.)]. Cambridge University Press, Cambridge, United Kingdom and New York, NY, USA.

International Energy Agency (IEA), 2012. World energy outlook. OECF/IEA, France.

International Energy Agency (IEA), 2013. CO_2 emissions from fuel combustion. Highlights. OECD/IEA, France.

International Energy Agency (IEA), 2014. CO_2 emissions from fuel combustion. Highlights. OECF/IEA, France.

Jeschke, A., Vosbeck, K., Dreybrodt, W., 2001. Surface controlled dissolution rates of gypsum in aqueous solutions exhibit nonlinear dissolution kinetics. Geochim. Cosmochim. Acta, 65, 27–34.

Jung, H.B., Kabilan, S., Carson, J.P., Kuprat, A.P., Um, W., Martin, P., Dahl, M., Kafentzis, T., Varga, T., Stephens, S., Arey, B., Carroll, K.C., Bonneville, A., Fernandez, C.A., 2014. Wellbore cement fracture evolution at the cement–basalt caprock interface during geologic carbon sequestration. Appl. Geochem. 47, 1–16.

Kampman, N., Bickle, M., Wigley, M., Dubacq, B., 2014. Fluid flow and CO_2 –fluid–mineral interactions during CO_2–storage in sedimentary basins. Chem. Geol. 369, 22–50.

Kaszuba, J.P., Janecky, D.R., Snow, M.G., 2005. Experimental evaluation of mixed fluid reactions between supercritical carbon dioxide and NaCl solution: Relevance to the integrity of a geologic carbon repository. Chem. Geol. 217, 277–293.

Ketzer, J.M., Iglesias, R., Einloft, S., Dullius, J., Ligabue, R., de Lima, V., 2009. Water–rock–CO_2 interactions in saline aquifers aimed for carbon dioxide storage: Experimental and numerical modeling studies of the Rio Bonito Formation (Permian), southern Brazil. Appl. Geochem. 24, 760–767.

Knauss, K.G., Nguyen, S.N., Weed, H.C., 1993. Diopside dissolution kinetics as a function of pH, $C0_2$, temperature, and time. Geochim. Cosmochim. Acta 57, 285–294.

Kohler, E., Parra, T., Vidal, O., 2009. Clayed Cap-rock behavior in H_2O–CO_2 media at low pressure and temperature conditions: An experimental approach. Clay Clay Miner. 57, 616–637.

Köhler, S.J., Dufaud, F., Oelkers, E.H., 2003. An experimental study of illite dissolution kinetics as a function of ph from 1.4 to 12.4 and temperature from 5 to 50°C. Geochim. Cosmochim. Acta 67, 3583–3594.

Korbøl, R., Kaddour, A., 1995. Sleipner vest CO_2 disposal-injection of removed CO_2 into the utsira formation. Energy Conversion and Management 36, 509–512.

Kristova, P., Hopkinson, L.J., Rutt, K.J. Hunter, H.M.A., Cressey, G., 2014. Carbonate mineral paragenesis and reaction kinetics in the system MgO–CaO–CO_2–H_2O in presence of chloride or nitrate ions at near surface ambient temperatures. Appl. Geochem. 50, 16–24.

Kutchko, B.G., Strazisar, B.R., Dzombak, D.A., Lowry, G.V.,Thaulow, N., 2007. Degradation of well cement by CO_2 under geologic sequestration conditions. Env. Sci. Technol. 41, 4787–4792.

Kutchko, B.G., Strazisar, B.R., Lowry, G.W., Dzomback, D.A., Thaulow, N., 2008. Rate of CO_2 attack on hydrated Class H well cement under geologic sequestration conditions. Env. Sci. Technol. 42, 6237–6242.

Lackner, K.S., 2003. A guide to CO_2 sequestration. Science, 300, 1677–1678.

Laurila, T., Vuorinen, V., Kivilahti, J.K., 2005. Interfacial reactions between lead-free solders and common base materials. Mater. Sci. Eng. 49, 1–60.

Liteanu, E., Spiers, C.J., 2011. Fracture healing and transport properties of wellbore cement in the presence of supercritical CO_2. Chem. Geol. 281, 195–210.

Liu, F., Lu, P., Griffith, C., Hedges, S.W., Soong, Y., Hellevang, H., Zhu, C., 2012. CO_2–solution–caprock interaction: Reactivity experiments on Eau Claire shale and a review of relevant literature. Int. J. Greenh. Gas Con. 7, 153–167.

Lowson, R.T., Brown, P.L., Comarmond, M-C.J., Rajaratnam, G., 2007. The kinetics of chlorite dissolution. Geochim. Cosmochim. Acta 71, 1431–1447.

Luquot, L., Abdoulghafour, H., Gouze, P., 2013. Hydro-dynamically controlled alteration of fractured Portland flowed by CO_2-rich brine cements. Int. J. Greenh. Gas Con. 16, 167–179.

Luquot, L., Andreani, M., Gouze, P., Camps, P., 2012. CO_2 percolation experiment through chlorite/zeolite-rich sandstone (Pretty Hill Formation – Otway Basin–Australia). Chem. Geol. 294-295, 75–88.

Luquot, L., Gouze, P., 2009. Experimental determination of porosity and permeability changes induced by injection of CO_2 into carbonate rocks. Chem. Geol. 265, 148–159.

Mo, L., Deng, M., Tang, M., Al-Tabbaa, A., 2014. MgO expansive cement and concrete in China: Past, present and feature. Cement Concrete Res. 57, 1-12.

Nogues, J.P., Fitts, J.P., Celia, M.A., Peters, C.A., 2013. Permeability evolution due to dissolution and precipitation of carbonates using reactive transport modeling in pore networks. Water Resour. Res. 49, 6006–6021.

Nogues, J.P., Nordbotten, J.M., Celia, M.A., 2011. Detecting leakage of brine or CO_2 through abandoned wells in a geological sequestration operation using pressure monitoring wells. Energy Procedia 4, 3620–3627.

Noiriel, C., Luquot, L., Madé, B., Raimbault, L., Gouze, P., van der Lee, J., 2009. Changes in reactive surface area during limestone dissolution: An experimental and modeling study. Chem. Geol. 265, 160–170.

Noiriel, C., Madé, B., Gouze, P., 2007. Impact of coating development on the hydraulic and transport properties in argillaceous limestone fracture. Water Resour. Res. 43, W09046.

Oelkers, E.H., 2001. General kinetic description of multioxide silicate mineral and glass dissolution. Geochim. Cosmochim. Acta 65, 3703–3719.

Oelkers, E.H., Cole, D.R., 2008. Carbon dioxide sequestration; a solution to a global problem. Elements 4, 305–310.

Oelkers, E.H., Gislason, S.R., Matter, J., 2008. Mineral carbonation of CO_2. Elements 4, 333–337.

Oelkers, E.H., Schott, J., 2005. Geochemical aspects of CO_2 sequestration. Chem. Geol. 217, 183–186.

Offeddu, F.G., Cama, J., Soler, J.M., Dávila, G., McDowell, A., Craciunescu, T., Tiseanu, I., 2015. Processes affecting the efficiency of limestone in passive treatments for AMD: Column experiments. J. Environ. Chem. Eng. 3, 304-316.

Offeddu, F.G., Cama, J., Soler, J.M., Putnis, C.V., 2014. Direct nanoscale observations of the coupled dissolution of calcite and dolomite and the precipitation of gypsum. Beilstein J. Nanotechnol. 5, 1245–1253.

Pacala, S., Socolow, R., 2004. Stabilization wedges: solving the climate problem for the next 50 years with current technologies. Science 305, 968–972.

Palandri, J.L. Kharaka, Y.K., 2004. A compilation of rate parameters of water-mineral interaction kinetics for application to geochemical modeling. Science for a changing world. U.S. Geol. Surv. Open File Report 2004-1068.

Park, C-H., Taron, J., Görke, U-J., Singh, A.K., Kolditz, O., 2011. The fluidal interface is where the action is in CO_2 sequestration and storage: Hydromechanical analysis of mechanical failure. Energy Procedia 4, 3691–3698.

Parkhurst, D.L., Appelo, C.A.J., 2013. Description of input and examples for PHREEQC (Version 3)-a computer program for speciation, batch-reaction, one-dimensional transport, and inverse geochemical calculations. U.S. Geological Survey Techniques and methods report. Book 6, 49.

Pokrovsky, O., Golubev, S.V., Schott, J., Castillo, A., 2009. Calcite, dolomite and magnesite dissolution kinetics in aqueous solutions at acid to circumneutral pH, 25 to 150 °C and 1 to 55 atm pCO_2: New constraints on CO_2 sequestration in sedimentary basins. Chem. Geol. 265, 20–32.

Pokrovsky, O.S., Schott, J., 1999. Processes at the magnesium-bearing carbonates/solution interface. II. Kinetics and mechanism of magnesite dissolution. Geochim. Cosmochim. Acta 6, 881– 897.

Rahman, M., Mansur, M.A., Chua, K.H., 1988. Evaluation of advanced cementitious composites for machine tool structures, Annals of the CIRP Annals Manufacturing Technology 37, 373–376.

Raines, M., Dewers, T., 1997. “Mixed” kinetics control of fluid-rock interaction in reservoir production scenarios. J. Pet. Sci. Eng. 17, 139–155.

Revil, A., Glover, P.W.J., 1997. Theory of ionic-surface electrical conduction in porous media, Phys. Rev. B, 55, 1757-1773.

Samson, E., Marchand, J., 2003. Calculation of ionic diffusion coefficients on the basis of migration test results. Mater. Structu. 36, 156–165.

Schaef, H.T, Windisch Jr, C.F, Mc Grail, B. P., Martin, P.F, Rosso, K.M., 2011. Brucite [$Mg(OH)_2$] carbonation in wet supercritical CO_2: An in situ high pressure X-ray diffraction study. Geochim. Cosmochim. Acta 75, 7458–7471.

Scherer, G.W., Celia, M.A., Prévost, J.-H., Bachu, S., Bruant, R., Duguid, A., Fuller, R., Gasda, S.E., Radonjic, M., Vichit-Vadakan, W., 2005: Leakage of CO_2 through abandoned wells: role of corrosion of cement, in: Thomas, D.C., Benson, S.M. (Eds.), Carbon Dioxide Capture for Storage in Deep Geologic Formations, Vol. 2, pp. 827-848.

Scherer, G.W., Kutchko, B., Thaulow, N., Duguid, A., Mook, B., 2011. Characterization of cement from a well at Teapot Dome Oil Field: Implications for geological sequestration. Int. J. Greenh. Gas Con. 5, 115–124.

Schrag, D.P., 2007. Preparing to capture carbon. Science 315, 812–813.

Shukla, R., Rajith, P., Haque, A., Choi, X., 2010. A review of studies on CO_2 sequestration and caprock integrity. Fuel 89, 2651–2664.

Singurindy, O., Berkowitz, B., 2005. The role of fractures on coupled dissolution and precipitation patterns in carbonate rocks. Adv. Water Resour. 28, 507-521.

Sjöberg, E.L., Rickard, D.T., 1984. Temperature-dependence of calcite dissolution kinetics between 1º C and 62 ºC at pH 2.7 to 8.4 in aqueous-solutions. Geochim. Cosmochim. Acta 48, 485–493.

Smith, M.M., Carroll, S.A., 2014. Experimental Determination of Chlorite Kinetics at Geothermal Conditions, in: Thirty-Ninth Workshop on Geothermal Reservoir Engineering, Stanford University, Stanford, California.

Smith, M.M., Sholokhova, Y., Hao, Y., Carroll, S.C., 2013. Evaporite Caprock Integrity: An Experimental Study of Reactive Mineralogy and Pore-Scale Heterogeneity during Brine-CO_2 Exposure. Environ. Sci. Technol. 47, 262–268.

Snow, D.T., 1969. Anisotropic Permeability on Fractured Media. Water Resour. Res. 6, 1273–1289.

Soler, J. M., Vuorio, M., Hautojärvi, A., 2011. Reactive transport modeling of the interaction between water and a cementitious grout in a fractured rock. Application to ONKALO (Finland). Appl. Geochem. 26, 1115–1129.

Soler, J.M., Boi, M., Mogollón, J.L., Cama, J., Ayora, C., Nico, P.S., Tamura, N., Kunz, M., 2008. The passivation of calcite by acid mine water. Column experiments with ferric sulfate and ferric chloride solutions at pH 2. Appl. Geochem. 23, 3579–3588.

Soler, J.M., Mäder, U.K., 2010. Cement-rock interaction: Infiltration of a high-pH solution into a fractured granite core. Geo. Acta 3, 221–233.

Steefel, C.I., Appelo, C.A.J., Arora, B., Jacques, D., Kalbacher, T., Kolditz, O., Lagneau, V., Lichtner, P.C., Mayer, K.U., Meeussen, J.C.L., Molins, S., Moulton, D., Shao, H., Šimůnek, J., Spycher, N., Yabusaki, S.B., Yeh, G.T., 2015. Reactive transport codes for subsurface environmental simulation. Computat. Geosci. 19, 445-478.

Szymczak, P., Ladd, A.J.C., 2009. Wormhole formation in dissolving fractures. J. Geophys. Res. 114, B06203.

Tian, H., Xu, T., Wang, F., Patil, V.V., Sun, Y., Yue, G., 2014. A numerical study of mineral alteration and self-sealing efficiency of a caprock for CO_2 geological storage. Acta Geotech. 9, 87–100.

Tongwa, P., Nygaard N., Blue, A., Bai, B., 2013. Evaluation of potential fracture-sealing materials for remediating CO_2 leakage pathways during CO_2 sequestration. Int. J. Greenh. Gas Con. 18, 128–138.

Tutolo, B.M., Luhmann, A.J., Kong, X.Z., Saar, M.O., Seyfried, W.E., 2015.CO_2 sequestration in feldspar-rich sandstone: Coupled evolution of fluid chemistry, mineral reaction rates, and hydrogeochemical properties. Geochim. Cosmochim. Acta 160, 132–154.

Ullman, W.J., Aller, R.C., 1982. Diffusion coefficients in near shore marine sediments. Limnol. Oceanog. 27, 552-534.

Unluer, C., Al-Tabbaa A., 2013. Impact of hydrated magnesium carbonate additives on the carbonation of reactive MgO cements. Cement Concrete Res. 54, 87–97.

Vilarrasa, V., Carrera J., Olivella, S., 2013. Hydromechanical characterization of CO_2 injection sites. Int. J. Greenh. Gas Con. 1, 665–677.

Watson, T.L., Bachu, S., 2008. Identification of wells with high CO_2-leakage potential in mature oil fields developed for CO_2-enhanced oil recovery. SPE Paper 112924, SPE Improved Oil Recovery Symposium, Tulsa, Oklahoma, U.S.A., 19–23 Apr.

Wigand, M., Carey, J.W., Schütt, H., Spangenberg, E., Erzinger, J., 2008. Geochemical effects of CO_2 sequestration in sandstones under simulated in situ conditions of deep saline aquifers. Appl. Geochem. 28, 2735-2745.

Wolery, T. J., Jackson, K.J., Bourcier, W.L., Bruton, C.J., Viani, B.E., Knauss, K.G. and Delany, J.M., 1990. Current status of the EQ3/6 software package for geochemical modeling, in: Melchior, C., Bassett, R.L. (Eds.), Chemical Modeling of Aqueous Systems II. Am. Chem. Soc. Symp. Ser. 416, 104-116.

Xu, J., Fan, C., Teng, H.H., 2012. Calcite dissolution kinetics in view of Gibbs free energy, dislocation density, and pCO_2. Chem. Geol. 322-323, 11–18.

Yalcinkaya, T., Radonjic, M., Willson, C., Bachu, S., 2011. Experimental study on a single cement-fracture using CO_2 rich brine. Energy Procedia 4, 5335–5342.

Young, R.A., 1995. The Rietveld Method, vol. 5, International Union of Crystallography Monographs on Crystallography. Oxford University Press, USA.

Yu, Z., Liu, L., Yang, S., Li, S., Yang, Y., 2012. An experimental study of CO_2–solution–rock interaction at in situ pressure–temperature reservoir conditions. Chem. Geol. 326–327, 88–101.